University of Strathclyde
Department of Mechanical & Aerospace Engineering

Data-based vibration structural health monitoring methodology for composite laminated structures

David García Cava

A thesis presented in fulfilment of the requirements
for the degree of Doctor of Philosophy

2016

Declaration of author's rights

This thesis is the result of the author's original research. It has been composed by the author and has not been previously submitted for examination which has led to the award of a degree.

The copyright of this thesis belongs to the author under the terms of the United Kingdom Copyright Acts as qualified by University of Strathclyde Regulation 3.50. Due acknowledgement must always be made of the use of any material contained in, or derived from, this thesis.

David García Cava

May 5, 2016

Supervisor

Dr. Irina Trendafilova
Department of Mechanical and Aerospace Engineering
University of Strathclyde
Glasgow, United Kingdom

Examiners

External examiner

Dr. Graeme Manson
Department of Mechanical Engineering
University of Sheffield
Sheffield, United Kingdom

Internal examiner

Dr. Matthew Stickland
Department of Mechanical and Aerospace Engineering
University of Strathclyde
Glasgow, United Kingdom

Acknowledgements

First and foremost sincere gratitude must go to my supervisor Dr Irina Trendafilova, without whom this work would not have been possible. Irina was always available to guide, help, support and encourage throughout this thesis. I have to especially thank her for keeping up with my mental thoughts and my constant worries. I have also to thank Irina for being a wonderful person and good friend.

Secondly, I would like to thank to Professor Daniel J. Inman at The University of Michigan for his support and guidance during my stay in Ann Arbor. I would like to thank The Royal Society of Edinburgh through John Moyes Lessells Travel Scholarship, The Institution of Mechanical Engineers through the Flatman grant, The Institution of Engineering and Technology through their Travel Award, The University of Strathclyde through the Travel Award and the department of Mechanical and Aerospace engineering for support this collaboration which without their financial support could have not been possible.

A lot of thanks must also go to Dr. Dmitri Tcherniak from Brüel & Kjær Sound & Vibration Measurements for being an essential part of my research. I would like to thank Dmitri for providing the data for the small wind turbine blade and the large SSP34m wind turbine blade. This collaboration have served to know each other, not only for future collaborations but also for having the chance to meet such a friendly person.

I would like to express my gratitude to Hussein Al-bugharbee for being at the University of Strathclyde at any time when I had the need of support, help and for sharing his great knowledge about life. Thanks Hussein for being such a good person.

I also would like to thank to the department of Mechanical and Aerospace Engineering at The University of Strathclyde for all support during these three and a half years. I would like to thank Dr Grzegorz Liśkiewicz, now Assistant Professor at Lodz University of Technology, for being at the University of Strathclyde from the very beginning of my PhD studies. Meet with Grzeg at Strathclyde has been wonderful and unique. I would also like to thank all and each one of my colleagues for making this period so enjoyable and unforgettable, especially to 'Los Domingueros.'

Finally, but by no means least important, I would like to express my deep gratitude to my parents and sister for their dedication and support over so many years and also to Margit for her support, encouragement, patience and unwavering love.

Abstract

Composite materials are steadily replacing traditional materials in a wide range of industry sectors thanks to their remarkable properties. Damage in composite materials exhibits complex failure modes which are difficult to identify by conventional techniques. Composite materials demonstrate complex nonlinear vibration behaviour where conventional vibration-based structural health monitoring (VSHM) methods might not give adequate information for damage identification. This thesis investigates the capabilities of singular spectrum analysis (SSA) as a technique for developing a completely data-based VSHM methodology. The methodology decomposes the vibration responses in a certain number of principal components having in consideration all rotational patterns at any frequency including the nonlinear oscillations. This thesis develops two approaches to use SSA in the time and frequency domain. The methodology has been validated using a numerical system and an experiment with delaminated beams. The results demonstrate the methodology capability for assessing damages at different locations and with different sizes. The progression of damage can also be tracked. Delamination was successfully assessed in composite laminated plates with different delamination locations, in-plane and through different layers. Damage in wind turbine blades was assessed by the damage assessment methodology with a statistical hypothesis inspection phase based on probability distribution functions. Different damage locations and sizes were assessed as well as damage progression. This thesis explores the use of smart materials which enable self-sensing and self-diagnosing of its structural integrity coupled with the data-based VSHM. The results demonstrate the substantial potential of this approach. Overall, the data-based VSHM methodology presented in this thesis is proven to give adequate information about the presence, location and extent of delamination and other defects in different composite laminated structures.

Publications

Journal publications

D. García, I. Trendafilova and D. J. Inman. A study on vibration-based self-monitoring capabilities of nano-enriched composite laminated beam. *Smart Materials and Structures*, 25:045-011, 2016.

D. García, R. Palazzetti, I. Trendafilova, C. Fiorini and A. Zucchelli. Vibration-based delamination diagnosis and modelling for composite laminate plates. *Composite Structures*, 130:155-162, 2015.

D. García, M. Stickland and G. Liskiewicz. Dynamical system analysis of unstable flow phenomena in centrifugal blower. *Open Engineering*, 5:332-342, 2015.

D. García and I. Trendafilova. A multivariate data analysis approach towards vibration analysis and vibration-based damage assessment. Application for delamination detection in composite materials. *Journal of Sound and Vibration*, 333(25):7036-7050, 2014.

Peer reviewed conference papers

D. García, D. Tcherniak and I. Trendafilova. Damage assessment for wind turbine blades based on a multivariate statistical approach. *In Proceedings of Journal of Physics: Conference Series*, (628) 012086, 2015. 11^{th} International Conference on Damage Assessment of Structures 2015, Ghent, 24-25 August, 2015.

D. García, M. Stickland and G. Liskiewicz. Dynamical system analysis of unstable flow phenomena in centrifugal blower. In Proceedings of 11^{th} International symposium on compressor and turbine flow systems theory and application areas, Lodz, 20-23 October, 2014.

D. García and I. Trendafilova. Singular Spectrum Analysis for identifying structural nonlinearity using free-decay responses. Application for delamination detection and diagnosis in composite laminates. In Proceedings of 26^{th} International Conference on Noise and Vibration Engineering, Leuven, Belgium, 15-17 September, 2014.

R. Palazzetti, D. García, I. Trendafilova, C. Fiorini and A. Zucchelli. An investigation in vibration modeling and vibration-based monitoring for composite laminates. In Proceedings of 26^{th} International Conference on Noise and Vibration Engineering, Leuven, Belgium, 15-17 September, 2014.

D. García, I. Trendafilova and H. Al-Bugharbee. Vibration-based health monitoring approach for composite structures using multivariate statistical analysis. In Proceedings of EWSHM-7th European workshop on structural health monitoring, Nantes, France, 8-11 July, 2014.

D. García, I. Trendafilova. Multivariate statistical analysis for damage and delamination detection in composite structures. In Proceedings of 11^{th} International Conference on Vibrations Problems, Lisbon, Portugal, 9-12, September, 2013.

Contents

List of figures

List of tables

Nomenclature

$\mathbf{A}_k$	k^{th} principal component of $\check{\mathbf{X}}$
α	risk level (probability)
$\mathbf{C}_{\mathbf{X}}$	covariance matrix of $\check{\mathbf{X}}$
c	category index
C	number of categories
$[\mathbf{C}]$	damping matrix in the numerical system
c_1, c_2, c_3	damping coefficients in the numerical system
$\mathbf{D}_i$	damage index of an i^{th} observation feature vector
$D_i(B_C)$	distance of i^{th} observation to category C
$\mathbf{D}_i(B_C)$	distances vector of an observation to all categories c
D	Damage indices of the training data set
D_T	Statistical hypothesis threshold
Δ_t	sampling rate
Δ_f	frequency resolution
ρ_k, $\mathbf{E}_k$	k^{th} eigenvector of $\mathbf{C}_{\mathbf{X}}$
$\mathbf{E}_X$	eigenvectors matrix of $\mathbf{C}_{\mathbf{X}}$
$\mathbf{E}_X^t$	transpose matrix of $\mathbf{E}_X$
erf	error function
$\mathbf{f}(\dot{\mathbf{x}}, \mathbf{x})$	nonlinear quadratic coupling function in the numerical system
$\mathcal{F}\{\mathbf{R}^m\}$	frequency spectrum matrix of $\mathbf{R}^m$ in the time domain
$f(D\|\mu, \sigma)$	lognormal probability density function of D
$F(D\|\mu, \sigma)$	lognormal cumulative density function
ϑ	threshold value
F^{-1}	inverse of lognormal cumulative density function
$\mathbf{H1}$, $\mathbf{H2}$	hypotheses of the decision making

i	variable of an observation feature vector
j	variable of a feature vector index
k	eigenvalue and eigenvector index
K	total number of eigenvalues and eigenvectors
$[\mathbf{K}]$	stiffness matrix in the numerical system
k_1, k_2, k_3	linear stiffness coefficients in the numerical system
k_n	nonlinear stiffness coefficient in the numerical system
κ	absolute percent value of the natural frequency change
λ_k	k^{th} eigenvalue of $\mathbf{C_X}$
Λ_k	eigenvalues matrix of $\mathbf{C_X}$
M	number of signal vector realisations
m	signal realisations index
$[\mathbf{M}]$	mass matrix in the numerical system
m_1, m_2	mass parameters in the numerical system
μ_m	mean of $\mathbf{x}_m$
μ_B	mean vector of each $\mathbf{T}^s$ in $\mathbf{T}_B$
μ	mean and of ln D
N	length of the signal vector $\mathbf{x}_m$
n	variable index in $\mathbf{x}_m$
p	reduced dimension of the feature space
P_{signal}	signal power
P_{noise}	noise power
σ_m^2	variance of $\mathbf{x}_m$
σ	standard deviation of $\mathbf{x}_m$
σ	standard deviation of ln D
$\mathbf{\Sigma}^{-1}$	inverse of the covariance matrix of $\mathbf{T}_B$
$\mathbf{R}_k$	k^{th} reconstructed component of $\check{\mathbf{X}}$
$\mathbf{R}$	full reconstructed components matrix of $\check{\mathbf{X}}$
$\mathbf{R}^m$	m reconstructed components matrix of $\check{\mathbf{X}}$. Reference state
s	variable of a baseline feature vector index

SNR	signal-to-noise-ratio
T_j	variable of a feature vector
$\mathbf{T}$	feature vector
$\mathbf{T}^s$	baseline feature vector
$\mathbf{T}_B$	baseline feature vectors matrix
$\mathbf{T}^i$	observation feature vector
t	continuous time ($t \in \mathbb{R}$)
T_s	acquisition time
w	sliding window size index
W	sliding window size
W_n	normalisation factor for $\mathbf{R}_k$
ω	natural frequency
$\mathbf{x}_m$	signal vector realisation m
$\bar{\mathbf{x}}_\mathbf{m}$	standardized signal vector $\mathbf{x}_m$
$\mathbf{X}$	signal vector realisations matrix
$\check{\mathbf{X}}_\mathbf{m}$	embedded matrix of $\mathbf{x}_m$
$\check{\mathbf{X}}$	full embedded matrix
$\check{\mathbf{X}}^t$	transpose matrix of $\check{\mathbf{X}}$
$\mathbf{x}$	displacement matrix in the numerical system
$\dot{\mathbf{x}}$	velocity matrix in the numerical system
$\ddot{\mathbf{x}}$	acceleration matrix in the numerical system
$\mathbf{Y}_m(k)$	frequency spectrum of each $\mathbf{x}_m$
$\|\mathbf{Y}_m(k)\|$	magnitude of the frequency spectrum of each $\mathbf{x}_m$

Acronyms

AC	Alternating Current
CB	Carbon Black
DC	Direct Current
DAQ	Data AcQuisition
DOF	Degree of freedom
FV	Feature Vector
FVs	Feature Vectors
FEM	Finite Element Model
FRP	Fibre Reinforcement Plastics
LE	Leading Edge
MSSA	Multichannel Singular Spectrum Analysis
NDT	Non-Destructive Testing
PCA	Principal Component Analysis
PCs	Principal Components
PC	Principal Component
PDF	Probability Density Function
RCs	Reconstructed Components
RC	Reconstructed Component
SSA	Singular Spectrum Analysis
SHM	Structural Health Monitoring
TE	Trailing Edge
VSHM	Vibration-based Structural Health Monitoring
WTB	Wind Turbine Blades

Chapter 1

Introduction

1.1 Motivation

Composite materials are continuously gaining more importance and their applications are constantly growing as a result of their advantageous properties, most notably their large strength-to-weight ratio, corrosion resistance, high impact strength and their magnificent design flexibility. They are steadily replacing traditional structures in a wide range of industry sectors, including the aerospace, wind energy, marine, nuclear engineering, oil and gas industries and even in every day structures [1]. The emergent industries of aerospace, aircraft and especially wind energy [2] placed these materials at the forefront of the contemporary research.

Damage in composite materials do not follow conventional patterns but they exhibit complex failure modes such as transverse cracks and delamination. Damage, such as delamination, is difficult to identify by visual or conventional techniques because it usually occurs internally between the laminates. These damages are locally originated and can grow without any notice until the entire structural member is severely affected. The visual inspections and maintenance procedures can be dangerous, time consuming, expensive and they might require a tedious planning, which can be different and particular for each case. Also these maintenance procedures require ready accessibility which in some occasions is very difficult due to the remote structure location. This is an important factor for the dramatic growth of the off-shore wind turbines because of their remote location which makes their inspection costly and difficult.

This is why structural health monitoring (SHM) plays an important role in the inspection of the structural integrity of these materials. SHM methodologies can be fully integrated and work as an on-line system. Most of these structures are subjected to vibrations and therefore, vibration-based structural health monitoring (VSHM) methods present an attractive possibility since they are global and as such can be used to inspect parts which are difficult or impossible to access. They are based on the fact that any change in a structure, including damage, introduces a change in its vibratory behaviour. By nature, these materials demonstrate complex nonlinear vibration behaviour which makes difficult to inspect for flaws and repair. Conventional linear structural dynamics like modal analysis cannot be applied to structures made of composite materials because they demonstrate complex nonlinear dynamic behaviour and such methods do not give sensible and informative results. The development of these models can be difficult to reproduce accurately the damage mechanisms or the boundary conditions which can introduce false indications of damage. Also, this process does not take advantage of changes in the system response that are caused by nonlinear effects such as delamination mechanism. The response of a nonlinearly vibrating structure is a nonlinear signal which has slight predictability in these conventional methods. For this reason data-based methodologies are more appropriate for structures made of composite materials. These methods are based on the measured vibration responses of the structure and they take into account all the rotational patterns included in such a vibration response which also include the nonlinear oscillations. The work covered in this thesis uses a technique known as singular spectrum analysis (SSA) which is able to decompose the vibration response in a certain number of components taking into consideration all the rotational patterns. Thereby, a free vibration response of a structure will contain information about the modal frequencies of the structure which are contained in the decomposed components by SSA. Based on these components, a reference state can be considered to obtain sensitive features for damage identification. This is aimed to be used for the development of a data-based VSHM system, which on the basis of the measured vibration response, will give information about the presence, the location and the extent of delamination and/or other defects in structures made of composite materials.

Another aspect which motivates this research is the consideration of smart materials which are able to dynamically self-sense and self-diagnose their structural integrity. This is motivated by the use of conductive nano-composites [3] embedded within the material to obtain a vibration response which is processed by the data-based vibration health assessment methodology. The concept is based on a non-intervention principle, coupled with new integrated sensing structure technology. This approach comprises a new self-sensing and self-diagnosing paradigm coupled with a data-based VSHM methodology for assessing damage in the structure.

1.2 An overview of Structural Health Monitoring

The aim of this Chapter is to provide a general overview of Structural Health Monitoring. This involves to define the aims of the SHM with the different damage states, the challenges that SHM has to confront, how to define a monitoring procedure and a selected literature overview of the advances in the recent years to frame the research objectives considered in the work presented in this thesis.

1.2.1 Aim of SHM

Structural health monitoring is a multidisciplinary technology which aims to identify and objectively quantify the information of any occurrence regarding to the structural integrity. The data information is generally measured from a proper array of sensors distributed on the structure in order to reduce the number of unnecessary maintenance inspections. It is important to identify any occurrence of damage at an early stage to avoid rapidly catastrophic failures. Alternative definitions and general information about SHM methodologies can be found in Sohn et al. [4].

A SHM process is expected to be global in the sense of covering the entire structure or significant part of it, automated or with minimum human interaction, cost-effective and capable of assessing the damage 'levels' defined by Rytter [5]. The main objectives of a SHM method are very well defined and formalised by Rytter's damage identification levels. They are summarised as follows in terms of difficulty in increasing order:

- Level I - *Damage detection*: Detect the presence of the damage in the structure.

- Level II - *Damage localisation*: Identification of the damage type and location in the structure domain.
- Level III - *Damage quantification*: Estimation of the extent/severity of the damage.
- Level IV - *Damage prognosis*: Prediction of the remaining service-life of the structure.

In recent years, different damage identification levels have been developed , which generally keep the same hierarchy as Rytters classification, but Level II is divided in two; one for identifying the *damage type* and other for *damage location.* In these distribution levels, the first three levels correspond to *damage diagnosis* and level IV to *damage prognosis.* In the recent years, the development of SHM procedures and more importantly the advances in smart materials have provided a natural combination because many of the best algorithms require known or controlled excitation and sensing rather than just sensing. This introduces the possibility of a self-sensing systems where the structures can be self-diagnosed. Also, the advances of smart materials has the potential to counteract damage when it is detected with the possibility of self-healing. In this sense Park and Inman [6] introduced an extension to the damage identification levels mentioned above. Two more levels are introduced as follows:

- Level V - *Self-diagnosis*: Detect, localise and quantify damage by the structure/system itself.
- Level VI - *Self-healing*: Materials/structures capable to repair damage caused by mechanical usage.

The idea of fulfilling the general objectives of SHM system presents an enormous potential for the current development within a wide range of industries (e.g. aircraft, automotive and wind energy). These industries are increasingly present in projects of great responsibility where a failure could lead to huge losses. Periodic maintenance inspections are often time consuming and expensive due to the required operational down-time. Therefore, an ideally integrated SHM system reduces the maintenance costs and may lead to a significant economic impact to boost industries within a competitive market (e.g. off-shore wind turbines). The development of SHM systems can also help to exploit the use of new advanced materials such as nanocomposites which are proving one of the most exciting advances within a wide range of industries. Nanocomposites predominantly introduce additional functionalities of existing materials such as composite laminates. One of these functionalities is to use embedded nanocomposites to build an integrated self-sensing and self-diagnosis material. As such, there is a need of the development of SHM systems which are capable to process the measured information through the new advanced materials.

SHM and the Non-Destructive Testing (NDT)

Historically, SHM may be thought to be an evolution of the Non-Destructive Testing (NDT) procedures [7]. In fact, NDT techniques are different in the sense that they work on demand, do not have permanent sensors located on the structure, generally work locally, do not necessarily work as an automated system and they are typically limited to the detection of damage/failure. Commonly, these techniques are based on X-ray, eddy current, electron-microscopy, and thermal field principles. Other NDT techniques which use structural dynamic properties to identify damage can be divided in two groups. 1) The techniques that rely on travelling waves characteristics (e.g. acoustic emission, guided waves and ultrasonic testing) which are considered to be sensitive to small damage, good for damage localisation and work at high frequencies. 2) The techniques that rely on wave patterns characteristics (e.g. vibration analysis and piezoelectric impedance) which are relatively easy to interpret, able to inspect large areas, generally work at low frequencies and can have limitations to detect small damage. On the other hand, SHM is closer to the philosophy of damage diagnosis and prognosis which is expected to be continuous, global and not only limited to damage detection but also provide information regarding the life-cycle of the structure [8]. Indeed SHM may use some of the NDT techniques for damage assessment.

1.2.2 Challenges of SHM

Structural health monitoring is one of the most appropriate procedures for damage identification for structures such as civil, aircraft, automotive, structures made of composite materials and structures with high complexity. However, there are many challenges that must be overcome before a SHM system can be considered as a reliable technique to be automatically installed. These challenges are that of what to measure, where to measure, measurement periods (how often), which instrumentations and sensor network must be implemented as well as how to overcome the sensor failure. Once the measurements are recorded, now the decision is what to analyse or monitor (features). Also which kind of damage identification levels can be addressed (see section 1.2.1 for damage identification levels). How to perform in complex structures to expect the highest reliability. And how to implement the decision making to identify changes caused by damage and not for changes in the environmental conditions, sensor failures or other factors which may lead to false alarms. The most relevant challenges that have to be considered before a SHM may be transfer from research to industrial implementation are summarised below. This section only attempts to introduce the importance of these considerations and therefore for further information readers are referred to [4].

Significant research in the field of SHM is dedicated to the *instrumentation and sensor network* because it requires a proper array of sensors and a transmission system. The challenges range from what, where and how to measure in the structure, the optimal sensor location, how to monitor the debonding of a sensor, how to handle the data measured, how to transmit the data as well as the system requirements for power supplier.

Another aspect is to select a *sensitive feature* which can be monitored for damage identification. The raw data will not be able to show the information necessary to identify the damage successfully. For this purpose, a larger number of damage features and *classifiers* have been studied along the history of the SHM to overcome this issue [9]. However, nowadays, there is not a unique feature which solves the problem of damage identification so that more research and advances must be done in this direction.

SHM procedures have been implemented for traditional structures such as bridges and buildings as well as traditional materials such as concrete and steel. The recent advances of new materials such as composite structures are more widely used every day in different industries due to their remarkable properties. These materials are in nature a 'structure' with more than two (or more) components and therefore they require a SHM. The SHM techniques have been applied on limited simple structures such as beams and plates with well defined artificial damage. However, the popular use of these materials generates *complex structures* which make the study of their integrity and damage identification more challenging. The development of SHM procedures for complex and realistic composite structures must be considered. The difficulty of modelling these structures makes the data-based techniques more suitable for this kind of structures.

The *damage identification levels* presented in section 1.2.1 define a set of challenges that have to be overcome in terms of damage identification. Damage detection (level I) and damage localisation (level II) are often achieved with a large number of SHM procedures. However, there are limited studies on the extent/severity (level III). As important as detect and localise damage is the study of damage progression because it can be used as a damage indicator to determine the remaining life of the structure (level IV). Also the rapid advance of smart materials puts SHM at the forefront of contemporary research. The nanocomposite inclusions in composite laminated materials provide additional properties to the material and the entire component/structure such as *self-diagnosis* and *self-healing* (level V and VI). The combination of a SHM procedure and these new materials must be investigated towards an autonomous monitoring systems.

One of the most important issues in SHM is the dependency of damage features on *operational and environmental conditions variability* (e.g. temperature, humidity, wind effect variability, loads, boundary conditions...). The changes in the environmental conditions adversely affect the damage features indicators, which could hide or magnify its presence. There is a real need for methods which are able to compress and separate the data information from damage features and environmental conditions. The study of methods which take into account these aspects are very important to give reliability and confidence to SHM methodologies. This is the reason why researches are moving forward to this direction [10–12].

1.2.3 A general vibration-based SHM procedure

The idea of vibration-based SHM is quite popular, as vibration responses can be measured from a natural or artificial excitation in many available structures such as aircraft, railway vehicles, bridges, wind turbines and so on. The health/state of the structure may be analysed by monitoring changes in its vibratory responses. The monitoring process requires the observation of the system/structure over certain periods of time and this is the reason why a monitoring procedure is required. Farrar et al. [13] present a monitoring procedure by four steps based on a statistical pattern recognition paradigm which is commonly used in the SHM community. In the following four steps a general vibration-based SHM procedure is presented:

> *Operational evaluation* consists of the evaluation of the implementation of the damage identification system. This is to answer questions such as what to monitor and how to monitor within the structure for defining the possible limitations. In this sense, it consists of answering questions related to economic justification, how to evaluate the damage, in what conditions the system normally works and what are the limitations of collecting data for a specific operational environment. This also involves a preliminary study to gain comprehensive information about the potential damage as well as their potential location if any.
>
> *Data acquisition* is to define the quantities to be measured, the type and quantity of sensors to be used as well as their locations, also sensor resolution, bandwidth and hardware used. This process depends on each specific application and it is heavily affected by economic factors. The so-called data fusion, which consists of integrating the data acquired from various sensors and measurement campaigns within the methodology should be also considered. Also, it is important to clean and select the relevant data from the measurements for the feature selection process.
>
> *Feature extraction* receives most of the attention in the literature [14, 15]. The best feature for damage identification depends on the case of study. One of the most important aspects is to parameterise the damage by means of its physical characteristics if this is possible in order to be sure that the damage in consideration can be successfully detected. In this sense finite element modelling is an important tool to reproduce numerically or analytically the fault mechanism and hence study the effect of the fault on the feature selected within a controlled system. This may help to understand better the possible fault mechanisms and further selection of sensitive

damage features. Other aspect is the consideration of purely data-based methods which do not require a model. These methods find their features in correlation functions or estimated parameters from the measured vibration responses.

Decision making and classification is to use the selected features for making a decision whether the structure is healthy or not [16]. Depending on the level of damage identification required, the classification algorithm must address the pertinent levels of identification from damaged or not, damage extent and quantification. Based on the measured data, a model is created to minimise the number of false alarms (e.g. statistical), which are commonly divided into two groups: 1) *False-positive*; indication of damage when it is not present and 2) *False-negative*; indication of no damage when it is present. Both must be reduced to make an efficient VSHM procedure. For the first case, a large number of false positive will increase the financial cost because of the loss of time and confidence due to unnecessary downtimes. The second is more focused on the safety and risk overtaken when the presence of damage is not detected.

1.2.4 Literature overview of vibration-based SHM

In this section, a short overview on the current status of vibration-based SHM approaches is presented. Vibration-based SHM methodologies are based on the concept that the vibration response of a structure changes when damage occurs within the boundaries of the structure itself. Damage alters the physical properties of the structure like mass, stiffness and damping. These parameters define a function which describes the dynamical behaviour of the structure and hence any change on these parameters will change its dynamical response.

Since the last decade, vibration-based SHM has been widely developed in diverse areas for damage identification methods. This can be observed by the immense number of publications in the area. For an overview of general vibration-based SHM methods see Doebling et al [8, 17], Salawu [18], Farrar et al. [19], DeRoeck et al. [20], Carden et al. [21], Inman et al. [22], Fritzen [23, 24], Kolakowski [25] and Adams [26] and a review with emphasis on nonlinear damage identification methods can be seen in Worden et al. [27].

This short review does not intend to compare the performance of the different methods. Each method has its own advantages and disadvantages regarding its application. In first place, a classification based on the different domains where the vibration features can be represented and therefore be used by the vibration-based SHM methods are presented. Secondly, an alternative classification on model and non-model based methods is also presented with a final emphasis to the purely data-based methods (non-model based) that frames the objectives of this thesis.

Vibration-based SHM approaches in different domains

In this section a list of different approaches for vibration-based SHM methods based on the different domains where the vibration response can be represented is presented. The classification is divided in the following four groups: modal domain, frequency domain, time domain and time domain within statistical context.

Modal domain. These methods are to extract the modal parameters by means of classical modal techniques. The modal parameters can be extracted by input-output or output-only measurements [28].

One of the most intuitive and classical methods is to monitor the natural frequencies of the structure/system. When a damage occurs, a frequency shift appears, therefore damage can be detected by relative changes in the natural frequencies. In [29] is proposed the damage location assurance (DLAC) which is a correlation between vectors of experimental natural frequencies. These methods present problems because changes in natural frequencies are small and they are normally embedded by the environmental conditions. Modal shapes introduce additional information for damage detection. With the co-ordinate MAC (COMAC) can be measured the correlation at each degree-of-freedom [30]. It can be also observed in [31] that the effect on modal shapes are more sensitive than the natural frequencies for the detection of delamination in composite laminated plates. More analysis have been done using modal domain as a damage feature, such as modal shape curvature [32] and modal damping [33]. A review of the field of modal analysis for damage detection can be found in [34].

Frequency domain. The concept of these methods is to use the frequency responses directly as a feature for damage identification without subtracting the modal parameters.

In [35] was introduced the frequency domain assurance criterion (FDAC) which measures the changes in the receptacle matrix due to modifications in the stiffness and mass matrices when damage occurs. Transmissibility ratios were used for damage identification when two Fourier transformed output signal are compared [36]. An overview regarding the impedance methods is presented in [37]. These methods rely on the changes of the impedance of the structure when damage occurs. Basically, the concept is to use different techniques to compare the impedance spectrum of the electro-mechanical structure/system. Also the study of antiresonance has been used as sensitive indicator. In [38] is observed that the distribution of antiresonances may be significantly altered by small changes in the structural model.

Time domain. In these methods the time histories of the vibration response of the structure were used to identify the presence of damage. These methods are normally divided into two groups 1) Non-parametric methods, which are mainly based on correlation functions of the vibration responses of the structure and 2) Parametric methods, which create a model from parameters obtained by the vibration responses.

Stochastic subspace based fault detection methods are output-only techniques with the assumption that the structure is excited by random Gaussian white noise. The stochastic responses are used to create the covariance represented in a Hankel matrix form with selected time shifts. The damage index is defined by a vector which computes the residual error of an estimated residual covariance matrix by comparing the past and future states of the structure [39]. A comparison between SSI and SSI-COV has been done in [40] where the stochastic subspace identification algorithm has been implemented on the Hankel matrix of the correlations and on the covariance of the estimated Hankel matrix, respectively. SSI is faster in computing than SSI-COV but the second approach uses less output responses in the computation. Auto-regressive (AR) and Auto-regressive with Exogenous (ARX) methods consists in identify a single-input single-output reference data-model based on coefficients which represents the dynamic behaviour of the reference state (Healthy structure). The data-model is then tested with a new data set to identify any deviation from the reference state. If deviations from the reference occurs, then it is considered to have changes in the physical properties of the structure [41]. There have been numerous attemps to generalise the model structure to the nonlinear case where the most versatile and enduring technique has been the NARMAX [42].

Time domain within statistical context. This group of methods is increasing rapidly in the context of vibration-based SHM because it does not require a model (e.g. analytical or numerical model) and it is only based on measured data from the structure in consideration. These methods are based on three elements to address the damage identification process: 1) vibration response signals, 2) statistical model and 3) statistical decision making. Numerous publications discuss these methods as presented in Basseville et al. [43], Sohn et al. [44], Carden et al. [45] and Fassois et al. [46].

In [47] a method is applied on the comparison between the power spectral densities (PSD) of the healthy and damaged structure when the excitation response is unknown. The data was normalised to differ between different level of excitation. The damage is identified by comparing the current structure to the reference structure. A Null hypothesis is created to be compared and eventually determine whether the structure is damaged or not. A similar approach is applied on the magnitude of the frequency responses (FRF) of the structure. This method can be applied when the excitation response is available or not. For the inspection phase, a statistical hypothesis is also constructed based on the probability distribution of the baseline [48, 49]. Statistical methods are also applied for the estimated model parameters on the vibration responses. These methods work in the characterisation of a defined parameter vector which parameterise the vibration responses of the reference state. The parameter vector of a new observation is compared with the defined reference (or baseline). In [50] an AR model with a statistical control was presented as a damage identification technique. Also in [51] a damage-sensitive feature (DSF) based on the AR coefficients are presented. In this study is found that there is a difference between the mean values of the DSF of the signals obtained from the damaged and undamaged cases. A technique based on the Output Error (OE) parameters obtained from the vibration responses were used to identify the damage in a six-story building with a statistical hypothesis testing procedure for damage diagnosis [52].

This classification frames the vibration-based SHM methods by different domains of representation. One can think that the features contained in a vibration response should be present in all the domains. This is true in the sense that features are embedded in the data-representation but perhaps they are not highlighted and hence they are not sensitive for damage identification. In the work presented in this thesis, the analysis was implemented in time and frequency domain. As explained in the following section and chapters, the use of one domain or other depends on the study in consideration. A frequency domain representation presents the oscillatory patterns contained in the vibration response in a more interpretable and ordered manner. However, the time domain requires correlation functions and parameter estimation to simplify and define the vibratory response. As alluded above, in this thesis both domains were used to find sensitive features for damage identification. The use of each domain and their considerations within the methodology is explained in Chapter 2.

Model and non-model based VSHM approaches

Another classification for the vibration-based SHM methods which is commonly considered in SHM literature is the division on two different approaches, *model based* and *non-model based* methods which are also known as a *data-based* methods. The two approaches are briefly introduced below, including key references and an overview of the advantages and disadvantages to each. Also a final emphasis on *purely data-based methods* is presented to frame the objectives and scope of the work presented in this thesis.

Model based methods are commonly associated with the development of analytical or numerical model (e.g. finite elements modelling) which represents the structure in consideration. Experimental vibration responses are compared with the corresponding model in order to find similarities between the experimental case and the simulated one. Model based methods are generally used for model updating which use experimental data to represent accurately the vibration behaviour of a real structure. The dynamic parameters such as mass, stiffness and damping matrices of a model are compared with the ones obtained from experimental data. One of the advantages of model based methods is that the use of an inverse problem could well be extended to provide information about damage detection, location and severity as well as damage prognosis, which can be predicted through simulation and past experience of the remaining useful life of the system. The work presented in [53] studies the free vibration of beams with multiple enveloping delamination using an analytical model based on Bernoulli-Euler beam theory. The influence of the delamination size and its location on the first two natural frequencies and mode shapes is discussed. A more sophisticated crack model is considered in [54] where contact effects are simulated between laminates at different delamination locations. The changes in the damping dissipation energy due to delamination was considered as a damage feature. On the other hand, complex structures are rather difficult to be accurately modelled. In this case model updating methods are susceptible to the effects of uncertainty which are caused by the variability of the measurements and hence the discrepancies with the model [55]. Another aspect is the modelling and simulation of the damage into the structure. Damage can be accurately modelled and hence describes the vibration behaviour. However, the relation with the real experiment is always a complicated task which generally uses damage parameter errors and experimental errors as an updating parameter for approximating the model.

Non-model based methods rely purely on the data measured from the structure under study. These methods somehow also involve the construction of a model, but this model is based on the data (e.g. statistical model) rather than numerical or analytical. The measurements in an early state, prior to the structure being in service, are considered as the reference state, where the measurements from the structure in service are compared. Any deviation of the new observations from the reference state may be considered as an indication of a damage. *Non-model based* methods have been shown to be capable of address levels 1-4 for damage identification [16]. These methods require of data-based models created with the features obtained for damage identification as alluded above. There are two main categories for these methods. 1) When there is data available from both the healthy and damaged structure, then the category is recognised as *supervised.* 2) When there is only data available from the healthy structure, the category is recognised as *unsupervised.* For an unsupervised category, the outlier detection algorithm is generally implemented. This algorithm consists of the creation of a reference state (generally healthy structure) where the observations can be compared. Therefore, a measurement which presents a deviation to the reference state is considered as a sign that an anomaly occurred within the structure [56]. Into the *non-model based* methods is also included the statistical time series methods [57, 58]. The main advantages of these methods are: there is no need of numerical or analytical models but the models are directly created on the measured data (training data), uncertainties are considered due to the statistical models, distributions are considered for the decision making phase (determination of healthy or damaged structure) and it is quite effective for low frequency range and random excitations. Some of the limitations of these methods are the location of damage which is difficult to be achieved and a model may be required. These methods rely heavily on the data considered to create the reference state (training data).

It is important to mention that the consideration of a baseline (or reference state) also involves to *model based* methods where the baseline data set can be obtained from the model (e.g. finite element model). There are methods that do not considered a baseline data set. In fact, this is a matter of terminology because they compare between two states where the 'non-baseline' is declared to be assumed as normal behaviour. Then, the damage identification occurs when there is a deviation from the normal behaviour [59].

Purely data-based methods for vibration-based SHM

An emphasis on the *purely data-based* methods is presented in this section to frame the main objectives of the damage assessment methodology presented in this work.

In practice most purely data based methodologies make use of data analysis techniques and utilise different statistical methods such as Bayesian methods [60] or *principal component analysis* (PCA) [61]. Principal component analysis is one such possibility and there are a number of papers that consider PCA-based damage assessment methods [62, 63]. In general, PCA is a technique used in data analysis to reduce the dimensionality of the available data. Since vibration signals in the time and/or a frequency domain have quite high dimension, it is obviously appropriate to apply such technique to the measured vibration signals (see Jolliffe [64] for further information). PCA also has other properties that are advantageous from the view point of VSHM and distinguishing between different categories e.g. those measured on non-damaged and damaged structures, or data measured on structures with different damage extents and/or locations. PCA is useful for categorical data because it possesses a clustering effect in the sense that it reduces the distance between vectors from the same category, whilst at the same time, increases the distance between data vectors from different categories. This is why a number of studies consider the application of PCA for structural damage assessment purposes [65, 66].

Some investigations suggest the selection of certain features from the time or frequency domain of the vibration response signals which can be considered as independent variables to subject them to PCA [67]. On most occasions, these are certain frequencies, peaks at a certain frequency or time moments which are far enough from each other to be considered independent. In the work presented in [68], only the higher variance principal components are retained and used as a model to predict/reconstruct the feature data which in this case are the first natural frequencies of a Z24-Bridge. The method sounds promising but the effect of nonlinearities due to changes in the environmental conditions affect on the performance of the methodology. This is why the authors applied local PCA algorithm [69]. In this case the PCA algorithm was applied two times. First, PCA was applied on the data-features obtained from the vibration responses and once the clusters were created, PCA was applied again on these clusters. Thereby, the principal directions accurately describe the data distribution and successfully take into account the nonlinear effects due to environmental variability.

Other studies consider a PCA algorithm on parametric and nonparametric feature vectors to reduce the dimension of the feature vectors for damage detection in lab-scale wind turbine blade with the consideration of different environment conditions [70]. The algorithm retains the least prominent elements (least amount of variance content) as they are expected to be affected by damage. In these studies, it can be observed the capability of PCA to compress and decompose the data in different principal components, which can be used in different manners with the aim of damage identification.

The point is that PCA is generally developed for multiple and independent variables, while time series elements are usually non-independent [64, 71], in the sense that they are related to each other and they should be considered as an entire measurement signal vector. This is one of the reasons why the methodology presented in this thesis uses singular spectrum analysis (SSA) technique, rather than PCA. This way it takes care of the inter-correlation between the individual signal vectors obtained in the measured vibration responses. In this sense, SSA considers all rotational patterns included in each vibratory signal rather than at particular frequency, which also includes the nonlinear oscillations. The aim of SSA is to decompose the original signal using a small number of independent and more interpretable components which can be used for trend identification, detection of oscillatory components, periodicity extraction, signal smoothing, noise reduction, feature extraction and detection of structural changes in time series. A general description of the method can be found in Golyandina et. al [72]. SSA has been applied for diverse applications ranging from weather forecasting [71], financial mathematics [73], historical sciences [74] and economical time series where the signals are highly non-stationary with no signs of periodicities [75], in this case the methodology acts as a kind of moving average for signal smoothing.

There are a small number of publications related to the application of SSA for structural vibration analysis and for vibration-based SHM. Some studies have already used SSA-based methods for SHM as shown in [76] where SSA was applied for structural monitoring and damage diagnosis of bridges by using an eigenvalue ratio difference between the first two eigenvalues. Therefore, when the difference between the first two eigenvalues increases, it is an indication that an irregularity occurs. In the same study, the residual errors were measured by comparing the reconstructed vibration responses based on the SSA decomposition with the measured ones. In [77], the performance of a SSA-based methodology was compared with SSI-COV method where the authors claim that the SSA-based method has a better and faster computation. Recently, SSA was used for the purpose of de-noising the vibration responses measured in a rotative machine before subjecting the signal to AR-modelling with application to fault detection in roller bearings [78]. It is the opinion of the author that this technique holds a lot of potential for the above applications because of its ability for trend estimation, decomposition, uncovering oscillation patterns and signal smoothing. Since the data measured on a vibrating structure usually consists of acceleration, velocity or displacement signals, SSA presents an attractive alternative for the development of purely data-based VSHM methodologies.

A natural extension of SSA is multichannel singular spectrum analysis (MSSA) where more than one signal was considered to build the embedding matrix. MSSA is a combination of SSA and PCA but with different emphasis. As the covariance matrix is calculated on the full embedding matrix, not only the auto-covariance of each signal vector is considered but also the cross-covariance between each signal vector realisation. In this sense MSSA combines the benefits of each method: 1) SSA with the consideration of all rotational patterns in a single signal vector and 2) PCA with the properties of data compression to find common structure between the number of signal vectors considered [79].

One of the contributions of the work presented in this thesis is to develop a damage assessment methodology which is based on MSSA technique [80, 81]. The methodology uses the measured vibration responses on the structure under study, that are processed by the MSSA-based methodology to extract sensitive features for damage identification.

It is important to mention that most studies that use SSA or MSSA apply it on the time domain, while in this thesis, it is suggested to apply in the frequency domain as well because frequency domain treatment generally offers easier computation and more intuitive interpretation. Several studies demonstrate that frequency domain representation can be used as input-data for damage identification as shown in [82]. The authors of that investigation demonstrated that time-frequency plots show the generation of resonant frequency harmonics in the freely vibrating, cracked cantilever beam as well as the change in stiffness state as the crack opens and closes. Therefore, the study clearly shows that the presence of nonlinearity adds considerable complexity to the frequency response characteristics of the system. The comparison of this increment of complexity in relation to the undamaged system can be used to infer the presence of damage. Also the complexity is not located in a particular frequency but distributed along the spectrum. Therefore, the consideration of all rotational patterns contained in the entire spectrum can benefit the damage detection.

A way to apply PCA in a vector which has been first transformed to the frequency domain by the Fourier transform was explained in [64] - page 329. It can be also observed that PCA was applied on the electro-mechanical impedance frequency responses to compress the data for the damage detection by using a different number of principal components [83]. In a different study [84], SSA has been applied on spectral lines defined by the Hyperspectral Imaging (HSI) for effective feature extraction. By removing noisy components in extracting features, the discriminating ability of the features improved considerably. Consequently, PCA was applied to the SSA reconstructed components in order to reduce the number of features (reduction of the dimensionality). As mentioned above, MSSA combine SSA and PCA for useful trend/feature extraction and dimensionality reduction. In Chapter 2 of this thesis, the performance of MSSA was discussed when it was applied on the time and frequency domain. When MSSA was applied on the frequency domain, a smooth and global decomposition was obtained where the first component contains the main trend of the spectral line, while the rest of components are responsible for the fluctuations over the general spectral line. On the other hand, when MSSA was applied on the time domain, it produces a local decomposition with separate and interpretable oscillatory components. Both methods are presented and considered in this thesis when the damage assessment is based on frequency domain (see Chapter 3 and 4) and when the damage assessment is based on time domain as shown in Chapter 5.

As alluded above, SSA is known to uncover the rotational patterns of the measured time series. Thus, if one considers a time series from the free response of a structure, it will contain information about the modal frequencies of the structure. From such a perspective, it can be argued that SSA should also contain and uncover the modal contents of a freely vibrating structure from its measured free response [85, 86]. But differently from modal analysis, SSA will uncover rotational patterns at any frequency rather than at specific frequencies only. Therefore, from the author view point SSA or MSSA based methods are extremely appropriate for nonlinearly vibrating structures which exhibit double or very close modes [87]. For the above reasons the work presented in this thesis suggests the application of MSSA-based methods for the purposes of structural health monitoring.

1.3 Composites structures

1.3.1 Fibre reinforced materials

A composite material is a material made of two or more materials with different physical or chemical properties which are combined to obtain a material with different properties than each individual constituent. The constituents work together as a new material and the properties of each individual constituent contribute in the performance of the new material. The typical engineering composite materials nowadays are cement and concrete, reinforced plastics (e.g. fibre-reinforced polymer), metal composites and ceramic composites.

In mechanical engineering a composite material refers to a polymer matrix and fibre reinforced materials such as carbon or glass. These materials are known as Fibre Reinforced Plastics (FRP) materials. Fibre reinforcement materials are generally made of long fibres with high modulus and strength which are the ones to support the mechanical loads in their direction, while the epoxy material (matrix) transfers the mechanical transverse loads between the fibres, binds fibres together and acts as a protector of the fibres against harsh environments. Composite materials can be tailored for each specific application from material level to structure level (see Figure 1.1). At material level, the composite materials can be designed at nano scale with the inclusions of nanocomposites that are able to increase dramatically the properties at the macro scale. By selecting a specific composition of nanocomposites, the material not only will increase its mechanical characteristics but also introduce additional properties to the material such as electro-mechanical, wear resistance, hydrophobia among many others. In the SHM context, the use of nanocomposites can introduce self-sensing and self-healing properties at the material level which eventually builds a structure capable to self-diagnose (see section 1.3.3). The flexibility of these materials for combining matrix and fibres is also an advantage. The different ways to design the lay-up provide the ability to adjust the manufacturing process for each specific application.

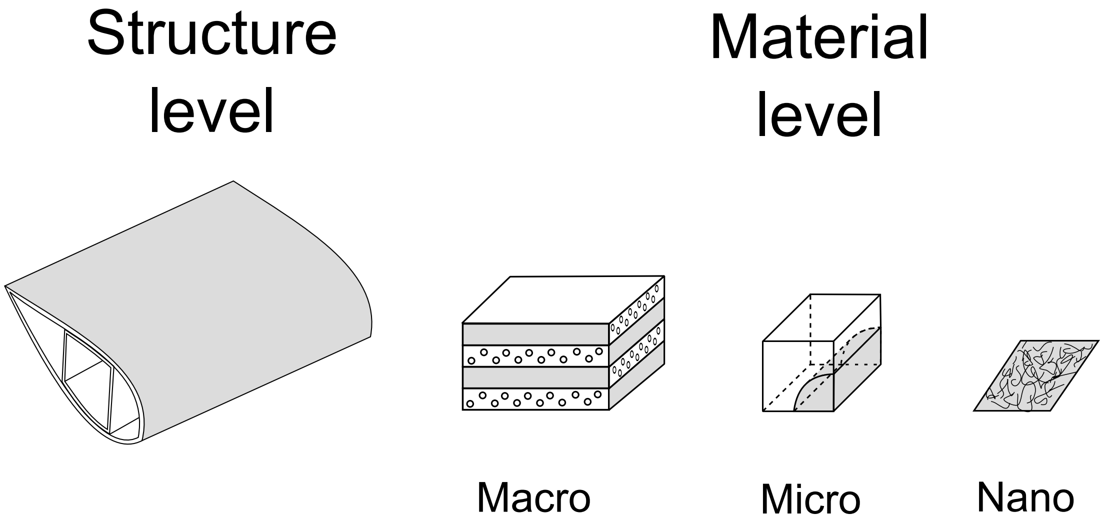

Figure 1.1: Multi-scale level of fibre reinforced laminates

Composite materials are generally designed for applications of high performance due to its fantastic properties in comparison with the traditional materials [88]. They have high strength and stiffness with a very low density, high fatigue strength, high impact properties and high corrosion resistance. They are able to be formed into complex shapes, which allows the manufacturing of curved structures (e.g. wind turbine blades), skin-stiffeners structures without any additional process such as welding or riveting. By using proper design and manufacturing procedures, composite materials can be tailored for specific applications with a low cost-effective ratio. These properties and characteristics are why research in composite materials is constantly growing and why their industrial implementation is present in a wide variety of sectors.

1.3.2 Type of damages

Due to their complex nature and structure, fibre reinforced materials suffer different damages and mode of failure which are not present in conventional materials (e.g. metals). One of the main reasons is that composite materials are by nature non-homogeneous and non-isotropic. Therefore, the presence of different materials such as fibres and matrix and their combination by layers with different orientations and configurations lead to a different distribution of stress that can produce different failures and damages. Damage is generally originated at material level but it also affects at structure level. Figure 1.2 presents the most common damage that occur in composite materials. The weakest component in fibre reinforced materials is the matrix. One of the failure mechanisms is known as transverse crack. It occurs when the matrix cracks and hence a failure originates its way towards one of the edges of the material. This failure normally starts on the surface of the material and travels parallel to the fibres through the thickness direction. These failures can be produced during the manufacturing process (e.g. difference in the thermal expansion coefficients of matrix and fibres) or service load (e.g. impact). These failures are very small at the beginning and it is difficult to be detected during the manufacturing process or by visual inspections. As these failures can go through the thickness, if they are not detected on time, they can be the origin of other failures such as delamination.

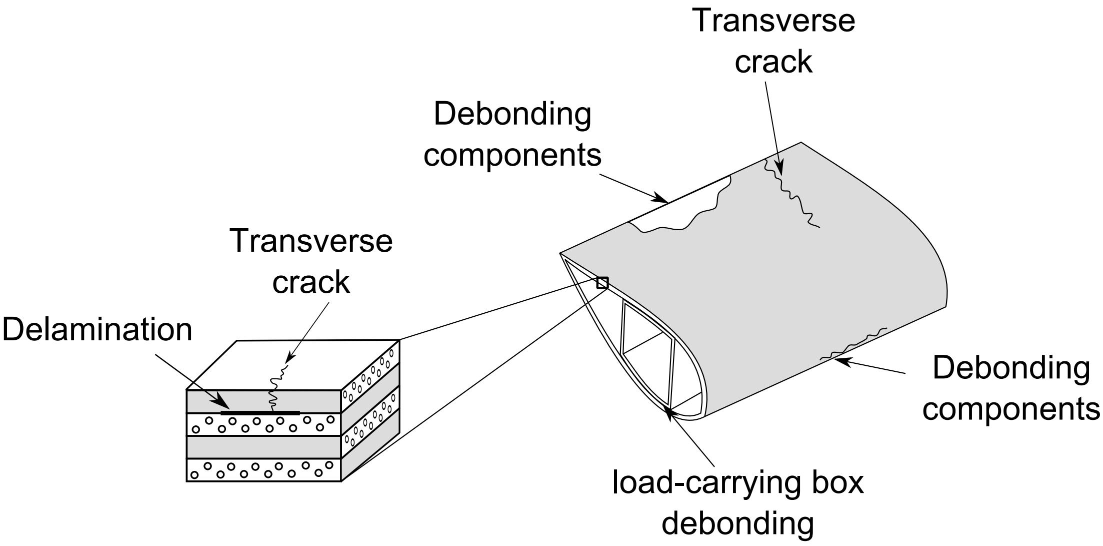

Figure 1.2: Schematic representation of common damages in composite laminated structures

Delamination is a damage that occurs between the interlaminar planes. The failure runs in the plane parallel to the plies (fibres) between two layers. Delamination can be originated by different factors such as interlaminar stress concentration at the edges, transverse cracks, out-of-plane loading, impact, loss of connection during the manufacturing process, internal ply drops, gaps and discontinuousness among many others [89]. Delamination occurs internally between the layers and it is very difficult to detect. Is is probably one of the most common failure modes in fibre reinforced materials and also one of the most dangerous phenomena in these material. Micro-crack formations occur in the material matrix and can grow to delamination which in turn can reduce the stiffness of the material section up to 60% without any significant visual change and eventually this can lead to the collapse of the entire structural member. Delamination rarely leads to complete fracture but it affects the thermal and mechanical properties of the material and structure. Typically these failure modes can involve local buckling of fibres, fibre breakage and fibre pull-out. A kind of delamination can also occur externally, but this time at structural level. The failure occurs between different structural components (e.g. debonding between upper and lower shells in wind turbine blades, debonding between stiffeners and plates). These failures are originated from transverse cracks or over load limits (e.g. torsional buckling effects). Originally they are small but can grow rapidly along the failure direction until the collapse of the entire structure. The debonding between structural components changes the original structural mechanism, considered in the design, and it can cause other mechanism failures.

1.3.3 SHM for composite materials

As alluded in the motivation of this thesis, there is an increasing demand on composite materials in a wide range of industries that require high reliability. These materials offer outstanding properties for industry needs but, because of their nature, can lead to complex failure modes that are difficult to detect before a catastrophe occurs. This is one of the reasons why a SHM system is needed to monitor the health of the material and/or structure from production until the maintenance stage.

Traditional NDT techniques have been used widely to detect damage. These techniques are time consuming and costly, and on some occasions impractical because of the difficult accessibility to the structure under inspection. These techniques typically can only provide local inspection, which generally requires an idea before hand of where the potential damaged regions are.

The aims, challenges and the experience gained during the last decades as explained in section 1.2, allocate vibration-based SHM techniques at the forefront of the contemporary research for application to composite structures. It is the author's opinion that the data-based approaches should be developed to monitor the health of structures made of composite materials because of their complexity for damage modelling.

Moreover, they are used in structures with a remote location and are known to have nonlinear vibration responses, where conventional linear methods do not always offer significant information for damage identification. Some studies have been done in this direction but there is still a large number of challenges that should be investigated. For a general overview of vibration-based SHM with emphasis in composite materials can be seen Zou et al. [90] and Montalvão et al. [91].

A short overview of smart materials within the SHM techniques

Contemporary research is focused on embodying intelligence in structures and on the development of integrated systems capable of monitoring the health and integrity of the structure. The study of smart structures with self-sensing and self-diagnosis capabilities oriented towards the structural integrity is in constant development. The idea of embedding conductive nano-inclusions within the matrix of composite materials to control their conductivity properties and as result their dynamic/vibratory characteristics contain a lot of potential for the purposes of structural health monitoring. Previous research has focused on monitoring and an analysis of the electrical resistance to detect damage existence [92–96].

Nanocomposites are experiencing one of the most exciting developments in the current research. They are at the forefront of contemporary research because of their wide variety of additional functionalities, which show promise for applications in many diverse sectors. The use of nanocomposites have aroused great interest to researches because of their remarkable properties at nanoscale which improve dramatically micro and macro properties such as electromechanical [97], piezorestivity [98, 99] and other mechanical properties [100]. Carbon nanocomposites possess remarkable electrical conductivity properties which can be related to their mechanical properties. Some studies have demonstrated that changes on the strain of the material are transformed to an increment of the resistance [101]. In such a way, monitoring the electrical resistance can be related to changes in the mechanical properties of the structure [102]. Damage introduces changes in the electrical conductivity and hence in the resistance. Monitoring the electrical resistance and its changes can be used for the purposes of damage detection and localisation within the boundaries of the specimen analysed [103]. Tallman et al. use an imaging technique known as electrical impedance tomography (EIT) to provide real time monitoring on glass/fibre enriched with CB nanoparticles. This technique has also been applied for thin films made of carbon nanotubes (CNT) [104] or in GFRP manufactued with nanocomposite coatings [105]. Most of the studies uses two or four point probe measurements [106] to obtain the static loads changes. Moreover, many studies are focused on the sensor behaviours under tensile strains and compressive strains [107]. Pham et al. [108] evaluate the sensitivity of the nanocomposite film sensors to show the relationship between CNT volume fraction and sensitivity. Loh et al. [106] study a single-walled carbon nanotube (SWNT)-polyelectrolyte composite thin film strain sensor fabricated with a layer-by-layer process and a commercial sensor to compare their ability for energy harvesting and self-sensing. And Kang et al. [102] compares the dynamic strain response measured by a laser vibrometer and by a CNT strain sensor. The above overview clearly determines that carbon nano-inclusions can be used as conductivity/resistance sensors. The material conductivity is related to a number of other mechanical properties, which are in turn related to presence of damage. The question is how to use these relations to develop self-sensing and self-diagnosis monitoring methods.

One of the studies presented in this thesis has, as a main goal, the use of laminated structures with carbon nano-inclusions to extract a vibration response from the nano-enriched structure by measuring changes in voltage due to changes in the mechanical properties of the structure. As explained above a great number of investigations have studied the electrical changes in nano-enriched structures for damage detection but these are mainly based on the loss of conductivity when the damage occurs. Jandro et al. [101] identify delamination using a quasi-static loading test with a nanocomposite sensor thread. Delamination is identified by the sudden decrease of the load in the load-deflection curve, and by the jump to infinity of the resistance in the resistance-deflection curve, which corresponds to breaking one of the sensor threads. However, a few studies have explored the analysis of the vibration response of the structure from measurement of the electrical properties. Kang et al. [102] analysed the piezoresistive effect for carbon nanotube polymer strain sensor measuring the vibratory response in a cantilever beam. Their study compares the vibratory responses from a healthy and damaged beam.

As presented in this short overview, the use of nanocomposite materials, as an additional constituent in the composition of the material to provide self-sensing and self-diagnosis capabilities within a structural element has potential. This is the reason that encouraged the exploratory study presented in Chapter 5. The idea is to monitor the health of the structure with no-interaction by coupling the integrated system based on the nano-enriched materials and data-based VSHM algorithms. The vibration responses measured through the conductive material are processed by the damage assessment methodology proposed in this thesis to find significant and sensitive features for damage identification.

1.4 Scope, objectives and contributions of the thesis

The main objective of the research presented in this thesis contributes to the development of a data-based vibration structural health monitoring methodology for composite structures through its mission, which is defined as:

> Development of a data-based vibration structural health monitoring methodology for extracting features sensitive to damage using a SSA-based technique. The methodology is used to develop a fully automatic system which on the basis of the measured vibration response will give information about the presence, the location and the extent of delamination and/or other defects in different composite structures.

This work also involves the following steps which have contributed in the development of the principal objective of this research:

(i) An overview of the vibration-based structural health monitoring methodologies with emphasis in purely data-based methods.

(ii) Frame of the SSA-based technique within a vibration response perspective for delamination/damage assessment. Demonstration and validation in a numerical system and an experiment with delaminated composite beams.

(iii) Study the effect of the selection of the methodology principal parameters, 1) frequency resolution and time acquisition, 2) sliding window size and 3) number of reconstructed components considered to build the feature vectors. The performance of the methodology is evaluated for the different cases of study mentioned in (ii).

(iv) Delamination assessment in composite laminated plates. The delamination assessment methodology is performed on the vibration responses measured on finite element models and on manufactured composite laminated plates for different spatial locations of the delamination (in-plane and through different layers).

(v) Development of a practical VSHM system for wind turbine blades with a statistical hypothesis threshold for the inspection phase based on probabilistic distributions. The integrated system is used to study 1) the different damage locations and severities located in a small wind turbine blade and 2) the damage detection performance for different points of actuation on a SSP34m wind turbine blade.

(vi) Study of the capabilities of conductive nano-inclusions for measuring vibration responses due to changes on the dynamic strain by an harmonic excitation.

(vii) An investigation of the no-intervention principle, coupled with the new integrated self-sensing technology.

(viii) Investigation of a dynamically self-sensing and self-diagnosis structure capable of measuring its vibration responses to diagnose its structural integrity coupled with the data-based VSHM methodology for detecting anomalies/damages.

(ix) Analysis of different damage included artificially in/on a nano-enriched laminated beam by the suggested self-diagnosis approach.

1.5 Thesis outline

The thesis outline is structured as follows.

Chapter 2 introduces the damage assessment methodology developed in this investigation. Validation and demonstration of the methodology is also presented first in a two degree of freedom system and secondly in an experiment with delaminated composite beams. A study on the selection of the methodology parameters is also presented on the same two case of studies.

Chapter 3 introduces a delamination assessment procedure for composite laminated plates. The analysis is developed in a finite element model and in an experimental study with delaminated composite plates. The effect of the delamination on the natural frequencies of the vibration plates is first studied. And secondly, it is compared with the capabilities of the damage assessment methodology for better damage identification.

Chapter 4 introduces a damage assessment methodology based on the one introduced in Chapter 2 with a statistical hypothesis threshold based on probability distribution functions. The analysis is first implemented in a lab-scale wind turbine blade for damage identification at different locations and with different damage severities. Secondly, the damage assessment methodology is implemented in a real SSP34m wind turbine blade for different locations of actuation.

Chapter 5 introduces an exploratory study of the vibration-based self-sensing capabilities of nano-enriched composite laminates. First an introduction of the concept of the self-sensing and self-diagnosis is presented. Secondly a demonstration in how to measure the vibration responses based on the changes of voltage due to the dynamic strain is presented. And finally, a demonstration of the self-sensing procedure is presented on a nano-enriched composite beam with different simulated damage scenarios.

Chapter 6 presents the important conclusions and provides the recommendations for further research.

Chapter 2

Methodology, validation and considerations

2.1 Chapter overview

This chapter introduces the damage assessment methodology for composite laminated structures developed for this investigation. The chapter presents first the basics of the methodology and a study of the interpretations when the methodology was implemented in the time or frequency domain. Secondly, the methodology was validated to perform an initial proof-of-concept using a numerical analysis and in an experimental test with real composite laminated beams. Finally, a study of the preliminary considerations for choosing the principal parameters in the methodology as well as their effect in the damage assessment was developed.

2.2 Damage assessment methodology

The methodology is considered as a simple, nonparametric method for data compression and information extraction, which finds combinations of variables that describe major trends and oscillations in the vibratory signals measured on the structure/system in consideration. The procedure is divided in four steps: data collection, creation of the reference state, feature extraction and damage assessment.

2.2.1 Data collection

The first step is to collect the data from the structure/system in consideration. A physical variable (e.g. acceleration, velocity, displacement, strain, voltage...) is measured at each instant of time to obtain a signal for each realisation. Each signal is discretised into a vector with N data points equally spaced at Δ_t as shown in Equation 2.1.

$$\mathbf{x}_m = (x_{1,m}, x_{2,m}, ..., x_{N,m}) \tag{2.1}$$

where m=1,...,M is the number of signal vector realisations measured from each structure/system.

Since the measured physical variables have different magnitudes, the signal vectors are standardised before applying any analysis. Here, the so-called autoscaling method is applied. It consists in standardizing the signal vectors to have zero mean and unity variance [109]. This is performed for each $\mathbf{x}_m$ signal vector as follows:

$$\mu_m = \frac{1}{N}\sum_{n=1}^{N} x_{nm} \tag{2.2}$$

$$\sigma_m^2 = \frac{1}{N-1}\sum_{n=1}^{N}(x_{nm} - \mu_{nm})^2 \tag{2.3}$$

$$\bar{x}_{nm} = \frac{x_{nm} - \mu_m}{\sigma_m} \tag{2.4}$$

where μ_m and σ_m^2 are the mean and variance of each $\mathbf{x}_m$ signal vector realisation. In order to simplify the nomenclature in the following sections of the methodology, it is considered that each $\mathbf{x}_m$ is already standardized, therefore $\bar{\mathbf{x}}_m = \mathbf{x}_m$.

The signal vectors for each realisation are arranged in columns into the matrix **X** with a dimension NxM.

$$\mathbf{X} = (\mathbf{x}_1, \mathbf{x}_2, ..., \mathbf{x}_M) \tag{2.5}$$

2.2.2 Creation of the reference state

The aim of this section is to create a reference state where the observation signal vectors can be compared. The steps to create the reference state are: embedding, decomposition and reconstruction. These steps are explained as follows.

Embedding

This step creates an embedding matrix of the signal vectors. Dynamic systems cannot be fully unfolded in the two dimensional space of their measured signals because of their highly complex behaviour. By creating an embedding space, more dimensions are introduced and thus more features of the signal vector are uncovered. In this sense, each vector signal $\mathbf{x}_m$ is embedded into a matrix $\check{\mathbf{X}}_m$ by W-lagged copies of itself as shown in Equation 2.6 where m=1,...,M and W are the number of signal vector realisations and the sliding window size, respectively. The dimension of the matrix $\check{\mathbf{X}}_m$ is N x W.

$$\check{\mathbf{X}}_m = \begin{pmatrix} x_{1,m} & x_{2,m} & x_{3,m} & \cdots & x_{W,m} \\ x_{2,m} & x_{3,m} & x_{4,m} & \cdots & x_{(W+1),m} \\ x_{3,m} & x_{4,m} & x_{5,m} & \cdots & \vdots \\ x_{4,m} & x_{5,m} & \vdots & \cdots & \vdots \\ x_{5,m} & \vdots & \vdots & \cdots & x_{N,m} \\ \vdots & \vdots & x_{(N-1),m} & \cdots & 0 \\ \vdots & x_{(N-1),m} & x_{N,m} & \cdots & 0 \\ x_{(N-1),m} & x_{N,m} & 0 & \cdots & 0 \\ x_{N,m} & 0 & 0 & \cdots & 0 \end{pmatrix} \tag{2.6}$$

The embedding process defined in Equation 2.6 is applied for each vector signal realisation. Then, all matrices $\check{\mathbf{X}}_m$ are used to create the full embedded matrix $\check{\mathbf{X}}$. The dimension of the full embedded matrix $\check{\mathbf{X}}$ detailed in Equation 2.7 is N x (MW). The number of M-signal vector realisations considered in the full embedded matrix $\check{\mathbf{X}}$ is normally selected by M≤W.

$$\check{\mathbf{X}} = (\check{\mathbf{X}}_1, \check{\mathbf{X}}_2, ..., \check{\mathbf{X}}_M) \tag{2.7}$$

Decomposition in Principal Components

This section explains the procedure to decompose the full embedding matrix $\check{\mathbf{X}}$ (see Equation 2.7) into a number of vector components based on their variance content. First, the covariance matrix of $\check{\mathbf{X}}$ is calculated as detailed in Equation 2.8.

$$\mathbf{C}_X = \frac{\check{\mathbf{X}}^t \check{\mathbf{X}}}{N} \tag{2.8}$$

The matrix $\mathbf{C}_X$ defines the covariance between the different signal vector realisations and has a dimension (MW) x (MW). In the Equation 2.8, $\check{\mathbf{X}}$ is the full embedding matrix, $\check{\mathbf{X}}^t$ is the transpose matrix of $\check{\mathbf{X}}$ and N is the signal vector dimension. As the covariance matrix is calculated on the full embedding matrix, not only the auto-covariance of each signal vector realisation is considered but also the cross-covariance between the signal vector realisations is also taken in to account.

The eigen-decomposition of $\mathbf{C}_X$ yields the eigenvalues $\boldsymbol{\lambda}_k$ and the eigenvectors $\boldsymbol{\rho}_k$ obtained by solving the following expression where the index k represents each eigenvector and eigenvalue.

$$\mathbf{C}_X \boldsymbol{\rho}_k = \boldsymbol{\lambda}_k \boldsymbol{\rho}_k \tag{2.9}$$

The eigenvalues $\boldsymbol{\lambda}_k$ are stored in the diagonal matrix $\boldsymbol{\Lambda}_k$ in decreasing order and the eigenvectors $\boldsymbol{\rho}_k$ are stored in columns into the matrix $\mathbf{E}_X$ in the same order than their corresponding eigenvalues. Each eigenvalue defines the partial variance in the direction of its corresponding eigenvector, therefore the sum of all eigenvalues gives the total variance of $\mathbf{X}$.

$$\mathbf{E}_X^t \mathbf{C}_X \mathbf{E}_X = \boldsymbol{\Lambda}_X \tag{2.10}$$

The matrix $\mathbf{E}_X$ contains all eigenvectors $\mathbf{E}^k$ with dimension $\{\mathbf{E}^k : 1 < k \leq MW\}$. Each eigenvector $\mathbf{E}^k$ is composed by M consecutive segments with a longitude W. Therefore each element of an eigenvector is denoted as $E^k_{m,w}$. The Principal Component (PC) $\mathbf{A}_k$ associated with each $\mathbf{E}^k$, is calculated by projecting the $\check{\mathbf{X}}$ onto the $\mathbf{E}_X$ as shown in Equation 2.11.

$$A_n^k = \sum_{w=1}^{W} \sum_{m=1}^{M} X_{m,n+w} E_{m,w}^k \tag{2.11}$$

Each element of a PC A_n^k is a linear combination of the W-values of each M-segment weighted by their corresponding $\mathbf{E}^k$. Therefore, each PC contains characteristics from all the M signal vector realisations.

Reconstruction of the reference state

This section explains how to obtain the Reconstructed Components (RCs) which are linear combinations of the PCs and the eigenvectors. The RCs are calculated by convolving the PCs with the associated $\mathbf{E}^k$, thus the k^{th} RC at n-value for each m-realisation is given by the Equation 2.12.

$$R_{m,n}^k = \frac{1}{W_n} \sum_{w=1}^{W} A_{n-w}^k E_{m,w}^k \tag{2.12}$$

Each $R_{m,n}^k$ value is normalised by the normalization factor W_n which is described by the Equation 2.13.

$$W_n = \begin{cases} n & 1 \leq n \leq W-1 \\ \\ W & W \leq n \leq N \end{cases} \tag{2.13}$$

The RCs are then arranged as columns into the matrix $\mathbf{R}$ with a dimension N x MW. The matrix $\mathbf{R}$ includes all RCs for all M-signal vectors and are distributed in sub-matrices as shown in Equation 2.14.

$$\mathbf{R} = (\mathbf{R}^1, \mathbf{R}^2, ..., \mathbf{R}^M) \tag{2.14}$$

Each of M-signal vector realisation is decomposed into W-reconstructed components arranged into the matrix $\mathbf{R}^m$ with a dimension N x W as shown in Equation 2.15.

$$\mathbf{R}^m = \begin{pmatrix} R^m_{1,1} & \cdots & R^m_{1,W} \\ \vdots & \ddots & \vdots \\ R^m_{N,1} & \cdots & R^m_{N,W} \end{pmatrix} \tag{2.15}$$

Then, $\mathbf{R}^m$ can be used as the reference state of the structure/system where the observation signal vectors are compared.

2.2.3 Feature extraction

In this section the procedure to obtain the feature vectors (FVs) is explained. A FV is obtained for each observation signal vector by comparing its similarity to the reference state calculated in Equation 2.15. Therefore, a FV is calculated by multiplying an observation signal vector $\mathbf{x}$ with each of W-columns of $\mathbf{R}^m$ as shown is Equation 2.16.

$$T_j = \sum_{n=1}^{N} x_n R^m_{n,j} \tag{2.16}$$

where j=1,..,W. Each T_j value represents the inner product between an observation signal vector and each reconstructed component contained into $\mathbf{R}^m$. All T_j are arranged into a vector $\mathbf{T}$ with dimension W. The feature vector $\mathbf{T}$ characterises the observation signal vector onto a feature space with a dimension W.

Therefore, when two feature vectors are compared onto the feature space, it is expected that if the two FVs are similar, the distance between them will decrease, however if they are different, the distance between them will increase.

2.2.4 Damage assessment

This section presents how damage is evaluated from the feature vectors defined in section 2.2.3. First, a baseline feature space $\mathbf{T}_B$ is created by a certain number of feature vectors $\mathbf{T}^s = (T_{1,s}, T_{2,s}, ..., T_{p,s})$ defined by signal vectors measured on the reference state as shown in Equation 2.17.

$$\mathbf{T}_B = \begin{pmatrix} T_{1,1} & T_{2,1} & \cdots & T_{p,1} \\ T_{1,2} & T_{2,2} & \cdots & T_{p,2} \\ \vdots & \vdots & \cdots & \vdots \\ T_{1,s} & T_{2,s} & \cdots & T_{p,s} \end{pmatrix} \tag{2.17}$$

In the above Equation 2.17, $\mathbf{T}_B$ is the baseline FV matrix with a dimension p x s where p is the dimension selected from the FV $\{p \leq W\}$ and s is the number of signal vectors utilised to define the baseline. Once the baseline is defined, an observation FV is then compared with the baseline $\mathbf{T}_B$. Each observation FV has to have the same dimension p as the baseline and is defined by $\mathbf{T}^i = (T_{1,i}, T_{2,i}, ..., T_{p,i})$ where i is the number of observation FVs.

The next step is to measure the similarity of an observation feature vector $\mathbf{T}^i$ to the set of baseline feature vectors $\mathbf{T}_B$. To demonstrate this, an outlier analysis using the Mahalanobis distance is carried out on the observation FVs. Outlier analysis calculates a measure of how similar or dissimilar an observation FV is to the baseline. The measured discordance is calculated as shown in Equation 2.18.

$$D_i = \sqrt{(\mathbf{T}^i - \boldsymbol{\mu}_B)^t \boldsymbol{\Sigma}^{-1} (\mathbf{T}^i - \boldsymbol{\mu}_B)} \tag{2.18}$$

In the above Equation 2.18, $\mathbf{T}^i$ is the observation FV, $\boldsymbol{\mu}_B$ is the mean row of the baseline feature matrix $\mathbf{T}_B$ and $\boldsymbol{\Sigma}$ is the corresponding covariance matrix. In order to label an observation as an outlier or inlier there is a need to set a threshold value ϑ against a new distance can be evaluated. The threshold is calculated based on the distances measured by baseline feature vectors $\mathbf{T}^s$ to the baseline matrix $\mathbf{T}_B$. Therefore, the classification of a new FV is based on the comparison of any damage index D_i to the defined threshold.

Two hypotheses are defined for FV classification as shown in Equation 2.19. **H1** when the D_i is equal or less than the threshold and **H2** when the D_i is greater than the threshold. In case of **H1**, the FV $\mathbf{T}^i$ is assigned to the baseline category (inlier) while in case of **H2**, the FV $\mathbf{T}^i$ is assigned as a non-baseline category (outlier).

$$\begin{aligned} \mathbf{H1} &: D_i \leq \vartheta \\ \mathbf{H2} &: D_i > \vartheta \end{aligned} \tag{2.19}$$

Then, as the baseline is based on the healthy scenario, any damage index D_i greater than the threshold is considered as an anomaly of the baseline and hence as a damaged scenario. On the other hand, any damage index D_i smaller than the threshold is considered as a damaged scenario.

2.3 Creation of the reference state in the time or frequency domain

The methodology introduced in section 2.2 is divided in four steps as described above: data collection, creation of the reference state, feature extraction and damage assessment. The data used to create the reference state determines how the information is contained in the reference state and therefore how meaningful and informative are the feature vectors for the damage assessment.

This section presents the effects on the creation of the reference state when the data used is represented in the time or frequency domain. Although the idea is similar and the creation of the reference state follows the same steps (see section 2.2.2), the results obtained are different and therefore a different interpretation should be addressed when the reference state is created based on vibratory signals represented in the time or frequency domain. In order to compare the effects on the creation of the reference state based on the time and frequency domain the same vibratory responses were considered in both analysis. The vibration signals utilised as input-data were obtained from the case of study introduced in section 2.4.2. The reference state was built on the vibration responses measured on the non-delaminated beam B1 (see Table 2.3) recorded at 1.6 s length and sampling rate of 1280 Hz.

Figure 2.1(a) represents a free-decay vibration responses obtained in the experiment and Figure 2.1(b) is its frequency spectrum representation.

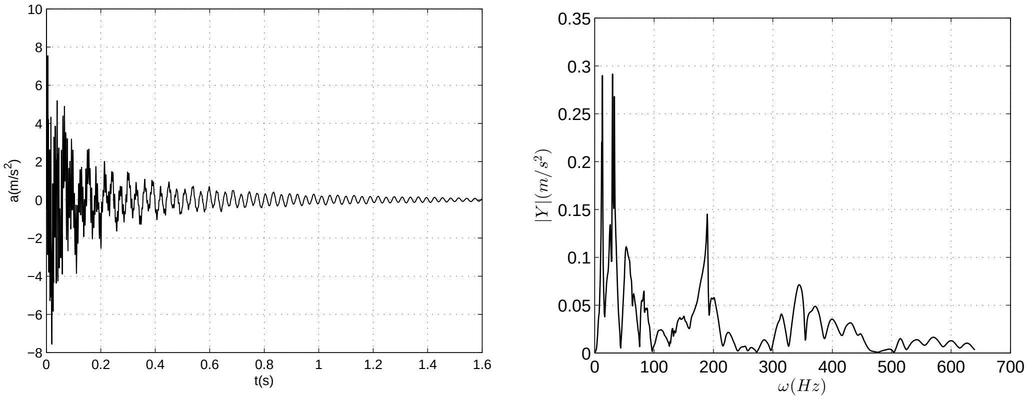

(a) (b)

Figure 2.1: Vibratory response of the composite laminated beam B1. a) Free-decay acceleration signal and b) Frequency spectrum of the free-decay acceleration signal

2.3.1 Reference state based on vibratory responses represented in the time domain

This section studies the effect on the creation of the reference state based on the vibratory responses in the time domain representation. Seven signal realisations were considered ($M = 7$) for this analysis. Each signal realisation was discretised into a vector $\mathbf{x}_m$ with a dimension of $N = 2048$ where the index m labels each realisation. The seven signal vectors were arranged in columns into the matrix $\mathbf{X}$ to define the data set considered for the construction of the reference state. The data set $\mathbf{X}$ is then processed by the steps described in the section 2.2.2.

Two sliding window sizes were considered in the creation of the embedding matrix. One case uses a $W = 7$ and other case $W = 50$ to create the embedding matrix shown in Equation 2.6. The eigendecomposition of the covariance matrix of the full embedding matrix $\mathbf{X}$ yields to a $(M \cdot W)$ total number of eigenvalues with their corresponding eigenvectors, which more specifically are 49 for the case of $W = 7$ and 350 for the case of $W = 50$. As explained in section 2.2.2, the eigenvalues and eigenvectors are ordered in decreasing order by means of their variance content in the vibratory signal. Each eigenvalue defines the percentage of variance contained in the direction of its corresponding eigenvector. The percent of the partial variance of each eigenvalue in the total decomposition is calculated by Equation 2.20 where λ_k are the eigenvalues and k is the eigenvalue index which varies from $k = 1, ..., K$ being K the total number of eigenvalues equal to $(M \cdot W)$.

$$\%\ variance = 100\ \frac{\lambda_k}{\sum_{k=1}^{K} \lambda_k} \tag{2.20}$$

Figure 2.2(a) and 2.2(b) represent the partial variance percent contained in each eigenvalue for the decomposition by using $W = 7$ and $W = 50$, respectively. These graphs represent the percentage variance only for 20 eigenvalues since the information contained in the rest of the eigenvalues is lower than zero percent. Comparing the two graphs can be observed that for the decomposition with $W = 50$ the variance information contained in the first eigenvalues is smaller than for $W = 7$. This behaviour stands in the fact that the information is distributed along the eigenvectors. As observed, for the case of $W = 50$ the number of eigenvalues increases and hence the variance percent contained in the first eigenvalues is reduced and distributed over all the components. However, for the case of $W = 7$ it can be observed that the variance percentage contained in the first eigenvalue is considerably larger than the rest of the eigenvalues.

As alluded to above, the decomposition of the covariance matrix of the data set in eigenvalues and eigenvectors is to distribute the oscillatory components contained in the original signal vectors by means of their variance content. In this case, when the value of W is small, the variance contained in the first eigenvalues is large because the eigenvector corresponding to the first eigenvalue contains more than one oscillatory component and hence more variance of the total vibratory signal. On the other hand, when W is relatively large, the variance in the first eigenvalue reduces and hence less oscillatory components are contained in its corresponding eigenvector. In this case, it can be stated that large values of W will give well separable components in comparison with small values of W [72].

As explained in section 2.2.2, the information contained in the eigenvectors is used to obtain the PCs. The PCs contains the information of the vibratory response projected onto the directions of the eigenvectors. Therefore, the data contained in the signal vectors are then transformed to the new space based on the directions of the eigenvectors. In order to compare the oscillatory components contained in each PC, it

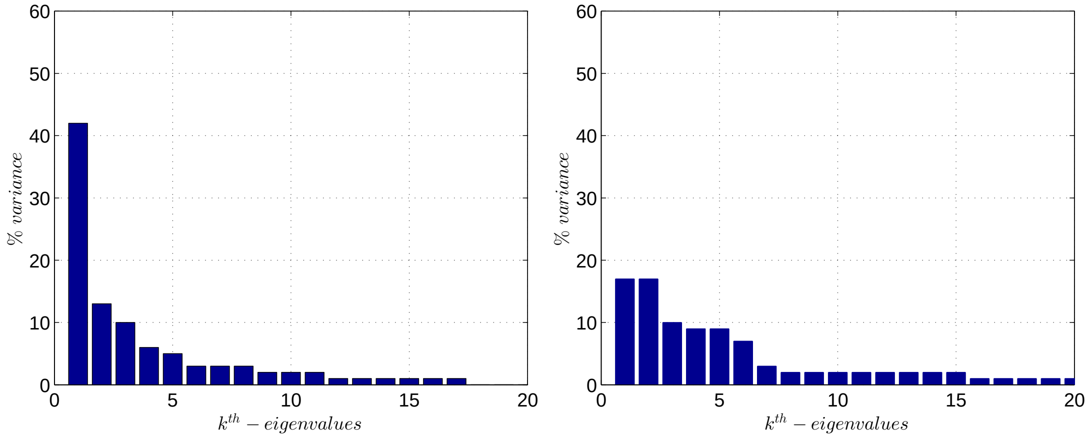

(a) (b)

Figure 2.2: Partial variance percent of each eigenvalue for a) $W = 7$ and b) $W = 50$ when the reference space is based in the time domain

is necessary to obtain the RCs by convolving the PCs onto the eigenvectors as explained in section 2.2.2.

Each RC is obtained based on the information contained in its corresponding PC weighted by its corresponding eigenvector. Each RC contains oscillatory components with the same content of variance in the vibratory response. The oscillatory components are less or more separated depending on the complexity of the vibratory system and also on the number of PCs obtained in the decomposition. In order to observe the oscillatory components contained in the RCs, the Fourier transform was applied to each RC of the matrix $\mathbf{R}^m$. Then, the matrix $\mathbf{R}^m$ is now transformed to $\mathcal{F}\{\mathbf{R}^m\}$ which is a new matrix with the frequency spectrum of each RC arranged in columns. Figure 2.3(a) and Figure 2.3(b) represent the reconstructed signal using only the first two RCs (RC_1 and RC_2) for the case of $W = 7$ and $W = 50$, respectively. Figures show the comparison of the reconstructed signal with the original signal to identify what oscillatory components are present in the reconstruction. In Figure 2.3(a) can be observed that the two first RCs contain the oscillatory components for low frequencies up to 200 Hz. It can be observed that the oscillatory components belonging to higher frequencies are not contained in these RCs. In a similar way, Figure 2.3(b) shows the frequency spectrum of the reconstructed signal using the first two RCs for a $W = 50$. It can be observed that only the oscillatory components belonging to the low frequencies upto 35 Hz are contained in the reconstructed signal. Also it can be observed that for the decomposition of the vibratory signal by using $W = 50$, the oscillatory components contained in the first RCs are very well depicted in comparison with the decomposition by $W = 7$ where more oscillatory components are contained in the reconstructed signal. As explained above, when the decomposition is done by large values of W the oscillatory components are better separated. Therefore, the RCs have interpretable oscillatory components which can be used to identify particular modes. This can be beneficial when the interest is to extract particular modes of vibration.

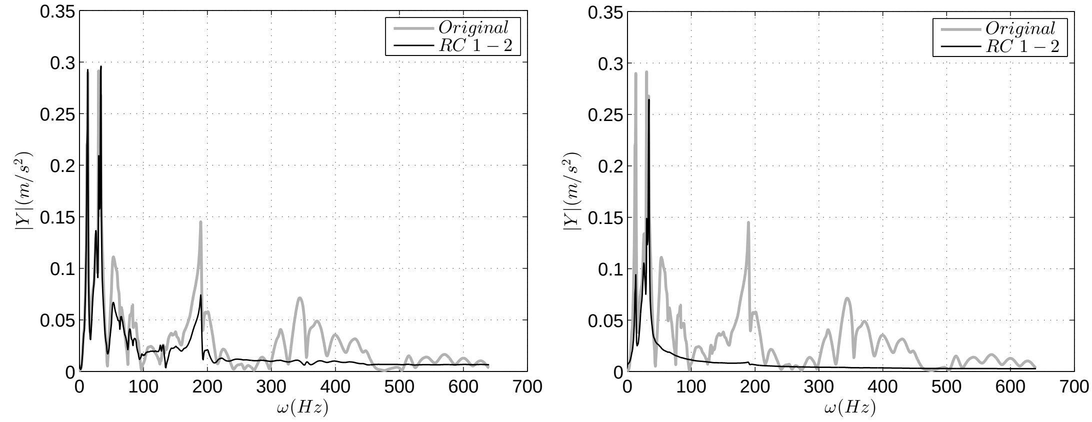

(a)

(b)

Figure 2.3: Comparison between the original vibratory signal and the reconstructed signal using 2-RCs. The graphs show the effect of the methodology performed in the time domain. a) Comparison when $W = 7$ and b) $W = 50$

In Chapter 5 is presented the self-sensing capabilities of a carbon nano-enriched laminated beam under vibration excitation for its auto-assessment. In this study the methodology was implemented in the time domain because the interest was to extract the predominant frequency of vibration. The results and findings of this study are detailed in Chapter 5. Other case of study where the methodology was implemented in the time domain can be found in [110]. In this study, the unsteady phenomena in a centrifugal blower was studied. The decomposition of the original signal onto RCs allow to draw the phase trajectory that clearly separated non-stable blower working conditions from its regular operation.

2.3.2 Reference state based on vibratory responses represented in the frequency domain

This section studies the effect on the creation of the reference state based on the vibratory responses in the frequency domain representation. The reference state is built on the vibratory signals measured on the non-delaminated beam B1 (see Table 2.3) recorded at 1.6 s length and sampling rate of 1280 Hz as shown in Figure 2.1(a). Seven signal realisations were considered ($M = 7$) for this analysis like in the previous section 2.3.1. Each signal realisation was discretised into a vector $\mathbf{x}_m$ with a dimension of $N = 2048$ where the index m labels each realisation. Each signal vector realisation was transformed to the frequency domain (see Figure 2.1(b)) by the Fourier transform as shown in Equation 2.21.

$$\mathbf{Y}_m(k) = \frac{1}{N} \sum_{n=0}^{N-1} x_{n,m} e^{-j2\pi kn} \tag{2.21}$$

where $k \in [0, N-1]$, m is each signal vector realisation and N is the vector length.

Therefore, the frequency domain signal vectors are now considered to create the reference state. Each $|\mathbf{Y}_m(k)|$ is arranged in columns into the matrix $\mathbf{X}$ with a dimension NxM where N is the signal vector dimension which for the case of the frequency domain representation is $N = N' = N/2 = 1024$.

$$\mathbf{X} = (|\mathbf{Y}_1(k)|, |\mathbf{Y}_2(k)|, ..., |\mathbf{Y}_M(k)|) \tag{2.22}$$

The data set $\mathbf{X}$ is then processed by the steps described in the section 2.2.2. Two sliding window sizes were considered in the creation of the embedding matrix. One case uses a $W = 7$, the other case $W = 50$ to create the embedding matrix shown in Equation 2.6. The same sliding window sizes that in section 2.3.1 were considered in this analysis. The eigendecomposition of the covariance matrix of the full embedding matrix $\mathbf{X}$ yields to 49 eigenvalues and eigenvectors for the case of $W = 7$ and 350 for the case of $W = 50$. In this way, the number of RCs obtained in the signal vectors decomposition will be the same that in section 2.3.1. The partial variance percent of each eigenvalue over the total eigenvalues was calculated by Equation 2.20.

Figure 2.4(a) and 2.4(b) represent the partial variance percent contained in each eigenvalue for the decomposition by using $W = 7$ and $W = 50$, respectively. These graphs represent the percentage variance only for 20 eigenvalues since the information contained in the rest of the eigenvalues is lower than zero percent. Comparing the two Figures, it can be observed that for the decomposition with $W = 50$, the variance information contained in the first eigenvalue is smaller than for $W = 7$. This behaviour stands in the fact that the information is distributed along the eigenvectors and when large values of W are considered the number of eigenvectors increases, and hence the information is then distributed over all of them. As observed, for the case of $W = 50$ the number of eigenvalues increases with respect to the case of $W = 7$ and hence the variance percent contained in the first eigenvalues is reduced and distributed over all the rest of the eigenvalues. However, the variance percent contained in the first eigenvalue is the largest in both cases ($W = 7$ and $W = 50$) with a significant difference in comparison with the other eigenvalues. Therefore, the first eigenvector contains the majority of the variance and it will have much more global contribution in the reconstruction of the signal vector. However, the rest of the eigenvectors have less variance content and their contribution in the reconstruction will be more local. Figures 2.5(a) and 2.5(b) represent the reconstruction of the original signal vector by using only the first two RCs (RC_1 and RC_2) for the case of $W = 7$ and $W = 50$, respectively.

In both graphs can be observed that the reconstructed signal describes approximately the general trend of the original frequency spectrum. The estimated reconstructed signal contains information along the entire spectrum but it is more significant in the frequencies where the higher peaks are presented, in other words, at frequencies where the maximum of energy contained in the spectrum is concentrated. For the case of $W = 7$ (see Figure 2.5(a)), the reconstructed signal is very good approximated and it contains well depicted peaks at low frequencies. However, for the case of $W = 50$ the reconstructed signal is smoother than in Figure 2.5(a), although the reconstruction still has a contribution to the entire spectrum (see Figure 2.5(b)). As mentioned above, the first eigenvectors contain the majority of the variability in terms of variance content and this is clearly represented in the reconstructed spectrum as observed in Figure 2.5(a) and 2.5(b) where a smooth trend is achieved by using only two RCs in the reconstruction. The selection of the sliding window size W is very important in the dimension of the decomposition and it depends on the goal of the study. Depending on what analysis is going to be addressed the selection of W will help to obtain more understandable information. A study in the sliding window size selection is explained in section 2.5.2.

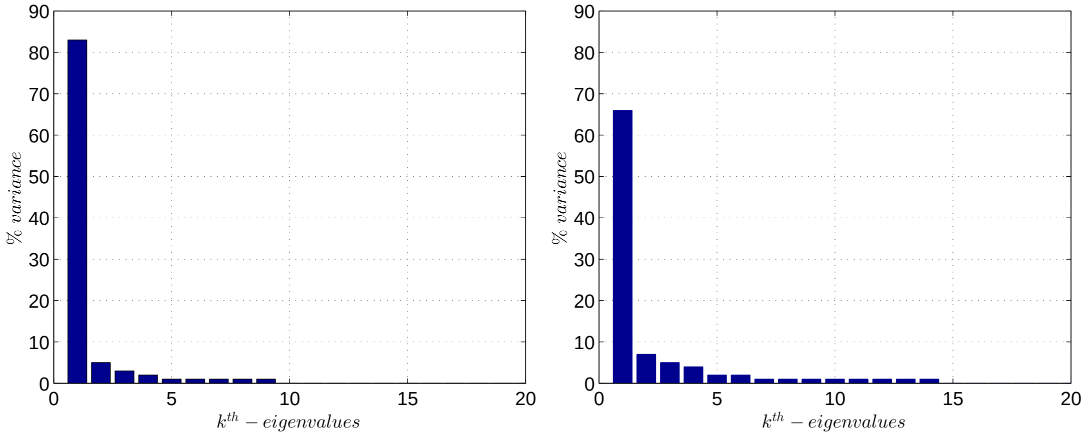

(a) (b)

Figure 2.4: Partial variance percent of each eigenvalue for a) $W = 7$ and b) $W = 50$ when the reference space is based in the frequency domain

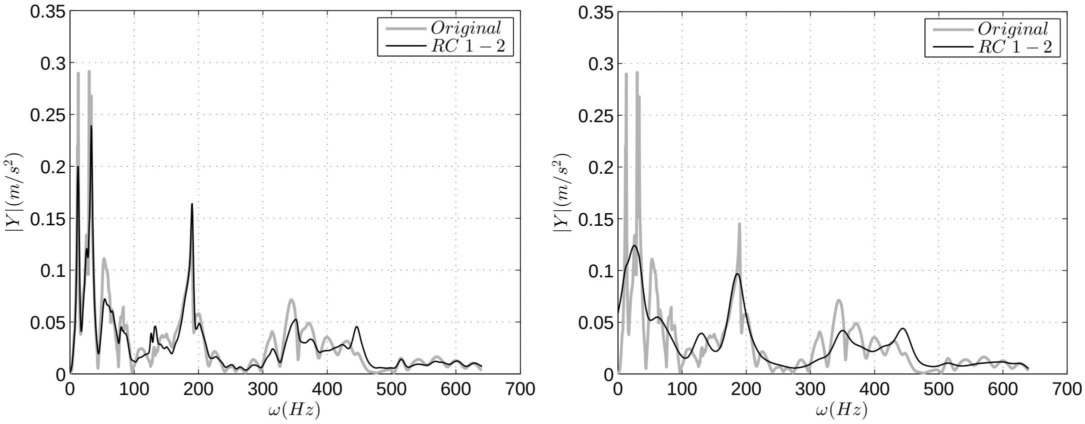

(a) (b)

Figure 2.5: Comparison between the original vibratory signal and the reconstructed signal using 2-RCs. The graphs show the effect of the methodology performed in the frequency domain. a) Comparison when $W = 7$ and b) $W = 50$

In Chapter 3 and 4, the methodology was implemented by using vibration responses in the frequency domain representation. In Chapter 3, the delamination assessment was studied in composite laminated plates. In Chapter 4, the disbond between the upper and lower shell of a wind turbine blade was first studied in a small blade from a residential wind turbine and secondly in a large scale wind turbine blade of 34m.

2.3.3 Discussion

The analysis in sections 2.3.1 and 2.3.2 was to explain the effects when the reference state is constructed in the time or frequency domain. The comparison in the eigendecomposition and in the reconstruction was analysed. For both cases, it was observed that the first eigenvalues contain the majority of the variance and it decreases for the rest of the eigenvalues. In order to compare the eigendecomposition for both, time and frequency domain, the eigenvalue spectra was calculated where the normalised eigenvalue and the normalised index [111] are defined in Equation 2.23, respectively

$$log\left(\frac{\lambda_k}{\sum_k^K = \lambda_k}\right) \ , \ k = \frac{k}{K} \tag{2.23}$$

λ_k is the eigenvalue. The results are represented in Figures 2.6(a) and 2.6(b) when the decomposition, based on the time and frequency domain, is compared for the case of $W = 7$ and $W = 50$, respectively. For both sliding window size cases, it is observed that the first eigenvalues are smaller for the time domain case in comparison with the frequency domain case. The magnitude of eigenvalues decreases for both cases even though in the time domain case, the eigenvalues are larger than in frequency domain. This can explain that for the time domain case the difference in variance content between the first and the rest of the eigenvalues is less than for the frequency domain case. It is observed that the variance content is constantly distributed as shown in Figure 2.6(a) for the time domain case, while a big jump can be observed between the first and the second eigenvalue for the case of the frequency domain. After this jump, the magnitude of the eigenvalues goes constantly down. In Figure 2.6(b), it is observed that groups of eigenvalues are created in the time domain decomposition which means that they have similar amount of variance content. This proves that large values of W leads to more separable oscillatory components in the time domain decomposition. For the case of the frequency domain, the separation is clearly achieved between the first and the rest of the eigenvalues. In this case the effect on the selection of W will change the variance content in the first eigenvalue.

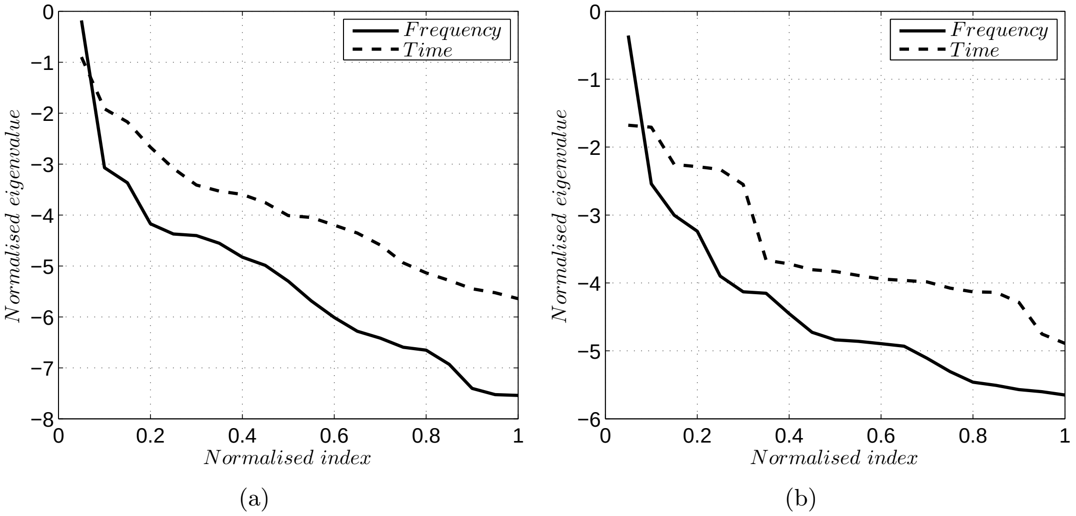

Figure 2.6: Comparison of the eigenvalue spectra between time and frequency domain decomposition for a) $W = 7$ and b) $W = 50$

This means that when the frequency domain is used, the first eigenvector will contain the general information in the spectrum which leads to a smooth trend in the reconstruction as shown in Figure 2.5. Then, all frequency modes captured in the original frequency domain are also included in the reconstructed spectrum. The rest of the eigenvectors will add the fluctuations on the spectrum trend described by the first RC. It is true that the reconstructed spectrum does not have the same amplitude as the original signal vector but it still conserves the general weight of distribution in the entire spectrum. It can be observed that the reconstructed spectrum gives more importance at frequency bands where the maximum energy is concentrated.

In the case of the time domain, the behaviour observed in the reconstruction has a different interpretation to that in the case of the frequency domain. The decomposition in the time domain leads to a number of oscillatory components which can be interpreted separately. As shown in Figure 2.3 only a few frequency bands are included in the reconstruction signal. The separability of these oscillatory components depends on the value of sliding window size. As a general rule, large values of W will give more separated oscillatory components. The benefit of obtaining separated oscillatory components is to identify the particular modes which can contain relevant information.

With the comparison of the creation of the reference state based on time or frequency domain developed in the above sections, it can be concluded that the selection of one of these analysis depends on the case to study. When a time domain representation is used in the methodology, separated oscillatory components are obtained. The information contained in the reconstructed signal will depend on which oscillatory components are considered in the reconstruction. The separability of these oscillatory components will depend on the complexity of the vibratory system and also on the dimension of decomposition defined by W. This analysis can be beneficial when a predominant mode of vibration is to be analysed and therefore the methodology can be useful for mode extraction or identification. However, when the frequency domain representation is used, it can be observed that a smoother version of the original spectrum is obtained by the reconstructed spectrum. The reconstructed spectrum is more approximated to the original one, when more RCs are considered in the reconstruction. This analysis can be beneficial when more than one vibration mode is considered in the analysis. As the reconstruction describes the general trend of the spectral line, all rotational patterns are considered in the reconstructed spectrum.

2.4 Demonstration and validation of the methodology

In this section, the methodology presented and described in section 2.2 is validated and studied on two case of studies. First, the methodology is processed in a two degree of freedom with non-linear spring-mass-damper simulated system and secondly in an experimental test with five composite laminated beams.

2.4.1 Case study I: 2-DOF nonlinear spring-mass-damper system

In order to demonstrate the described damage assessment methodology introduced in section 2.2, here is considered a two degree-of-freedom (DOF) system described by the second order, nonlinear, ordinary differential Equation 2.24. The system is illustrated in Figure 2.7. The use of the simulated system is a controlled manner to study the effect of any alteration in the system and to evaluate the sensitivity for detection and further diagnosis obtained by the methodology.

$$[\mathbf{M}]\ddot{\mathbf{x}} + [\mathbf{C}]\dot{\mathbf{x}} + [\mathbf{K}]\mathbf{x} + \mathbf{f}(\dot{\mathbf{x}}, \mathbf{x}) = 0 \tag{2.24}$$

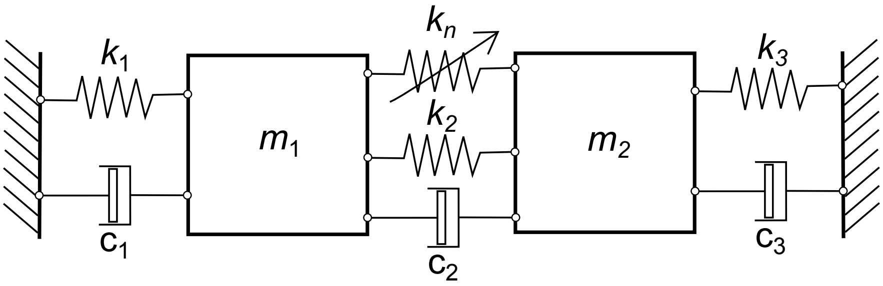

Figure 2.7: 2-DoF spring-mass damper with nonlinear stiffness simulated system

In the above Equation 2.24, [**M**], [**C**] and [**K**] are the mass, damping and stiffness matrices respectively defined in Equation (2.25). The function $\mathbf{f}(\dot{\mathbf{x}}, \mathbf{x})$ provides a nonlinear quadratic coupling between the two masses (m_1 and m_2) as defined in Equation (2.26).

$$[\mathbf{M}] = \begin{bmatrix} m_1 & 0 \\ 0 & m_2 \end{bmatrix} [\mathbf{C}] = \begin{bmatrix} c_1 + c_2 & -c_2 \\ -c_2 & c_2 + c_3 \end{bmatrix} [\mathbf{K}] = \begin{bmatrix} k_1 + k_2 & -k_2 \\ -k_2 & k_2 + k_3 \end{bmatrix} \tag{2.25}$$

$$\mathbf{f}(\dot{\mathbf{x}}, \mathbf{x}) = \left\{ \begin{array}{c} -k_n(x_2 - x_1)^2 \\ k_n(x_2 - x_1)^2 \end{array} \right\} \tag{2.26}$$

In Equation 2.25, m_1 and m_2 are the masses parameters of each block, mass respectively. k_1, k_2 and k_3 are the linear stiffness coefficients for each simulated spring and c_1, c_2 and c_3 the damping coefficients for each simulated damper, respectively. In Equation 2.26, k_n is the nonlinear stiffness coefficient. The parameters and coefficients values used in generating the response signal are defined and detailed in the Table 2.1.

Parameter	Value	Units
$m_1 = m_2$	5	kg
$c_1 = c_2 = c_3$	6	Ns/m
$k_1 = k_2 = k_3$	2000	N/m
k_n	10000	N/m^2

Table 2.1: Initial parameters in the 2-DoF simulated system

The acceleration free-decay response was obtained by numerically integrating Equation 2.24 with a time step $\Delta_t = 0.00125$ s for $N = 2480$ data points so that discrete and continuous time are related via $t = n\Delta_t$. Therefore, the vibratory signal was measured for 3.1 s long and sampled at 800 Hz. The initial conditions were set to the values detailed in Table 2.2.

Parameter	Value	Units
$x_0^{(1)} = x_0^{(2)}$	0	m
$\dot{x}_0^{(1)}$	0	m/s
$\dot{x}_0^{(2)}$	1	m/s

Table 2.2: Initial conditions in the 2-DoF simulated system

The system is excited by applying an initial velocity of 1 m/s in the m_2. The acceleration free-decay response is then measued in the m_1. The vibration responses measured, when the system is defined by the initial parameters detailed in Table 2.1, are considered as the vibration responses from the reference system which simulates the *undamaged system*.

In order to introduce some changes in the initial parameters and therefore simulate an alteration in the system, the stiffness parameters were reduced. More than one system alteration is considered by reducing k_1, k_2 and k_n stiffness parameters. Each time when a certain stiffness parameter was modified the rest of the parameters remained constant in order to control where the alteration was introduced. In this way, four system scenarios were generated: one for the system with the initial parameters detailed in Table 2.1 and three system alterations by reducing the initial parameters of k_1, k_2 and k_n. Each stiffness parameter was reduced from 1% to 30% by increments of 1%. These reductions were applied for each stiffness parameter separately to see the effect on the progression of the alteration, caused by the stiffness reduction, on the behaviour of the system. Therefore, one vibratory response was measured for each stiffness reduction, in this case 30 signals for each stiffness scenario k_1, k_2 and k_n and additionally one for the system with the initial parameters detailed in Table 2.1.

Consequently, the methodology presented in section 2.2 is applied on this simulated system. The vibratory response measured from the system defined with the initial parameters is used to create the reference state as defined in section 2.2.2. The number of vibration signals used for this analysis was $M = 1$ and the sliding window size

$W = 7$. In this way the vibratory response is discretised into a vector $\mathbf{x}$ with a dimension $N = 2480$. The vibratory responses measured on the system describe a free-decay response due to the procedure of the excitation, where an initial velocity was applied and the system was released to vibrate freely without the interaction of any external force (free vibration). In this way all the modes of vibration were excited and then presented as resonant peaks in the frequency domain representation. As explained in section 2.3 when more than one mode wants to be considered, it is better to create the reference state in the frequency domain. When a stiffness reduction is introduced, it can modify some modes of vibration but it is difficult to predict which ones are the most sensitive to damage [112]. For this reason considering the frequency domain analysis will help to consider all vibration modes in the analysis.

The signal vector $\mathbf{x}$ is then transformed to the frequency domain by the Equation 2.21 and arranged into $\mathbf{X} = |\mathbf{Y}(k)|$ with a new dimension $N = 1240$. The vector $\mathbf{X}$ is then copied and lagged $W = 7$ times to create the embedding matrix $\check{\mathbf{X}}$ as explained in Equation 2.6. Posteriorly, the eigendecomposition is applied on the embedding matrix to obtain the eigenvalues and eigenvectors, PCs and finally the RCs which define the reference state $\mathbf{R}$ with a dimension 1240 x 7. The reference state has 7-RCs which are based on the variance content in the direction of their corresponding PC. Therefore, the reference state is then used to obtain the FVs for each observation signal vector (see section 2.2.3). Multiplying each observation signal vector by each RC of the reference state yields to the FVs $\mathbf{T}$, as shown in Equation 2.16, with a dimension equal to W which is equal to 7 for this study. Therefore, each observation signal vector is compressed and converted in a multi-dimensional FV by means of the *similarity* to each reconstructed component contained in the reference state.

The FVs are compared onto the feature space. As the values of the FV are in the same order as the RCs, it is clear that the value in the first place was calculated by the first RC, the second value by the second RC and so on. As mentioned before, the contribution of the first RC in the reconstruction of the original spectrum is larger than the other ones because it contains most of the variance. For this reason the first values of the FV contain also an equivalent information regarding to their first RCs. In this case the most relevant information (global) is then concentrated in the first values of the FVs. Then, this information can be used to find the similarity between different FVs. The dimension of the FVs used in this analysis was $p = 2$. The FVs for each scenario were projected onto the feature space as shown in Figure 2.8.

Figure 2.8(a) shows how the evolution of the stiffness reduction on k_1 behaves onto a 2-dimensional space defined by the FVs obtained through the methodology. The stiffness reduction is very well detected not only when a certain reduction occurs but also when the reduction increases. It can be observed that for reductions smaller than 15%, T_1 has more influence in comparison with T_2. However, T_2 plays an important role for reductions between 15% and 20%. For reductions larger than 20% the contribution of T_1 and T_2 are similar and hence both contribute in the detection of the stiffness reduction. It is then important to mention that the influence of T_1 and T_2 is not linear and it depends on how much the stiffness was reduced. Figure 2.8(b) shows the behaviour of the stiffness reduction of k_2. It can be observed that the influence of T_1 and T_2 is similar for all stiffness reductions apart from small and large stiffness reductions where T_2 has more contribution. All stiffness reductions are very well depicted except for smaller reductions than 8% and larger than 26% where the distances between points does not increase significantly. Finally, Figure 2.8(c) represents the effect on the stiffness reduction of k_n. In a similar way that in the case of the reduction of k_2 the influence of T_1 and T_2 is similar. It can be observed that for small reductions the detection is much smaller than for the case of larger reductions. When the reductions increase, the distance does not only increase from the case of no-reduction but also between increments of reduction and hence this will help to track the evolution of the stiffness reduction.

Analysis in three stiffness reduction cases

Three examples were selected for further analysis. The examples were selected when the stiffness has been reduced by 10%, 20% and 30%. These three stiffness reduction cases has been applied on k_1, k_2 and k_n. Figure 2.9 represents the effect on the spectra lines of the frequency spectrum when the stiffness reduction occurs. Figure 2.9(a) shows the effect of the stiffness reduction of k_1, which affects to all the peaks. Figure 2.9(b) represents the effect of the reduction severity of k_2, which shows a clear systematic

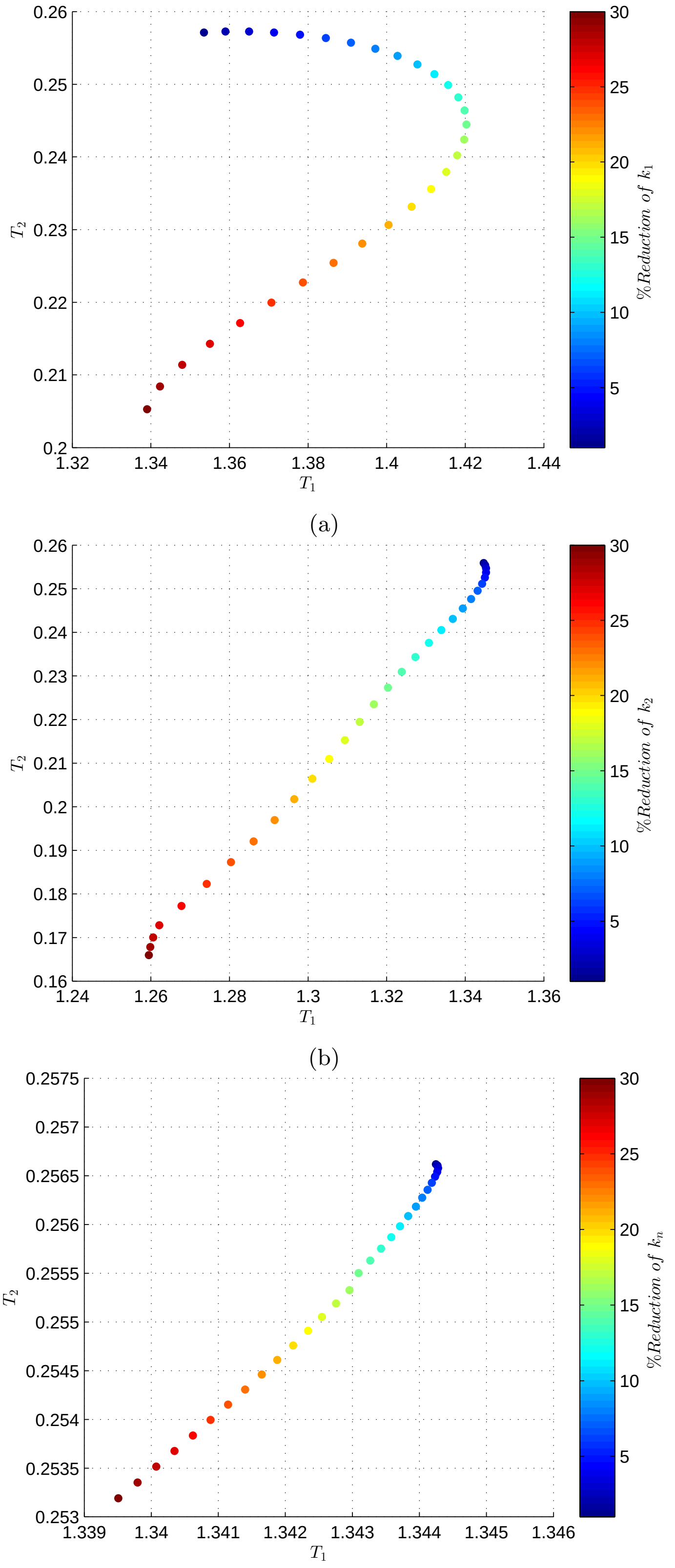

(a)

(b)

(c)

Figure 2.8: Effect on the 2-Dimensional feature space when the stiffness is reduced from 1% to 30% by increments of 1% in a) k_1, b) k_2 and c) k_n.

variation in the second and third peak. While, Figure 2.9(c) represents the effect of the stiffness reduction of k_n. Here, it is shown that changes occur mainly in the third peak and very little in the second peak by changes on the amplitude.

In order to accomplish the novelty detection explained in section 2.2.4, ten signal realisations were obtained for each scenario: no stiffness reduction and 10%, 20% and 30% respectively for each $k_\#$ case. In total, a set of 40 vibration signals were obtained by adding random white Gaussian noise defined by signal-to-noise ratio SNR=P_{signal}/P_{noise} in dB where P_{signal} and P_{noise} are the signal and the noise power, respectively. For this study the additive noise was set at 20 dB (e.g. the power of the signal was 20 times greater than the power of the noise).

The reference state was created with the following parameters $M = 7$ and $W = 7$. In this case the reference state is constructed based on 7 signal vector which yields to 49 eigenvalues and their respective eigenvectors. Each signal vector was divided in 7 PCs and hence 7 RCs, which were used as the reference state $\mathbf{R}$ with dimension 1240 x 7. Figure 2.10(a) represents the scree diagram of the eigen-decomposition where can be observed the partial variance percentage contained in each eigenvalue. The value of the partial variance was calculated by the Equation 2.20. It can be observed that the percentage of variance contained in the first eigenvalue is the largest. The first eigenvalue and its corresponding eigenvector contributes to the construction of the first RC, which describes the general trend of the spectral line. Figure 2.10(b) shows the reconstructed spectrum by using only the 80% contained in the first two RCs. The reconstructed spectrum approximates relatively well the trend of the original spectrum and depicts very well the three peaks represented.

Based on the reference state created by the 7 signal vectors from the case when the system was defined by the initial parameters, the FVs for each observation signal vector were calculated. Each set of FVs, corresponding to each stiffness reduction scenario, were compared and projected onto the feature space separately. The projection onto the feature space will reduce the distances between FVs from the same stiffness reduction severity but also will increase the distances between FVs from different stiffness reduction severities. This effect can be observed in Figures 2.11, 2.13(a) and 2.14(a) that represent the cluster effect onto the feature space when the stiffness reduction was

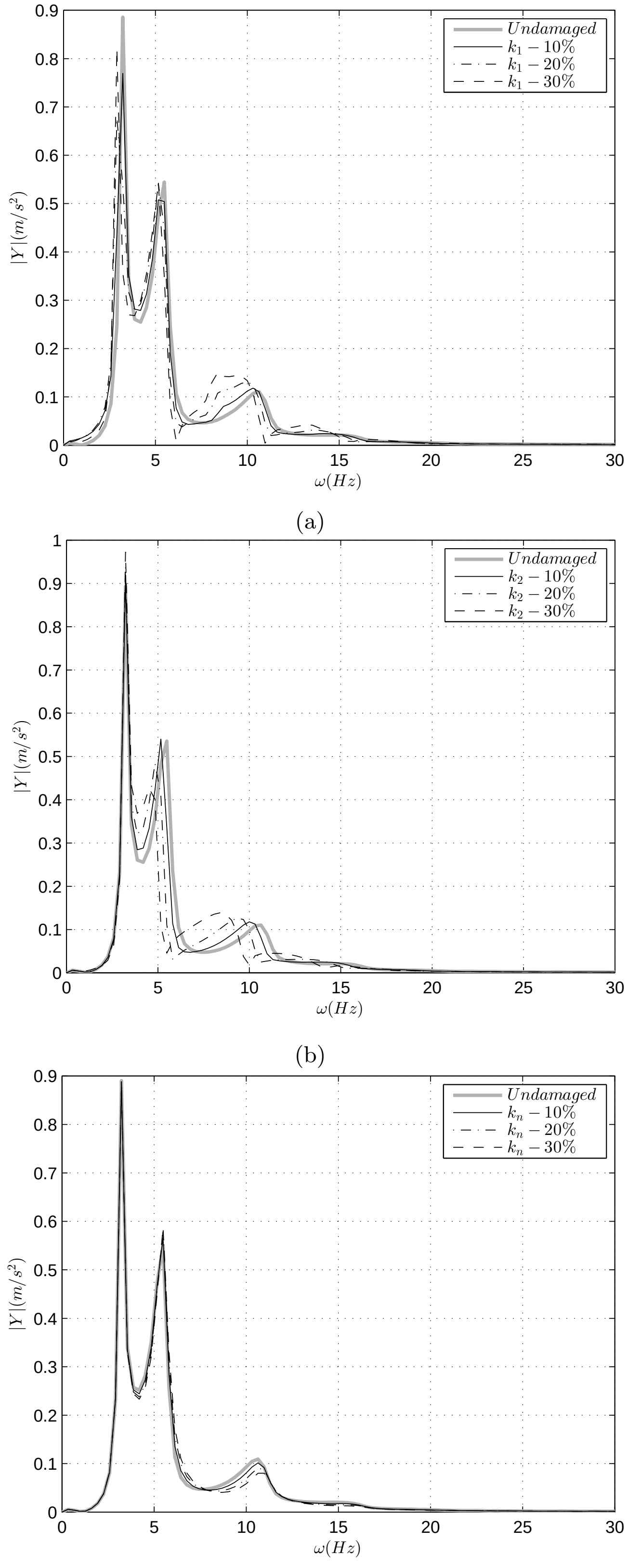

(a)

(b)

(c)

Figure 2.9: Effect on the frequency spectrum plot of the vibration response when the stiffness is reduced by 10%, 20% and 30% in a) k_1, b) k_2 and c) k_n.

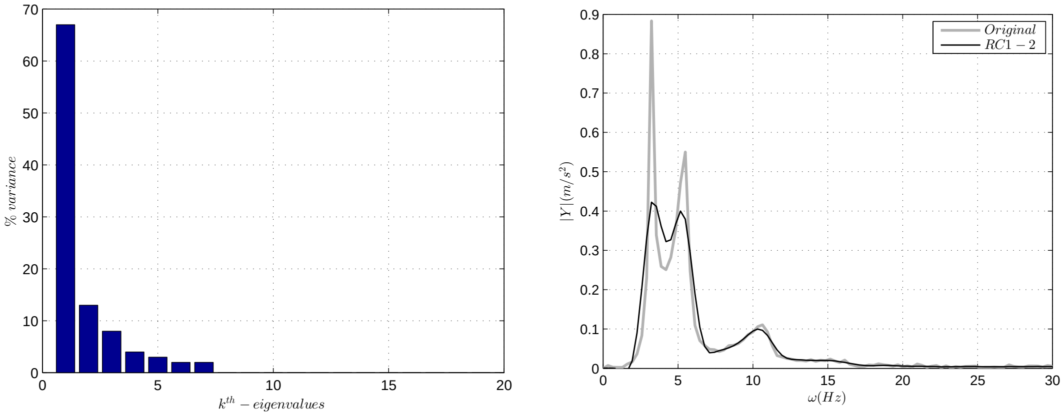

(a) (b)

Figure 2.10: a) Scree diagram of the decomposition of the vibratory response of the reference scenario (non-stiffness reduction, *undamaged* system). Only 20 eigenvalues are represented. b) Comparison of the original frequency spectrum and the reconstructed frequency spectrum with two RCs (RC_1 and RC_2).

applied on k_1, k_2 and k_n, respectively.

The effect of these clusters is successfully achieved and enable to distinguish between different stiffness reduction severities. The stiffness reduction severity is then evaluated by the procedure described in section 2.2.4. A baseline FV matrix was created by the 10 FV corresponding to the observation signal vectors from the reference system defined by the initial parameters. Therefore, the distances between the FV matrix, $\mathbf{T}_B$ and the observation signal vectors were measured for further evaluation of the stiffness severity as defined in the Equation 2.18. Based on this procedure the effect on the stiffness reduction is analysed and commented separately for each k_1, k_2 and k_n scenario.

Figure 2.11 represents the clustering of different stiffness reductions in k_1. It is observed that clusters were successfully obtained by the projection of the FVs onto the feature space defined on T_1 and T_2 (see Figure 2.11(a)), T_1 and T_3 (see Figure 2.11(b)) and T_2 and T_3 (see Figure 2.11(c)). As previously alluded, when the FVs are projected onto the space defined on T_1 and T_2 the contribution of T_1 is insignificant for the separation between stiffness reduction interval 10% and 20%. For this reason the importance of more variables can be determinant for the correct detection. The same effect is observed when the FVs are projected onto the 2 dimensional space defined on T_1 and T_3. The contribution of T_3 describes a similar trend than T_2. However, when the FVs are

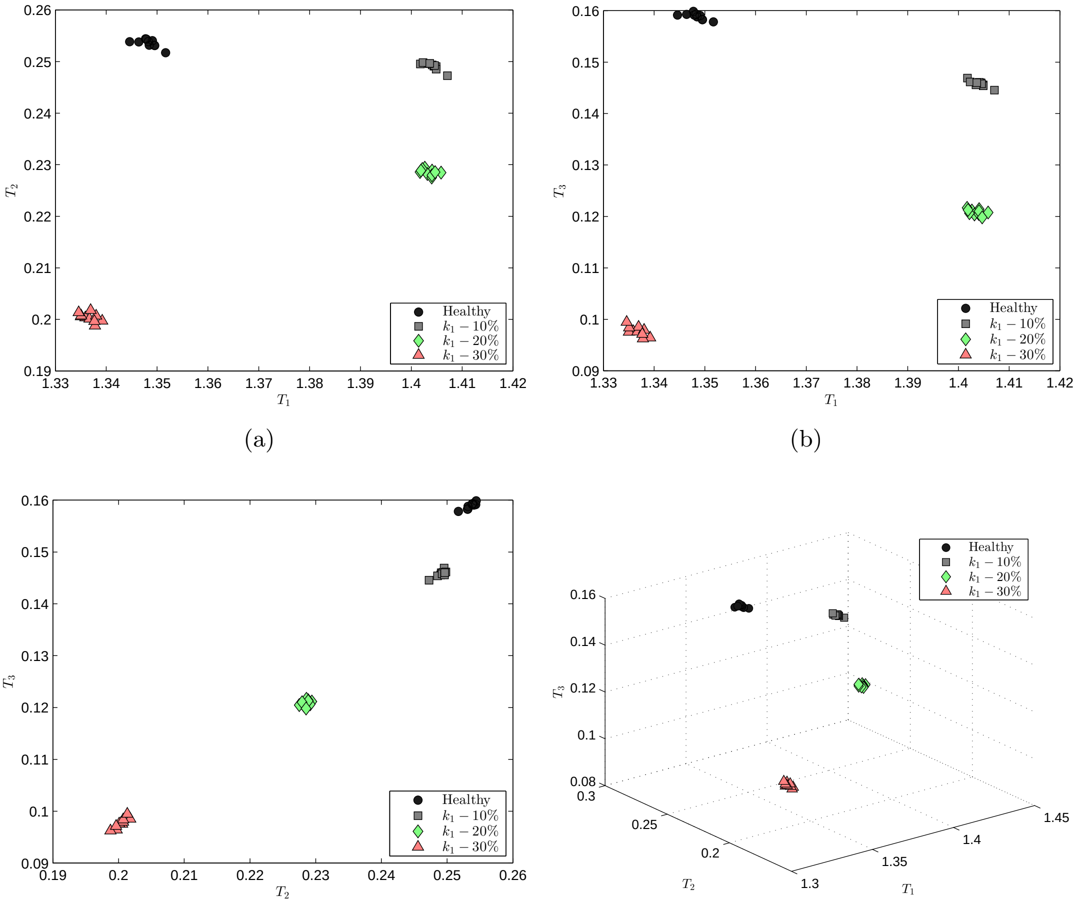

(a) (b)

(c) (d)

Figure 2.11: Cluster effect on the feature space when the stiffness parameter k_1 is reduced by 10%, 20% and 30%. a) Representation onto a 2-D space defined by $T_1 - T_2$, b) onto a 2-D space defined by $T_1 - T_3$, c) onto a 2-D space defined by $T_2 - T_3$ and d) onto a 3-D space defined by $T_1 - T_2 - T_3$.

observed onto a 2 dimensional space defined on T_2 and T_3, the stiffness reductions are clearly detected not only by the comparison between healthy (no-stiffness reduction) and the stiffness reductions in general, but also between different stiffness reduction severities. This effect is also observed by computing the distances between the baseline defined on the reference signal vectors and the different observation signals. Figure 2.12(a) shows the distances of the observations to the baseline when a 2-dimensional signal vector (T_1 and T_2) was used. It was observed that the observations of all stiffness reductions were detected in comparison with the baseline (no stiffness reduction) and an increment of the distance was also observed when the stiffness reduction was incremented. However, when the stiffness was reduced at 10% and 20%, the increment of the stiffness reduction could not be detected with a 2-dimensional FV (T_1 and T_2).

However, with this two dimensional FV (T_1 and T_2), the differences between stiffness reductions at 10% and 20% cannot be detected.

On the other hand by increasing the dimension of the FV to 3 (T_1, T_2 and T_3), the difference between the two scenarios is then successfully detected (see Figure 2.12(b)). Also, it is observed that the distance of the other scenarios increases and hence the damage index becomes larger which is beneficial for cases when the detection between altered and non-altered system cannot be achieved with low dimension FVs.

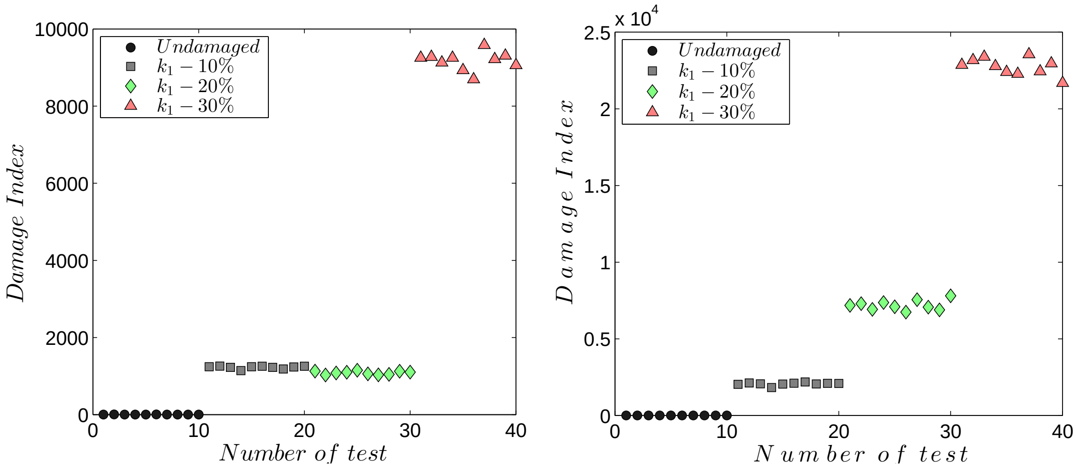

(a)

(b)

Figure 2.12: Damage detection index plots applied on the reduction of the stiffness parameter k_1 by 10%, 20% and 30%. a) Damage index using a two dimension FV (T_1 and T_2) and b) Damage index using a three dimensions FV (T_1, T_2 and T_3).

Similarly, the stiffness reduction severity is detected for the case of any alterations in k_2. Here, the detection was achieved with a 2-dimensional FV (T_1 and T_2). Figure 2.13(a) represents the clustering effect of the FVs onto the feature space and Figure 2.13(b) shows the damage index based on the same 2-dimensional FVs. The contribution of T_1 and T_2 is similar in this case, and then any of the three stiffness alterations on k_2 is perfectly detected. The damage index is larger when the stiffness reduction severity increases so that each stiffness alteration in k_2 is successfully detected and distinguished in comparison with the others. The alterations in the stiffness parameter k_n are also analysed. Figure 2.14(a) shows that different clusters are obtained for each

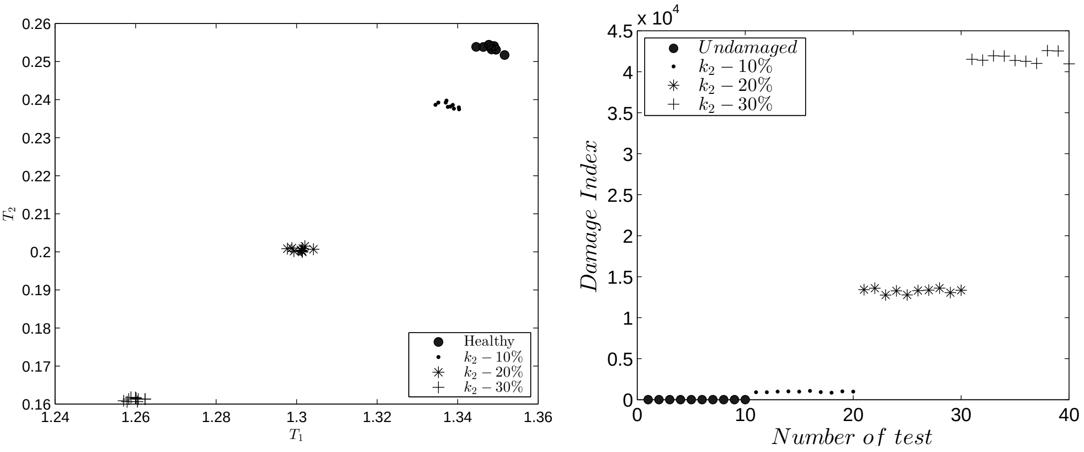

(a) (b)

Figure 2.13: Damage detection index plots applied on the reduction of the stiffness parameter k_2 by 10%, 20% and 30%. a) Cluster effect onto 2-D space defined by $T_1 - T_2$ b) Damage index using a two dimension FV (T_1 and T_2).

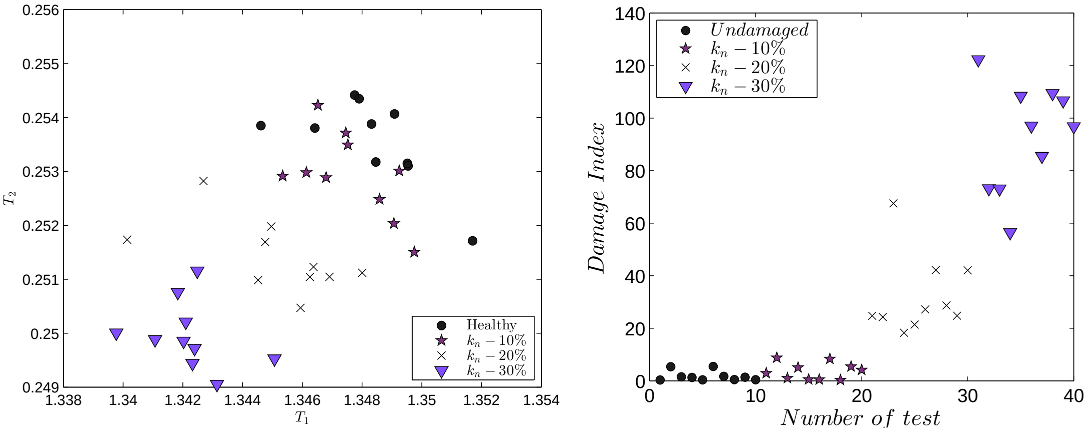

(a) (b)

Figure 2.14: Damage detection index plots applied on the reduction of the stiffness parameter k_n by 10%, 20% and 30%. a) Cluster effect onto 2-D space defined by $T_1 - T_2$ b) Damage index using a two dimension FV (T_1 and T_2).

stiffness reduction severity. The alterations on k_n affect slightly the system and for this reason the clusters are a bit more dispersed in comparison with the reduction on the linear stiffness k_1 and k_2. However, as the contribution in T_1 and T_2 is similar, it is observed that the cluster points corresponding to larger alterations in k_n moves away form the cluster points corresponding to the unaltered system (healthy). This effect can be measured when the damage index is computed by the same 2-dimensional FVs as shown in Figure 2.14(b). The value of the damage index increases as the stiffness alteration increases. This helps in the differentiation between system alterations. The study in the alterations of k_n demonstrates that changes on the simulated system because non-linearities can also be detected. This is beneficial because damage introduces non-linearities in the vibratory response which can be used for damage detection [54].

2.4.2 Case study II: Composite laminated beams with one healthy and four delaminated scenarios

The methodology demonstrated and validated in the simulated system in section 2.4.1 is now performed and validated in this case of study with five composite laminated beams. In this section it is presented, first the material characteristics and manufacturing process of the composite laminated beams, secondly the experimental setup for data collection and finally the delamination assessment through the methodology.

Material and manufacturing process of the composite laminated beams

Five carbon fibre/epoxy laminated beams were manufactured by hand lay-up and reinforced using woven laminated multiprepeg E-722 with 1.21 g/m^3 resin density at 23^{o}C. A total of 10 layers were used to produce 2.5 mm thickness of the beam. The beams were moulded to obtain the right dimensions and placed into a vacuum bag for the process of curing inside the autoclave. The parameters of the curing recipe were selected as follows: The air temperature was incremented at 3^{o}C/min and posterior hold at 120^{o}C for one hour. The pressure in the vacuum bag was at 1.4 bar and then the pressure of the autoclave was incremented up to 5 bar. After an hour at 120^{o}C the temperature slowly decreased to cool down to 50^{o}C before removal of pressure. The final dimensions of the beams were 980 x 42 x 2.5 mm.

Four of the five beams were designed to have different delamination configurations as detailed in table 2.3, see also Figure 2.15. The delamination was introduced during the manufacturing process. A Teflon sheet was introduced, with the dimensions and locations detailed in Table 2.3, before the manufacturing process to obtain four delaminated beams as shown in Figure 2.16(a). The non-adherent property of the Teflon sheet defines a region where the connection between the laminates, in both upper and lower sides, does not bond and hence an adhesive or cohesive failure is simulated. Figure 2.16(b) shows the introduction of the Teflon sheet. One of the five beams does not contain any delamination. This beam is considered as a baseline to characterise the healthy beam scenario.

Beam	Delamination (mm)			
	Location		Size	
	Lengthwise (L)	Layers	Width (w)	Length (d)
B1	Non-Delamination			
B2	465	$5^{th} - 6^{th}$	42	50
B3	450	$5^{th} - 6^{th}$	42	80
B4	220	$5^{th} - 6^{th}$	42	50
B5	220	$2^{nd} - 3^{rd}$	42	50

Table 2.3: Composite laminated beams. Delamination scenarios

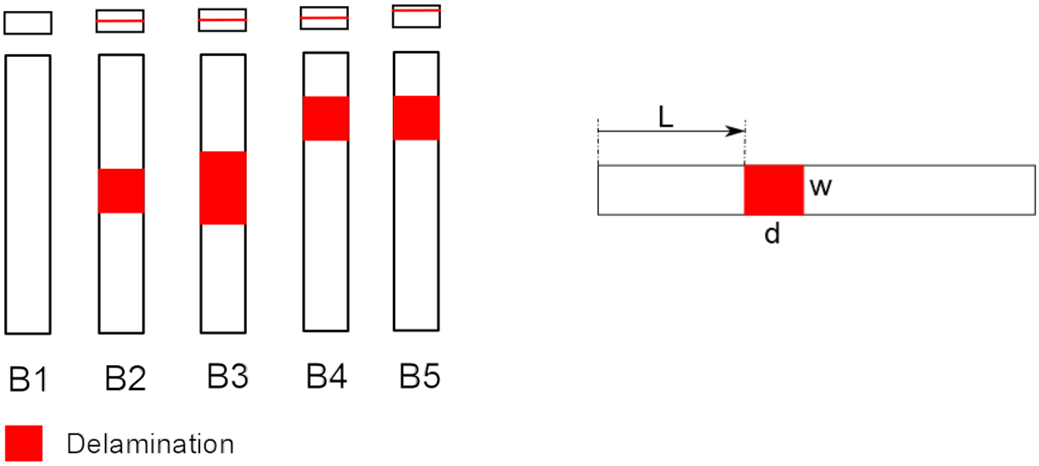

(a) (b)

Figure 2.15: Delamination scenarios. a) Scheme of the beams scenarios and b) scheme of the delamination location

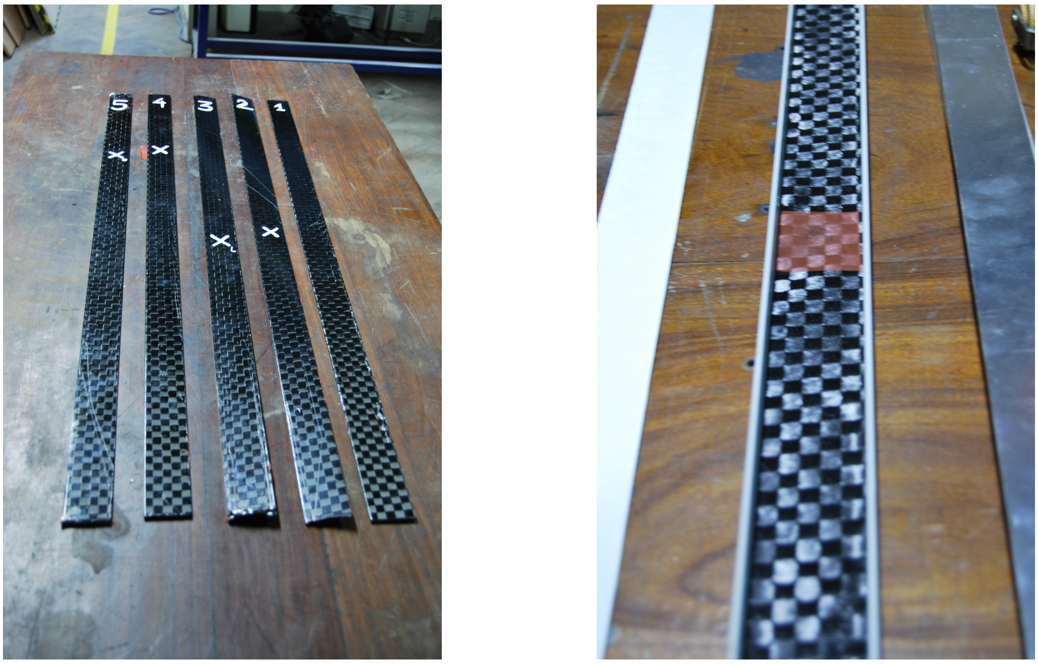

(a) (b)

Figure 2.16: Composite laminated beams manufactured. a) Different five beam scenarios and b) delamination introduction by a Teflon sheet

Experiment set up for data collection

With the possession of the five composite laminated beams, the next step was to actually measure the vibratory response of the beams. The beams were clamped in both sides of their shorted edges as shown in Figure 2.17. The clamp region was 40 mm in each side and the free spam of the beam was 900mm. An accelerometer was allocated at 1/3 from the left support and mounted on the top surface of the beam by bee wax. The beam was excited by a sharp impact introduced with a hammer in the middle of the span. The free-decay acceleration response of each beam was recorded by an SKF RT-440 portable analyser. The procedure was repeated to obtain a certain number of realisations for each beam scenario. Each beam was precisely allocated in the test rig to have the same free span. The force applied on each clamp was controlled by a torque wrench to guarantee that the same boundary conditions were applied to each beam scenario. The position of the accelerometer was strictly located in the same position. During the experiment's procedure, all beams were clamped in the supports with care and precision to guarantee that they were placed in the same location. The only interest was to detect changes due to the internal delamination introduced during the manufacturing process.

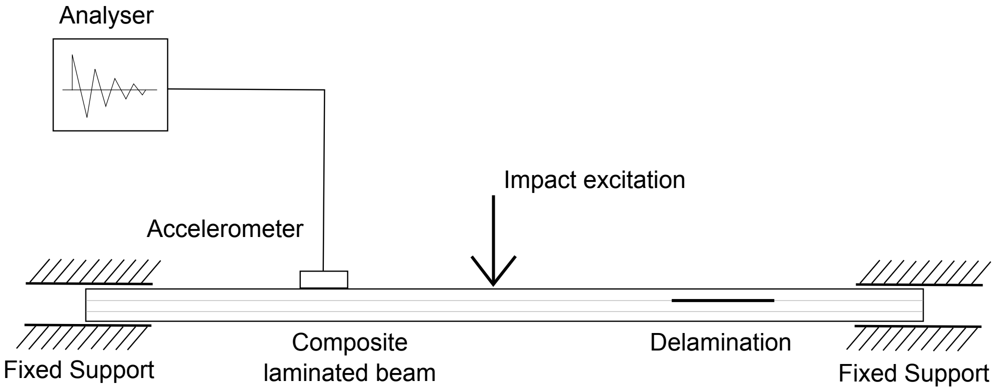

Figure 2.17: Experiment set up for measuring the vibratory responses of the composite laminated beams

Delamination assessment in composite laminated beams

The data collected was made up of acceleration responses measured on the vibrating beams under an impact excitation as described in section 2.4.2. Multiple realisations of the acceleration response were measured. Each vibration response (see Figure 2.1(a)) was discretised into a vector with length N=2048. A Fourier transform was applied to each signal vector to obtain the frequency spectrum for each signal vector (see Figure 2.1(b)) with now a dimension of N=N'=1024 by Equation 2.21. Seven signal vectors were recorded from each beam scenario with a total of 70 signal vectors. The reference state was constructed with $M = 7$ signal vectors recorded on the Healthy beam B1 (no-delamination). The sliding window size was selected as W=7 which yields to a reference state with a dimension 1024 x 7 (for more detailed information regarding to the calculation of the reference state see section 2.2.2). An approximated reconstruction of the original frequency spectrum by two RCs (RC_1 and RC_2) can be observed in Figure 2.5(a) in section 2.3.2. The reconstruction approximates relatively well the peaks that store more energy. It can be observed that the first RCs are based on the eigenvectors-directions with larger variance content. For this reason the reconstruction with the first two RCs approximates better the frequencies that concentrate more energy. It can be also observed that the general trend of the frequency spectrum is described with a smooth spectral line.

The FVs were calculated by the multiplication of each observation signal vector with the reference state as defined in Equation 2.16. The dimension of each FV is 7 corresponding to the number of RCs contained in the reference state. In order to visualise the performance of the FVs onto the features space, all FVs were projected onto a two dimensional space built by T_1 and T_2. It can be observed that different clusters are formed by FVs corresponding to the same beam scenario. By using only a two-dimensional FVs, the clusters obtained are able to distinguish between different beam scenarios as shown in Figure 2.18(a). This means that the methodology is not only able to detect delamination but also able to distinguish between the different delamination scenarios which involve different delamination sizes and locations.

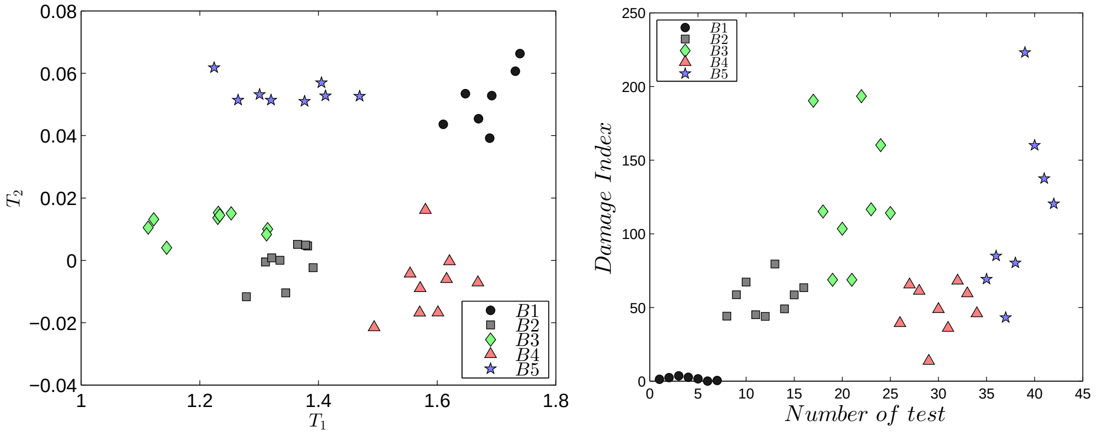

(a) (b)

Figure 2.18: Cluster and damage detection index plots for the five composite laminated beams. a) Cluster effect onto 2-D space defined by $T_1 - T_2$ b) Damage index using a two dimension FV (T_1 and T_2).

In order to evaluate the effect of these clusters a damage assessment is performed as shown in section 2.2.4. The FVs which characterise the healthy beam were used to construct a baseline matrix where the observation FVs can be compared. The Mahalanobis distance was measured from each observation FV to the baseline matrix. In this case FVs corresponding to the healthy beam should give the minimum distance (relatively close to zero, for an ideal case) because they belong to the same beam scenario that the FVs used to construct the baseline matrix. On the other hand, FVs corresponding to any other beam scenario should increment its distance to the baseline matrix. In this way, any anomaly caused by the delamination should be detected and highlighted with an increment of the distance. Similarly to the clusters obtained in Figure 2.18(a), FVs corresponding to the same beam scenario should have a similar distance magnitude. The results obtained are presented in Figure 2.18(b). This figure represents the damage index for each observation FV. The dimension considered to build the FVs was 2 which means that only the contribution of the first two RCs was considered. It could be observed that all the FVs corresponding to the delaminated beams have a damage index larger than zero which means that delamination introduces an anomaly in the vibration response, which could be detected by the methodology. This plot contains the damage index for all beam scenarios where all sizes and localizations are considered. Beam B2 and beam B3 are both delaminated beams with a delamination in the same location but with different size. The extension of the delamination of B3 is only 30mm more than the delamination in B2 (delamination extended 15mm to each size). However, it can be observed an increment of the damage index for FVs corresponding to B3 in comparison with B2. This effect was represented with an increment of the damage index, which can be associated to an increment of the damage as demonstrated in the previous section 2.4.1 when the severity of the stiffness reduction was incremented. Looking at beam B4 and beam B5 which are also delaminated beams with a delamination in different locations compared to each other and to B2 and B3. In this case,the damage indices do not provide any information in relation with the location of the delamination since they have similar magnitudes for different delamination scenarios, hence can be confused among each other.

As alluded in the analysis of the simulated system, when the dimension of the FVs was incremented the damage index was more significant in some aspects not only for detection but also for severity assessment. With this intention the dimension of the FVs was increased to 4 because as shown in the scree diagram in Figure 2.4(a), the partial variance decreases until the eigenvalue 4 and after there is a change of slope which remains constant and almost horizontal. This is a subjective procedure of selecting the number of components based on the slope of the scree diagram as discussed in [113].

Figure 2.19(a) represents the comparison between the original frequency spectrum and the reconstructed frequency spectrum by the first four RCs (RC_1, RC_2, RC_3 and

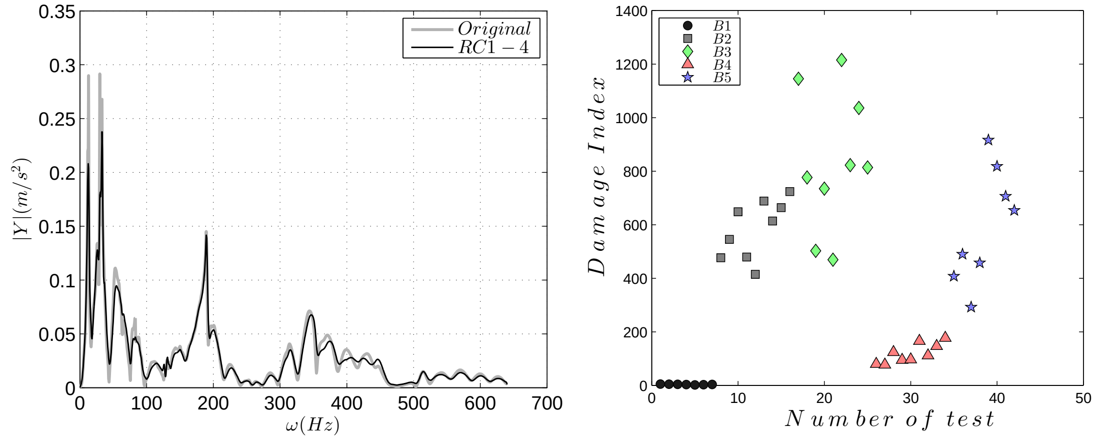

(a) (b)

Figure 2.19: a) Reconstructed frequency spectrum with the first four RCs (RC_1, RC_2, RC_3 and RC_4). b) Damage index using a four dimension FV (T_1, T_2, T_3 and T_4).

RC_4). It can be observed that the effect of the two additional RCs (RC_3 and RC_4) has more contribution in the reconstruction of the higher frequencies in the interval 300-400Hz (compare with Figure 2.5(a), reconstruction with 2RCs). The contribution to the smaller frequencies is also presented but it is not so characteristic as it is in the higher frequencies. Then, the damage index was calculated with FVs of dimension 4 as shown in Figure 2.19(b) and there are some changes in comparison with the damage index represented in Figure 2.18(b). The damage index increases for all observation FVs corresponding to the delaminated beams whilst remaining similar for the non-delaminated beam. The damage indexes of B4 are compressed and the difference between beams with other delamination location differs with respect to them. The damage index for beam B5 still can be confused with other beam scenarios so it is still difficult to find any relation with this damage index and localisation of the delamination. However, it can be observed that by considering more RCs in the reconstruction and hence higher dimension in the FVs, the damage index improves and it is able to better distinguish between different beam scenarios. As mentioned in [114] damage detection and especially delamination could be more pronounced at higher frequencies. This depends on the size and localisation of the delamination where higher modes of vibrations should be excited for delamination detection. The delamination in beam B4 and B5 is at 220 mm from one edge and for this reason is more prone to be excited by modes of vibration at higher frequencies because it is located in a region of high shear stress. The reconstruction with four RCs better approximates the higher frequencies and as a consequence this improves the damage index for all the beams but especially for B4 and B5.

2.4.3 Discussion

This section presents the performance of the methodology introduced in section 2.2 in a two degree-of-freedom (DOF) system described by a second order, nonlinear, ordinary differential equation and in the experiment of five composite laminated beams.

In the simulated system, the effect of the reduction of the stiffness parameters of linear and nonlinear coupling was studied. The same reduction ratios were separately applied on the different stiffness parameters to compare the detection performance for each stiffness parameter. It is observed that the detection on the stiffness parameter reductions which contribute to the linear coupling is clearly detected and presents very well defined clusters for each stiffness reduction scenario. Changes in the stiffness parameter of nonlinear coupling slightly affects the system behaviour, and hence less-defined clusters were obtained. However, there was an increment to the damage index, when the stiffness reduction was increased. These results demonstrate that when nonlinear effects occur in the system, the methodology is able to take them into account for the detection of any alteration in the system. It is also important to mention that the detection does not always track the progression of the stiffness reduction severity. This effect is observed when alterations are introduced in k_1. It is observed that the severity of the stiffness reduction does not affect systematically in the spectral lines of the frequency spectrum. This can be explained because the feature selected is not sensitive for this effect and additional features must be selected. Also, it was observed that reductions in k_1, introduce changes in the system that do not follow a linear behaviour. As a consequence of this behaviour, the detection in the severity of the stiffness reduction does not follow a monotonic function and it can be difficult to track the severity of the stiffness reduction [87]. Nevertheless, the methodology is able to decompose the vibratory signal in multivariate FVs which have the benefit of distributing the information over more than one variable. In this case, it was observed that when the dimension of the FVs was increased the detection between different stiffness reduction severities were clearly detected as shown in Figure 2.12(b). In this way, an increment of the dimension of the FVs provides changes in the damage index, which improves the detection of the system alterations.

Similarly, the performance of the methodology was studied and validated in the vibratory responses of five composite laminated beams with different delamination scenarios. The results demonstrate the creation of clusters which are able to distinguish between different beam scenarios. This means that the methodology is not only able to detect delamination but also able to distinguish among the different delamination scenarios which involve different delamination sizes and locations. The damage assessment procedure allows to choose the dimension of the FVs which can be determinant in the improvement of the damage index for further analysis of the delamination progression and localisation.

The effect on the behaviour of the damage index can be associated, to some extent, to the vibration response of the beam because of the contribution in the frequency spectrum reconstruction by using more or less RCs. The fact that the damage index and the reconstruction of the spectrum can be related, gives a better understanding of the structural analysis of the beams. One of the best characteristics of this methodology is the capability to decompose a vibratory response in a number of RCs which yields to a multivariate FVs. The selection of the dimension of the FVs depends on the requirements of the analysis and gives an additional flexibility for the damage assessment.

2.5 Study of the choice of the methodology parameters

In the previous sections, the outline of the methodology for damage/delamination detection as well as the validation of the methodology in a 2-DoF system and in an experiment with five composite laminated beams has been presented. As observed, the methodology has four sections which are interconnected for the best damage/delamination assessment. These sections are data collection, creation of reference state, feature extraction and damage assessment. The first two steps (data collection and creation of the reference state) are crucial for the good performance of the following feature extraction and damage assessment sections. The last two steps depend on how the reference state has been defined in order to obtain well defined clusters, which are used for damage/delamination assessment. Nevertheless, of utmost consideration is the categorization or clustering which can be achieved in terms of the new variable FVs. But this ability to recognize among different classes depends on a number of factors including the signal length and frequency resolution for the discretisation of the signal vector and the sliding window size for the RCs decomposition. The following section is to investigate the influence of the parameters of acquisition time, frequency resolution and sliding window size on the performance of the methodology. The study will analyse the effect on the reconstruction of the original frequency spectrum, the effect on the categorisation or clustering and the effect on the damage/delamination assessment based on the number of RCs considered. The effect of these parameters has been studied in both of the cases introduced above. First in the simulated system presented in section 2.4.1 for different severities in the reduction of the stiffness parameter k_n, and secondly in the delamination assessment of the five composite laminated beams presented in section 2.4.2.

2.5.1 Effect of the frequency resolution and acquisition time

This section investigates the influence of the frequency resolution (Δ_f) and therefore the acquisition time on the performance of the methodology. To see the influence of these parameters on the methodology, the sliding window length and the sampling frequency have been fixed for the entire analysis.

Generally small values of Δ_f provide a finer resolution in the vibration signal recorded and hence the discretised signal vectors will better depict all vibration modes contained in the frequency spectrum. This is present in the decomposition of the original frequency spectrum where the information contained in the first RCs is based on the directions with most of the variance. Therefore, the reconstruction will be better detailed and the method will be able to detect better the variations in the embedded signals within the sliding window size chosen [115]. However, a finer resolution in the frequency spectrum does not always provide a better categorisation. This do not vary significantly the results of the clustering effect, which can be even adversely affected.

Study on the simulated system

As alluded above the sliding window size has been fixed at $W = 7$ and the sampling frequency at 800 Hz. The number of signal vector realisations considered in the creation of the reference state was $M = 7$. The analysis was only applied for the reduction in the stiffness parameter of the nonlinear spring k_n. The change of this stiffness produces smaller changes on the system response compared to the linear stiffness k_1 and k_2 due to its quadratic coupling as shown in section 2.4.1. Changes in this parameter produces less distinguishable clusters (see Figure 2.14(a)) by the performance of the methodology and hence the right selection of the frequency resolution can be more significant for the damage assessment. Therefore, changes in the frequency resolution (Δ_f) has been introduced by the modification of the acquisition time in T = 1, 2 and 2.56s for the measurement of the vibratory response.

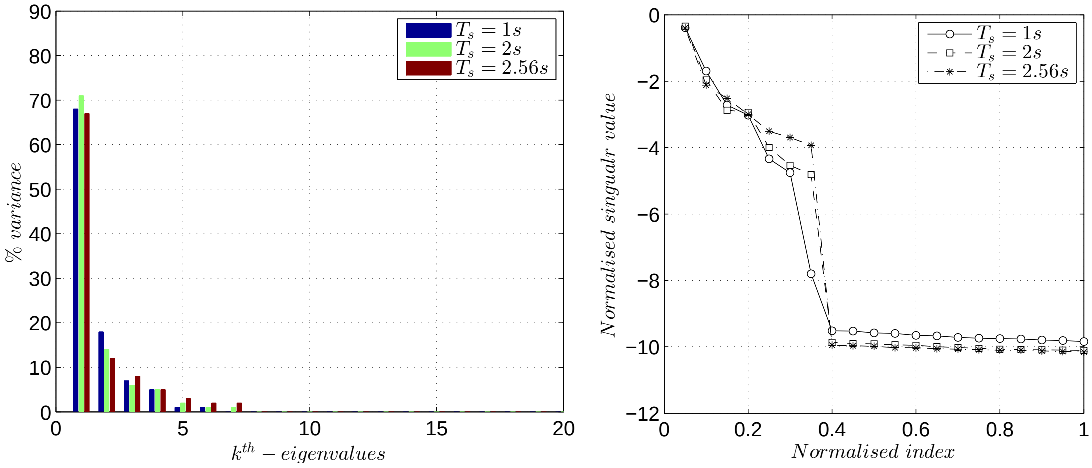

(a) (b)

Figure 2.20: Scree diagrams of the simulated system for three different acquisition times (T$_s$=1s, 2s and 2.56s). a) Partial variance contained in each eigenvalue. b) Normalised eigenvalue spectra.

Figure 2.20 represents the scree diagram of the decomposition of the discretised signal vectors measured on the simulated system for three different acquisition times. Figure 2.20(a) represents the partial variance contained in each eigenvalue calculated by Equation 2.20 and Figure 2.20(b) represents the normalised eigenvalue spectra calculated by Equation 2.23. It can be observed that the percent of variance contained in the first eigenvalue is different for each acquisition time but the largest variance content is for the case of T$_s$=2s. The variance content in the following eigenvalues decreases drastically in comparison with the first eigenvalue for all the different acquisition times. the first eigenvalue clearly contains most of the variance in the decomposition and therefore the RC constructed in the direction of its corresponding eigenvector will describe the general trend of the original frequency spectrum. It can be also observed in Figure 2.20(b) that for higher acquisition times (or higher frequency resolutions) the variance content is distributed over more eigenvalues. The variance contained in the 6^{th} and 7^{th} eigenvalues is still visible for T$_s$=2 and 2.56s as shown in Figure 2.20(a). This means that for high frequency resolutions, the signal vectors contain more precise information of the global behaviour of the vibratory signal that not only introduces useful information but also noise in the RCs decomposition.

Figure 2.21 represents the reconstruction of the frequency spectrum by using 2-RCs and 4-RCs, and the clustering of the FVs from healthy and different k_n reductions onto a two dimensional feature space for different acquisition times. It can be observed that the reconstruction of the frequency spectrum by 2-RCs is very smooth for all vibration signals recorded with different acquisition times. However, not all reconstructions are able to draw an approximate spectral line which uncover all the vibration modes described in the spectrum. The reconstruction of the frequency spectrum by 4-RCs provides a better reconstruction for all vibration signals recorded at different acquisition times. The reconstruction by 4-RCs is able to depict all the peaks of the frequency spectrum in comparison with the reconstruction by 2-RCs. It is observed that when the frequency resolution increases the reconstruction by 2-RCs is better approximated. In Figure 2.21(a) the peaks are not very well depicted and therefore the behaviour of the vibratory response is not very well characterised by the reconstruction with 2-RCs for an acquisition time of 1s. This effect can be observed in Figure 2.21(a) were the projection of the FVs onto the two dimensional space built by T_1 and T_2 does not create any cluster between the different stiffness reduction scenarios. In Figure 2.21(d) can be seen an improvement in the results and successful clustering for the different stiffness reduction scenarios for an acquisition time of 2s. The eigen-decomposition is slightly different than for T$_s$=1s. The percentage of variance contained by the first component increases by 3 percent only while the percentage of variance contained in the second

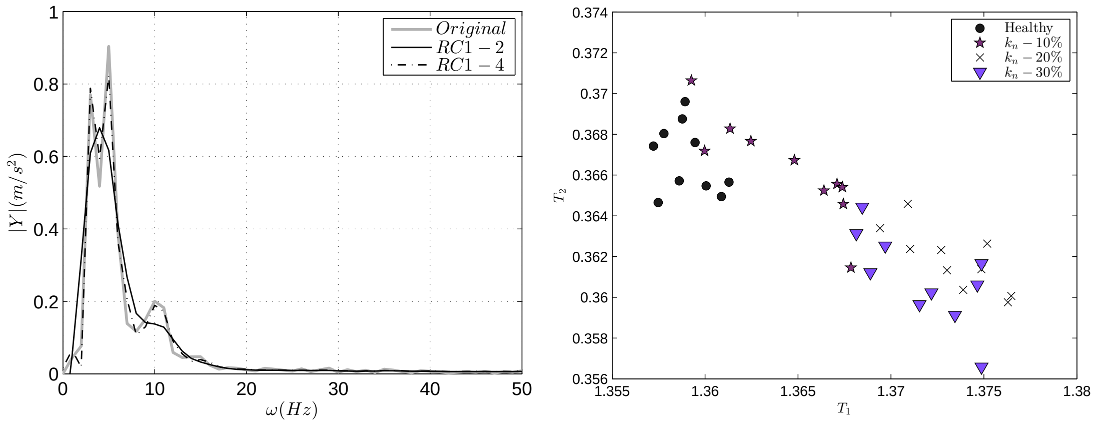

(a) Reconstruction. T$_s$=1s (b) Clustering T_1-T_2. T$_s$=1s

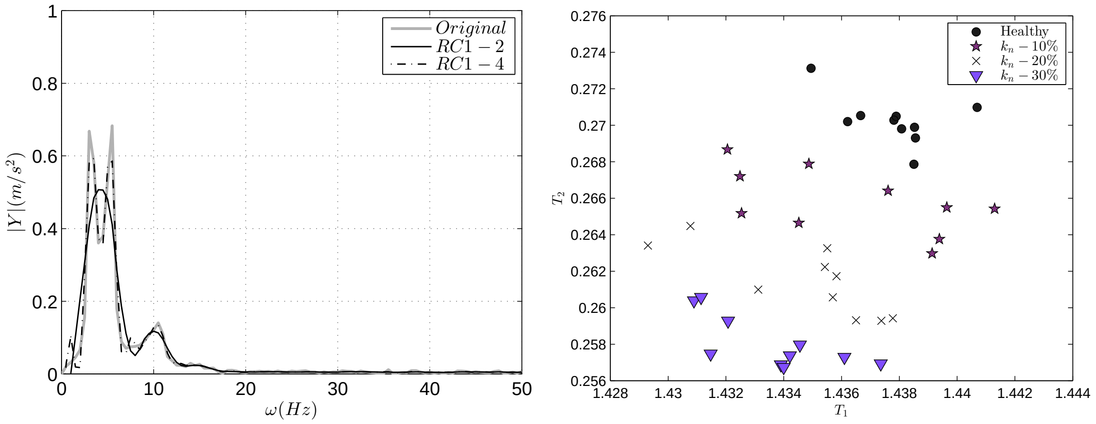

(c) Reconstruction. T$_s$=2s (d) Clustering T_1-T_2. T$_s$=2s

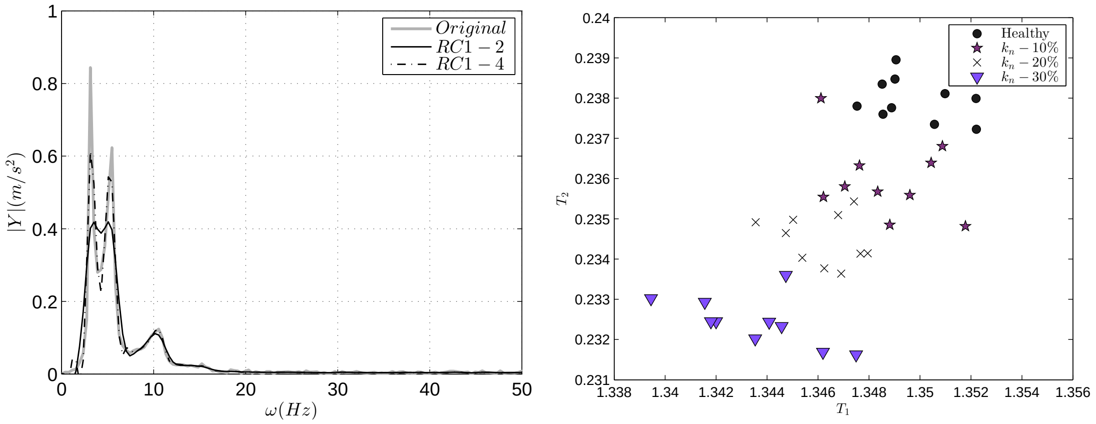

(e) Reconstruction. T$_s$=2.56s (f) Clustering T_1-T_2. T$_s$=2.56s

Figure 2.21: Reconstruction and cluster plots for stiffness reductions on k_n of the simulated system at different acquisition times (T$_s$=1s, 2s and 2.56s).

component falls by 4 percent (see Figure 2.20(a)). However, this small redistribution results in a better signal reconstruction as shown in Figure 2.21(c). The effect on a better reconstruction by 2-RCs is clearly beneficial for the formation of clusters between different stiffness reduction scenarios as shown in Figure 2.21(d). Finally, the methodology was applied on signal vectors discretised by vibratory signals recorded at 2.56s. Figure 2.21(e) represents very good reconstruction of the original frequency spectrum where all the peaks were very good depicted by using only 2-RCs. Figure 2.21(f) shows the clustering effect and it can be observed that a rather fine frequency resolution can adversely affect the capabilities of the methodology towards clustering effect. A better reconstruction of the frequency spectrum does not always provides the best clustering. It can be observed that a finer resolution compress the clusters in both directions T_1 and T_2 and this effect can introduce some misclassification as seen between stiffness reduction scenarios at 10% and 20%. However, it should be kept in mind that this misclassification was developed using only 2-RCs for visualization purposes. As mentioned in the previous sections the consideration of more RCs might introduce more relevant information which could be used for damage/delamination assessment. The consideration of more RCs and their effect in the damage/delamination assessment is studied in section 2.5.3.

Study on the five composite laminated beams

This section presents the same analysis as that in the previous section 2.5.1 but this time applied to the experiment of five composite laminated beams.

To study the effect on the frequency resolution and the acquisition time, some parameters have been fixed. The sliding window size $W = 7$ and the sampling frequency was set at 1280 Hz. The number of signal vector realisations considered in the creation of the reference state was $M = 7$. In the same way that in section 2.5.1, the analysis was done using the scree diagrams (see Figure 2.22), the reconstructed spectrum and the clustering plots (see Figure 2.23).

Figure 2.22 represents the scree diagrams of the decomposition of the discretised signal vectors measured on the beam B1 at three different acquisition times (T_s=1, 1.6 and 2s). Figure 2.22(a) represents the partial variance contained in each eigenvalue

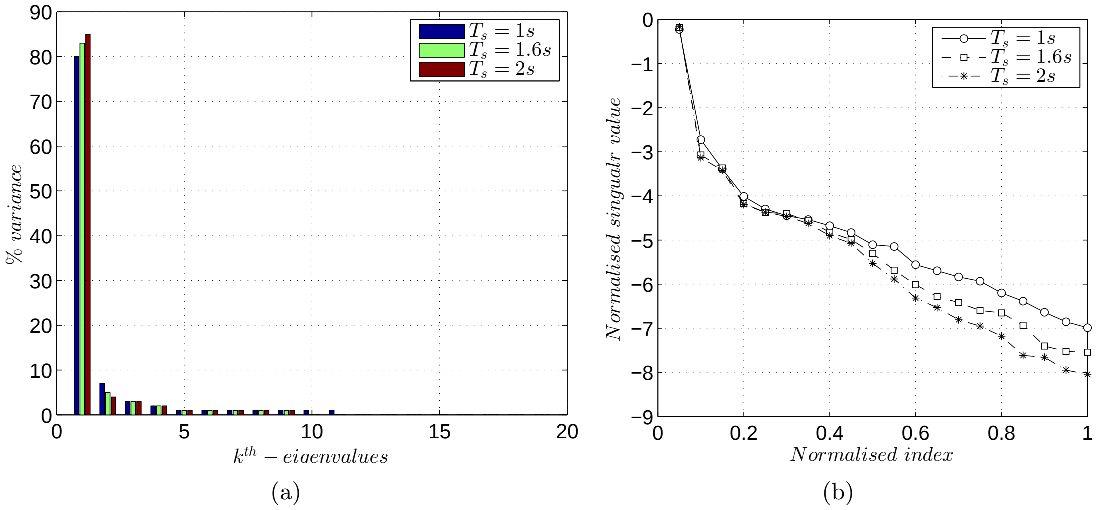

(a) (b)

Figure 2.22: Scree diagrams of the five composite laminated beams experiment for three different acquisition times (T$_s$=1s, 1.6s and 2s). a) Partial variance contained in each eigenvalue b) Normalised eigenvalue spectra.

calculated by Equation 2.20 and Figure 2.22(b) represents the normalised eigenvalue spectra calculated by Equation 2.23. It can be observed that the percent of variance contained in the first eigenvalue is different for each acquisition time but the largest variance content is for the case of T$_s$=2s where the frequency resolution is the highest. The variance content in the following eigenvalues decreases drastically in comparison with the first eigenvalue. Similarly to the simulated system case, the first eigenvalue contains most of the variance in the decomposition and therefore the RC constructed in the direction of its corresponding eigenvector will describe the general trend of the original frequency spectrum. It can be also observed that when the frequency resolution increases, the variance content in the first eigenvalue also increases.

Figure 2.23(a) represents the reconstructed frequency spectrum by 2 and 4 RCs when the signal vectors were discretised by an acquisition time at T$_s$=1s. The first and second RCs were obtained by the eigenvectors corresponding to the first and the second eigenvalue with a variance content of 80 and 7 percent respectively as shown in Figure 2.22(a). The reconstructed spectrum, by the first two RCs, describes the general trend of the original frequency spectrum fairly accurately except at higher frequencies. However, the reconstructed spectrum improves when 4-RCs are considered in the reconstruction. It can be seen that the reconstruction approximates much bet-

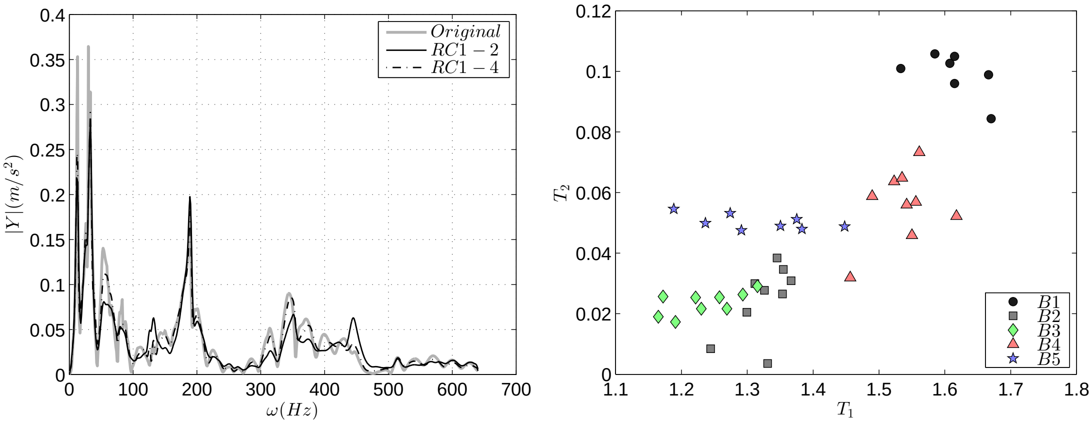

(a) Reconstruction. T$_s$=1s (b) Clustering T_1-T_2. T$_s$=1s

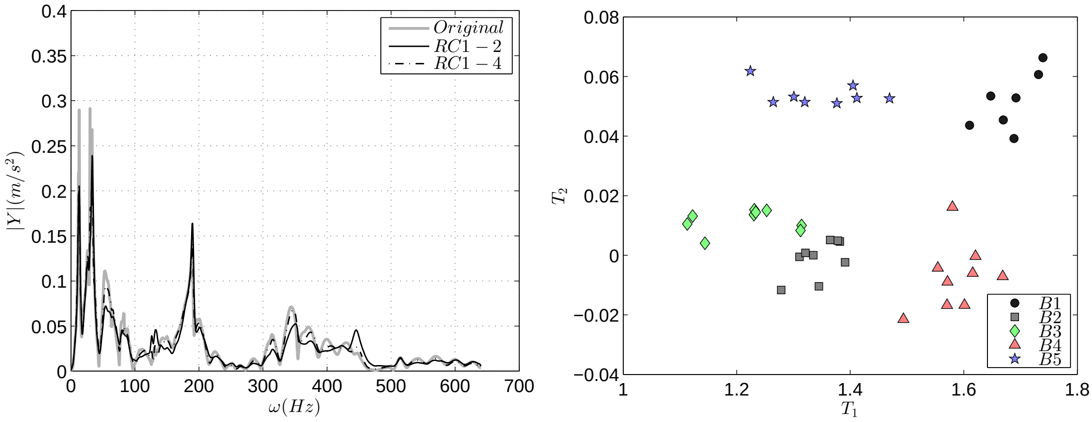

(c) Reconstruction. T$_s$=1.6s (d) Clustering T_1-T_2. T$_s$=1.6s

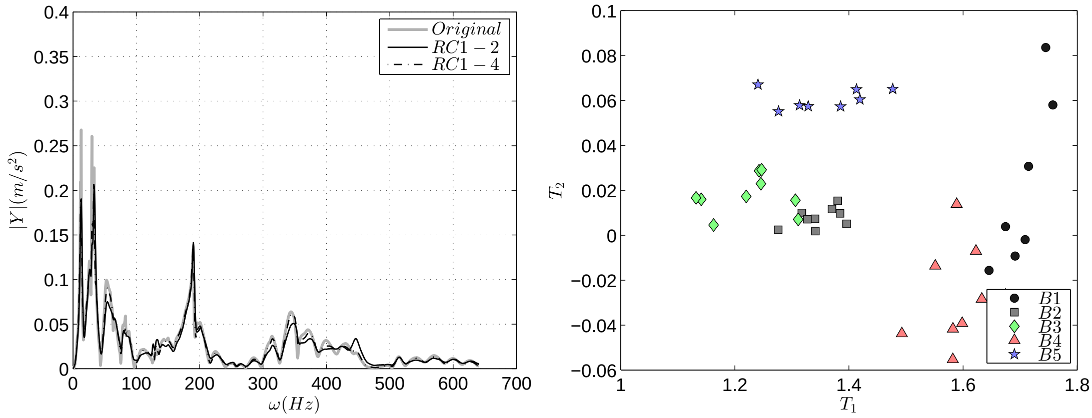

(e) Reconstruction. T$_s$=2s (f) Clustering T_1-T_2. T$_s$=2s

Figure 2.23: Reconstruction and cluster plots of the five composite laminated beams experiment for different acquisition times (T$_s$=1s, 1.6s and 2s).

ter at higher frequencies by increasing the variance content in only a 6 percent. It is important to mention that when the frequency resolution increases (T_s=1.6s and 2s), the reconstructed frequency spectrum by 2-RCs improves not only at low frequencies but also at high frequencies (see Figures 2.23(c) and 2.23(e)). As explained above, the increment of the frequency resolution concentrates more variance in the first eigenvalues and this produces a better reconstructed frequency spectrum with only 2-RCs. Similar to the example with an acquisition time of T_s=1s, the consideration of 4-RCs in the reconstruction provides a better reconstructed frequency spectrum for both cases T_s=1.6 and 2s.

Figure 2.23(b) represents the clustering effect of the FVs obtained from vibration responses measured at T_s=1s. The FVs of each beam scenarios (B2, B3, B4, B5) were projected onto a 2-dimensional feature space defined by T_1 and T_2. It can be appreciated that the clustering effect is not well achieved. The methodology is able to recognise between the healthy (B1) and the delaminated (B2, B3, B4, B5) beams, however it cannot distinguish between the different delaminated scenarios. By increasing the acquisition time to 1.6s, it results in an increment of variance content for the first eigenvalue up to 83 percent while the variance of the second component decreases by 2 percent (to 5 percent) as observed in Figure 2.22(a). This small redistribution gives a better clustering representation where the FVs of the healthy and the different delaminated beams are perfectly distinguished as shown in Figure 2.23(d). In this case not only the detection between healthy and delaminated beams is observed but also between different delaminated scenarios. However, when the acquisition time is increased to 2s, the clustering effect does not improve but introduces some misclassification between the FVs of different delaminated beams scenarios as shown in Figure 2.23(f). Therefore, an excessive frequency resolution can adversely affect the clustering effect. The same effect was also observed in the simulated system studied above, where an increment in the frequency resolution gave worse results for the clustering effect.

2.5.2 Effect of the window sliding size

This section discusses the principal considerations for selecting the sliding window size (W) for successful damage and/or delamination detection and its posterior assessment.

The sliding window size W has a particular importance on the form of the reconstructed signal [115]. The selection of a proper sliding window size depends on the problem at hand and on the preliminarily information in the vibratory signal. The main principle for selecting a proper sliding window size is to find the value which produces separable and independent principal components but at the same time contains the relevant information of the vibration signal. This is important for the creation of the reference state that directly affects the performance of the methodology. It is more beneficial to use the minimum possible number of RCs for the reconstruction because the use of large number of RCs can introduce noise into the reconstructed spectrum.

Generally, large values of W will increase the number of components in the decomposition. Then, the variance contained in the first PCs will be reduced and distributed over the other PCs. Consequently, the information which is not contained in the first RCs is distributed over the other RCs. Therefore, in order to obtain a reasonably good reconstructed signal, more RCs have to be considered. The consideration of more RCs can introduce irrelevant information such as noise.

As discussed in section 2.3.1, when the reference state is created by signal vectors in the time domain representation, large values of W generate very well separated RCs unless the complexity of the vibration response is significant and the separation of oscillatory components will be more difficult. This can be beneficial for extracting singular oscillatory components of the vibration response which can describe a particular mode of vibration. For small values of W, the variance contained in the first eigenvalues increases which means that more than one oscillatory component is included in the first RCs. However, they are not necessarily the most representative ones of the vibratory response. In order to obtain a good reconstructed signal, more than one RC has to be considered with the inconvenience that irrelevant oscillatory components (e.g. noise...) will be included in the reconstruction. For more information of the influence of W in the time domain see [72].

Differently, as discussed in the previous section 2.3.2 when the reference state is created by signal vectors in the frequency domain representation, the decomposition concentrates the larger amount of variance in the first eigenvalue. This means that the first RC will contain the general trend of the original frequency spectrum and the rest of the RCs will contain the fluctuations on the main spectral line. Therefore, large values of W create smooth reconstructions of the frequency spectrum by the consideration of the RCs obtained in the directions of larger amount of variance. On the other hand, small values of W concentrate the variance in the first eigenvalues and therefore the reconstruction by their corresponding RCs will be much more detailed.

In general no universal rules and unambiguous recommendations can be given for the selection of the sliding window size. The main difficulty here is caused by the fact that variations in the sliding window size may influence both weak and strong separability features which can have different performance in the methodology. To see the influence of this parameter in the methodology, the frequency resolution and the sampling frequency have been fixed for the entire analysis.

Study on the simulated system

This section represents the study of the sliding window size W in the simulated system described in section 2.4.1. To study the effect of the changes in W, the acquisition time at 2.56s and the sampling rate at 800 Hz have been fixed. The number of signal vector realisations used to build the reference state were $M = 7$. The effect of the sliding window size has been studied for four different values of W=7, 8, 25 and 50.

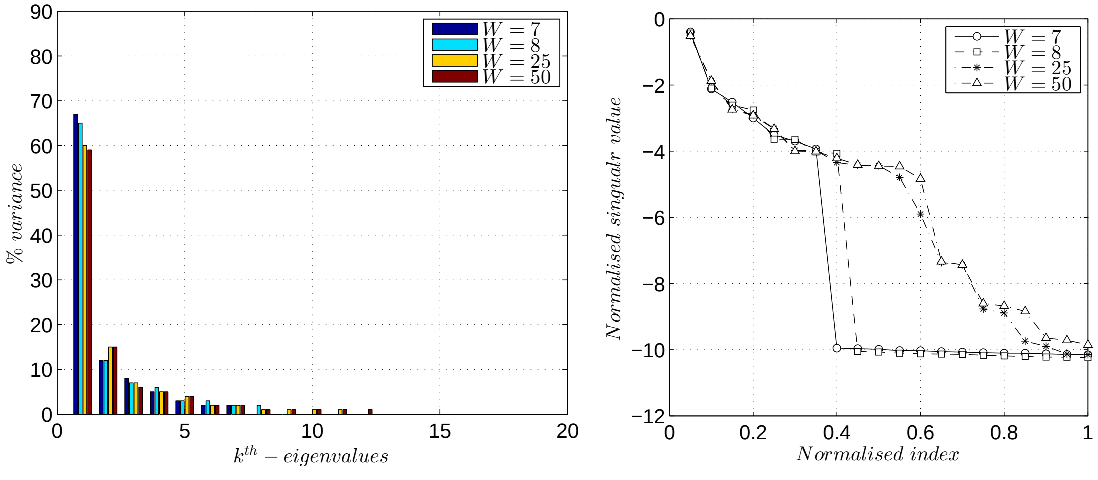

(a) (b)

Figure 2.24: Scree diagrams of the simulated system for different sliding window sizes (W=7, 8, 25 and 50). a) Partial variance contained in each eigenvalue. b) Normalised eigenvalue spectra.

Figure 2.24 represents the scree diagrams for the four different values of W when the decomposition has been applied on the vibratory responses from the simulated system. It can be observed that the amount of variance contained in the first eigenvalue decreases when the value of W increase. The amount of variance contained in the second eigenvalue increases for large values of W, while the amount of variance in the rest of the eigenvalues decreases as shown in Figure 2.24(a).

This demonstrates that most of the variance is allocated in the first eigenvalues, so that the global information of the vibration response is contained in the directions of their corresponding eigenvectors. Also it can be observed that for large values of W, the number of components needed for the decomposition increases. For values of $W = 7$ and 8, there is a sharp decay after the $7^{th} - 8^{th}$ eigenvalue while the distribution of variance decreases slower for large values of W as shown in Figure 2.24(b).

Figure 2.25 represents the effect of the values of W on the reconstruction of the frequency spectrum, by 2-RCs and 4-RCs as well as the effect on the clustering between different FVs projected onto a two dimensional space defined by T_1 and T_2. It is observed that the reconstruction by the first 2-RCs improves for small values of W. For all different values of W, the reconstructed spectral line describes the main trend of the original frequency spectrum. The reconstructed spectral line for $W = 7$ is able to depict all three peaks even though the amplitudes are not the same than in the original frequency spectrum as shown in Figure 2.25(a). For the case of $W = 8$, the two main peaks join in one but with a bit larger overall amplitude as shown in Figure 2.25(c). For the other two cases $W = 25$ and 50 the reconstructed spectral line is less approximated in terms of peak and amplitude approximation (see Figures 2.25(e) and 2.25(g)). However, the general trend of the spectral line is still well described by only 2-RCs. The frequency bands that have large peaks/amplitude are depicted by the reconstruction, therefore the vibration behaviour is well represented. It is also important to mention that as expected, the reconstructed spectral line improves considerably for all different W cases of study when 4RCs were used in the reconstruction. This behaviour occurs for all different values of W.

The effect of the variance content in the first 2-RCs is also appreciated in the clustering effect of the FVs onto the two dimensional space. It can be observed that for small values of $W = 7$ and 8, the clustering is successfully achieved not only between

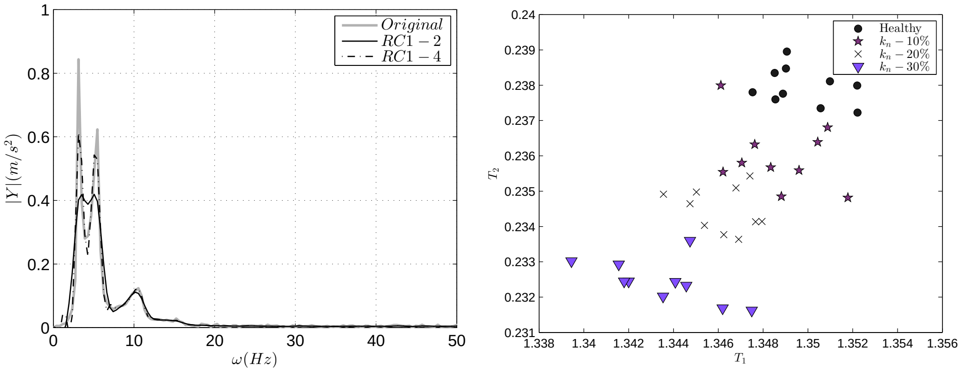

(a) Reconstruction. $W = 7$ (b) Clustering T_1-T_2. $W = 7$

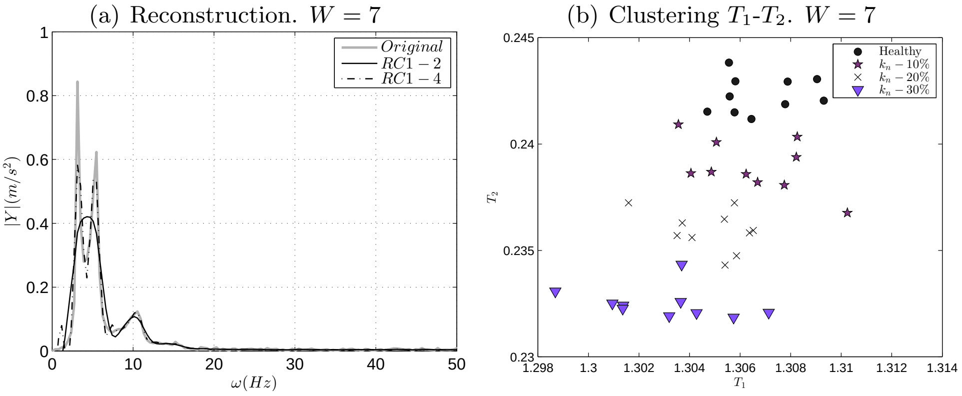

(c) Reconstruction. $W = 8$ (d) Clustering T_1-T_2. $W = 8$

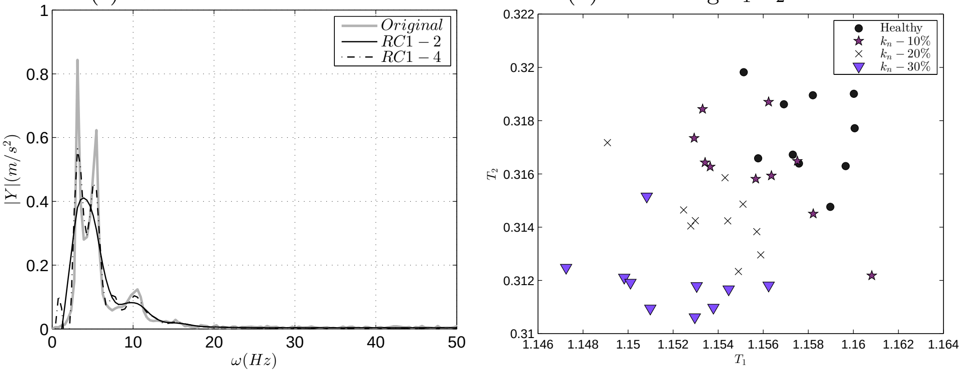

(e) Reconstruction. $W = 25$ (f) Clustering T_1-T_2. $W = 25$

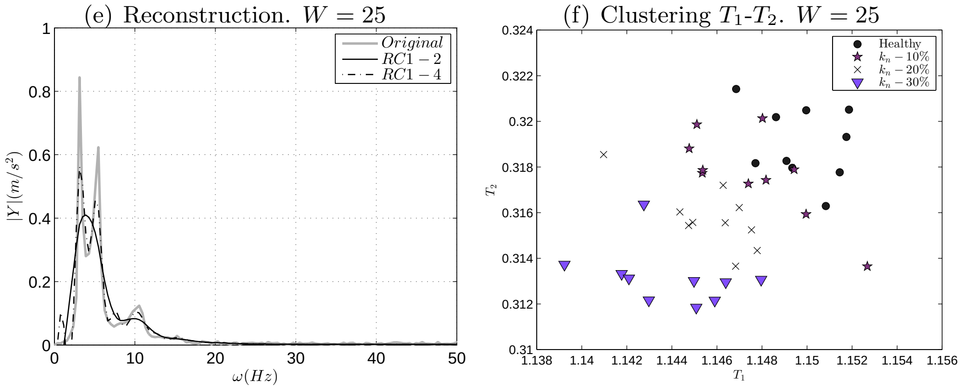

(g) Reconstruction. $W = 50$ (h) Clustering T_1-T_2. $W = 50$

Figure 2.25: Reconstruction and cluster plots for stiffness reductions on k_n of the simulated system at different sliding window sizes (W=7, 8, 25 and 50).

observations with and without stiffness alteration but also between observations with different stiffness reduction scenarios (see Figure 2.25(b) and 2.25(d)). A tracking of the severity in the stiffness reduction was also detected, where the observations with the largest stiffness reduction moves away from the healthy case. For the case of $W = 8$, the clusters are more compressed and this is beneficial for differencing between stiffness reduction severities. However, for large values of $W = 25$ and 50, the clustering is not very well achieved (see Figure 2.25(f) and 2.25(h)). For the case of large stiffness reductions, it can be observed that points corresponding to stiffness with high reductions are well away from the ones corresponding to the healthy state. Thus, high stiffness reductions can still be recognized from the healthy state. But the points corresponding to 10 percent reduction are mixed with the ones corresponding to the healthy state. Therefore, high stiffness reductions can be recognized and distinguished when high values of W are considered but small stiffness reductions are not able to be distinguished from the healthy state. This demonstrates that large values of W still keep the general trend of the frequency spectrum and it provides useful results for large changes in the system, so that large or global changes can be detected.

Study on the five composite laminated beams

Similarly to the case of the simulated system, the effect on the values of W was studied in the experiment of five composite laminated beams with different delamination scenarios as described in section 2.4.2. As alluded above, the acquisition time and the sampling rate have been fixed at 1.6s and 1280 Hz respectively in order to study the effect of $W = 7, 25, 50$ and 100 in the performance of the methodology. The number of signal vector realisations used to create the reference state was fixed at $M = 7$.

The amount of variance contained in the first eigenvalue decreases when the value of W increases as shown in Figure 2.26(a). As expected, the number of eigenvalues increases when the values of W also increases and therefore the information contained in the vibratory response must be distributed over all eigenvalues. Nevertheless, most of the variance content is still in the first two eigenvalues for all different values of W. In Figure 2.26(b) is observed that for small values of $W = 7$, the amount of variance is concentrated in the first eigenvalue by means of variance content. However, the amount

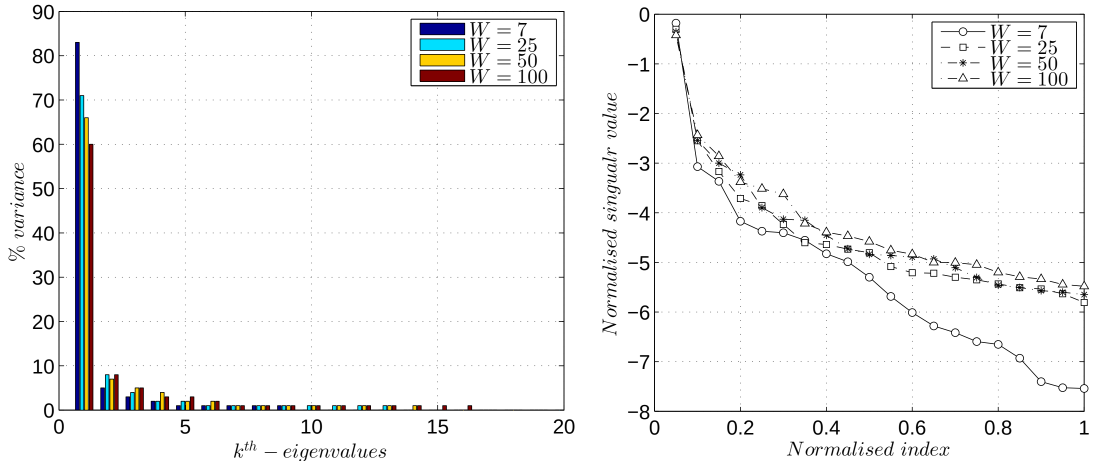

(a) (b)

Figure 2.26: Scree diagrams of the five composite laminated beams experiment for different sliding window sizes (W=7, 25, 50, and 100). a) Partial variance contained in each eigenvalue b) Normalised eigenvalue spectra.

of variance decreases rapidly in comparison when large values of W were considered in the methodology.

Figure 2.27 represents the reconstructed spectral lines by 2-RCs and 4-RCs as well as the clustering effect on the projection of the observation FVs onto a two dimensional feature space defined by T_1 and T_2. A similar behaviour to that the simulated system studied in the previous section was observed. The reconstructed frequency spectrum is more detailed when small values of the sliding window size are used. For $W = 7$ the peaks are better approximated and described as shown in Figure 2.27(a). However, the consideration of large values of W reduce the amount of variance contained in the first eigenvalues. Therefore the RCs obtained by their corresponding eigenvectors contain less information of the vibratory response. For this reason the reconstruction is smoother than when small values of W were considered as can be seen in Figures 2.27(c), 2.27(e) and 2.27(g). Nevertheless, all the reconstructions of the spectral line with 2-RCs describe very well the general behaviour of the original frequency spectrum. The region, where the amplitudes are larger due to an accumulation of energy, is still represented in the reconstructed spectral lines. Although large values of W (see Figure 2.27(g)) provide RCs which reconstruct the frequency spectrum very smooth, the mimic of large and small amplitudes is still distributed in the same location than in the original

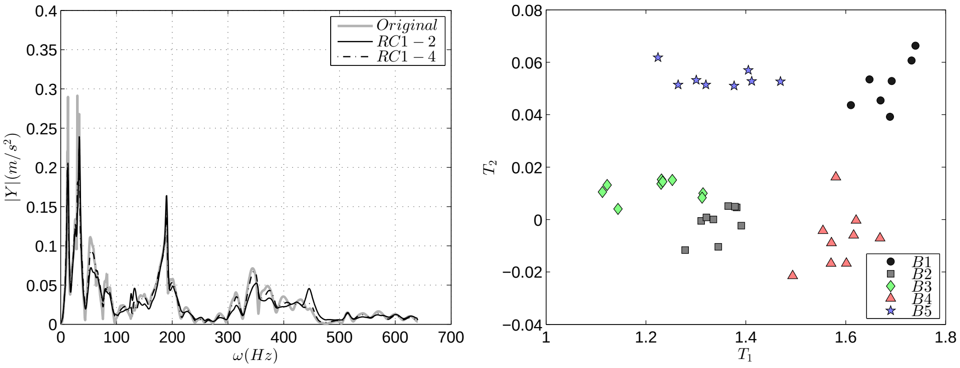

(a) Reconstruction. $W = 7$ (b) Clustering T_1-T_2. $W = 7$

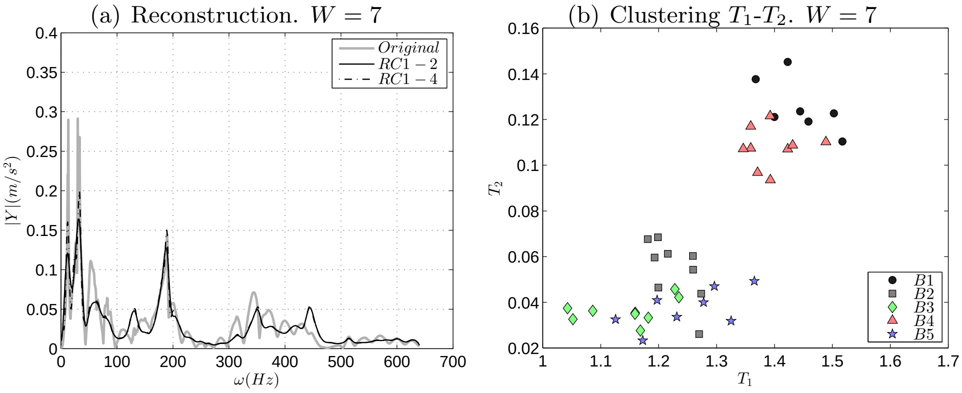

(c) Reconstruction. $W = 25$ (d) Clustering T_1-T_2. $W = 25$

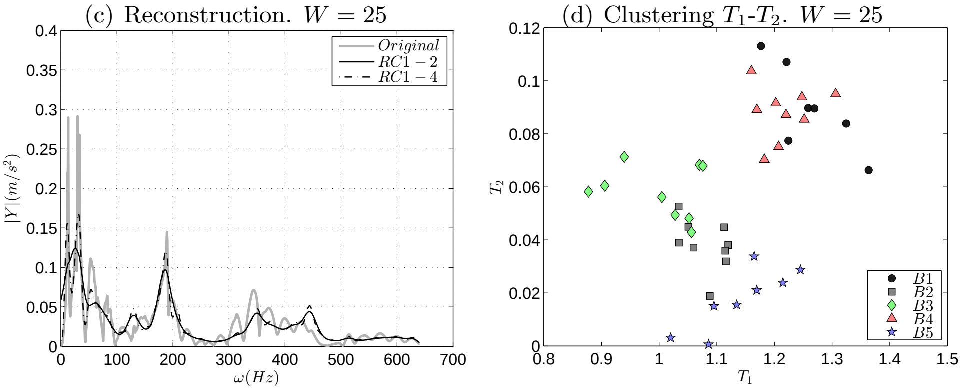

(e) Reconstruction. $W = 50$ (f) Clustering T_1-T_2. $W = 50$

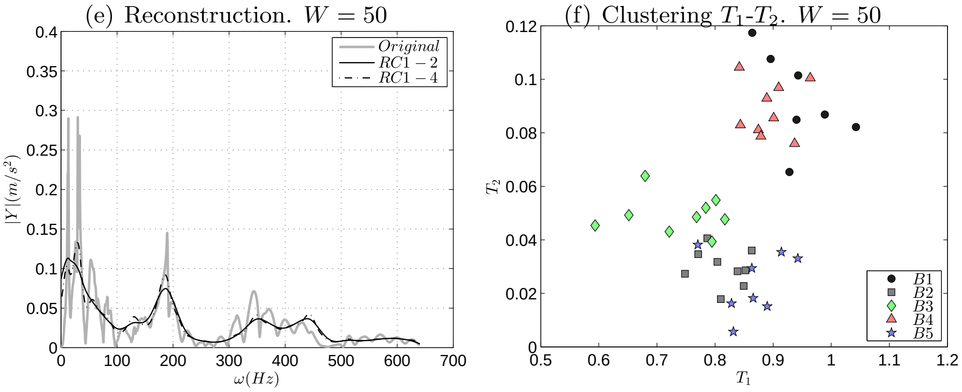

(g) Reconstruction. $W = 100$ (h) Clustering T_1-T_2. $W = 100$

Figure 2.27: Reconstruction and cluster plots of the five composite laminated beams experiment for different sliding window sizes (W=7, 25, 50 and 100).

frequency spectrum.

The clustering effect is also affected when different values of W are used in the methodology. When the reconstruction components provide a smooth reconstruction, the FVs obtained by these RCs do not contain a precise information of the vibratory response. This can be observed in Figure 2.27(h), where FVs of the different delaminated beam scenarios are mixed. The cluster do not distinguish between different beam scenarios. For $W = 100, 50$ and 25, it can be observed that the FVs of the delaminated beams B2, B3 and B5 are clustering together but away from B1, which is the undelaminated beam. However, the delaminated beam B4 cannot be identified as a delaminated beam (see Figures 2.27(h), 2.27(f) and 2.27(d)). On the other hand, for $W = 7$ very well detailed clusters are observed not only between beams with and without demalination but also between different delaminated beam scenarios as shown in Figure 2.18(a).

2.5.3 Effect of the selection of the number of the reconstructed components

As introduced in section 2.4.1 and 2.4.2, an increment of the dimension of the FVs or in order words the consideration of more RCs in the reconstruction can improve the damage/delamination assessment. In this manner, the FVs will be represented onto a feature space with a p-dimension, where the observations are more observable and distinguishable. As explained in section 2.2.3, each observation signal vector is characterised in a FV with the dimension of the number of components contained in the reference state. Therefore, the dimension of each FV is defined by the value of the sliding window size considered in the decomposition ($p \leq W$). Then, each value contained in the FVs is related to the information contained in its corresponding RC.

This section studies the effect of the selection of the number of RCs for damage/delamination assessment. As alluded above, an increment of the dimension of the FVs not only increases the distance between different clusters but also compresses the clusters themselves. This is the concept of clusterability [116] which is a measure of how well a given set of instances can be clustered. Intuitively, this is a measure of how 'tight' the results of clustering are. Having tight clustering means that intra cluster distances tend to be much larger than inter cluster distances. The consideration of a large dimensional FVs (or more RCs in the reconstruction) affects on the clusterability and this is the aim of the analysis presented in this section. To evaluate this effect, a supervised classification is performed in the clusters obtained in the projection of the FVs onto a 2, 3 and 4-dimensional feature space, respectively. This is equivalent to use 2, 3 or 4-RCs in the reconstruction or 2, 3 or 4-dimensions in the FVs. The classification criterion is based on the *minimum distance* classifier and it is explained in the following steps.

(1) Obtain the clusters by the projection of the FVs onto the p-dimensional feature space. Each observation is labelled corresponding to the category from where it was obtained. Then, it is possible to control if one observation belongs to one category or to other.
(2) Based on the clusters obtained in the step 1, now the distance of each instance observation is measured to each cluster/category by the Equation 2.18. This requires to calculate the baseline matrix $\mathbf{T}_B$ based on the p-dimensional FVs corresponding to the category considered as baseline each time.

$$\begin{aligned}
&D_i(B_1) \equiv distance\ of\ an\ i^{th} - observation\ to\ category\ 1\\
&D_i(B_2) \equiv distance\ of\ an\ i^{th} - observation\ to\ category\ 2\\
&\vdots\\
&D_i(B_C) \equiv distance\ of\ an\ i^{th} - observation\ to\ category\ C
\end{aligned} \tag{2.27}$$

$$\mathbf{D}_i(B_C) = (D_i(B_1), D_i(B_2), ..., D_i(B_C)) \tag{2.28}$$

The distances of an i^{th}-observation to each category are arranged into a vector $\mathbf{D}_i(B_C)$ with a dimension C-number of categories.
(3) The criteria of classification is considered as *minimum distance classifier* and it follows the following rule.

$$An\ i^{th} - observation \quad \in \quad B_c = arg\ min\{\mathbf{D}_i(B_C)\} \qquad where\ c = 1...C \tag{2.29}$$

(4) The visualisation of the results obtained in the classification are represented in a confusion matrix. Therefore, all the observation FVs which have previously generated the clusters, are now tested by this classification procedure. This test is applied for different dimensions of FVs.

To understand the classification procedure, an example which focus on the first confusion matrix in the Figure 2.29 is commented. This confusion matrix represents the results of the classification when the methodology was implemented in signal vectors with an acquisition time Ts=1s and the FVs were projected onto a 2-dimensional feature space. Each row of the confusion matrix represents the category to test and each column represents to which category, each observation of the category to test, was classified. Then, if we look at the 1^{st}-row of this confusion matrix, it can be observed that 100% of the observations belonging to the category $B1$ have their minimum distance to its own category. This means that the cluster of the observations of $B1$ is very well defined because there is not any misclassification with other category. However, if we look at now to the 3^{rd}-row of the same confusion matrix, it is observed that 20% of the observations belonging to the category $B3$ are misclassified to the category $B2$. In this case only 80% of the observations belonging to the category $B3$ have their minimum distance to its own category. This means that the cluster of the observations of $B3$ is not perfectly defined and it mixes with the category $B2$.

The effect on the selection of the number of RCs has been studied first when the signal vectors were measured for different frequency resolution (or different acquisition times) as explained in section 2.5.1 and secondly when the signal vectors were decomposed by different values of sliding window size as explained in section 2.5.2.

Study of the number of RCs for variations in the frequency resolution

In section 2.5.1 was studied the effect of the frequency resolution in the measured vibration responses within the methodology. As demonstrated, the frequency resolution

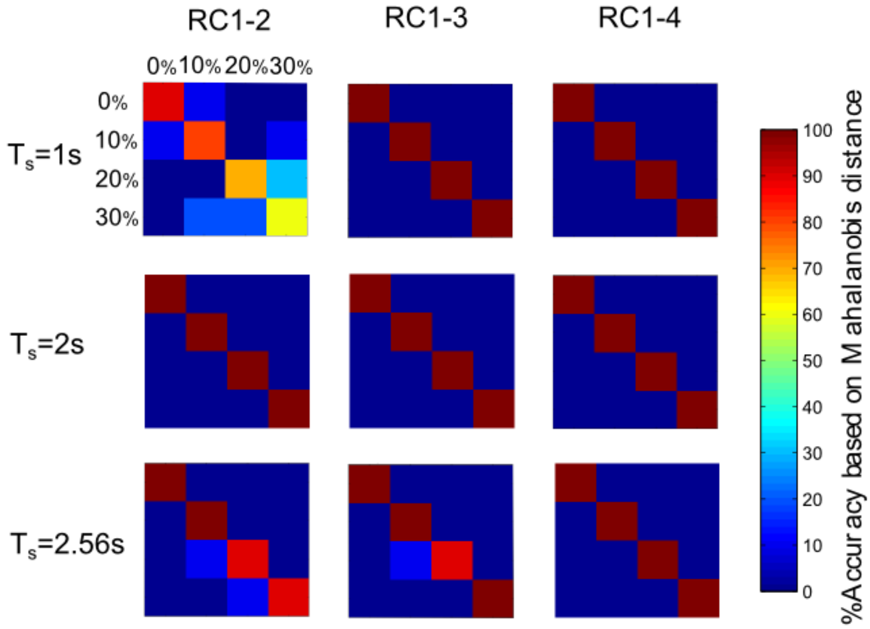

Figure 2.28: Confusion Matrices of different stiffness reduction severities (0%, 10%, 20% and 30%) of k_n in the simulated system at different acquisition times. Vertical direction shows changes on T_s=1s, 2s and 2.56s and horizontal direction shows the number of RC considered (First 2RCs, 3RCs and 4RCs).

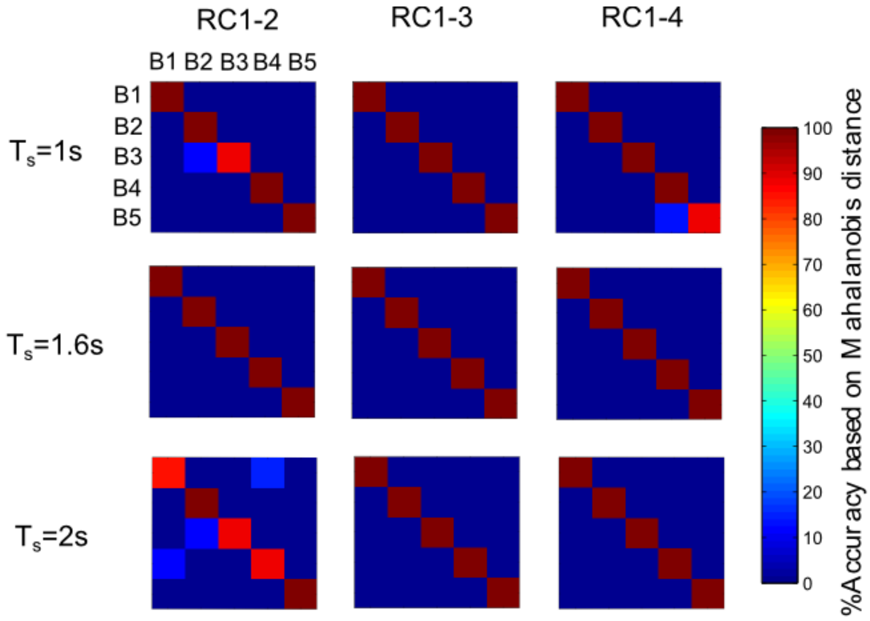

Figure 2.29: Confusion Matrices of the five composite laminated beams experiment (B1, B2, B3, B4 and B5) for different acquisition times. Vertical direction shows changes on T_s=1s, 1.6s and 2s and horizontal direction shows the number of RC considered (First 2RCs, 3RCs and 4RCs).

has a direct influence in the quality of the clusters generated for each category. In order to visualise this effect only a two-dimensional feature space was considered in the analysis. In this section, the consideration of more RCs or in other words an increment of the dimension of the FVs is studied. First, when the first two RCs were considered (RC_1 and RC_2), when the first three RCs were considered (RC_1, RC_2 and RC_3) and finally when the first four RCs were considerd (RC_1, RC_2, RC_3 and RC_4). The effect of the selection of the number of RCs was studied for different frequency resolutions (or acquisition times). Also the study was implemented first in the simulated system (see section 2.4.1) and secondly in the experiment of five composite laminated beams (see section 2.4.2).

To visualise the effect of the selection of the number of RCs, the procedure explained above was implemented in this study. The confusion matrices represented in Figure 2.28 and 2.29 were calculated for the case of the simulated system and the five composite laminated beams, respectively.

In Figure 2.28 can be observed the effect of the number of RCs for the case of the simulated system. When the frequency resolution is low (T_s=1s), the consideration of more RCs (or higher dimension of the FVs) is required to obtain a very well defined clusters. By increasing the dimension of the FVs to 3, the clusters were very well defined where the 100% of the observations of all the categories have their minimum distance to its own category. Similarly, when the frequency resolution is high (for an acquisition time T_s=2.56s), it is necessary to increase the dimension of the FVs upto 4 in order to obtain a 100% classification for all the categories.

The same analysis was implemented for the case of the five composite laminated beams. The results of the classification is presented in Figure 2.29. The same behaviour than for the simulated system was observed. For low frequency resolutions (T_s=1s) and for high frequency resolutions (T_s=2s), it is necessary to increase the dimension of the FVs to obtain a 100% correct classification for all the categories. However, it is also observed that the increment of the dimension of FVs, it is not always beneficial. It is observed that for the case of 4-dimensional FVs at T_s=1s, there is some misclassification in the observations of the category B5 to the category B4. Therefore, the consideration of more RCs in the reconstruction approximate better the reconstructed spectral line to the original one and this introduces additional information but also more noise which adversely affects on the clusters.

Study of the number of RCs for variations in the sliding window size

In section 2.5.2 was studied the effect of the sliding window size within the methodology. As observed, the sliding window size has a direct influence in the quality of the clusters generated for each category onto a 2-dimensional feature space. In this section, the consideration of more RCs or in other words an increment of the dimension of the FVs is studied. First, when the first two RCs were considered (RC_1 and RC_2), when the first three RCs were considered (RC_1, RC_2 and RC_3) and finally when the first four RCs were considerd (RC_1, RC_2, RC_3 and RC_4). The effect of the selection of the number of RCs was studied for different sliding window sizes. Also here the study was implemented first in the simulated system (see section 2.4.1) and secondly in the experiment of five composite laminated beams (see section 2.4.2). The classification procedure which was explained previously was implemented in this study.

Figure 2.30 represents the confusion matrices when the study was implemented in the simulated system. As a general conclusion, it can be observed that for small values of $W = 7$ and 8, the quality of the classification is better than for higher values of $W = 25$ and 50. Also, it can be observed that for small values of W (7 and 8), the consideration of more RCs or an increment of the dimension of the FVs, improves the quality of the clusters. In these cases the consideration of 4-dimensional FVs gives clusters very well defined where the 100% of the observations of all categories have their minimum distance to its own category. However, when the values of W are large (25 and 50), it is not enough the consideration of 4-RCs in the reconstruction to obtain good classifications. This can be explained because the amount of variance contained in the first eigenvalues reduces and the information contained in the first RCs is not enough to reconstruct the behaviour of the vibratory response. In this case, more than 4-RCs are needed to obtain better clusters and therefore better classifications.

A similar study was applied for the case of the five laminated beams and the results are represented in Figure 2.31. Similarly to the analysis for the simulated system, small values of W provide better classifications for all the categories than large values

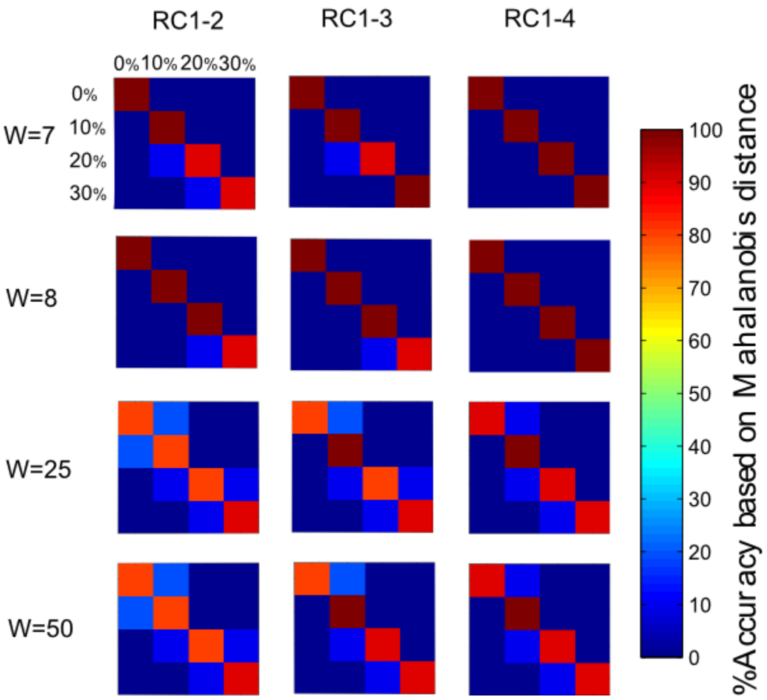

Figure 2.30: Confusion Matrices of different stiffness reduction severities (0%, 10%, 20% and 30%) of k_n in the simulated system at different sliding window sizes. Vertical direction shows changes on W=7, 8, 25 and 50 and horizontal direction shows the number of RC considered (Firsts 2RCs, 3RCs and 4RCs).

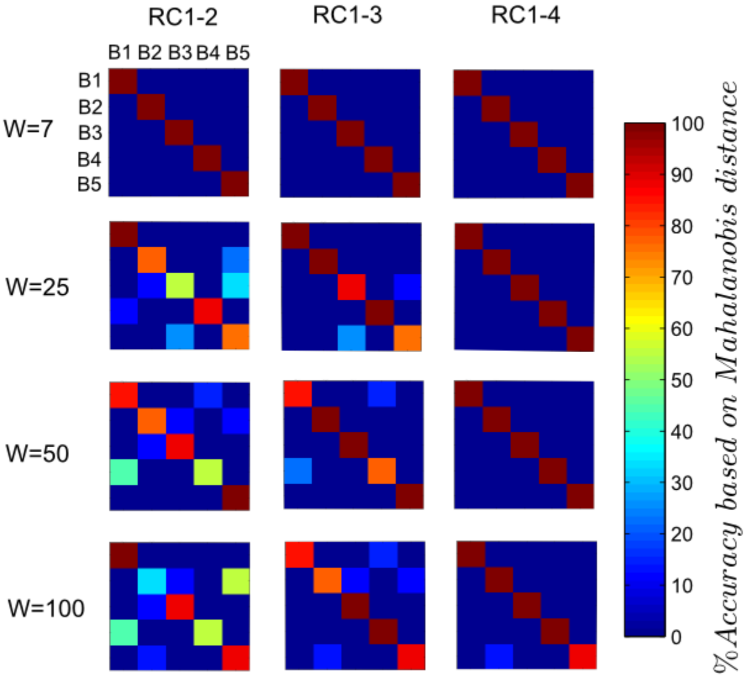

Figure 2.31: Confusion Matrices of the five composite laminated beams experiment (B1, B2, B3, B4 and B5) for different sliding window sizes. Vertical direction shows changes on W=7, 25, 50 and 100 and horizontal direction shows the number of RC considered (Firsts 2RCs, 3RCs and 4RCs).

of W. This can be explained as before, when the values of W are small the amount of variance contained in the first eigenvalues is higher. This means that the information also concentrate in the first RCs, which eventually is contained in the first scalars of the FVs. For this reason the classification is perfect for the value of $W = 7$, where 100% of the observations have their minimum distance to its own category by using only a 2-dimensional FVs. Obviously, the classification onto 2-dimensional space gets worse when the values of W increase because the amount of variance contained in the first eigenvalues decreases and the information contained in the first RCs is not sufficient to depict all the changes caused by the delamination. However, the classification improves when more RCs are considered in the reconstruction.

2.5.4 Discussion

The analysis developed in this section explains the importance of the choice of some parameters and their effect on the methodology such as the frequency resolution (or acquisition time) in the vibration responses and the sliding window size. The analysis studies the effect of these parameters on the reconstruction of the original frequency spectrum, on the clusters obtained by projecting the FVs onto the feature space and also the influence on the selection of the number of RCs for the quality of these clusters.

The effect of the *frequency resolution* in the methodology can be summarised in the following lines. A low frequency resolution can miss relevant information for the damage assessment. The loss of information affects on the reconstruction of the frequency spectrum and in the clusterisation, which makes more difficult the differentiation between categories. Generally, finer frequency resolution will improve the reconstruction and hence the clustering. However, an excessive fine frequency resolution could introduce additional information, such as background noise which can adversely affect on the clusterisation.

The selection of the *sliding window size* depends on the problem at hand and on the preliminarily information in the vibratory signal. As described in the literature review and also in section 2.2, the sliding window size has to follow these limitations $M \leq W$ and $W \leq N/2$. However, the main principle for selecting a proper sliding window size is to find the value which produces separable and independent principal components but at the same time contains the relevant information of the vibration signal. The study of the effect of the sliding window size (see section 2.5.2) demonstrates that small values of W concentrate the information in the first RCs, while large values of W reduce the information in the first RCs. Small values of W generate well defined clusters, while large values of W generate less descriptive clusters. In order to obtain good distinguishable clusters by using a reduced number of components, it is better to choose small values for sliding window size. The results show that values of W close to the number of signal vectors M, for the creation of the reference state, give well defined clusters.

Finally, an increment of the *dimension of the* FVs (or the consideration of more RCs in the reconstruction) generally improves the damage assessment. When the clusters are not well defined by the parameter selected of frequency resolution or sliding window size, an increment of the dimension of the FVs could give an additional information for better interpretation of the results. The consideration of FVs with larger dimension does not only increase the damage index, in terms of an increment of the Mahalanobis distance to the baseline set, but also compress the damage indices of observations from the same category. However, the consideration of more dimensions within the FVs should be considered with care because it could adversely affect on the clusterisation or categorisation. The consideration of more dimensions within the FVs is equivalent to consider more RCs in the reconstruction. Therefore, the reconstructed signal is much better approximate to the original one with the consideration of the noise removed in the decomposition. This noise could affect negatively in the clusterisation and hence in the damage identification.

2.6 Chapter summary

This chapter introduces the basics of the proposed damage assessment methodology for composite laminated structures, as well as its validation and the study of the principal parameters. The interpretation of the methodology in the time and frequency domain was analysed. The construction of the reference state in the time domain provides separated and interpretable oscillatory components. Therefore, the information contained in the reconstructed signal will depend on that oscillation components are included in the principal components. This can be beneficial when the identification and detection of a predominant mode of vibration is the aim of the analysis. On the other hand, when the methodology is performed in the frequency domain, the RCs used in the reconstruction provide a smooth version of the original spectrum. This analysis gives a general information of the vibration response since all the rotational patterns are included in the reconstruction. The first RC describes the general trend of frequency spectrum and the rest of RCs are the fluctuations over the spectral line.

The methodology was validated in a numerical system and in an experiment with five delaminated composite laminated beams. For both cases, the methodology provides information about the detection and localisation of the stiffness alteration and delamination, as well as the progression of the increment in the stiffness reduction severity and the growth of the delamination. The analysis clearly demonstrated the importance of multidimensional space, which is constructed by the FVs obtained within the methodology. The use of a multidimensional space improves the capabilities of the methodology to distinguish between different damage scenarios, that involves different delamination sizes and locations.

Finally, the importance of the choice of some parameters and their effect on the methodology such as the frequency resolution (or acquisition time) in the vibration responses and the sliding window size were studied. A fine frequency resolution provides better clusterisation and therefore better damage/delamination assessment. However, an excessive frequency resolution could introduce additional information, which can adversely affect the clusterisation. The selection of a proper sliding window size is to find the value which produces separable and independent principal components but at the same time contains the relevant information of the vibration signal. Small values of W condense the information within the first RCs, while large values of W reduce the information in the first RC. However, with large values of W, the global information is still contained in the first RCs. Generally, an increment of the dimension of the FVs improves the damage assessment. However, this should be considered with care, because more dimensions could not contribute to the damage assessment and thus affect adversely.

Chapter 3

Delamination assessment in composite laminated plates

3.1 Chapter overview

The delamination assessment in composite laminated plates has been studied and presented in this chapter. To address this study, a finite element model has been used to obtain controlled vibration responses from different composite plates with and without delamination. The effect of the delamination on the natural frequencies has been considered and studied. Similarly, four composite plates were manufactured with the same delamination scenarios to demonstrate and validate the numerical model in comparison with the experiment. The vibration responses of both cases of study were processed by the methodology introduced in Chapter 2 to assess the delamination in composite plates. This analysis presents the capabilities of the methodology for the detection and localisation of the delamination induced in the composite plates. The results by the performance of the methodology have been compared and discussed between the numerical and experimental case.

3.2 Finite element modelling of the composite laminated plates

The finite element model (FEM) used for analysing the vibration responses of the composite laminated plates is a 20-nodes solid element that exhibits quadratic displacement behaviour with three degrees of freedom (x,y,z). Solid186 was the element used from the commercial software ANSYS, which is suitable for layered thick shells or solids (see [117] for more information regarding the element selection). In this case 225 elements were used per layer. The square laminated plates have the dimensions of 150 mm and 10 layers with an approximate total thickness of 1.6 mm. Table 3.1 contains the material characteristics used in the model.

Parameter	Value	Units
$E_1 = E_2$	59	GPa
E_3	9	GPa
$G_{12} = G_{13} = G_{23}$	7.17	GPa
$\nu_{12} = \nu_{13} = \nu_{23}$	0.3	-.-
ρ	1500	kg/m^3

Table 3.1: Material properties of the composite laminates

Four plates were modelled and labelled as: undelaminated plate (H) and three delaminated plates which were labelled as D1, D2 and D3. For all plate configurations, the delamination size was 40 mm x 40 mm. Figure 3.1 shows the three delamination configurations explained below:

- D1 configuration, delamination is placed in the middle of the plate, between the 5^{th} and 6^{th} layers;
- D2 configuration, delamination is again in the middle of the plate, placed between the 8^{th} and 9^{th} layers;
- D3 configuration, delamination is moved closer to a corner, having its centre at 3/4 of each side, between the 5^{th} and 6^{th} layers.

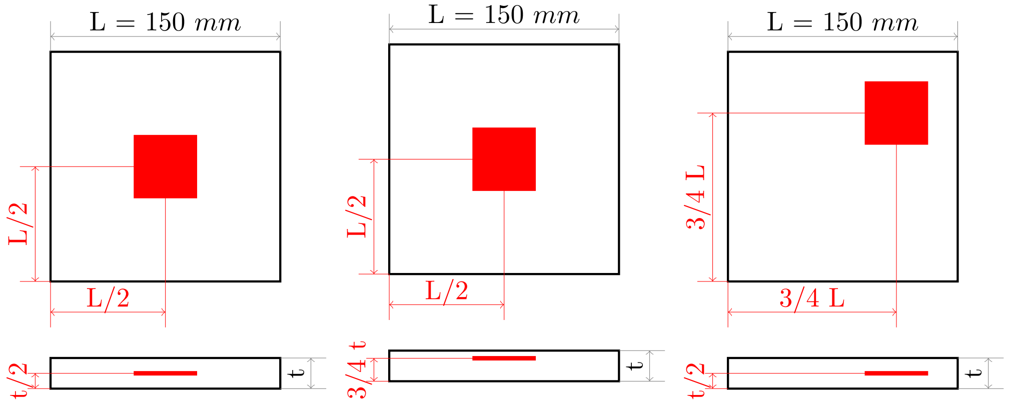

(a) D1 (b) D2 (c) D3

Figure 3.1: a) Delamination scenario D1. b) Delamination scenario D2. c) Delamination scenario D3.

The plates were fully fixed in the left hand side edge, if the pictures in Figure 3.1 are taken as a reference, and they were free in the rest of the edges. In order to obtain the first five natural frequencies of the undelaminated plate, modal analysis was implemented by the software ANSYS (see [117] for more detail). The software uses a Block Lanczos algorithm to extract the vibration modes, which is an eigenvalue solver where the Lanczos recursion is performed with a block of vectors [118]. This algorithm was useful for obtaining the natural frequencies of the undelaminated plate but it cannot be used for delaminated plates because it does not consider any non-linearities such as gaps. However, these results can be used as a reference point for obtaining the natural frequencies of the delaminated plates.

To simulate the delaminated plates, the four regions approach was taken into account, as explained in [119, 120]. To illustrate the concept, a basic scheme is shown in Figure 3.2. The delaminated specimen is divided in four regions where two belong to the non-delaminated region (regions 1 and 4) and other two for the delaminated region (regions 2 and 3). The delaminated region is composed of two separated blocks which are joined at their ends to the non-delaminated regions. Basically, one of the regions belongs to the laminates above the delamination (region 2) and the other belongs to the laminates below the delamination (region 3). The constitutive equations in the nodes that connect the regions must consider the continuity conditions of transverse displacements, slopes, bending moment and shear stress in the delaminated region and also the continuity of axial displacements and forces in the entire specimen.

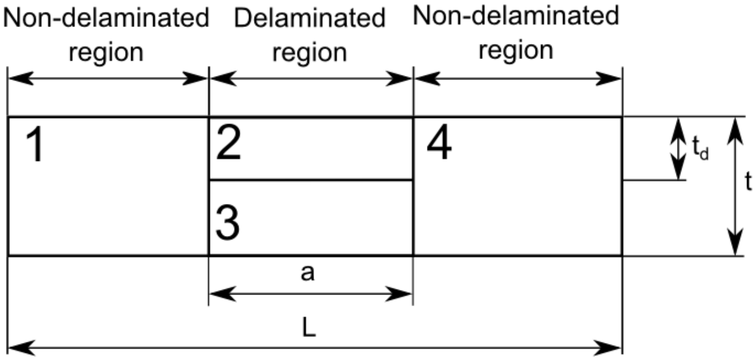

Figure 3.2: Scheme of the four areas approach for modelling of the delamination region.

The two surfaces identifying the delamination were modelled using targe170 (upper surface) and conta174 (lower surface, the target) elements, which break the contact in the delaminated region. The mesh was finer in the region where the delamination was allocated.

The vibration response was obtained by applying a short/burst impulse on the plate. The free-decay response was recorded after the application of the pulse load by measuring the in-plane strain in one of the nodes with a similar location to the strain gauge placed on the composite plates (see section 3.3.2). The vibration responses were recorded for 1 s and sampling frequency 4098 Hz.

The natural frequencies of the delaminated plates were obtained by performing a transient analysis in order to include the non-linear effects due to contact breakage, delamination opening and closing (delamination breathing) and contact/impacts between the delaminated layers during vibration. The frequency spectrum of the vibratory response was calculated from the time-domain response via the Fast Fourier transformation. Composite laminated structures have a small damping and then the resonant frequencies are approximately equal to the natural frequencies of the system. Therefore, the frequencies with larger amplitude can be considered to be the natural frequencies of vibration. In order to obtain the natural frequencies a peak-picking technique on the frequency spectrum was applied [121, 122].

Mode	Undelaminated	D1		D2		D3	
	ω(Hz)	ω(Hz)	κ(%)	ω(Hz)	κ(%)	ω(Hz)	κ(%)
1	74.06	74.02	0.05	74.03	0.04	74.13	0.09
2	442.00	442.01	0.002	441.83	0.03	439.81	0.49
3	521.98	522.26	0.05	521.95	0.005	517.10	0.93
4	853.25	853.93	0.07	852.08	0.13	850.54	0.31
5	1206.60	1175.40	2.58	1190.20	1.35	1203.70	0.24

Table 3.2: Numerical results of the first five natural frequencies (Hz) of the undelaminated and delaminated composite plates.

Table 3.2 contains the first five natural frequencies obtained from the numerical model of the composite laminated plates for undelaminated and delaminated scenarios. It also contains the absolute percent value of the natural frequency change calculated by Equation 3.1.

$$\kappa(\%) = \frac{|\omega_{delaminated} - \omega_{undelaminated}|}{\omega_{undelaminated}} 100 \tag{3.1}$$

It can be observed that the introduction of the delamination within the composite plate decreases the natural frequency. However, it can be seen that the effect of delamination on the natural frequencies is very small for the five modes of vibration where the highest reduction is 2.58 percent in the fifth mode of the delaminated plate D1. Higher modes are more sensitive than lower modes for all delamination scenarios. It is also noticed that the decrease of natural frequencies is not the same for different modes and does not follow any particular trend.

3.3 Experiment with composite laminated plates

Four specimens with the same configurations as those numerically simulated have been manufactured and tested in order to first validate the FEM and second to obtain vibration signals for performing the delamination assessment methodology introduced in Chapter 2.

3.3.1 Manufacturing process of the experiment specimens

Each composite laminated plate was manufactured by 10 layers of multi-prepreg woven carbon fibre/epoxy laminates. The 10 laminates were laid upon one-by-one to produce 1.6mm total thickness. The laminates were cut with the required dimensions and placed on a steel plate to guarantee an uniform flat shape for the entire specimen. They were covered by a vacuum bag for the process of curing inside of the autoclave. The parameters of the curing recipe were selected as follow: the air temperature was incremented at 2^{o}C/min and posterior hold at 120^{o}C for one hour. A second increment of temperature was introduced by 2^{o}C/min upto 150^{o}C and held for 2.5 hours. The pressure into the vacuum bag was at 1 bar and then the pressure of the autoclave was incremented upto 6 bar and remained constant for the entire process. After 2.5 hours at 150^{o}C the temperature was slowly decreased to cool down to 50^{o}C before removal of pressure. The plates were trimmed in all edges to remove the excess of resin and to give the final dimensions. The specimens have been manufactured 20 mm longer on the side of the clamping region to permit the constrains of the specimens themselves.

A Teflon sheet was introduced, with the dimension of 40mm x 40mm, at the locations detailed in Figure 3.1, during the manufacturing process to obtain the three delaminated composite plates as shown in Figure 3.3(a). Finally, four composite plates were manufactured: one undelaminated and three with different delamination scenarios.

3.3.2 Experiment set up

The composite plates were clamped on the side where the plate was extended 20mm to configure a 150mm free-span cantilever plate as shown in Figure 3.3(c). Two strain gauges were placed on the upper surface of the plates corresponding to the same location as in the modelled plates, as shown in Figure 3.3(b). The weight of the strain gauges can be neglected and hence they do not affect on the vibration response. The plates were excited by a sharp impact with a hard hammer to excite the maximum number of vibration modes. The external in-plane strain was recorded by strain gauges powered with a P-3550 Strain Indicator. An analogue-to-digital acquisition device digitalised the signal which was then acquired on a personal computer by a Labview executable program. Each plate was precisely located in the test rig to have the same free span. The force applied on each clamp was controlled and a thick steel plate was placed on the clamp region to guarantee that the plate was fully fixed along the entire edge. The plates were carefully placed in the same location because the only interest was to detect changes due to the internal delamination introduced during the manufacturing process. The vibration responses were recorded for 1.64 s and sampling frequency 1.25 kHz.

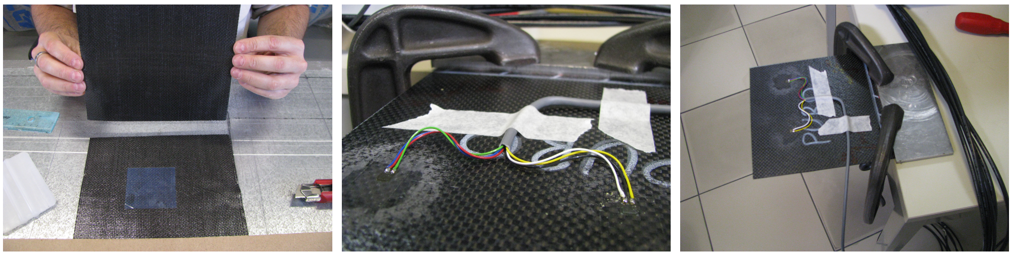

(a) (b) (c)

Figure 3.3: a) Teflon to induce delamination. b) Strain gauge location. c) Experiment set up.

3.3.3 Delamination effect on the natural frequencies in the experiments with manufactured composite plates

The vibration responses obtained from the experiment described in section 3.3.2 were used to obtain the natural frequencies of each composite plate. The responses recorded in time domain were transformed to the frequency domain by the fast Fourier transform. In this way the peak-picking technique was applied for selecting the frequencies corresponding to the resonant peaks which can be associated with the natural frequencies of the plates.

Mode	Undelaminated	D1		D2		D3	
	ω(Hz)	ω(Hz)	κ(%)	ω(Hz)	κ(%)	ω(Hz)	κ(%)
1	73.06	75.89	3.87	74.74	2.29	74.13	1.46
2	450.73	468.7	3.98	459.22	1.88	465.98	3.38
3	540.35	531.36	1.66	528.25	2.23	549.63	1.71
4	872.36	857.91	1.65	876.40	0.46	878.87	0.74
5	1307.7	1309.98	0.17	1314.39	0.51	1331.27	1.87

Table 3.3: Experimental results of the first five natural frequencies (Hz) of the undelaminated and delaminated composite plate.

For each plate scenario, 8 vibratory responses were measured. The natural frequencies were measured for each vibration response and the mean value of each natural frequency is represented in Table 3.3. It can be observed that the presence of the delamination produces small changes in the natural frequencies which are very difficult to track. In the first natural frequencies, the value of the natural frequency increases rather than decrease. However, the values of the higher natural frequencies decreases with the presence of the delamination. From this observation, it can be seen that the higher natural frequencies are more sensitive to delamiantion than the small ones. However, the absolute percent value of the natural frequency change due to delamiantion is very small and it is not a robust feature for delamination assessment.

3.4 Numerical and experimental validation

This section compares the natural frequencies obtained in the numerical model and in the experiment. In Table 3.4, it can be observed that the experimental natural frequencies are very close to the ones found by the numerical analysis. The standard deviation and the mean ratio is for all the cases less than 10 percent. This means that the values of the natural frequencies found in the experiments do not vary a lot from the mean value and then the results are robust. Moreover, this ratio is very small for the first natural frequencies and it tends to increase for higher natural frequencies. This phenomenon demonstrates that higher natural frequencies were more difficult to catch and the values were more dispersed because it was difficult to accurately depict the value of high natural frequencies. On the other hand, it is also important to mention that the percent ratio defined by the standard deviation and the mean value is larger than the absolute change percent value observed in Table 3.3. In this way, the possible error in obtaining the natural frequency varies more than the effect of the delamination in the natural frequency. This conclusion was also observed in [31] where the effect of the delamination on the natural frequencies was also analysed for a finite element model of composite laminated plates. Additionally, composite laminated structures are known to have double/very close modes of vibration [123, 124] which can also be an inconvenience for detecting the natural frequencies [125]. This behaviour is observed in the results where two natural frequencies are included in the frequency range of

440 – 520 Hz. Having close modes can confuse the mode identification, that makes it more difficult to catch the changes in the natural frequencies due to delamination.

Mode	Undelaminated			Delamination 1		
	Numerical	Experiments		Numerical	Experiments	
	ω(Hz)	μ	σ/μ(%)	ω(Hz)	μ	σ/μ(%)
1	74.06	73.59	0.32	74.02	75.89	0.16
2	442.00	450.73	4.04	442.01	468.70	2.26
3	521.98	540.35	5.97	522.26	531.36	2.19
4	853.25	872.36	2.11	853.93	857.91	4.04
5	1206.60	1307.70	6.10	1175.40	1309.98	4.99
Mode	Delamination 2			Delamination 3		
	Numerical	Experiments		Numerical	Experiments	
	ω(Hz)	μ	σ/μ(%)	ω(Hz)	μ	σ/μ(%)
1	74.03	74.74	0.41	74.13	75.47	0.26
2	441.83	459.22	5.71	439.81	465.98	1.92
3	521.95	528.25	2.94	517.10	549.63	4.16
4	852.08	876.40	1.57	850.54	878.87	0.82
5	1190.20	1314.39	1.10	1203.70	1332.27	1.08

Table 3.4: Experimental and numerical results of the first five natural frequencies (Hz). μ: mean value of experimental ω(Hz) - σ: standard deviation

Therefore, the numerical and experimental results show that changes in natural frequencies due to delamination are slightly sensitive to delamination but not enough to be a good delamination indicator. It seems that high frequencies are more prone to be affected by delamination, although it is difficult to determine that natural frequency is more sensitive to delamination. However, higher frequencies are difficult to catch. In this way, methods which consider all the rotational patterns or somehow an energy dissipation can be more beneficial because they can consider the effects on the contact between delamination parts [126]. Therefore, when delamination happens somewhere in a composite plate, there may be an interactive motion or impact within the delamination region during the vibration of the plate. This effect is difficult to catch for this reason the consideration of all the rotational patterns will include this effect as well.

3.5 Delamination assessment technique for composite laminated plates

As explained in the previous section, a technique which is able to uncover all the rotational patterns of the measured response will be beneficial for the delamination assessment. The methodology presented in Chapter 2 is a non-model based technique which is simply based on the analysis of the measured vibration responses. Delamination is likely to introduce nonlinearities in the vibration response such as the friction between layers or local bending of the layers and these effects are rather difficult to detect. Such modes cannot be detected by using modal analysis and by using simple spectral analysis, while this methodology is capable of contain such oscillation patterns because they are included in the measured vibration response.

The methodology used in this study transforms the initial vibration responses into new variables which retain most of its variance and the variance has been observed to change as a result of delamination. These new variables are based on the undelaminated plate that creates a reference state, where the features obtained from the vibration responses of different composite plates, with delamination are compared and assessed. Additionally, the methodology reduces the dimension of the measured data. Furthermore, it possesses clustering and categorization properties in the sense that the new components tend to make clusters corresponding to the different categories of data. Therefore, signals from intact structures and those from structures with different locations of delamination can be divided in clusters. This is achieved by reducing the distance between data vectors from the same category, while at the same time increasing the distance between data vectors from different categories. It also preserves the information contained in the original signals in terms of variability.

In this section, the novel methodology is applied on the vibration responses measured on the composite plates. First, the analysis is applied on the vibratory responses obtained in the FEM and secondly on the vibratory responses obtained in the experiment with different composite laminated plates.

3.5.1 Delamination assessment in the vibration responses of the numerical model of the composite laminated plates

This section presents the delamination assessment of the numerical model of the composite laminated plates. The vibration responses measured on the composite laminated plates described in section 3.2 are now processed by the methodology described in Chapter 2.

The in-plane strain was measured in each plate as detailed before. In order to generate more than one realisation white Gaussian noise was added by signal-to-noise ratio (SNR) in dB. For this study the additive noise was set at 10 dB. This noise contamination is used to introduce small alterations in the vibratory response and then generate a set of 10 vibration responses for each plate with a total of 40 vibration responses considering the sum of all the plates.

The reference state was created in the vibration responses of the undelaminated plate with the following parameters $M = 10$ and $W = 11$. The selection of the sliding window size parameter is based on the study developed in section 2.5.2. Generally the selection of small values for W and relatively close to M gives well defined clusters. The vibration responses were transformed to the frequency domain by Equation 2.21 and then the frequency spectrum of each realisation was considered in the analysis. Therefore, the reference state was constructed by 10 signal vectors embedded in 11 lag-copies for each signal vector, which yields 110 eigenvalues and their corresponding eigenvectors. Each signal vector was then divided in 11 PCs and reconstructed into 11 RCs which were used to define the reference state $\mathbf{R}$ with a dimension 11. Figure 3.4(c) represents the scree diagram of the eigen-decomposition of the signal vectors used to create the reference state, where the partial variance percent contained in each eigenvalue can be seen. The amount of variance contained in the first eigenvalue is 72 percent and 15 percent in the second eigenvalue. The rest of the eigenvalues have less than 10 percent of the total variance which decreases down to the seventh eigenvalue and thereafter, it remains constant and very close to zero percent. It can also be observed that the first two eigenvalues are well separated from the rest with 87 percent of the total variance. Figure 3.4(a) shows the comparison of the frequency spectrum reconstructed by the first two RCs (RC_1 and RC_2) and the original frequency

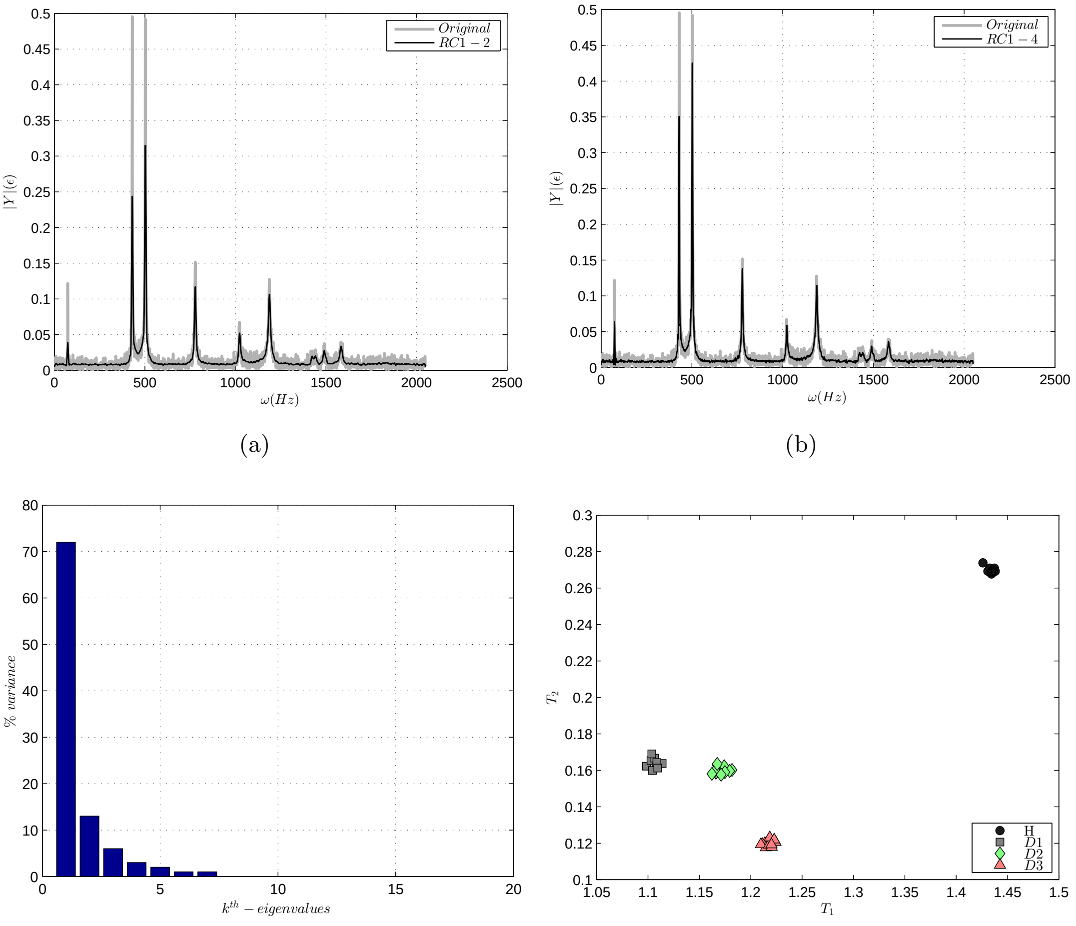

(a) (b)

(c) (d)

Figure 3.4: Based on the undelaminated vibration response of the numerical model. a) Comparison between the reconstructed frequency spectrum by the first two RCs (RC_1-RC_2) and the original frequency spectrum. b) Comparison between the reconstructed frequency spectrum by the first four RCs (RC_1-RC_4) and the original frequency spectrum. c) Scree diagram of the first 20 eigenvalues. d) Clustering effect on the projection of the FVs onto a 2-Dimensional space (T_1-T_2).

spectrum obtained by the vibratory response of the undelaminated plate. It can be observed that the reconstructed spectrum approximates very well the principal modes of vibration and removes the background noise. Therefore, the general trend of the frequency spectrum is very well defined by using only two RCs in the reconstruction. In Figure 3.4(b) the comparison of the reconstructed spectrum by the first four RCs and the original frequency spectrum is represented and compared. It can be observed that there is an intensification of the amplitudes in all the peaks but especially in the peaks within the range $400 - 520$ Hz which correspond to the region where there are two modes of vibration very close. Based on the reference state created by the 10 signal vectors, the FVs for each observation signal vector were calculated. Each set of FVs, corresponding to each plate scenario (three with delamination and one without delamination) were projected onto a two-dimensional feature space constructed by T_1 and T_2. Figure 3.4(d) represents the cluster effect of all observations onto the feature space. It is clearly observed that the observation points corresponding to the same plate scenario reduce their distances and increase their distances to the observation points corresponding to other plate scenarios. In this case, all observation points from plates with delamination are very well separated from the observations of undelaminated plates. Besides, the clusters are also able to distinguish between observation points from the different delaminated plates which involve different delamination locations.

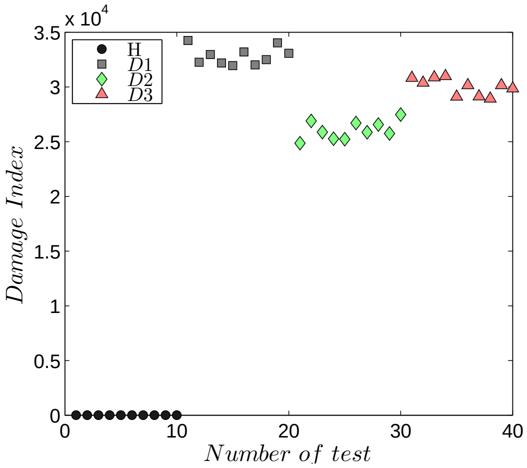

Figure 3.5: Damage index using a two dimension FV (T_1 and T_2) of the vibration responses of the numerical model.

In order to evaluate the effect of these clusters, a damage assessment is performed as shown in section 2.2.4. The FVs which characterises the undelaminated plate were used to construct a baseline matrix where the observation FVs can be compared. The Mahalanobis distance is then measured from each observation FV to the Baseline matrix. Figure 3.5 represents the distances of each observation to the baseline set. The dimension of the FVs used to compute the distance was $p = 2$. It can be clearly observed that all distances of the observation points corresponding to the plates with delamination are the greatest and the distances of the observation points corresponding to the undelaminated plates are the smallest. In addition, the distances from observations corresponding to the same delaminated plate are compressed and represent values very similar which benefits the differentiation between different delaminated plates. The differentiation between the different delaminated plates shows the potential of the methodology not to only detect delamination but also to distinguish among different delamination locations.

3.5.2 Delamination assessment in the vibration responses of the experiment with composite laminated plates

The collected data was made up of in-plane strain responses measured on the vibrating composite plates under a sharp impact excitation. Eight realisations were measured on each composite laminated plate which were transformed to the frequency domain and discretised into a signal vector with dimension N equal to the length of the vibration response. Therefore a total set of 32 signal vectors were considered in the analysis. The reference state was constructed with $M = 8$ signal vectors from the undelaminated composite plate and the sliding window size was selected as $W = 11$. The selection of the sliding window size parameter is based on the study developed in section 2.5.2. Generally the selection of small values for W and relatively close to M gives well defined clusters. The eigendecomposition of the covariance matrix of the full embedding matrix yields to 88 eigenvalues and eigenvectors. Figure 3.6(c) represents the scree diagram of the decomposition and defines the partial variance percent contained in each eigenvalue. Similarly as in the numerical case, the concentration of variance in the first eigenvalues is the largest, with 72 percent in the first eigenvalue and 12 percent in the second eigenvalue. It can also be observed in this Figure 3.6(c) that after the fifth eigenvalue, the amount of variance contained in the eigenvalues remains constant and very close to zero. This means that the information contained in their corresponding eigenvectors does not have significant variability in the original frequency spectrum. Based on this decomposition each signal vector was then divided in 11 RCs which are used to define the reference state with a dimension 11. In Figure 3.6(a) can be observed the comparison between the reconstructed frequency spectrum by the first two RCs and the original frequency spectrum. It can be observed that the reconstructed spectrum describes the trend of the original frequency spectrum quite well approximated with only 84 percent of the total variance. Similarly, Figure 3.6(b) compares the reconstructed spectrum by the first four RCs and the original frequency spectrum. In this case the reconstructed spectrum does not only describes the general trend of the original spectrum but also depicts very well all the peaks even in the two close peaks between $400 - 500$ Hz. The feature vectors were calculated by projecting the observation signal vectors onto the reference state. In this case, 32 observation FVs with a dimension of 11 were obtained. Figure 3.6(d) represents the clustering effect when the observation FVs were projected onto a two-dimensional feature space constructed by T_1 and T_2. Four different clusters were obtained, one for each composite plate scenario.

In order to evaluate the delamination for each composite plate, the Mahalanobis distance has been measured from the FVs of each composite plate to the baseline matrix, created by the FVs of the undelaminated composite plate. A threshold was found through the distances of the observation points of the undelaminated composite plate to the baseline set. For this study, the threshold ϑ was set at the maximum value obtained when the distance is measured to the FVs corresponding to the observations of the undelaminated plate itself.

Figure 3.7(a) represents the Mahalanobis damage index when the dimension of the FVs was considered as 2. It can be observed that all the distances calculated from the observation FVs of the composite plates with delamination are greater than the threshold. Therefore, the methodology was able to detect when a plate contains a delamination for all observations studied. The distances represent a similar magnitude for observations of the same composite plates. In this manner, it can be observed three regions which allows to roughly distinguish between different composite delamination scenarios. Although, these three regions can be roughly interpreted, it is also observed that the observations from D2 and D3 can be confused as well as the observations from D3 and D1. As shown in Chapter 2, if the dimension of the FVs is incremented, a clear improvement of the delamination assessment could be obtained (see Figure 2.19(b)). For this reason, the dimension of the FVs was incremented up to 4 because, after the fourth eigenvalue, the scree diagram has a change in the slope and this can be used as a technique for selecting the number of components considered in the analysis. Figure 3.7(b) represents the Mahalanobis distance of each observation to the baseline matrix

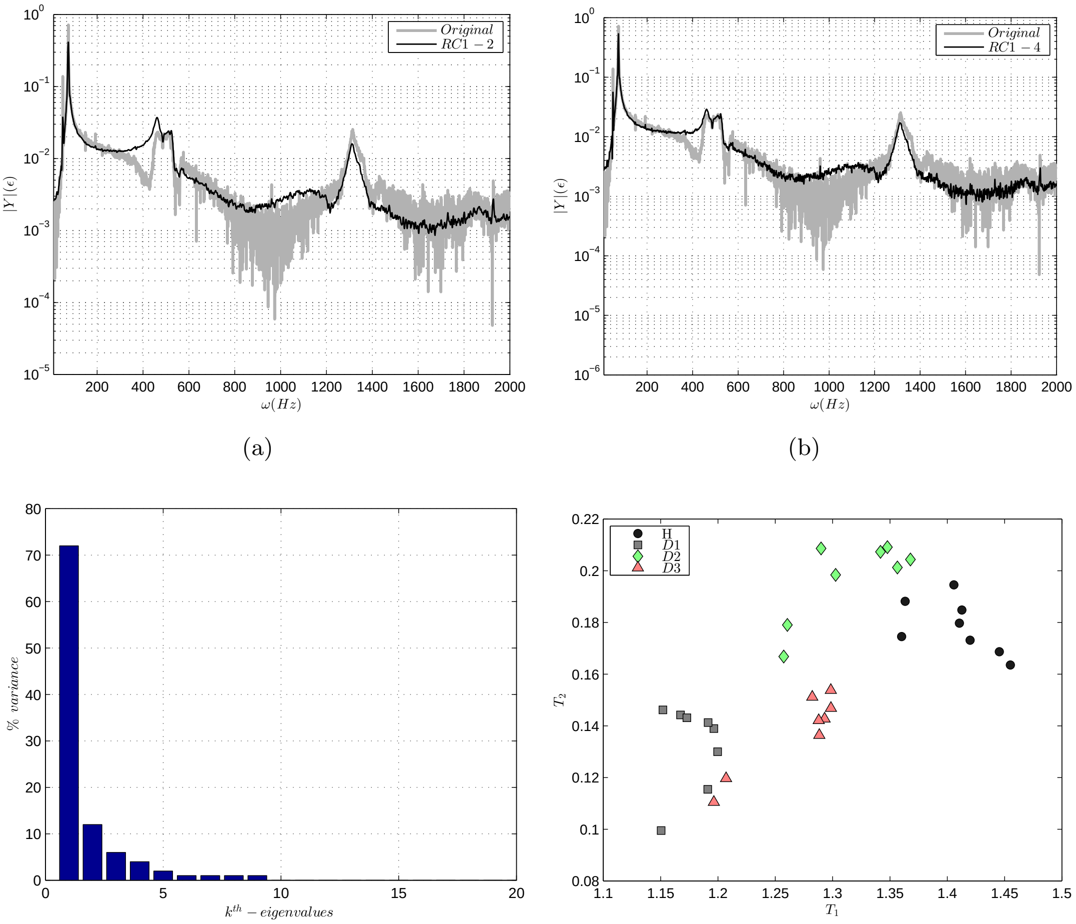

(a) (b)

(c) (d)

Figure 3.6: Based on the undelaminated vibration response of the experiment with composite plates. a) Comparison between the reconstructed frequency spectrum by the first two RCs (RC_1-RC_2) and the original frequency spectrum in logarithm scale. b) Comparison between the reconstructed frequency spectrum by the first four RCs (RC_1-RC_4) and the original frequency spectrum in logarithm scale. c) Scree diagram of the first 20 eigenvalues. d) Clustering effect in the projection of the FVs onto a 2-Dimensional space (T_1-T_2).

when the dimension of the FVs is 4. Figure 3.7(b) shows the distances measured to the observations of the delaminated plates increase and clearly improve the delamination detection. Moreover, the distances computed in observations from the same plate scenario, compress and give similar values. Because of the increment of the dimension of the FVs, it can be distinguished between observations from different plates which involves different delamination locations.

As explained before, when 4-RCs were used in the reconstruction of the frequency spectrum, the spectral line describes the original one much better (see Figure 3.6(b)).

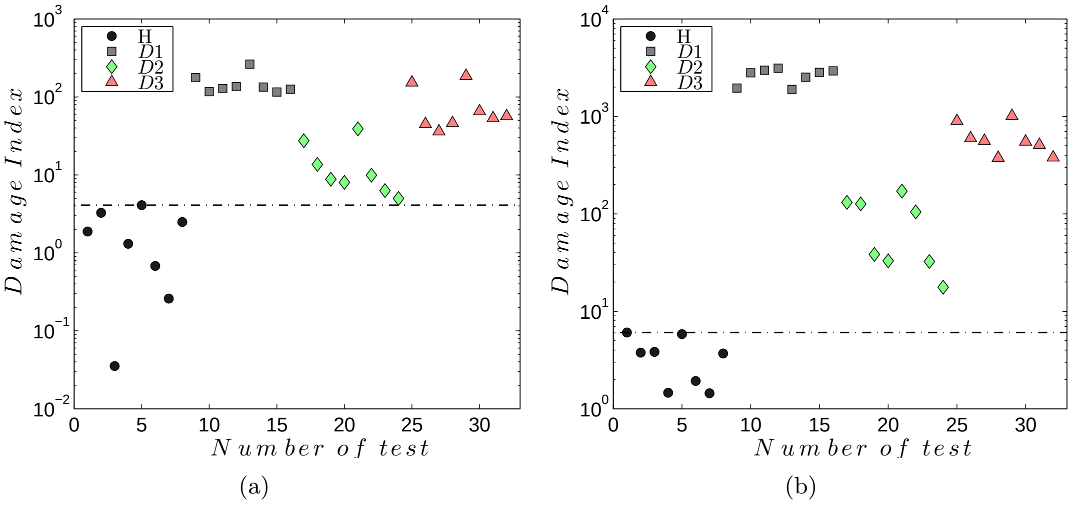

(a) (b)

Figure 3.7: Based on the vibration response of the experiment with composite laminated plates. a) Damage index using a two dimension FV (T_1 and T_2) and b) Damage index using a four dimension FV (T_1, T_2, T_3 and T_4). The dashed line represents the threshold.

This reconstructed spectrum approximates better on the frequency range where there are two modes of vibration very close (400−500 Hz). These two modes correspond to the 2^{nd} and the 3^{rd} natural frequencies which commands the 2^{nd} and the 3^{rd} modal shapes. As shown in [31], there is information related to the delamination, which cannot be appreciated in the natural frequencies, it can however be significant in the analysis of the modal shape due to its relation with the energy dissipation. At the modal shapes which act in the delamination region, the phenomenon of the interaction between laminates in the delamination region, will somehow be included in the analysis. It can be observed in Table 3.3 that the changes in the 2^{nd} and the 3^{rd} natural frequencies are more significant because of the delamination and hence considering two additional dimensions in the FVs, it can also be appreciate in the damage index as shown Figure 3.7(b). It can be observed that the distances corresponding to each delaminated scenario are now different and they can eventually be distinguished.

3.6 Discussion

The delamination assessment in composite laminated plates was studied first in a numerical model and second in an experiment within the methodology presented in Chapter 2. As alluded above, the effect of the delamination in the natural frequencies generates very small changes and they are not a good feature for the delamination assessment. These changes are predominant in higher frequencies but they are still smaller than the error caused in the experimental selection of the natural frequencies. In this case one cannot guarantee that changes in the natural frequencies are due to delamination [127]. Then, delamination is more a local problem and if the modes of vibration, which excite the delamination region are not correctly selected, the established mechanical model will not be effective for structural damage detection [128]. However, when the delamination is excited locally by a particular mode of vibration, there will be an interactive motion by the effects of opening and closing of the delamination region that dissipate energy which is contained in the vibration response.

The methodology applied for the delamination assessment contains all the rotational patterns of the vibration response. The rotational patterns are more or less excited depending on the excitation. Therefore, they will be more or less significant in the vibratory response. The vibratory responses are characterised in FVs, based on the comparison with the reference state, which in this case was constructed in the undelaminated composite plate. As shown in the results for both numerical and experimental analysis, it can be observed that the vibratory response is reduced to a two-dimensional space which is able to differentiate between plates with and without delamination. Also for the experimental case, where the delamination assessment between different delamination scenarios was not very clear, an increment of the dimension of the FVs works positively for better observability and distinction between delamination scenarios. The results have a similar trend for the numerical model and the experimental case. It can be observed that the distances for D2 in the FEM (see Figure 3.5) and in the experimental case (see Figure 3.7(a) and 3.7(b)) have the smallest damage indices. Also, the delamination scenarios of D1 and D3 describe a similar trend in both analysis, numerical and experimental.

3.7 Chapter summary

The delamination problem has been analysed using a finite element model and an experiment with composite laminated plates. First modal analysis was implemented in the vibration responses measured on the composite plates. The effect of the delamination produces slight changes on the natural frequencies of the composite laminated plates, although the natural frequency variation increases with the order of the natural frequency. However, the error in obtaining the experimental natural frequencies is greater than the changes produced by the effect of delamination. In this case, it can be mentioned that the effect of the delamination in the natural frequencies is not sensitive enough to be used as delamination assessment feature.

Therefore, the vibration responses has been processed through the methodology for delamination assessment introduced in Chapter 2. In this manner, all the rotational patterns included in the vibration response are considered in the analysis. The effect of the delamination in the vibration response will be highlighted, if a particular mode of vibration excites the delamination region. For this reason, the consideration of all the vibration modes contained in the vibration response could benefit the delamination identification. The methodology decomposes the vibratory response in FVs, which contains information of the vibratory response by means of the variance content. The FVs are directly related to the RCs, which gives an idea about the frequency range of the spectrum that takes part, when different dimension of FVs are considered. The results show that the data-based VSHM methodology successfully detects delamination and also distinguishes between different delamination scenarios. This demonstrates the potential of the methodology for delamination localisation due to the ability to cluster different delaminated composite plate scenarios. The results encourage to use the data-based VSHM methodology for the identification of the delamination location and extent in future investigations.

Chapter 4

Damage assessment for wind turbine blades

4.1 Chapter Overview

This chapter introduces a data-based vibration structural health monitoring technique for wind turbine blades. The technique is based on the methodology introduced in Chapter 2, where the vibration responses measured on the wind turbine blades (WTB) were processed by the methodology for damage assessment. The vibration responses are characterised in observations defined by multidimensional FVs. The study of these observations is crucial for damage identification. For this purpose a practical inspection phase was implemented to maximize the damage detection and minimize the healthy false alarms. The nature of the threshold is based on the probability distribution of the observations considered as a baseline. The damage assessment was first implemented in a lab-scale WTB with an automatic electromagnetic actuator and accelerometers distributed along the WTB. This first study was focused on the detection and evaluation of different damage locations as well as their progression. Secondly, the same methodology was implemented in a large SSP34m WTB for detection and evaluation of an artificial damage introduced in the blade. In this case, the distributed accelerometers recorded the free-decay acceleration responses for four different actuation locations. The experiment studied the damage assessment performance by the influence of the different sensor and actuator locations.

4.2 Practical SHM technique implementation for wind turbine blades

Nowadays, vibration-based structural health monitoring became a trend in the future techniques for monitoring the health of modern civil engineering and aerospace engineering among many other sectors. Indeed, the growth of off-shore wind turbines place VSHM at the forefront of the contemporary research. Visual inspections of these structures are dangerous, expensive and might require a tedious planning, which can be particular and different for each case. The idea of developing an on-line remote system to monitor the health of the structure is of great interest for these kind of structures. There are many different approaches to VSHM which can be implemented for wind turbine blades. In this chapter a technique is presented which is based on an active system for VSHM of WTB. This means that the vibrations are introduced artificially by an actuator to excite the WTB and monitor its vibration response, that is measured by means of the distributed accelerometers along the WTB.

The recorded signals are then processed by the methodology algorithm to determine the observation damage indices. The damage indices are compared to the defined threshold to determine whether or not the WTB is damaged. The proposed VSHM methodology uses a medium frequency range excitation which is a compromise between the propagation range and detection resolution. As mentioned in [129], the range of frequencies employed in damage location has a great influence on the resolution of the results and also the physical range of application. The great advantage of using low frequency vibration measurements is that the low frequency modes are generally global and so the vibration sensors may be mounted remotely from the damage site. Equally fewer sensors may be used. The problem with low frequency modes are that the spatial wavelengths of the modes are large, and typically are far larger than the extent of the damage [130]. Damage in wind turbine blades appear firstly locally which is more difficult to be detected. However the analysis of damage growth, it might have more global effects which contributes in its detection. The proposed methodology studies the effect on the sensors distributed along the blade to roughly relate the sensor location with the actual damage location. This may contribute to the damage detection and location.

4.3 Integrated vibration-based structural health monitoring system

An online VSHM is introduced based on an unsupervised active system which means that only data from the healthy blade was considered to create the reference state and the blade was excited by an active actuator located on the blade. With the reference state created on the vibration responses of the healthy blade, a baseline set was constructed to measure the distances of any observation to the baseline set and thus obtain the damage index for each observation (see Chapter 2). The nature of the damage assessment methodology heavily relies on statistics in order to improve the robustness detection rate and minimize the number of false alarms. In order to perform an inspection phase of the damage indices obtained, an automatic threshold procedure was considered. Each damage index can be evaluated to be the healthy or damaged blade by comparing with the threshold.

4.3.1 Threshold setting for inspection phase

A probabilistic threshold is based on the probability density function (pdf) of the data considered as a training set. As explained in section 2.2, each vibration response observation is characterised through the methodology, in a single value D, that defines the damage index of each observation. These damage indices are expected to be different when the observations belong to different structure categories or similar, if they are obtained from the same structure category. These values were obtained by computing the Mahalanobis distance as shown in section 2.2.4. The damage indices are always positive ($D > 0$). Based on this assumption, a log-normal probability density function is used to approximately fit the data considered as training set (observations from the healthy structure), in order to set a threshold to distinguish between observations from healthy and damaged structure. This kind of damage classification, using a probability test, was also studied in [131] where different probability distributions were considered. (See Appendix A to visualize an example of data distribution based on the example detailed in section 4.4). A lognormal probability density function is described by Equation 4.1.

$$f(D|\mu,\sigma) = \frac{1}{D\sigma\sqrt{2\pi}} exp\left[\frac{-(lnD-\mu)^2}{2\sigma^2}\right] \quad ; \quad D > 0 \tag{4.1}$$

where:

D: Damage indices obtained by observations of the healthy blade considered as training data set

ln D: is the natural logarithm of D

μ, σ: are mean and standard deviation of ln D, respectively

Then, the threshold D_T is selected by a particular risk level which determinates the false alarm probability equal to α in the lognormal density function as shown in Figure 4.1(a). The threshold is calculated by the inverse of the lognormal cumulative density function[1] which gives the value with a probability $1-\alpha$ in the cumulative density function, described by the equation 4.2 (see Figure 4.1(b)).

$$D_T = F^{-1}(p|\mu,\sigma) = \{D_T : F(D|\mu,\sigma) = p\} \tag{4.2}$$

$$p = F(D|\mu,\sigma) = \frac{1}{2}\left[1 + erf\left(\frac{lnD-\mu}{\sigma\sqrt{2}}\right)\right] \tag{4.3}$$

where:

p: is the lognormal cumulative density function described by Equation 4.3

erf: is the error function[2] defined as $erf(D) = \frac{2}{\sqrt{\pi}}\int_0^D e^{-t^2}dt$ (see [132] p.110)

D_T: is the value of the sampling training data with probability $1-\alpha$ selected to be the threshold

Therefore, any observation damage index D_i in the range [0, D_T] will be considered as an observation from the healthy structure and anything else will be considered as a damaged structure as described by the following decision rules.

$$\begin{aligned} &\textbf{H1}: \quad D_i \leq D_T \quad \Rightarrow \quad \text{Healthy structure} \\ &\textbf{H2}: \quad \quad \text{Else} \quad \;\; \Rightarrow \quad \text{Damaged structure} \end{aligned} \tag{4.4}$$

---

[1] The inverse of the lognormal cumulative density function was implemented by the Matlab function *logninv.m*

[2] The erf function was not calculated separate but as part of the Matlab function *logninv.m*

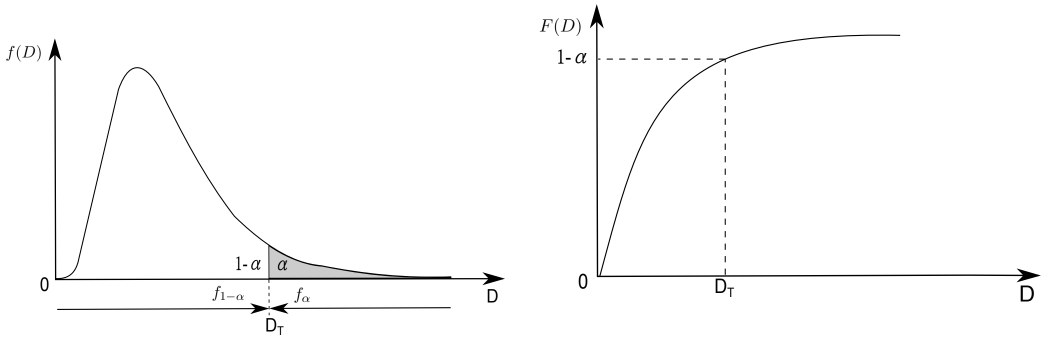

(a) (b)

Figure 4.1: Statistical hypothesis threshold based on lognormal distribution (one-side only). a) Probability density distribution. b) Cumulative density function.

4.4 Damage assessment for small lab-scale wind turbine blade

Wind turbine blades are manufactured by two half shells made by composite laminates which are glued together to form the entire structural member. This connection must be carefully controlled due to its high probability to disbond which might result in the collapse of the entire structure. In this section, a lab-scale blade manufactured for the Wind Car project at Wind Energy department of Technical University of Denmark was analysed for damage detection and localisation. The similarity in the manufacturing process of these blades to a real WTB serves as lab-scale test for the real WTB. The objective of this analysis is to detect different damage locations introduced in the blade. For each damage location three different damage sizes were also introduced to see the effect on the damage progression by means of the methodology. The analysis was implemented by the measurements of one accelerometer each time. The aim was to evaluate the damage assessment methodology for each accelerometer location and study the relation between the location of the sensors and the actual damage location. In this section the experimental work is described first, and secondly the damage assessment of a lab-scale WTB.

4.4.1 Experimental work

Test rig

A dedicated test setup was created to evaluate the damage on a lab-scale wind blade manufactured in the DTU Wind Energy department of Technical University of Denmark. The blade consists of two parts manufactured separately from composite laminates (see [133] for details of blade design and implementation). The two parts, pressure and suction sides, were joined together by means of a big number of small bolts (50 bolts), placed along the leading and the trailing edges a 25 mm distance from each other. This connection was applied on the same area where the two blade parts are generally glued. Once the blade was finalised, it was placed in a test rig where the root end was clamped in a cantilever configuration as it is supposed to be mounted on the rotor hub (see Figure 4.2(b)).

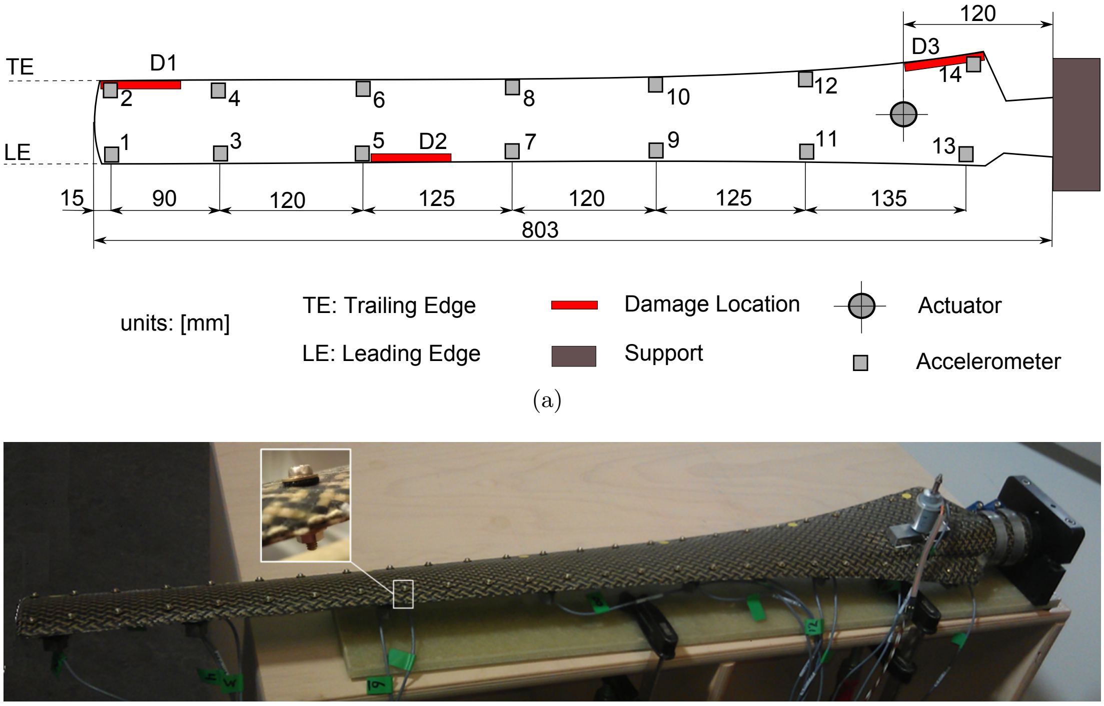

(a)

(b)

Figure 4.2: Experiment set up of the lab-scale wind turbine blade. a) Experiment scheme. b) Experiment set up

A total of fourteen B&K Type 4507 B4 monoaxial accelerometers were mounted along both edges. Seven along the Leading Edge (LE) and seven along the Trailing

Edge (TE), separated from each other at the distances shown in Figure 4.2(a).

During the test, the blade was artificially excited by a small electro-mechanical actuator mounted at 120mm from the root end, as shown in Figures 4.2(a) and 4.3(a). The actuator was driven by a signal generator. This set up configuration enables periodic highly repeatable force impulses to be introduced into the blade structure. Therefore, the vibration responses were measured by the the array of accelerometers distributed along the blade for each actuator impact. The data acquisition was conducted using B&K Pulse LAN-Xi modules Type 3053-B-120 and 3160-A-042, the latter also includes the signal generator. In total, 15 channels were recorded: 14 acceleration signals and the driven signal from the signal generator, the latter to facilitate triggering during the post-processing.

Damage simulation

As described above one of the most common form of damage in this kind of structures is the loss of connection between the pressure and suction part. When the damage occurs, it appears in one of the edges on the blade. Due to the stress concentration around the damaged region, the small failure can grow to levels when the failure mechanism is impossible to control and eventually results in the collapse of the entire structure.

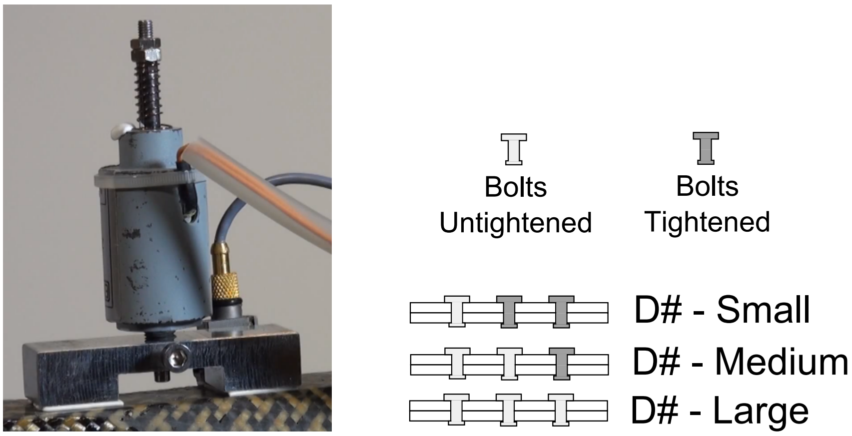

(a) (b)

Figure 4.3: a) Electromagnetic Actuator b) Damages severity scenarios.

In the small WTB considered in this study, the two parts were connected to each other by bolts along both edges. This solution greatly simplifies introducing damage into the blade. One shall simply undo some of the bolts which, in this way, it is easy to control the damage location and size by untightening more than one bolt. For the damage 'repair', the loosened bolts need to be re-tightened. This approach allows modelling of when the damage occurs by debonding of the leading and trailing edge. However, there are other types of damages, which cannot be modelled with the current setup.

With this experiment setup, three different damage locations were introduced as shown in Figure 4.2(b). First Damage (D1) was placed close to the tip of the blade in the trailing edge (between sensors 2 and 4). Secondly, Damage (D2) allocated more or less in the middle of the blade in the leading edge (between sensors 5 and 7) and finally, Damage (D3) which is very close to the root end along the trailing edge (between sensors 12 and 14). For each damage location, a set of three damage severities was considered. As shown in Figure 4.3(b), the three damage severities were named as D-Small when only one bolt was untightened, D-Medium when two consecutive bolts were untightened and D-Large when three consecutive bolts were untightened. For the case when the blade was considered as a healthy structure, all the bolts were tightened. In this case, not only a damage was introduced in the blade but also different damage severities which enables the study of damage progression. It is important to note that the loosened the bolts were not removed from the blade, thus the total mass of the structure kept unchanged. The soft rubber washers keep the bolts fixed in the holes, thus preventing the bolt rattling. The reason for this was to avoid any possible side effects of loosening the bolts, which the algorithm can confuse with changes in local structural stiffness.

Data collection procedure

The data considered for the damage assessment methodology was the acceleration signals measured by the sensors distributed along the blade. Each damage location was separately studied and the consideration of multiple damages was not analysed. The data collection procedure followed the steps: 1) A set of vibration signals were measured for a Healthy blade with all bolts tightened. 2) Damage was introduced at any of the locations described in Figure 4.2(a) by untightened one bolt (D-small). Then, a set of vibration signals were measured for this damage location and severity. 3) The first damage severity was incremented when the neighbouring bolt was untightened (D-medium) and a set of vibration signals measured. 4) Finally the first damage location were completed by measuring a set of vibration signals when a third consecutive bolt was untightened for this damage location. In this case not only the damage location was studied but also the damage progression. Before the start of the same procedure for another damage location, all bolts where tightened to model again the healthy blade. Because it was rather difficult to tight all bolts in the exact same manner as it was at the original healthy blade, for the analysis of the next damage scenario a new healthy reference blade was considered. Then, a new set of healthy vibration responses were measured for the new tightened bolts configuration. The damage data collection was repeated following the same steps described above. When a new damage location was considered, the healthy reference blade was again reconsidered. Table 4.1 contains the number of vibration signals considered for each blade scenario.

Number of signals			
	Location		
Scenario	D1	D2	D3
H	231	209	195
D-Small	40	44	59
D-Medium	44	43	55
D-Large	41	40	55

Table 4.1: Number of signals for each blade scenario in the lab-scale WTB test

4.4.2 Damage detection and evaluation

In this section the different damage locations and severities were assessed. The vibratory responses measured by the accelerometers distributed along the blade were performed by the methodology introduced in Chapter 2. It is important to mention that the damage detection and evaluation was considered by the measurements from one sensor each time. Therefore, the measurements from multiple sensors were not considered in the analysis. However, the measurements in each sensor was separately considered in order to see the effect of the sensor location in the methodology performance. The idea of this analysis was to considered the minimum number of sensors and study the effect of its location on damage detection and evaluation. It should be mentioned that a systematic approach for selecting the number of accelerometers and their placement as well as the actuator location was not considered. The only reason for this distribution of accelerometers was to cover both edges which was the region where the damage was introduced.

Creation of the reference state of each accelerometer measurement

As the methodology was performed for the measurements by each accelerometer separately, the reference state was created for the vibration responses measured by each accelerometer. Therefore, the vibration responses from the healthy blade measured from one accelerometer were used to create the reference state of the blade based on this accelerometer and similarly for all of the other accelerometers. Thereby, a total of 14 different reference states were obtained. As mentioned before, when a damage location was analysed, the blade was 'repaired' by tightening again the untightened bolts. Because it is difficult to obtain the same original blade state, the reference state was created based on the new healthy blade.

With the considerations explained above the reference states (see section 2.2.2) were created by the free-decay acceleration responses sampled at 32768 Hz. Every time when the actuator introduced an impact on the blade, 14 vibration responses were measured in the distributed accelerometers which were transmitted to the computer installed for the data collection.

Each reference state was created with $M = 10$ signal vector realisations and with a sliding window size $W = 10$. The selection of the sliding window size parameter is based on the study developed in section 2.5.2. Generally the selection of small values for W and relatively close to M gives well defined clusters. Each free-decay acceleration was transformed to the frequency domain by the Fourier transform and discretised into a vector of length N=1024. Then, the embedding matrix $\check{\mathbf{X}}$ was created with a dimension 1024 x 100. The covariance matrix of $\check{\mathbf{X}}$ was decomposed in a total of 100 eigenvalues and their corresponding eigenvectors, which were used to create a reference state, $\mathbf{R}$ with a dimension 1024 x 10.

Figure 4.4 contains the scree diagrams and the reconstructed frequency spectrum by 2, 3 and 4 RCs of the vibration responses measured on the healthy blade from the analysis of damage location D1 by the accelerometer 1, for the vibration responses measured on the healthy blade from the analysis of damage location D2 by the accelerometer 7 and for the vibration responses measured on the healthy blade from the analysis of damage location D3 by the accelerometer 12. It can be observed that in the three scree diagrams, the largest amount of variance is contained in the first eigenvalue which drastically decreases for the other eigenvalues. It can also be observed that until the 4^{th} eigenvalue, the amount of variance constantly decreases, while after this eigenvalue, the amount of variance decreases to insignificant values.

In Figures 4.4(a), 4.4(c) and 4.4(e) can be clearly observed that the vibration responses measured by each accelerometer give different decomposition scenarios and hence a different reference state will be created corresponding to its own decomposition. It can be observed that the amount of variance contained in the first eigenvalue for signal vectors obtained by sensor 1 (see Figure 4.4(a)) is 84%, that is larger than the amount of variance contained by signal vectors obtained by sensor 7 and 12 which are 78% and 74%, respectively (see Figures 4.4(c) and 4.4(e)). Then, it can be observed that even though the decompositions are similar, they cannot be considered as the same. Figures 4.4(b), 4.4(d) and 4.4(f) represent the comparison of the original frequency spectrum and the reconstructed frequency spectrum by 2, 3 and 4 RCs for the signal vectors obtained by sensor 1, 7 and 12, respectively. In all cases, it is observed that the reconstruction by 2 RCs gives a smooth spectral line which follows the general trend of the original one. The reconstruction by 2 RCs describes very well the general spectral line, being more descriptive in regions where the energy concentrates by means of large amplitudes at the frequencies where it occurs. Also it can be observed that the consideration of more RCs in the reconstruction helps to improve the approximation to the original frequency spectrum. These results can be observed in the three examples (sensor 1, 7 and 12) and it will act similarly for each reference state obtained by the 14 sensors distributed on the blade.

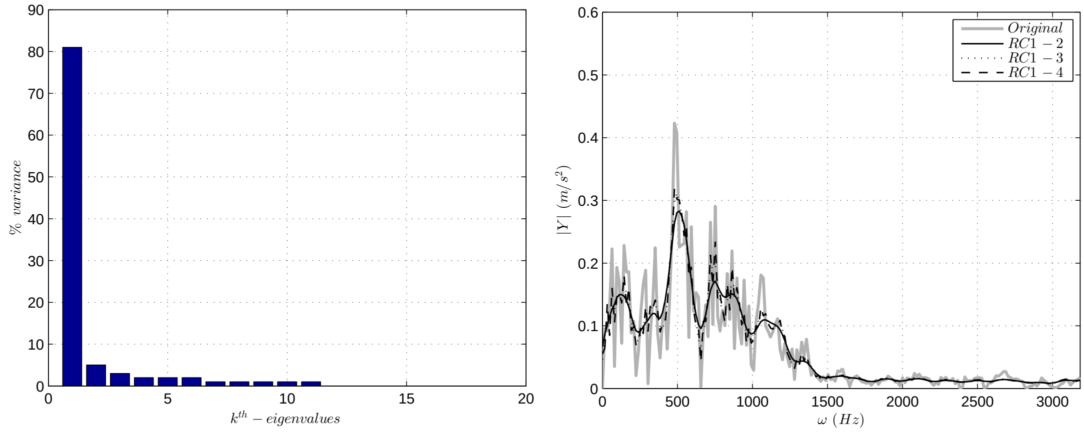

(a) Scree diagram by sensor 1 (b) Reconstruction by sensor 1

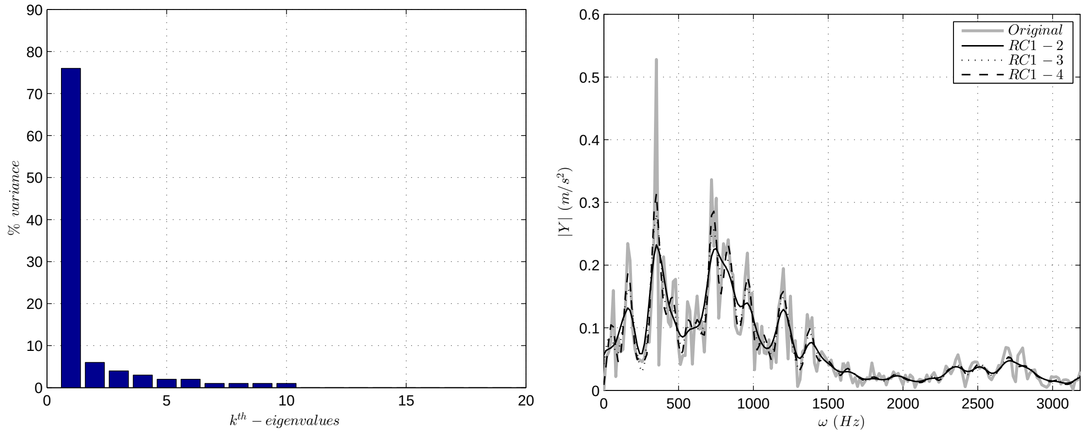

(c) Scree diagram by sensor 7 (d) Reconstruction by sensor 7

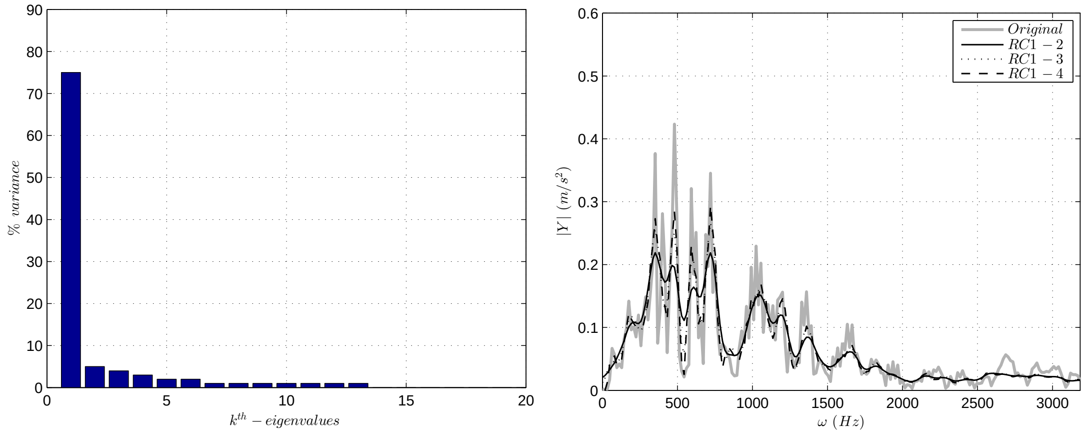

(e) Scree diagram by sensor 12 (f) Reconstruction by sensor 12

Figure 4.4: Scree diagram and reconstructed spectrum by 2, 3 and 4 RCs for the vibration responses measured on the healthy blade from the analysis of damage location D1 by the accelerometer 1, from the analysis of damage location D2 by the accelerometer 7 and from the analysis of damage location D3 by the accelerometer 12 on the lab-scale wind turbine blade.

Damage assessment

The FVs for each observation signal vector were calculated by the reference state created with the vibration responses measured by each accelerometer. The analysis was implemented by each sensor separately and therefore the number of FVs calculated for each accelerometer analysis was the same as the number of signals detailed in Table 4.1. The maximum dimension of each FV is 10 which is equal to all number of RCs contained in the reference state. The clustering effect obtained by projecting the FVs onto a two-dimensional feature space is represented in Figure 4.5. The clustering effect is present for the three damage locations obtained by the analysis of accelerometer 1 for D1, accelerometer 7 for D2 and accelerometer 12 for D3 as shown in Figures 4.5(a), 4.5(c) and 4.5(e), respectively. In all Figures, it can be observed that different clusters were formed corresponding to each damage severity. For the analysis of these three accelerometers, it can be observed that by the projection of the observation FVs onto a two dimensional space, the clusters obtained were able to distinguish between different damage severities when one, two or three bolts were untightened. This effect was observed for all the three analysis of accelerometers 1, 7 and 12 which are located relatively close to the location of the damage.

In order to study the progression of the damage for each damage location, the damage assessment technique introduced in section 2.2.4 was performed. The FVs that characterise the healthy blade were used to create a baseline matrix where the observation FVs can be compared. Different baseline matrices were created for each accelerometer analysis where the observation FVs were compared. The dimension of the baseline matrices was p x s where p=2 (dimension of the FVs, in this case (T_1-T_2)) and s=150 (number of observation FVs considered to create each baseline matrix).

Figures 4.5(b), 4.5(d) and 4.5(f) represent the damage index of each observation based on the Mahalanobis distance of two-dimensional observation FVs to the baseline matrix. A threshold was found through the damage indices of the observation points of the healthy blade considered as training set (s=150) to the baseline matrix. For this case the threshold was selected to have a risk of false alarm probability equal to α=0.05. As explained in section 4.3.1, the data of the healthy blade, considered as training data, was considered to follow a log-normal probability distribution. As an example, the probability distribution function of the training data obtained for the measured vibration responses by each accelerometer (1 to 14) can be observed in Figure A.1 in Appendix A.

Consequently, it is expected that the observations that are obtained from the same category used in the creation of the baseline set (healthy blade) will result in a distance that will be smaller than the defined threshold. However, observations from a different category that healthy blade will result in a distance larger than the defined threshold. Figure 4.5(b) shows the damage index for damage location D1 when it was evaluated by the accelerometer 1. It can be observed that the observation points characterised from the damaged blade gave a distance larger than the threshold and hence they were considered as observations from the damaged blade. Additionally, it can be observed that when the damage severity was incremented by untightening one, two and three bolts, the observations from these damage categories did not only result in distances larger than the threshold but also a relative increment of the distance with respect to the damage indices obtained from smaller damage scenarios. With these results the damage severity/progression can be tracked with a clear tendency to increase the distance when the damage increases. This effect can be also found in Figures 4.5(d) and 4.5(f), where the damage was located in locations D2 and D3, respectively. For both cases, the damage was detected and the damage progression/severity was also tracked. It is important to mention that these sensors 1, 7 and 12 are relatively close to the damage and their damage detection performance was perfectly achieved.

Figure 4.6 represents the mean of the Mahalanobis distances of the observations corresponding to each damage severity scenario when the damage was at location D1 (Figure 4.6(a)), at location D2 (Figure 4.6(b)) and at location D3 (Figure 4.6(c)) evaluated separately for each accelerometer. The mean of Mahalanobis distances was calculated for the damage indices obtained by each sensor separately and in this sense the performance of the methodology for each sensor can be observed. In Figure 4.6(a) is analysed the damage in the location D1, that is close to the accelerometers 1-4 as highlighted with the coloured area. It can be observed that the accelerometers on the left-hand side of the blade (closer to the tip) were the ones that gave the greatest damage indices in comparison with the right-hand side accelerometers. For the damage location D2

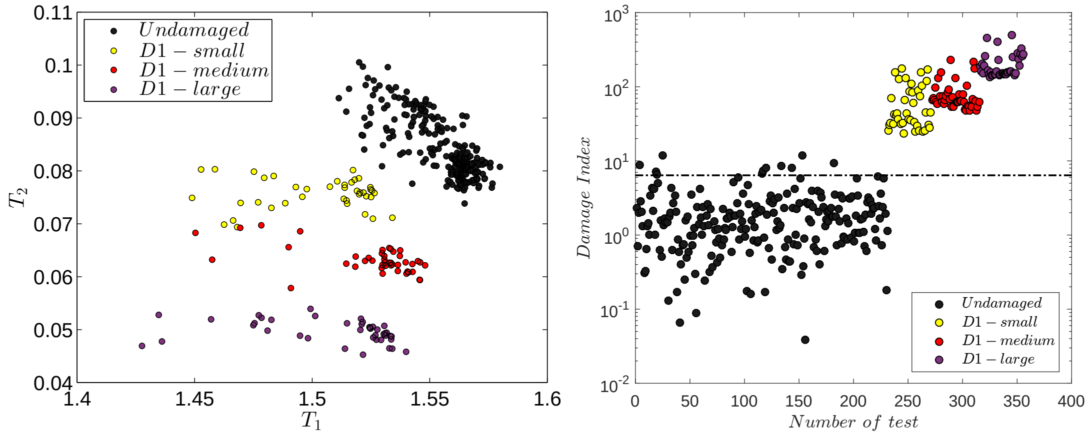

(a) D1: Clustering by sensor 1 (b) D1: Damage Index by sensor 1

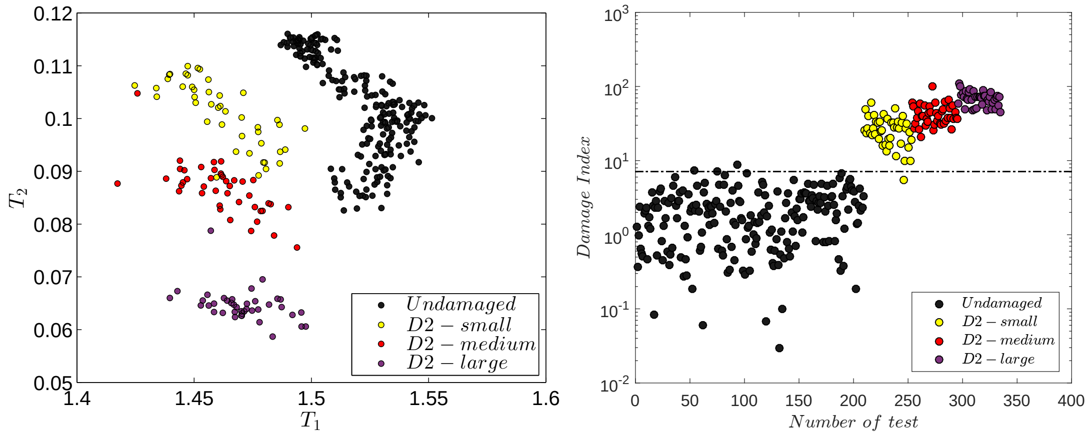

(c) D2: Clustering by sensor 7 (d) D2: Damage Index by sensor 7

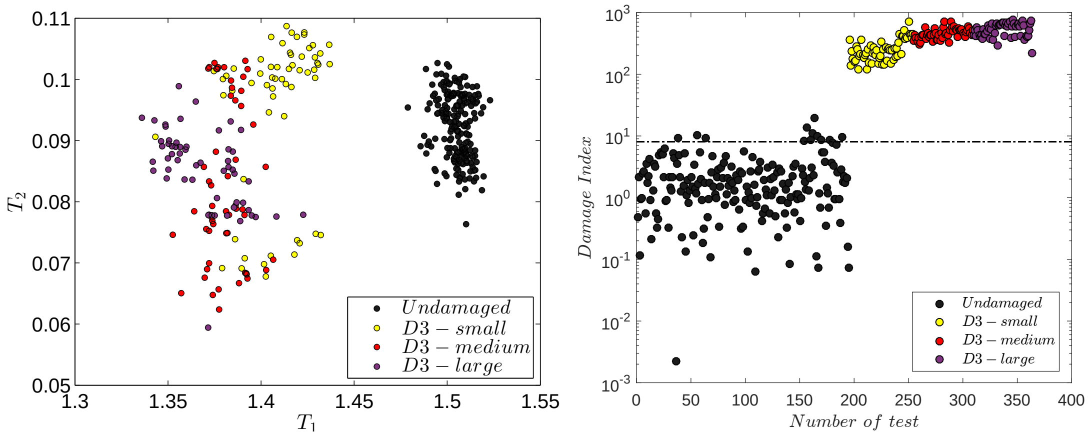

(e) D3: Clustering by sensor 12 (f) D3: Damage Index by sensor 12

Figure 4.5: Clustering effect onto a 2-dimensional feature space (T_1-T_2) and Mahalanobis damage index for three damage locations D1, D2, D3 and three level of severities D-Small, D-Medium and D-Large in a lab-scale wind turbine blade. The dashed line defines the threshold calculated for a risk of false alarm probability equal to α=0.05.

as shown in Figure 4.6(b), the accelerometers on the left-hand side were also the ones which give the greatest values of damage indices with a slight displacement towards the accelerometers in the middle of the blade.

And for damage location D3, the accelerometer placed very close to the damage (sensor 12) was the only one that gave a significantly large damage index in comparison with the other accelerometers as shown in Figure 4.6(b). As mentioned in section 4.2, low/medium frequency range vibration measurements are generally global and then sensors can be mounted remotely from the site of the damage for the purposes of damage detection. Although, the location of the accelerometers can be remotely located, it can be observed that the accelerometers which are closer to the damage location provide a larger damage index. This phenomena is also observed in [134] where the damage locations were related to the greatest magnitudes of the Mahalanobis distances. Although, this is a sign that sensors closer to the damage's region are more sensitive to the damage effects, it is still insufficient to be an indicator for damage location and further analysis has to be done in this direction. On the other hand, the majority of the accelerometers which gave a significant magnitude of the damage index were also able to monitor the damage progression by an increment of the damage index as the damage severity increased.

The results obtained by the damage assessment methodology were evaluated for the correct classification rate of observations from healthy and damaged blade. It was applied for the three damage severities (D-Small, D-Medium and D-Large) and the three damage locations (D1, D2 and D3). Each observation was compared to the defined threshold (risk of false alarm probability equal to α=0.05) as explained in section 4.3.1. Table 4.2 contains the results of the correct classified observations (Healthy - Damaged) when the dimension of the FVs was considered as p=4 (T_1-T_2-T_3-T_4). The average of variance content in the reference states created by four RCs on the 14 sensors was 90%, 91% and 90% when the reference state was created by the vibration responses measured in the healthy blade for the analysis of damage locations D1, D2 and D3, respectively (see Tables in Appendix B).

The percentage of correct classification for observations at damage location D1 was 100% for the majority of the sensors when the damage severity was D-Medium and

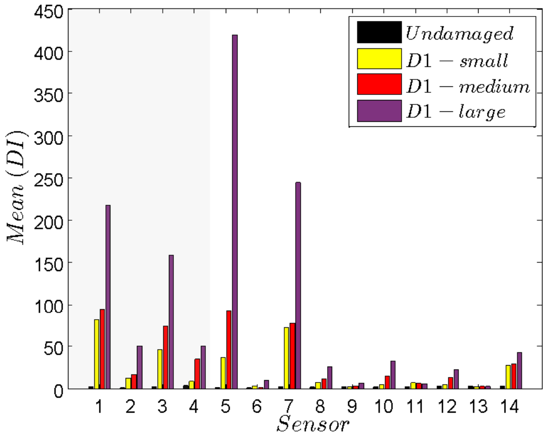

(a) Damage location D1

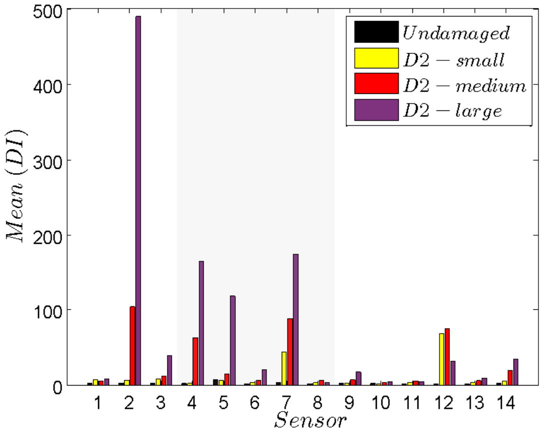

(b) Damage location D2

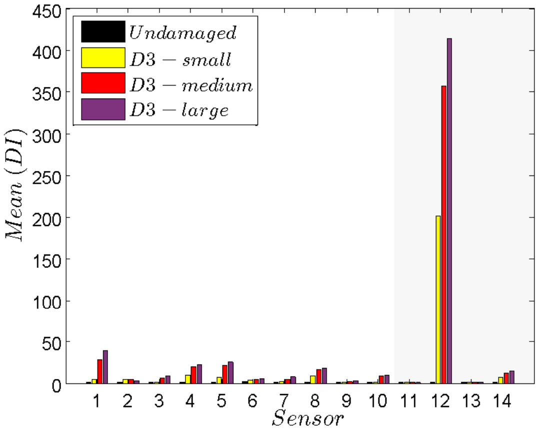

(c) Damage location D3

Figure 4.6: Mean of the damage indices obtained for each damage location and severity obtained for each sensor separately. The highlighted area indicates the sensors which are the closest to the damage scenario in consideration

	Damage location											
	D1				D2				D3			
Sensor	H	D1S	D1M	D1L	H	D2S	D2M	D2L	H	D3S	D3M	D3L
1	**94**	100	100	100	**97**	50	98	100	**94**	63	95	100
2	**99**	78	100	100	**95**	39	100	100	**94**	75	76	85
3	**94**	100	100	100	**100**	30	90	100	**92**	41	55	58
4	**93**	38	100	100	**94**	89	100	100	**92**	59	95	95
5	**94**	100	100	100	**94**	41	93	100	**92**	20	62	69
6	**94**	35	9	93	**94**	25	60	98	**93**	25	42	36
7	**93**	100	100	100	**96**	100	100	100	**94**	69	76	100
8	**94**	75	95	100	**99**	43	83	90	**96**	76	96	100
9	**95**	23	23	98	**98**	27	76	100	**93**	14	44	55
10	**91**	40	100	100	**99**	18	86	100	**96**	64	84	80
11	**94**	78	100	95	**100**	2	5	95	**92**	34	51	42
12	**92**	93	100	100	**94**	100	100	100	89	100	100	100
13	**95**	15	2	17	**98**	20	45	65	**95**	7	33	56
14	**96**	78	91	100	**98**	25	76	88	**95**	54	93	96

Table 4.2: Percentage of correctly classified (Healthy and Damaged) observations when the damage is in location D1, D2 and D3 for all damage severities. In bold and highlighted in grey the percentages greater than 90% for **Healthy** and Damaged observations, respectively. Threshold was set up at risk of false alarm probability equal to $\alpha = 0.05$. The FVs dimension considered was p=4 (T_1-T_2-T_3-T_4). The number of observations tested is detailed in Table 4.1.
H: Healthy wind turbine blade (without loose screws)
D#S: Damage location D# - small
D#M: Damage location D# - medium
D#L: Damage location D# - large
#: 1, 2 or 3

D-Large. However, for the damage severity D-Small, the correct classification of the damaged observations was lower than 90% for most of the cases. On the other hand, the damage detection obtained for the accelerometers close to the damage (sensors located in the left-hand side of the blade or close to the tip of the blade) gave high percentage of correct classification. The percentage of correct classification for observations of the healthy beam was always more than 90% for all the sensors.

For the case of damage location D2, the small damage severity was rather difficult to be detected and only accelerometers 7 and 12 were able to give 100% correct classification. For D2-Medium, the accelerometers on the left-hand side of the damage location (or close to tip of the blade) gave more than 90% correct classification. However, the largest damage was perfectly detected for the majority of the accelerometers with more than 95% correct classification rate. Finally, the evaluation of damage at the location D3 was more difficult to be detected. Only some sensors were able to gave a larger than 90% correct classification rate of the observations. Only the accelerometers located very close to the damage (sensor 12 and 14) were able to classify correctly the majority of the observations. It is important to mention that for all three damage locations, the percentage of correct healthy classification was always greater than 90%. Also the accelerometers placed close to the damage gave 100% classification rate for all different damage severities. These sensors were perfectly able to track the damage progression as shown in Figure 4.5. Appendix B contains tables of percentage of correct classification for observation measured for all damage locations and severities when the dimension of the FVs were 2, 3 and 4. It is generally observed that for higher dimension of the FVs, the correct classification of damaged observations improves, however the correct classification of healthy observations slightly decreases for all damage scenarios.

4.5 Damage assessment for large SSP34m wind turbine blade

This section presents the damage assessment methodology, first validated in section 4.4 in a lab-scale wind turbine blade, which was now implemented in a large SSP34m wind turbine blade. The SSP34m blade was mounted on a test rig at DTU Wind Energy facilities in Roskilde, Denmark. In this study the main objective was to assess the artificially introduced damage in the trailing edge of the blade. As mentioned above, the VSHM technique is based on an active system and therefore the blade was excited by an electromechanical actuator. The aim of the analysis was to detect the damage when the blade was excited at different actuation locations. The performance of the methodology was also evaluated by one sensor each time in order to relate the location of the sensors and the damage location. In this section, the description of the experiment is introduced and secondly the damage assessment evaluated by the damage detection and by the inspection phase based on the defined threshold.

4.5.1 Description of the experiment set up

Test rig

The SSP34m blade was mounted in a cantilever position in a test rig as shown in Figure 4.7(b). The blade was clamped at the root-end as it would be mounted on the rotor hub of the wind turbine. As shown in Figure 4.7(a), the blade was instrumented with 20 B&K triaxial accelerometers Type 4524-B. The disposition of the accelerometers was similar to the lab-scale blade presented in the previous section, 10 on the leading edge (LE) and 10 on the trailing edge (TE). Although the accelerometers were triaxial, only the data that corresponds to the perpendicular direction of the blade surface was utilised. A specially manufactured template was used to place the accelerometers having the same coordinate directions. In this way, the accelerometers were mounted with sufficiently high precision. Swivel bases B&K Type UA1473 were used to facilitate accelerometer mounting with the required orientation. As described in the previous experiment, the placement of the accelerometers did not follow any systematic approach for selecting the optimum number of accelerometers and location. The accelerometer cables length were reduced by a distributed data acquisition system. Every four accelerometers were connected to a 12-channel data acquisition module B&K Type 3053-B located nearby the accelerometers. The data acquisition modules were connected to a Cisco Ethernet switch (SG300-10MP), which solved module powering and synchronization issues (see [130] for further information). The system also contained a signal generator, which was set to generate an amplified rectangular pulse fed to the actuator for each actuator hit.

The vibration-based structural health monitoring methodology conducted in this study is based on an active excitation system. This means that the blade is artificially excited by an electromechanical actuator. Figure 4.7(c) presents the electromechanical actuator implemented in the test. It consists of three parts: a steel plunger with plastic tip, the coil and the electronics box. When an electrical pulse is driven through the coil, it applies an impulse to the plunger which impact the structure; after the hit, the plunger returns to its initial position by a spring and it waits until another electrical pulse is transferred by the coil. Although, it can be useful to know the force applied on the structure, it was not measured due to the complication of mounting a practical

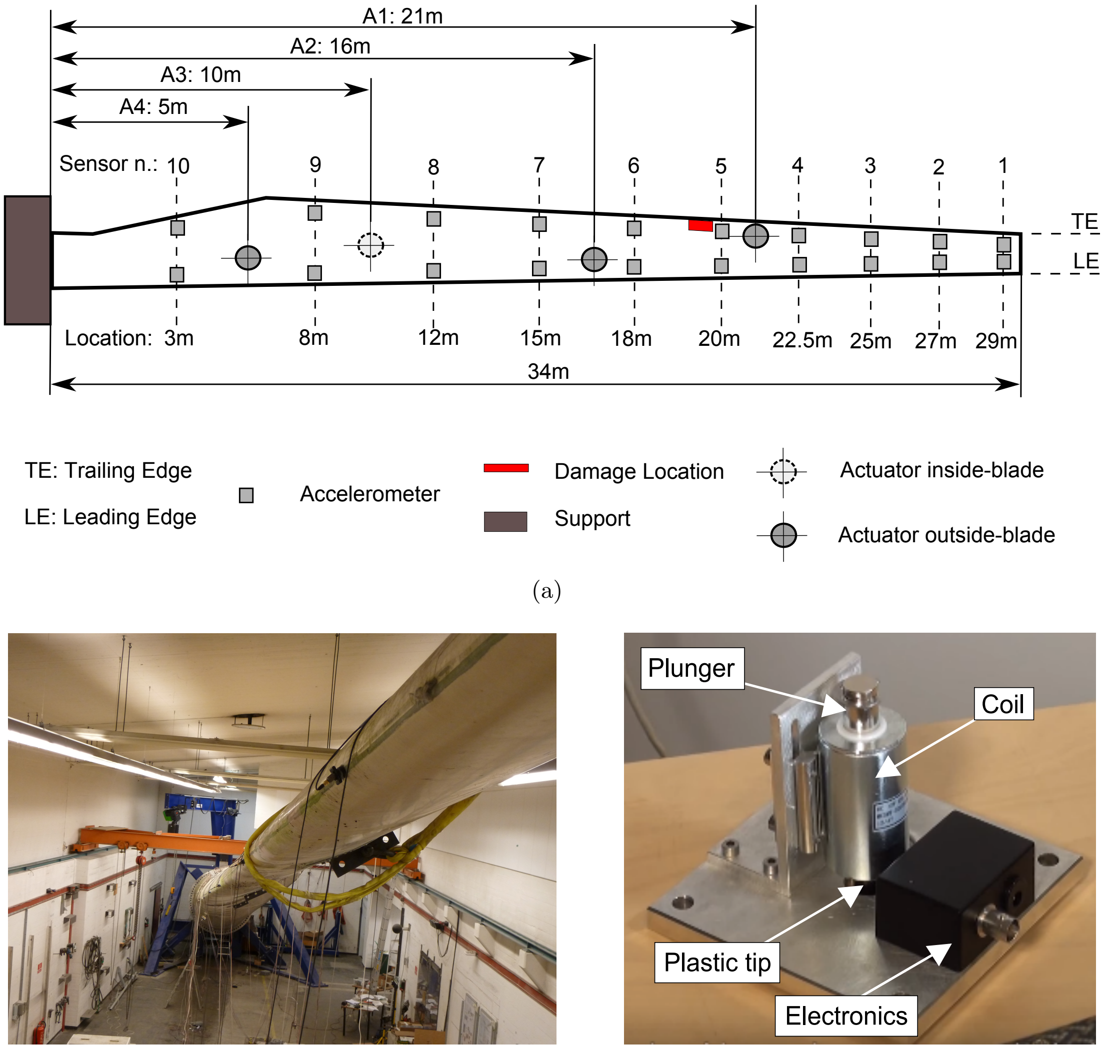

(a)

(b)

(c)

Figure 4.7: Experiment set up of the SSP34 wind turbine blade. a) Experiment scheme. b) Experiment set up. c) Electromechanical actuator.

sensor on the actuator.

Artificial damage simulation

The same damage topology as in section 4.4 was tested in the presented study. The debonding of one of the edges (TE or LE) between the top and bottom shell is a common damage which occurs in this kind of structures. The damage was introduced artificially into the blade by drilling a series of holes through the glue between the shells of the blade in the trailing edge (TE). Then, using a saw the holes were merged into a failure which was opened by a chisel and a hammer. The crack was gradually extended up to 120 cm (see Figure 4.8(a)). Because the opening of the crack was executed with a heavy hammer and chisel, it could introduce some other unwanted changes into the blade (see [62] for more details). In order to avoid this and ensure that the only anomaly was introduced because of the damage, the experiment was performed with the following artificial damage: the debonded parts were connected by bolts, placed at 10 cm from each other. The glue removed between the shells was replaced by thin metal plates (see Figure 4.8(b)). Thereby the healthy blade was considered to have all bolts tightened and the damaged blade was considered when the bolts were untightened. The bolts were not removed from the blade in order to consider only the change on the local stiffness because of the crack but not because of the mass reduction.

Data collection procedure

The data considered for the damage assessment methodology was the acceleration signals measured by the sensors distributed along the blade. The nature of the algorithm requires data from the healthy and damaged state of the blade. Table 4.3 details the number of signals measured for each blade state.

As the damage was already introduced in the blade, the time between the successive hits was selected one to five minutes. However, in a real life application, the time between measurements can be extended for one hour or more depending on the industrial requirements.

Scenario	Number of signals
Healthy blade	42
Damaged blade	39

Table 4.3: Number of signals measured on each experimental test for SSP34m blade

The data collection procedure was repeated four times, one time for each actuator location. The actuator placements are detailed in Figure 4.7(a). Actuator A1 was located very close to the accelerometer 5 in the trailing edge which is also the closest actuator to the damage. It was placed on the bottom surface of the blade (see Figure 4.9(a)). Actuator A2 was placed close to the leading edge between accelerometers 6-

(a) (b)

Figure 4.8: Damage introduced in SSP34 wind turbine blade. a) Damage introduced by chisel in the trailing edge. b) Damage bolted to control the damage size and any additional anomalies introduced by the impact to generate the damage

(a) Actuator in location A1 (b) Actuator in location A2

(c) Actuator in location A3 (d) Actuator in location A4

Figure 4.9: Actuator locations on the SSP34 wind turbine blade

7. This actuator was mounted on the top surface of the blade (see Figure 4.9(b)). Actuator A3 is the only one mounted inside the blade located on the bottom surface of the blade. It was placed between accelerometers 8-9 approximately in the middle between the trailing and leading edge (see Figure 4.9(c)). Finally, actuator A4 was placed very close to the clamped end between accelerometers 9-10. In this region, the blade is almost cylindrical but it was located from the farthest side to the damage (see Figure 4.9(d)).

The data collection procedure was implemented by the following steps: 1) The vibration responses of the healthy blade were measured by a particular location of the actuator. 2) Once the data collection of the healthy blade was finished, the damage was introduced by untightening the bolts. With the damage introduced, the vibration responses corresponding to the damaged blade were measured. Before, the start of the next test with a different actuator location, the blade was 'repaired' by tightening all the bolts. Then, the measurements for the new healthy blade were measured. This procedure was repeated for all tests with different actuator locations.

4.5.2 Damage assessment procedure

The 120 cm artificial damage introduced in the SPP34m blade was assessed by the vibration-based structural health monitoring methodology introduced in Chapter 2. The damage detection was evaluated at four different actuation locations. The methodology was separately performed by the measurements obtained for one sensor each time. The aim of this analysis was to use only one sensor each time and observe its performance based on the different sensor and actuator locations for the damage detection.

Damage detection analysis

As described above, the damage detection analysis was separately implemented for one sensor each time. In this case 20 reference states were created for each actuator location. The reference states were created by the free-decay acceleration responses sampled at 16384 Hz. For each actuator hit, 20 vibration signals were measured by the system instrumentation located on the blade.

Each reference state was created with $M = 10$ signal vector realisations from the healthy blade and a sliding window size $W = 10$. The selection of the sliding window size parameter is based on the study developed in section 2.5.2. Generally the selection of small values for W and relatively close to M gives well defined clusters. The vibration responses were transformed to the frequency domain, and hence discretised into a vector of length N=2048. With these signal vectors, the embedding matrix $\check{\mathbf{X}}$ used for the methodology algorithm had a dimension 2048 x 100. The eigen-decomposition of the covariance matrix of the embedding matrix yielded a total of 100 eigenvalues and their corresponding eigenvectors. Therefore, each reference state $\mathbf{R}$ created through the methodology had a dimension 2048 x 10.

The FVs were obtained by projecting the observation FVs onto the reference state. Based on the dimension of the reference state, the maximum dimension of each FV was 10. The dimension of the FVs utilised in this analysis was reduced to p=4 (T_1-T_2-T_3-T_4). Therefore, all observation FVs were projected onto a 4-dimensional feature space where they were now represented by means of the reference state. The variance contained in each reference state created with the first 4-RCs presented in Table 4.4. The data measured on the healthy blade was divided into two groups of 21 signal vectors for each one. One of these groups was considered as training data to create the baseline matrix where the observation FVs could be compared. Therefore, the baseline matrix $\mathbf{T}_B$ was constructed by s=21 FVs with a dimension p=4. The Mahalanobis distance of each observation to the baseline matrix was measured to determine the damage index of each observation.

A threshold was found through the distances of the observation points of the healthy blade considered as training (s=21) to the baseline matrix. The threshold was found as explained in section 4.3.1 with a risk of false alarm probability equal to $\alpha = 0.01$. In this case the threshold was incremented because of the separation between healthy and damaged observations it was very clear for the majority of the measurements of accelerometers. An increment of the threshold gives a more robust classification in terms of the reduction of positive false alarms. It is important to mention that the threshold was different for each accelerometer analysis because the reference state created for each accelerometer was different.

As a visualization of the methodology performance, the damage indices obtained

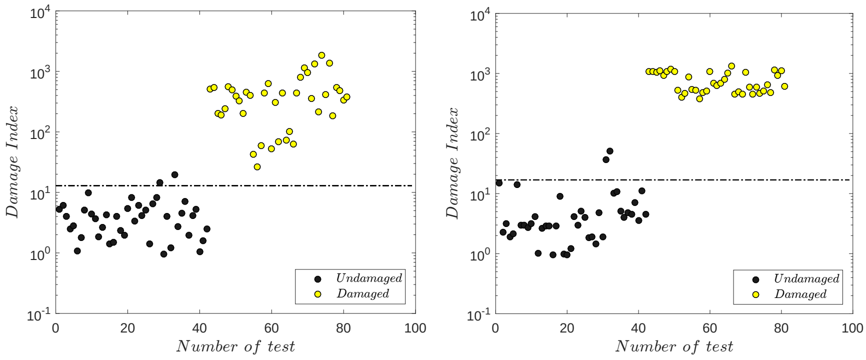

(a) Sensor TE 4 - Actuator 1 (b) Sensor TE 4 - Actuator 2

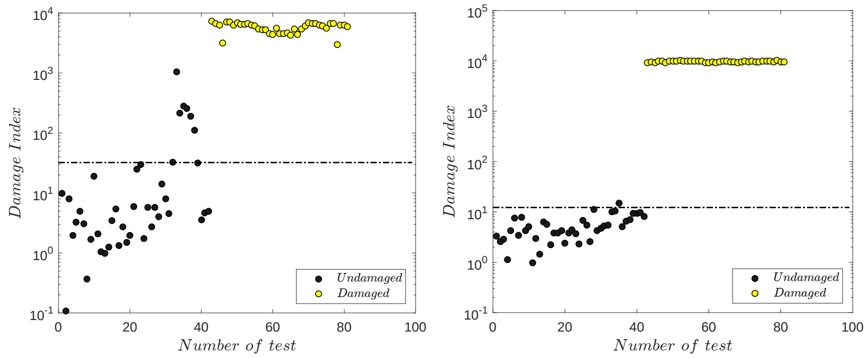

(c) Sensor TE 4 - Actuator 3 (d) Sensor TE 4 - Actuator 4

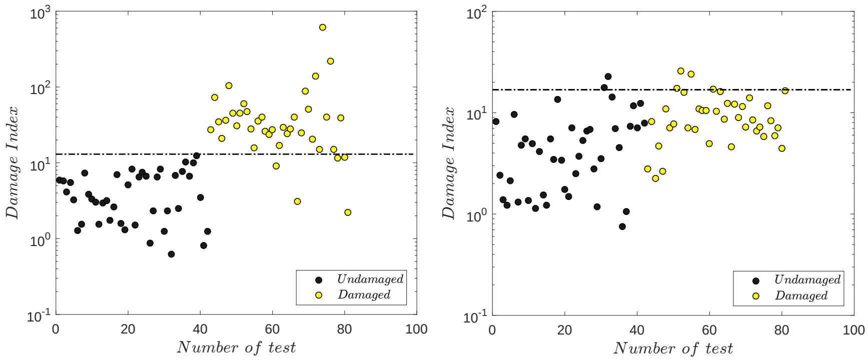

(e) Sensor LE 4 - Actuator 1 (f) Sensor LE 4 - Actuator 2

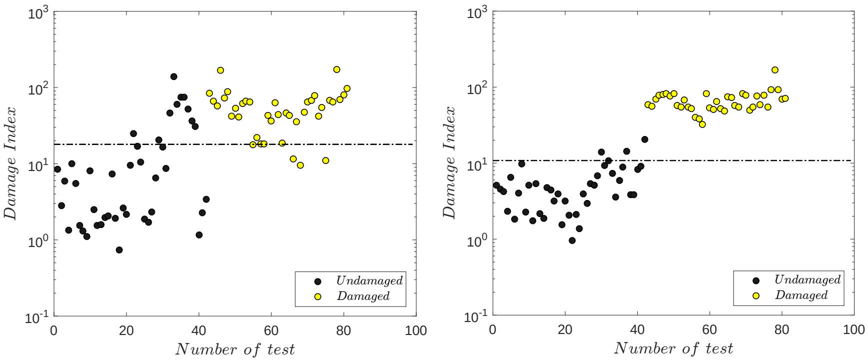

(g) Sensor LE 4 - Actuator 3 (h) Sensor LE 4 - Actuator 4

Figure 4.10: Mahalanobis damage index computed by measurements obtained in sensor 4 (TE - LE) for the four different actuation positions in SSP34m-WTB. The dimension of the FVs was considered p=4 (T_1-T_2-T_3-T_4). The dashed line is the threshold calculated by a risk of false alarm probability equal to $\alpha = 0.01$.

Variance content (%)										
	Trailing edge									
Sensor #	1	2	3	4	5	6	7	8	9	10
A1	99	98	94	95	97	92	92	92	96	91
A2	91	88	94	90	93	93	95	92	90	89
A3	89	95	91	91	89	90	93	96	96	92
A4	80	85	84	81	81	81	82	85	87	87
	Leading edge									
Sensor #	1	2	3	4	5	6	7	8	9	10
A1	96	98	97	99	98	95	93	96	95	91
A2	98	98	97	96	94	97	98	94	94	92
A3	93	92	93	92	92	94	92	98	95	92
A4	93	94	91	91	93	93	91	94	96	88

Table 4.4: Percentage of variance content in a reference state based on the first 4-RCs (RC_1-RC_2-RC_3-RC_4)

by the sensor 4 at the trailing edge and leading edge are presented in Figure 4.10 when the blade was excited at the different actuator locations.

From Figure 4.10(a) to Figure 4.10(d), the performance of sensor 4 on the trailing edge (TE) is represented for all different actuation locations. It can be observed that for the four cases, the observations from the damaged blade were clearly detected. The number of false alarms was low for all the cases except when the actuation was at the location A3. It can be observed a peak in the last damage indices corresponding to the healthy blade which significantly increases the number of false alarms at this actuation location. When the actuation was implemented in location A3 and A4, the damage indices of the observations from the damaged blade were very large in comparison with the actuation in location A1 and A2.

The performance of sensor 4 in the leading edge is represented from Figure 4.10(e) to Figure 4.10(h). It can be observed that the damage detection was clearly achieved when the actuation was applied on location A1 and A4. In both cases, the number of false alarms as well as the number of misclassification for damaged observations was low. However, when the excitation of the blade was applied on location A2 and A3, the detection was not very well achieved. Similarly as for the analysis of the sensor 4 (TE), a peak in the last damage indices of the healthy blade was observed in the sensor 4 (LE) when the blade was excited on the actuation location A3. This effect was also observed in other sensors for the same actuation location. As this effect was repeated in more than one sensor, an irregularity perhaps happened during the test with actuation in the location A3. The increment of the damage indices of observations from the healthy blade may affect on the threshold setup. The threshold line increases because of the outliers and adversely affects to the damage detection.

Inspection phase

The inspection phase was implemented for sensors located in the trailing edge and leading edge separately as shown in Table 4.5. The reason for this presentation is to easily visualise the damage detection performance for both sensor arrays. Table 4.5 represents the percentage of correct classification of healthy and damaged observations based on the defined threshold with a risk $\alpha = 0.01$ (one-side only).

The classification rate of observations from the damaged blade by sensors located in the trailing edge (TE) was in its majority 100% correctly detected for all different actuation locations although there are some of them with a classification rate lower than 90%. It can be observed that for the actuation location A1, sensors 5 and 6 that are the closest to the damage did not give a good classification rate. For this actuation test, the actuator was located very close to the trailing edge and also close to the sensor 5 that is basically on top of the damage. This was perhaps the reason why these sensors did not give a good classification rate. Probably an interaction between the actuator and the sensors occurred because these sensors gave a good classification rate for other actuation locations. However the classification rate of the rest of the sensors, for this localisation of the actuator, was always greater than 95% for healthy and damaged observations. For the actuation location A2, all sensors have a 100% classification rate for damaged observations. The correct classification rate for healthy observations was not always more than 95% but it was relatively high. Only sensor 3 had a classification rate lower than 80%. For actuation location A3, the correct classification rate for damaged observations was 100% for sensors between 1-7. However, the correct classification rate for healthy observations was very low for all the sensors, less than 90%. As mentioned before, when the actuation was applied on the location A3, a significant peak of false alarms occurs for the majority of sensors (see Figure 4.10(c) and 4.10(g) as an example). In Table 4.5 this is also observed with a significant increment of false alarms (more than 10) in the majority of sensors. Finally, for actuation location A4, the correct classification of damaged observations was 100% for the majority of the sensors. The correct classification rate for healthy observations varies between 100% to 79% depending on the sensor location but in their majority is more than 90%.

The results obtained by the sensors distributed in the leading edge (LE) of the blade are also presented in Table 4.5. Generally, the correct classification for both damaged and healthy observations was better achieved when the actuation was applied on the location A1 and A2. However, the classification rate for the actuation A3 and A4 was very low. For actuation location A1, the correct classification rate for damaged observations is better achieved for sensors 5-10 with 100% rate for the majority of these sensors. The correct classification rate of healthy observations was always more than 90% for all sensors. It seems that all sensors located after the damage in the direction to the root-end are more sensitive to the damage when the actuation was applied on this location. For actuation location A2, the correct classification rate was more than 90% for damaged and healthy observations in the majority of sensors. For this location of the actuator was observed a good balance between correct classification for healthy and damaged observations. For actuator location A3, the correct classification rate was in its majority less than 90% for damaged and healthy observations. The low rate of correct classification for healthy observations can be also explained by the phenomena observed when the excitation was applied on the actuation location A3, as shown in sensors along the trailing edge. However for actuator A4, the correct classification rate for healthy observations was greater than 93% for all sensors. The classification rate for damaged observations was only significantly achieved for sensors between 2-5 with 100% rate. In Appendix C can be observed the tables with the percentage of correct classification when the analysis was implemented by two and three dimensional FVs. It can be observed that as highest is the dimension, the classification for observations from a damaged blade were better detected. However, the number of false alarms increases with the consideration of higher dimension feature vectors.

		Sensors Trailing Edge (TE)									
		1	2	3	4	5	6	7	8	9	10
A1	n. MH	0	1	2	2	0	0	0	0	2	2
	n. MD	0	0	3	0	15	17	0	0	0	0
	Correct H (%)	**100**	**98**	**95**	**95**	**100**	**100**	**100**	**100**	**95**	**95**
	Correct D (%)	100	100	92	100	62	56	100	100	100	100
A2	n. MH	2	6	10	2	1	1	1	6	2	1
	n. MD	0	0	0	0	0	0	0	0	0	0
	Correct H (%)	**95**	86	76	**95**	**98**	**98**	**98**	86	**95**	**98**
	Correct D (%)	100	100	100	100	100	100	100	100	100	100
A3	n. MH	13	11	1	7	7	10	8	7	12	15
	n. MD	0	0	0	0	0	0	0	8	8	11
	Correct H (%)	69	74	**98**	83	83	76	81	83	71	64
	Correct D (%)	100	100	100	100	100	100	100	79	79	72
A4	n. MH	7	0	6	1	9	4	3	5	2	7
	n. MD	0	3	0	0	0	0	0	0	0	12
	Correct H (%)	83	**100**	86	**98**	79	**90**	**93**	88	**95**	83
	Correct D (%)	100	92	100	100	100	100	100	100	100	69
		Sensors Leading Edge (LE)									
		1	2	3	4	5	6	7	8	9	10
A1	n. MH	2	0	0	0	0	0	5	4	2	2
	n. MD	0	10	31	5	0	5	0	0	0	0
	Correct H (%)	**95**	**100**	**100**	**100**	**100**	**100**	88	**90**	**95**	**95**
	Correct D (%)	100	74	21	87	100	87	100	100	100	100
A2	n. MH	0	6	2	2	3	3	2	3	8	0
	n. MD	0	0	1	35	0	0	6	0	0	2
	Correct H (%)	**100**	86	**95**	**95**	**93**	**93**	**95**	**93**	81	**100**
	Correct D (%)	100	100	97	10	100	100	85	100	100	95
A3	n. MH	8	5	10	10	0	12	12	13	11	9
	n. MD	1	8	13	4	29	11	4	7	4	12
	Correct H (%)	81	88	76	76	**100**	71	71	69	74	79
	Correct D (%)	97	79	67	90	26	72	90	82	90	69
A4	n. MH	2	1	0	3	0	1	0	0	0	0
	n. MD	15	0	0	0	0	39	39	26	36	39
	Correct H (%)	**95**	**98**	**100**	**93**	**100**	**98**	**100**	**100**	**100**	**100**
	Correct D (%)	62	100	100	100	100	0	0	33	8	0

Table 4.5: Percent of correct classification of Healthy and Damaged observations for the SSP34m-WTB. In bold and highlighted in grey the percentages greater than 90% for **Healthy** and Damaged observations respectively. Threshold at risk of false alarm probability equal to $\alpha = 0.01$. The FV dimension is 4 (T_1-T_2-T_3-T_4). n.MH: Number of Healthy misclassified, n.MD: Number of Damaged misclassified. Total Healthy observations = 42, Total Damaged observations = 39.

4.6 Discussion

In this Chapter the damage assessment of two wind turbine blades was presented. For both blades, the only damage studied was the debonding between the suction and pressure shells. This section discusses the main results and findings for both analysis.

The first analysis was implemented in a lab-scale blade where different damage locations and severities were analysed. Generally damage location D1 and D2 were reasonably well detected. D-Small severity was hardly detected for the majority of the sensors and only the ones which were located close to the damage location were actually able to detect the presence of damage. For the location D1, sensors on the leading edge but close to the tip of the blade were also able to detect this damage severity. These sensors were located opposite to the damage location (trailing edge) but in the same area of the damage. The severity D-Medium was detected for almost all sensors when the damage was located on the tip of the blade (D1). For damage location D2, only sensors after the damage in the direction to the tip were able to detect it. However, for damage severity D-Large, the majority of the sensors were able to detect the damage for both location D1 and D2. The damage located in D3 was hardly detected by the majority of the sensors. The location of damage D3 affects locally to the stiffness of the blade and hence only sensors very close to the damage were able to detect all damage severities at this location. For all damage locations, sensors close to the damage were able to successfully track the progression of the damage by an increment of the damage indices when the damage was incremented. In this analysis can be observed that the location of the sensors affects on the damage detection. This was more significant for small damage sizes. As alluded above, low frequency excitations give spatial wavelengths which are far larger than the extent of the damage and hence they can miss the damage. It can be also observed that when sensors were close to the damage, the damage index magnitudes corresponding to these sensors were larger than the other sensors. This finding aligns with [134] where the damage location was related to the magnitude of the damage index. Although, this effect could be used as a damage location indicator, there is not enough evidence that this will occur for all the cases. In the same way that this damage index is not always a good indication of the damage progression because the features extracted do not follow a monotonic function (see section 2.4.1), it could also happen with this delamination location indicator.

The second analysis was implemented in a SSP34m wind turbine blade. For this case, a 120 cm damage in the trailing edge was assessed for different actuation locations. Also, the damage detection was separately evaluated for each sensor allocated along the blade. The damage was detected for the majority of the sensors located in the trailing edge with a relatively low level of false alarms. Only when the actuation was applied on the location A3, the number of false alarms incremented. As explained above, for this actuation location, the majority of the sensors described a similar phenomena for some damage indices obtained on the healthy blade responses. It could be observed a sharp peak of values that went up and down for the same observations. This maybe a symbol of outliers because it was repeated in several sensors when the blade was excited at this location (see Figures 4.10(c) and 4.10(g)). The correct detection of damage in sensors located along the leading edge were hardly achieved for actuation locations A3 and A4. Similarly as in the actuation location A3, the same outliers phenomenon was observed. For the actuation location A4 only the sensors located after the damage in the direction to the tip were able to detect the damage. However, when the actuation was applied on location A1 and A2, the damage detection was improved for most of the sensors (for actuator A2) and for actuation location A1 was less significant. This analysis demonstrates that the location of the sensors plays an important role in the damage detection performance.

Sensors along the trailing edge detect better the damage for all actuation locations than sensors located along the leading edge. The detection was better achieved when the actuation was implemented in the location A1 and A2 for sensors in the leading edge. Sensors in the leading edge are far away from the damage and it affects in the detection. Also when the blade was excited by A3 and A4, the excitation on the blade had less amplitude of vibration and then not all the blade was excited equally. It seems that actuations closer to the tip of the blade excite better the entire structure, and hence it eases the damage detection for the majority of the sensors in the trailing and leading edge. However, for a practical industrialisation, the location of the actuator is better to be located around at 1/3 of the root end. As observed for excitations at these actuator location (A3 and A4), the sensors located in the same edge of the damage gave better detection performance. Also it is important to mention that when the actuator was located very close to the damage, it may affect the damage detection. As shown in Table 4.5, when the actuation was applied on the location A1, the sensors 5 and 6 that were very close to the damage, did not give a good classification rate. However, these sensors detected the damage by 100% classification rate when the actuation was applied on any other location.

4.7 Chapter summary

In this Chapter the damage assessment methodology was performed on wind turbine blades with an artificial damage introduced locally along the leading and trailing edges. The effect of different damage locations and sizes as well as its progression was evaluated in a lab-scale blade. Similarly, the capabilities for damage detection was also applied on a SSP34m wind turbine blade where damage was introduced in the trailing edge. The proposed methodology was performed by an unsupervised active system, which means that only data from the healthy blade was considered to create the reference state and the wind turbine blade was excited by an active actuator located on the blade. The methodology was applied on one sensor each time, and the percentage of correct classification for healthy and damaged observations was evaluated. The inspection phase relies on the statical distribution of the damage indices obtained by the methodology from vibration responses measured on the healthy blade. Based on this premise, a damage classifier was constructed using the probability distribution of the considered training data set.

In the first part of the Chapter, the damage assessment methodology was applied on a lab-scale wind turbine blade. The damage location and size was studied. As observed, the location of the accelerometer plays an important role in the damage detection. When the damage was small, only the sensors close to the damage were albe to detect it. However, large damages affect more globally in the vibration response and therefore, they were better detected for the majority of the sensors. On the other hand, when the damage was located in a region that affects locally to the vibration response of the whole blade, only sensors very close to the damage were sensitive to damage (e.g. damage location D3). The progression of the damage was achieved on most of the sensors for damage locations D1 and D2 but the best performance was achieved for sensors located close to the damage. Again, for damages with a high local effect, only sensors close to damage were able to track the progression. A relation between the magnitude of the damage indices and sensor locations was observed for damage location. The results showed that sensors closer to the damage gave greater damage indices.

The second part of the Chapter was to study the effect of the actuation locations in relation with the damage detection on a large-scale wind turbine blade SSP34m. The results showed that the actuation location affects on the damage detection performance obtained by the distributed sensors. When the actuator was located closer to the blade tip, the damage detection was generally achieved for all sensors. However, when the actuator was located closer to the root end, only sensors located along the trailing edge (where the damage was introduced) were sensitive to damage. For this actuation location, the damage was not perfectly detected by sensors located on the leading edge (opposite to damage location). An excessive closeness of the actuator to the sensors located on the damage, it may affect on the damage detection. Therefore, the results obtained in this analysis demonstrate that the location of sensors can affect on the damage assessment. Sensors on the trailing edge detect better the damage than sensors on the leading edge.

Chapter 5

A study on vibration-based self-sensing and self-diagnosis capabilities of nano-enriched composite laminates

5.1 Chapter overview

This Chapter presents an exploratory study on the self-sensing capabilities of nano-enriched glass/fibre laminates for damage detection purposes through changes in the dynamic responses, which are estimated by measuring the changes in voltage due to a dynamic strain. The data-based vibration methodology explained in Chapter 2 is applied to the estimated vibratory signals using the conductivity properties of the embedded nano-particles for damage detection. The structure considered in this study is a glass/fibre laminated beam enriched with carbon black nanoparticles (CB). The structure is subjected to a direct electric current and the voltage signal is measured. Consequently, the damage index estimated from the vibratory signals measured on a beam with simulated damage are compared to the healthy state for damage detection procedure. The damage was simulated firstly by adding an additional mass on the beam tip and secondly by drilling a hole on the beam tip.

5.2 Concept of a self-sensing structure

The main goal of this study was to investigates a dynamically self-sensing and self-diagnosing structure which is capable of measuring its vibrations and use them to diagnose its structural integrity. This was achieved by using conductive nano-inclusions and applying vibration-based monitoring and health assessment methods. The idea of self-diagnosing structures opens the road towards autonomous structures capable to not only self-diagnose their condition but eventually even to take some repair steps [135]. This is applicable for a wide variety of structures including aerospace, mechanical and civil engineering ones like e.g. aircraft, turbine blades, buildings and bridges. In this study the idea of using nano-inclusions as sensors is based on the piezoresistive property of some materials. They relate the conductivity to the strain of the structure and hence its vibration. This research suggests employing piezoresistive nano-inclusions for measuring and assessment of the structural vibrations and using them to estimate the structural health. The rationale for using vibration-based structural health monitoring is two-fold: 1) there is a vast amount of research and more than 30 years experience in VSHM and 2) most structures are naturally subjected to some kind of vibrations which can come from the work of an engine or motor, or from traffic and wind.

The concept is based on a no-intervention principle, coupled with new, integrated within the structure sensing technology. It proposes a unified approach comprising 1) a new self-sensing and self-diagnosing paradigm, coupled with 2) a VSHM for detecting anomalies over both short term (damage) and long term (fatigue or wear) scales. A VSHM approach is suggested, which deals with the extraction and handling of appropriate information obtained from the measured voltage signals and with the derivation of damage detection and assessment methods.

5.3 Material and laminates specifications

A glass fibre/epoxy laminated beam was manufactured by hand lay-up and reinforced using stitched unidirectional E-glass with 225 g/m^2 area weight (see [103] for further information in the manufacturing process). Epon 8132 epoxy resin with bisphenol-A-based epoxide diluted with alkyl glycidyl ether and JEFFAMINTE T-403 polyetheramine curing agent compounds as the matrix material. The mix ratio of the epoxide to curing agent was 100 : 40 by weight. Due to their high structure clusters concentration, Cabot Black Pearls 2000 CB were chosen as nanofillers. The CB nano-particles with high structure clusters have an elongated shape which facilitates the formation of percolate electrical networks at low filler volume fractions [136]. The CB nano-particles were uniformly dispersed in epoxide by a magnetic stirrer and a sonication bath. The CB mixture was firstly magnetically stirred in epoxide for 15 minutes at 250 rpm and secondly was mixed for 4 hours in an ultrasonic bath operating at 45 kHz and 55 W average power. Finally the mixture was stirred for an additional 15 minutes at 250 rpm. BYK A-501 air release and curing agent were subsequently added to the mixture and stirred by hand during 5 minutes. Eventually the mixture was degassed for another 30 minutes. The concentration of CB in epoxide/curing agent mixture was 0.5 $wt\%$. A total of 26 layers were used to produce 4 mm thickness of the beam. Each layer was impregnated with the CB-epoxide using a hand roller (see Figure 5.1). The staking sequence of the laminates is $[[0/90]_6/0]_s$. For the curing process the lay-up laminates were placed over aluminium foil electrodes (top and bottom) in order to apply an alternating current (AC) field to the laminate while the matrix was uncured. This field polarizes and links the highly conductive of CB nano-particles through the thickness direction via dielectrophoresis [137]. As a results of the polarization the laminates were nearly electrically isotropic in the three directions. Although within an individual laminate layer, the conductivity can be several orders of magnitude higher along the fiber direction than perpendicular to the fibers, the equal numbers of layers at 0° and 90° approximate an isotropic in-plane conductivity. The field parameters were defined as 1000 V/cm and 1 kHz based on [137]. The AC electric field was applied during the curing process. The parameters of the curing recipe were selected as follows: 30 minutes at 65°C, 2 hours at 80°C and 3 hours at 125°C. Once the laminates were cured, the edges were cut and sanded in order to guarantee the exposure of the CB mixture. The final dimensions of the beams were 120 x 12 x 4 mm.

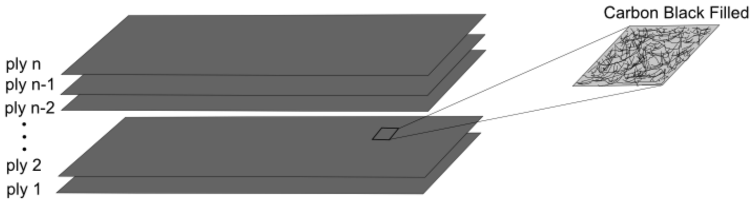

Figure 5.1: Cabot Black Pearls 2000 CB particles are impregnated in each glass laminate by a hand roller.

5.4 Electrical conductivity and piezoresistivity of a carbon nano-enriched laminated beam

High structure CB nano-particles embedded between the laminates generate elongated clusters which facilitate the electrical conductivity [138]. Once the CB-nanoparticles are connected, the electrical conductivity occurs due to the mechanical contact between the conductive particles. However, when there is no mechanical contact the electrical connection is realised by the tunneling effect. Tunneling effect theory explains that electrical current can flow through a non-conductive material such as an insulator or through an air gap when the conductive components are close enough [139, 140]. The tunneling effect is generally modelled as a resistor connecting a pair of conductive inclusions where the electrons can pass from one inclusion cluster structure to the closest one as shown in Figure 5.2. The distance between the two inclusion clusters plays an important role in the electrical conductivity. Some studies consider a tunneling distance threshold which determines a limit for this effect to occur. In [139] can be seen that the tunneling effect decreases drastically when the tunneling distance increases.

Another aspect that must be considered regarding the electrical conductivity is the volume fraction of conductive particles. Nano-enriched materials can be divided into three types depending on their electrical conductivity. The first type is when the electrical conductivity is very low since the volume fraction of conductive particles is small. However, when high structure clusters are formed, the electrical conductivity increases thanks to the tunneling effect explained above but it does not have a fully connected electrical path. The second type contains a higher volume fraction of conductive particles and then a fully connected electrical path exists. And finally, the third type contains a very high volume fraction of conductive particles which increases the number of electrical paths and eventually the material behaves as a conductor (metal) [107].

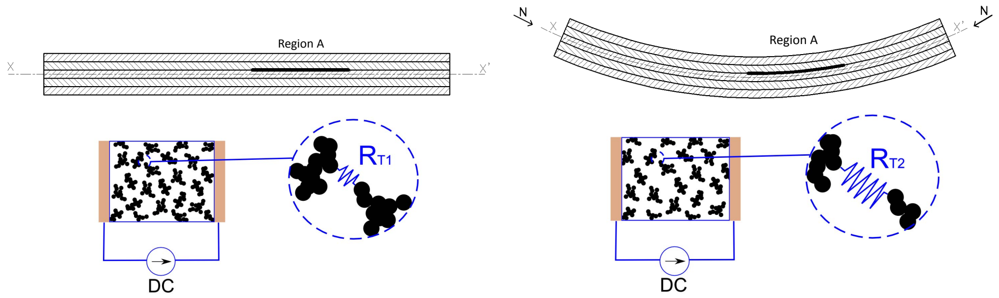

(a) (b)

Figure 5.2: Tunneling effect is modelled by electrical resistance between CB conductive clusters. Under deformation the CB clusters increase the distance and hence the electrical resistance changes which alters the electrical paths. (a) Shows an initial configuration of CB clusters without any deformation and (b) presents changes on the CB clusters under a certain deformation.

The electrical conductivity can be explained and understood based on the percolation phenomenon [141]. A material can be conductive due to the formation of percolate electrical networks when it possesses isolated clusters of particles and the electric current is due to the tunnelling effect. The piezoresistivity is defined as the change of the electrical resistance caused by the change in the mechanical strain of the specimen. Then, the piezoresitivity can be measured by the change in the electrical resistance. The effect of the piezoresistivity has been studied under tensile strains [108], under compressive strains [106] and under vibratory excitation [102]. The piezoresistive properties in the nanoparticles can be attributed to two kinds of mechanism which are able to introduce changes in the electrical resistance: 1) the loss of contact between the clusters of nanoparticles, which can introduce considerable variation in the electrical conductivity and 2) the above mentioned tunneling effect which affects in the tunneling resistance due to the changes in the distances between the conductive particle clusters (see Figure 5.2). These two mechanisms affect the electrical conductivity, and hence it alters the resistance which is measured in order to estimate the dynamic response.

Then, consider a constant direct current (DC) through the material which follows an electrical path through the conductive particles along the specimen/beam. This electrical current provides a certain value of voltage which is proportional to the resistance defined by the electrical path chosen. Applying a mechanical load to the beam causes deformation and then because of the strain, the distances between the clusters of the conductive particles increase and therefore this introduces changes in the tunneling resistance between the clusters. The increment of this distance increases the tunneling resistance gradually. Therefore, the loss of contact or the changes of the tunneling resistance breaks the conductivity paths and forces the electrical current to choose an alternative path with smaller tunneling resistance. This phenomena occurs under small strains [142]. Additionally, it is important to mention that to obtain good piezoresistivity, it is better to include low fraction of conductive particles rather than high fraction as the probability to obtain tunneling effects is higher and hence more significant changes in the global resistance are measured [143].

Once a dynamic excitation is applied, it causes strain variations and the initial distribution of the nanoparticles along the specimen is altered. This alters the tunneling resistance and the electrical current path changes following the minimum resistance path. This behaviour provides variations in the global voltage measured between both ends of the beam (see section 5.3). The variations in the voltage are measured and recorded during the time of the dynamic excitation to obtain an estimate of the dynamic signal. In other words, the voltage measured through the conductivity of the CB-nanoparticles is used to estimate the dynamic signal. To verify this behaviour the following experiment was done. First, a constant DC was introduced through the beam and the voltage was then measured without any dynamic excitation. Secondly, the same beam was excited harmonically at 30Hz by a shaker. For both cases the boundary conditions were kept constant by clamping one end of the beam in a cantilever configuration. More information about the test rig is given in section 5.5. The two recorded signals were represented in the same Figure 5.3 and it can be observed that the 30Hz harmonic due to the dynamic excitation can be clearly detected by the sharp peak at this frequency which did not appear for the case of no vibration.

As shown in Figure 5.3 the vibratory response can be measured through the voltage measurements of the CB filler. The voltage vibratory response characterises the health/damage state of the beam and any alteration due to damage or additional mass can be detected through it. Accordingly it can be concluded that the embedded nanoparticles provide self-sensing capabilities to the structure.

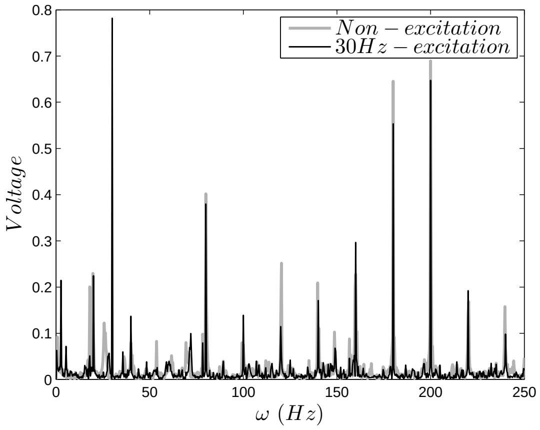

Figure 5.3: Differences on the voltage measurements between a beam without any excitation (grey line) and the same beam harmonically excited at 30Hz (black line).

5.5 Experimental verification

The following experiment was designed to verify the self-assessment properties of the considered nano-enriched laminates. The beam manufactured for this experiment, which is explained in section 5.3, was subjected to simple harmonic vibration and to constant direct electric current. The voltage was measured at both ends of the beam as shown in Figure 5.4. The measured voltage signals were used as inputs to the damage assessment procedure explained in section 2.2.1. Firstly for the study and comparison of the effect of the damage in the reference state and secondly for the damage assessment stage detailed in section 2.2.4. The results are presented and discussed in section 5.6.

5.5.1 Experiment test rig

The experiment rig to measure the voltage dynamic signals of the nano-enriched beam is shown in Figure 5.4. A constant electrical Direct Current was generated by Keithley 2140 Source-Meter and the voltage was measured with National Instruments 90253-Channel, 200 mV to ±10 V, 16-Bit Analog Input Module data acquisition (DAQ) card. Because of the high resistivity of the beam, a voltage buffer was constructed from OP-AMP TL07 to control the current leakage, and hence to protect the overload of the DAQ. The vibration excitation was performed by a shaker and controlled by Laser vibrometer Polytec OFV-5000 and PCB accelerometer in order to apply exactly the same vibration excitation for all measurements. The manufactured beam detailed in section 5.3 was clamped in one end with a free span of 100 mm. The clamp-support was perfectly connected to the excitation base of the shaker. This structure configuration guarantees the transmission of the vibration excitation to the composite laminated beam. Two electrodes were placed at both ends of the beam to guarantee a constant current along the entire beam and to allow voltage measurements through the material. Electrodes were prepared by first sanding the material in both edges. Secondly, a high conductive silver epoxy was applied on the edge surface and a copper tape on the top of the silver paint to design a permanent electrode as shown in Figure 5.5. Electrodes were manufactured carefully to reduce the additional effects on the measurements.

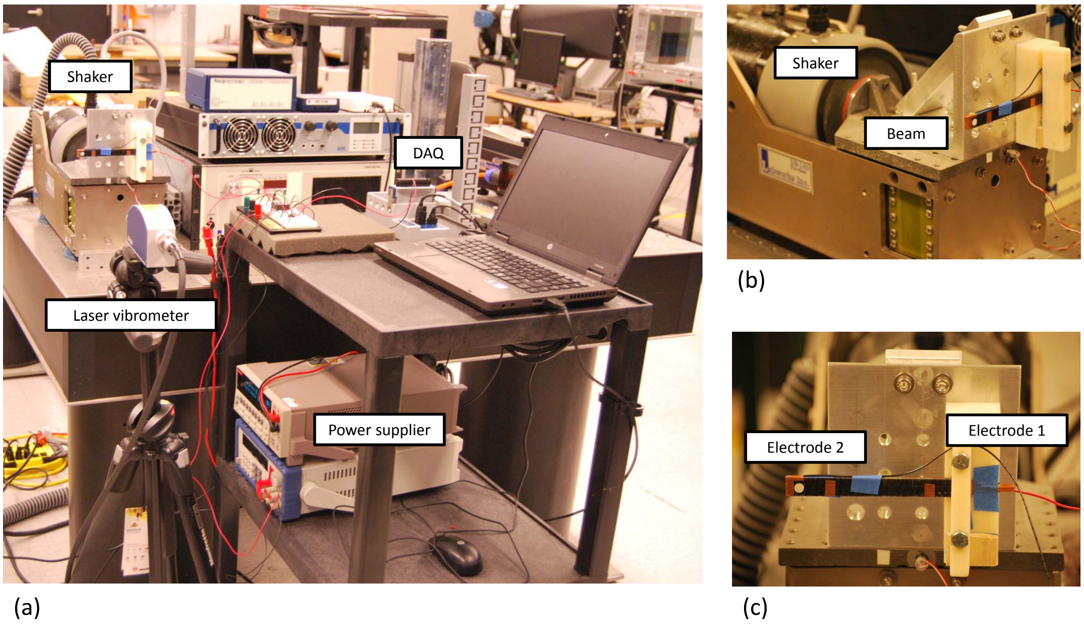

Figure 5.4: Test Rig. a) General picture of the test rig, b) how the beam is clamped on the shaker and c) the location of the two electrodes on the beam.

5.5.2 Experiment procedure

A constant DC current, lower than the limit imposed by the DAQ card, was applied on the beam (see Figure 5.5). Once a constant voltage can be measured through the beam, a simple harmonic excitation at 30 Hz by the shaker was applied. Vibration signals were estimated by measuring the voltage through the two electrodes. The amplitude/acceleration of the source excitation was controlled and configured to be constant for all the measurements in order to provide the same vibration excitation for each beam scenario (healthy and damaged). Damage was introduced in two different manners: 1) Damage introduced by adding an additional mass on the tip of the beam and 2) Damage introduced by drilling a hole in the tip of the beam. For each damage configuration two damage scenarios were introduced 1) by adding two different masses (5% and 10% of the total mass of the beam, respectively) and 2) by introducing two hole diameters (2 mm and 4 mm, respectively). Damage was introduced in the locations shown on Figure 5.6. Damage was introduced without removing the beam from the test rig and hence the boundary conditions remained constant during the whole experiment. The idea was to avoid any influence of the support changes. For each beam scenario, 20 measurements were taken for 4s and sampled at 500 Hz. A 60 Hz bandstop filter was applied on the recorded signals to remove the presence of the Hum frequency. All the experiments were performed at room temperature.

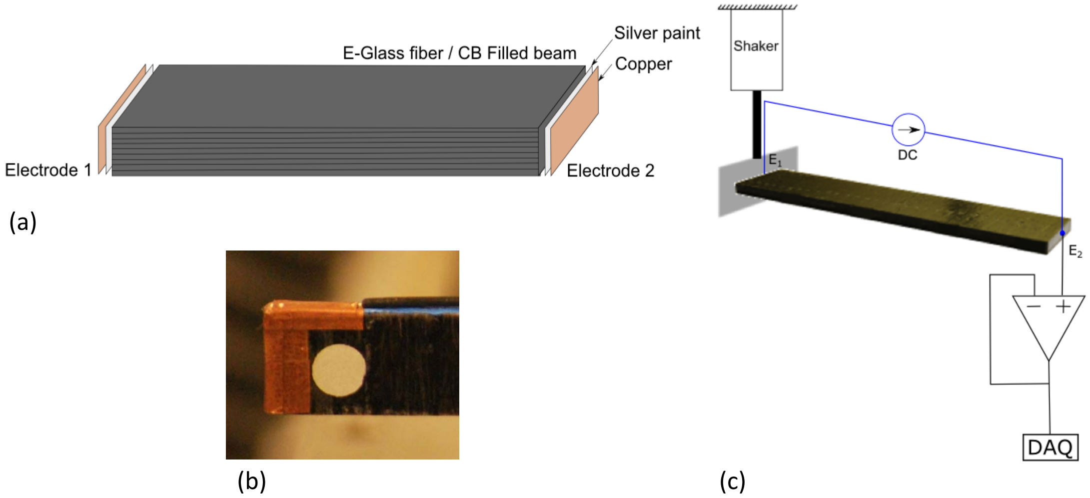

(a)

(b)

(c)

Figure 5.5: Electrode and measurement system. a) Silver epoxy material and copper tape were used to build the electrodes, b) final picture of an electrode and c) schematic picture of the measurements test rig.

5.6 Self-sensing damage assessment

First, the estimated vibratory responses from all beam categories described in Figure 5.6 were processed separately to obtain a reference state for each beam category (healthy and damaged beams) as described in section 2.2.2. The reference state of each beam

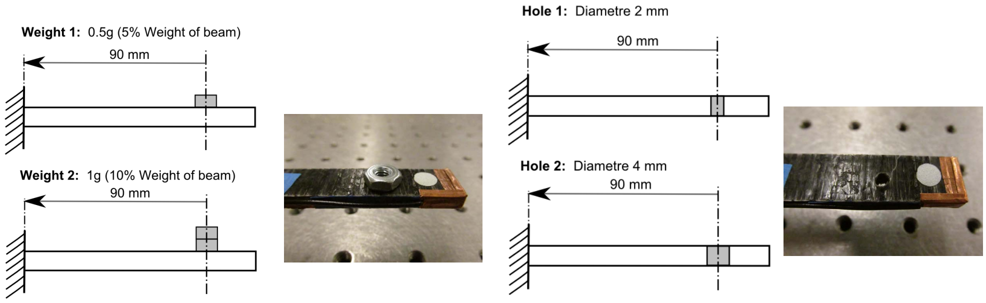

(a) (b)

Figure 5.6: Description of the different damages introduced in the beam. a) Damage introduced by adding an additional mass and b) damage introduced by drilling a hole in the tip of the beam.

scenario was compared to see the effect of damage in the voltages signals. Secondly, the entire vibration-based damage assessment procedure detailed in section 2.2 was applied on the estimated vibratory signals of the healthy beam to create a reference state. Then, the observation damage indices were compared to the baseline space for damage assessment as described in section 2.2.4.

5.6.1 Decomposition of the signal in reconstructed components

The vibratory responses estimated by measuring the voltage in the nano-enriched beam were processed by the method detailed in section 2.2.2 in order to obtain a reference state and discuss the effect of the damage by comparing all categories. For the purposes of comparison, all signals recorded from different categories, healthy (no mass and no hole introduced) and damaged beams (with one or two masses added and with a small or a big hole), were processed by the same method. The parameters selected for this analysis were $M = 5$ realisation signal vectors for each beam scenario and sliding window size $W = 10$. The selection of the sliding window size parameter is based on the study developed in section 2.5.2. Generally the selection of small values for W and relatively close to M gives well defined clusters. Figure 5.7 represents the reconstructed signals by using only the first RC compared with the raw signal for all beam configurations, healthy and the two different damages scenarios. In both cases the noise is significantly reduced and only the predominant frequencies of vibration are contained in the first RC. The 30 Hz frequency of vibration introduced by the shaker excitation is present in the signals for both damage scenarios (with an added mass and with a hole drilled). This finding is also coherent with the results obtained by Loh et al., who observed the effect of constant sinusoidal frequency of 20 Hz by a shaker in the vibration response obtained by a CNT based thin film strain sensors [144].

The frequency spectrum of the beam with added mass and the one with hole drilled are compared in Figure 5.8. It can be observed that for the case of the beam damaged by a hole, higher peaks appear at higher frequencies as compared to the peaks of the beam with mass added. However, in both cases the 30 Hz frequency is present in the reconstructed signals as shown in Figures 5.8(a) and 5.8(b). The peaks at higher frequencies between 180 and 200 Hz are due to the electrical conductivity and peaks appear because of the harmonics of the hum frequency. This is very well depicted in the frequency spectrum of signals from the beam with a hole drilled (see Figure 5.8(b)) because in this case not only the beam is damaged but also the CB-nanocomposites embedded through the laminates. The hole reduces the electrical conductivity paths and as a result the correspondence/relation between the dynamic and the voltage signals is also reduced. This finding is coherent with the results obtained in [103] where a hole-drilled in a CB-nanoparticle enriched laminated was detected by changes in the voltage measured in the edge electrodes within the specimen domain.

Figures 5.9(a) and 5.9(b) present the phase maps[1] which can be estimated by plotting the first two RCs from the voltage signal decomposition [115]. Each plot contains three signals: one from the healthy beam and the other two corresponding to the different damage scenarios. Time series were presented in the 2-dimensional space reconstructed from the first two reconstructed components, RC_1 and RC_2. Figure 5.9 shows that the areas covered by the first two RCs for the different damage scenarios are well distinguishable. The one for the healthy voltage signal is shifted with regards to the damaged ones and the two damaged signals are also shifted with respect to each other. As it is shown in [102], changes in amplitude were found in the vibration response obtained by carbon nanotube strain sensor when the responses were measured in cantilever beam with and without a crack induced. This is also coherent with the

---

[1] An example of the analysis of the phase maps constructed by the reconstructed components was developed by Garcia et al. in [110] to study the dynamical system analysis of unstable flow phenomena in a centrifugal blower. In this study, phase maps were constructed by the pressure signals gathered at different points close to the surge onset. Projection of the original signal onto its PCs allowed to draw the phase trajectory plots based on the reconstructed components that clearly separated non-stable blower working conditions from its regular operation.

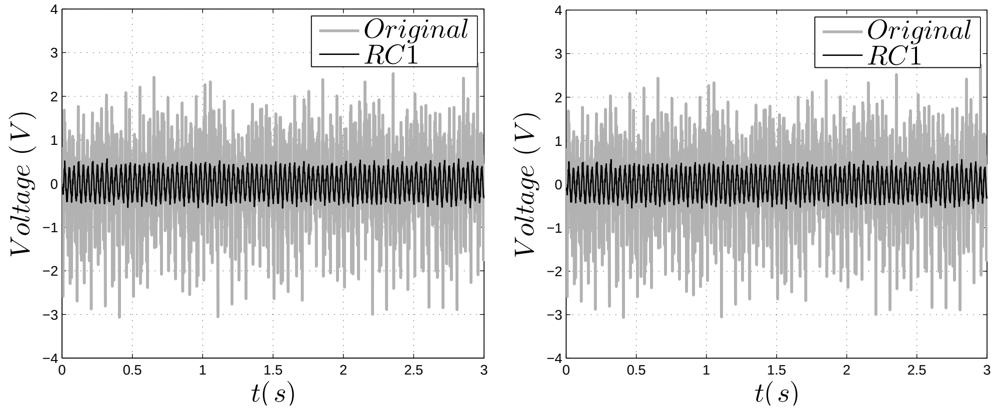

(a) No mass added (b) No hole drilled

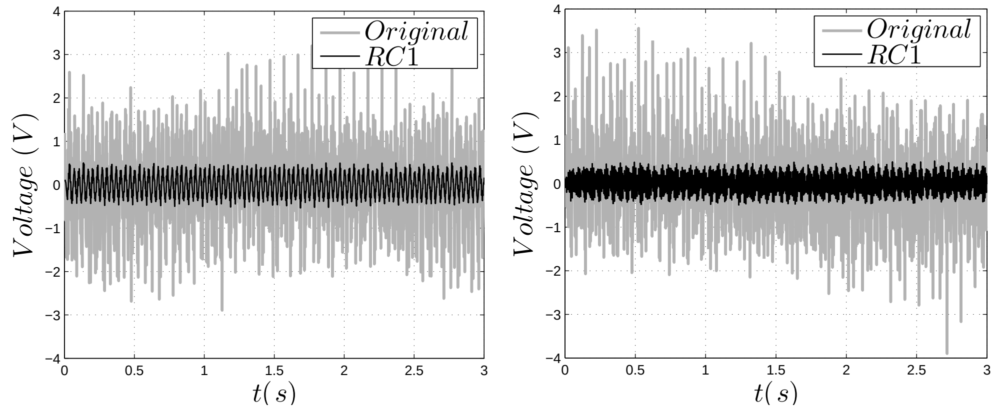

(c) 0.5g mass added (d) 2mm hole drilled

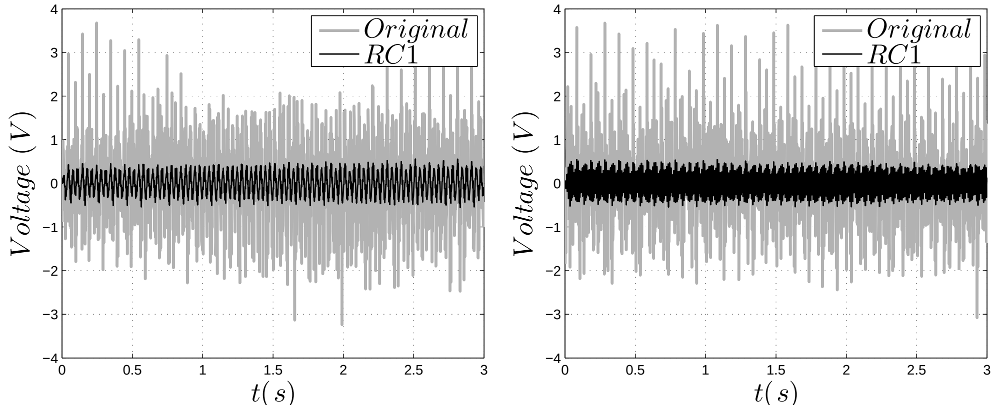

(e) 1g mass added (f) 4mm hole drilled

Figure 5.7: Comparison between the original raw voltage signal and the reconstructed signal by one RC for healthy and artificially damaged beams.

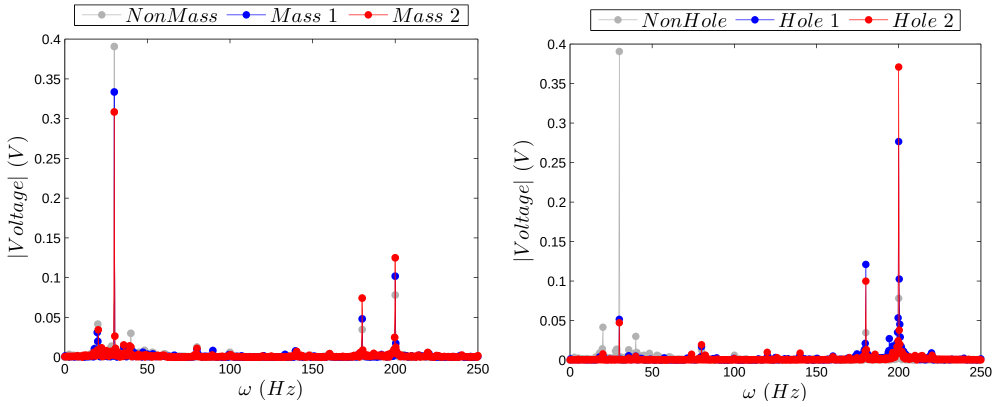

(a) (b)

Figure 5.8: Comparison of the frequency spectrum of the first reconstructed component for a) the case of the beam with damage introduced by adding a mass and b) the case of the beam with damage introduced by drilling a hole.

results, where the voltage signal measurements can provide indication for the presence of damage and they can be used to distinguish between the healthy and the two damage scenarios. Changes in the areas corresponding to the beam with a hole are less observable as compared to the changes for the added mass. This can be explained again by the damaged conductivity paths which affect the relation between the dynamic and the voltage signal (see Figure 5.9(b)).

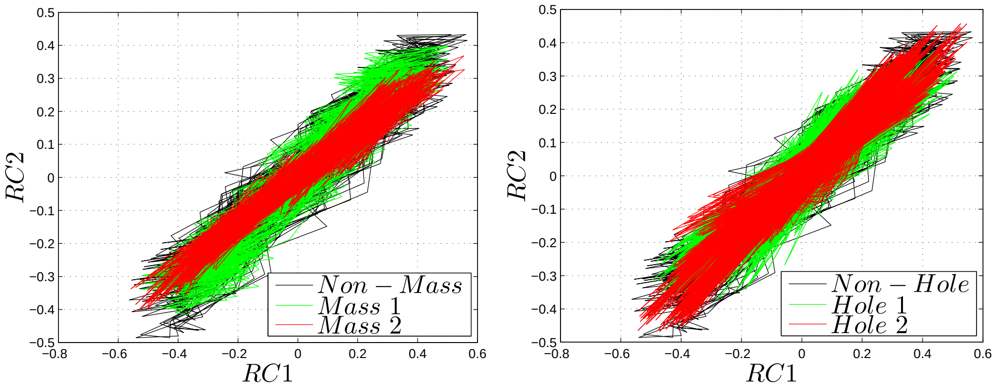

(a) (b)

Figure 5.9: Comparison of the phase portraits of the time series using RC_1 and RC_2 for the case of a) the beam with damage introduced by adding a mass and b) the beam with damage introduced by drilling a hole.

5.6.2 Damage assessment on the nano-enriched composite laminated beams

As presented in section 5.6.1, the signals obtained from the voltage measurements between the two electrodes on the beam can provide indication for the presence of damage and hence be used for damage assessment. Therefore, the voltage signals were processed by the entire methodology as described in section 2.2. The same procedure has been applied for the case of the beam with mass added and the beam with a hole drilled. The sliding window size was considered at $W = 10$ and the number of vector signal realisations to build the reference state was $M = 5$ from the healthy beam.

For visualisation purposes, the projection of the observation FVs onto a two dimensional feature space generates different clusters based on the similarity between the observation FVs. The FVs obtained from the same category reduce their distances between themselves when are projected onto the feature space while they increase their distances to FVs from other categories. These clusters can be observed in Figures 5.10(a) and 5.11(a) for the beam with damage introduced by adding a mass on the tip and for the beam with a damage introduced by drilling a hole in the tip, respectively. Then, a baseline space was built based on the FVs of the healthy beam (without any mass or hole introduced) where each observation FV can be compared with dimension $s = 10$ and $p = 2$. The distance of each observation FV to the baseline set was measured as shown in Equation 2.18. For this analysis a simple threshold line was calculated based on the distances of FVs utilised to build the baseline respect to the baseline itself. For this case, the damage indices obtained on the observations from the healthy beam were assumed normally distributed. The threshold was set up to be the mean value plus one standard deviation of the observations considered as a baseline ($s = 10$). Therefore, the distances from new observation FVs were compared to this threshold for damage assessment. A damage index below the threshold was considered as a FV obtained from the healthy beam while a damage index over the threshold was considered as a FV obtained from a damaged beam. Figures 5.10(b) and 5.11(b) show clearly that the damage indices obtained from damaged beams increased their distances with respect to the baseline threshold and hence the points were placed over the threshold dashed line. On the other hand, FVs from healthy beam observations

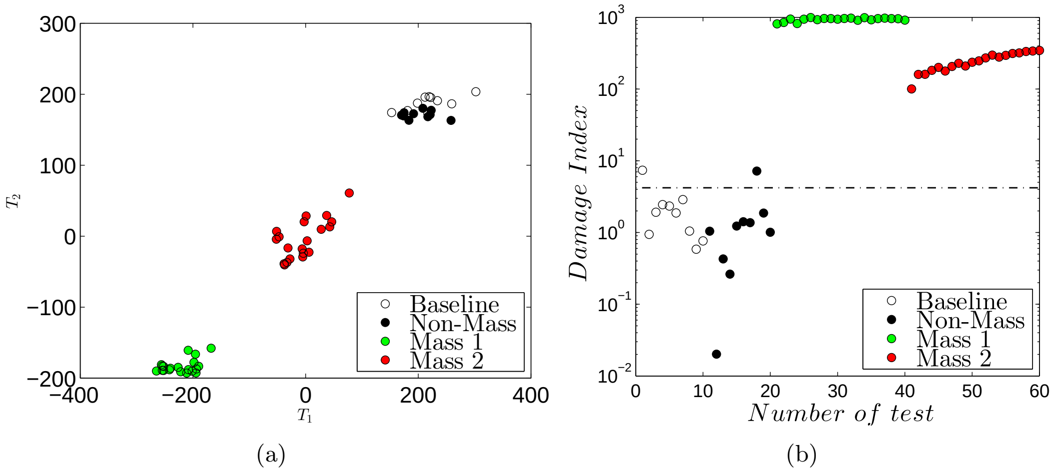

Figure 5.10: For the case of beam with damage introduced by adding a mass a) clusters obtained in a 2-dimensional feature space and b) Mahalanobis distances of the different damages scenarios to the healthy scenario.

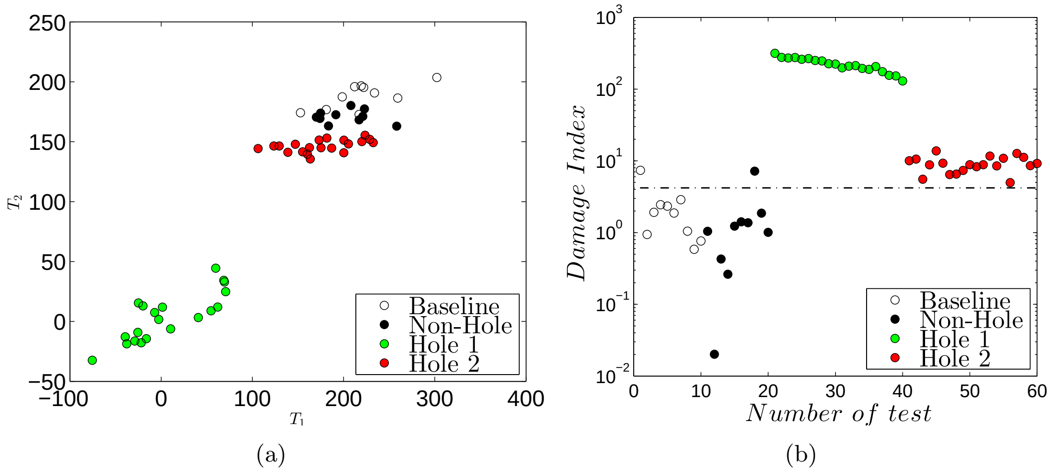

Figure 5.11: For the case of beam with damage introduced by drilling a hole a) clusters obtained in a 2-dimensional feature space and b) Mahalanobis distances of the the different damages scenarios to the healthy scenario.

had distances that were smaller than the threshold and hence they were considered as observations from the healthy beam. It is also important to mention, that the severity of the damage cannot be monitored because the damage indices did not increase when the severity of the damage was incremented. This behaviour occurred for both damage scenarios having the same trend for the beam with mass added and for the beam with a hole drilled. However, damage was successfully detected for the both damage scenarios because all the distances measured from observation FVs of damaged beams were greater than the threshold. Then, the damage was successfully detected for both cases but the damage index used cannot be used to infer severity from the measured features.

As mentioned above in section 5.6.1 the sensitivity for damage detection in the case of the beam with a hole drilled was smaller than for the case of mass added. This was observed because the distances were smaller in comparison with the case of mass added. However, for both damage sizes the detection was successfully achieved.

5.7 Chapter summary

This study explores the self-sensing capabilities of a beam manufactured with CB nano-particles embedded between the glass/fibre laminates. The voltage was measured through the beam due to the electrical conductivity capabilities of the CB nano-particles. The dynamic strain introduced in the beam changes the CB nano-particles clusters and hence changes in the electrical resistance were introduced. Voltage signals were measured to construct estimated vibratory responses.

A data-based VSHM methodology was utilised for features extraction by the decomposition of the measured voltage signals of the healthy beam into a number of reconstructed components. The new reconstructed signal vectors were used to create a reference state where new observation vectors were compared for the purposes of self-damage assessment. This analysis has been performed for two different beam categories. Firstly, the damage has been introduced by adding one and two masses (5% and 10% of the total mass of the beam) and secondly by drilling two different hole sizes (2 mm and 4 mm respectively) near the tip of the beam. The damage detection was successfully achieved for both cases.

Therefore in this analysis it can be observed that 1) vibratory signals can be estimated by measuring changes in voltage due to the electromechanical properties of the CB nano-particles embedded in a glass/fibre laminated beam. 2) The voltage signal measurements can provide indication for the presence of damage and they can be used to distinguish between the two damage scenarios. 3) The voltage signal responses were processed by the data-based VSHM methodology which was able to extract features qualifying the state/health of the beam, which eventually results in the self-damage assessment.

Based on the results, one can say that conductive nano-enriched composite laminates have substantial potential for self-sensing capabilities. The results open a new path of investigation towards vibration self-sensing structural health monitoring with nanocomposite inclusions. Further work must be done in the configuration and distribution of the nanocomposites for reducing the high resistivity of the material, as well as the development of novel methodologies to obtain the most from the measurements.

Chapter 6

Conclusions and Future Work

This thesis has focused on the development of a data-based vibration structural health monitoring methodology for extracting sensitive features to delamination/damage in structures made of composite materials. The methodology is based on singular spectrum analysis which is an extension of principal component analysis for non-independent variables such as the vibration response of a structure. This methodology takes into consideration the inter-correlations between the variables contained in an individual signal vector. This is beneficial because it uncovers all the rotational patterns at any frequency of a measured vibration response which is appropriate for nonlinearly vibrating structures that exhibit double or very close modes of vibration. Based on the reconstructed components obtained by the methodology, sensitive feature vectors were obtained to develop an VSHM system which gives information about the presence, the location and the extent of the delamination and/or other defects in composite structures. The methodology has been initially implemented in composite materials but also in other research collaborations for condition monitoring of turbocompressors [110]. In this sense, the proposed approach is applicable in a wider context for damage assessment and condition monitoring systems.

6.1 Conclusions

The major conclusions of this work with respect to the objective of this thesis are presented below.

Chapter 2 introduces the basics, the demonstration, validation, and principal considerations of the methodology parameters. The main conclusions are detailed below:

- The damage assessment methodology is based on the constructed *reference state* to determine how meaningful and informative are the feature vectors for the damage assessment. Although the construction of the reference state in the time and frequency domain follows the same steps within the methodology, their interpretation was slightly different. The construction of the reference state in the time domain representation provides separate and interpretable oscillatory components. Therefore, the information contained in the FVs will depend on the oscillatory components contained in the RCs considered in the reconstruction. On the other hand, when the reference state was created based on the frequency domain representation, the first RC contains most of the variance in the decomposition. The first RC describes the general trend of the original spectral line of the frequency spectrum. The reconstructed spectrum with only the first RC gives more importance at the frequencies bands where the maximum energy is concentrated by means of the amplitude/peaks at each frequency. This can be considered as kind of an envelope of the spectral line. The rest of the RCs represents the fluctuations along the spectral line and they will contribute to the approximation to the original spectral line. As the reconstructed response describes the general trend of the spectral line, all the rotational patterns are considered with only the first RCs. In both cases, the decomposition of the vibration responses in RCs will depend on the complexity of the vibration response and on the dimension of the sliding window size.
- The *performance of the methodology*[1] was demonstrated and validated in two cases of study 1) in a 2-DOF system with nonlinear coupling and 2) in an experiment with delaminated composite beams. The first case demonstrates the performance when damage was simulated by reducing the different stiffness parameters of the system. The methodology was able to detect variations in linear and nonlinear stiffness parameters within the range of study $1-30\%$ stiffness

---

[1] The introduction and performance of the data-based vibration structural health monitoring methodology was presented in Garcia et al. [80].

parameter reduction. The damage was not only detected but the increment of the stiffness reduction was also monitored. The methodology was able to create well-defined clusters for each stiffness reduction, even when the effect of the non-linearities was highly presented. The severity of the stiffness reduction does not always affect systematically in the spectral lines of the frequency spectrum and it can have an effect on the damage index for detecting the progression of the stiffness reduction. This can be explained because the feature vector selected is not sensitive to this effect and additional features must be considered. In consequence of this behaviour, the damage index to monitor the severity of the stiffness reduction does not always follow a monotonic function and it can hardly track the severity of the stiffness reduction. However, the consideration of a higher dimension in the feature vector can help to detect this behaviour and hence a monitoring of the increment of the stiffness variations. The same analysis was implemented in an experiment with five delaminated beams. For all cases, the effect of the delamination introduced anomalies in the vibration response which were able to be present in the feature vectors. The size of the delamination was also monitored by an increment of damage index when a delamination, in the same location, incremented its size. In a similar way as in the simulated system the increment of the dimension in the FVs helped to distinguish between different delamination sizes and locations. Therefore, in both cases was clear the importance of the multidimensional space which was constructed by the FVs obtained by the methodology. The relation between the damage index and the estimated reconstruction of the frequency spectrum can give a better understanding in the structural analysis of the composite beams.

- The choice of *the principal parameters*[2] of the methodology, frequency resolution, sliding window size and the number of reconstructed components was studied. The effect of these parameters on the performance of the methodology is summarized as follows. Low frequency resolution in the measured vibration response can miss relevant information that is not present in the reconstruction of the

---

[2] An introduction to the effect of the preliminary parameters on the methodology was presented in Garcia et al. [145].

frequency spectrum, and hence it does not produce very well-defined clusters which makes difficult the differentiation between categories. A fine frequency resolution provides better clusterisation between different categories which will help the damage/delamination assessment. However, an excessive frequency resolution could introduce additional information which adversely affects the clusterisation. A proper selection of the sliding window size is to choose a value which gives separable and independent principal components but at the same time contains significant information of the vibration response. The sliding window size has to respect the following limits $M \leq W$ and $W \leq N/2$. Small values of W condense the principal components with large amount of variance in the first RCs. These RCs give informative FVs for a good clusterisation using only two dimensional FVs. On the other hand, large values of W result in very well separated principal components with reduced information in the first RCs, which makes more difficult the clusterisation with a reduce dimension of the FVs. The selection of a proper sliding window size depends on the problem at hand and on the preliminary information in the vibratory response as well as the aim of the analysis to be considered. Generally, a consideration of more RCs in the reconstruction[3] (or a consideration of more variables within the FVs for the damage assessment procedure) improves the clusterisation. The consideration of a higher dimension of the FVs could give an additional information for better interpretation of the results. On the other hand, this should be analysed with care because the consideration of more dimensions within the FVs does not always contribute in the damage assessment and thus adversely affects the categorisation. As shown in the results, there is not a clear and concise solution for the selection of the parameters of the methodology. Their selection requires a preliminary study that depends on the objective of the analysis.

The problem of delamination has been analysed in *composite laminated plates*[4] as shown in Chapter 3. The study was implemented in a finite element model and in

---

[3] A preliminary study in the consideration of more RCs in the reconstruction and hence more dimension in the FVs was presented in Garcia et al. [146].

[4] The investigation of the substantial potential of the delamination assessment methodology for composite laminated plates was presented in Garcia et al. [81].

an experiment with different delaminated composite plates. The effect of the delamination produces slight changes on the natural frequencies of the composite laminate plates although the extent of the natural frequency variation increases with the order of the natural frequency. However, the error in obtaining the experimental natural frequencies is greater than the changes produced by the effect of delamination. The results demonstrate that the detection of the delamination based on changes of natural frequencies does not provide a significant information to be used as a damage feature. The effect of the delamination in the vibration response will be highlighted if a particular mode of vibration excites the delamination region, so it demonstrates the local effect of the delamination [31]. The damage assessment methodology introduced in Chapter 2 was implemented in the vibration responses measured on the composite plates. In the methodology all rotational patterns contained in the vibration response are considered. Then, all the vibration modes are considered and when the delamination is excited by any mode, its effect will be present within the spectrum. The results show that the data-based vibration methodology successfully detects delamination and also distinguishes between different delamination scenarios. An increment of the dimension of the FVs improves the results that not only detects delamination but also distinguish between observations from different delaminated composite plate scenarios.

A practical VSHM system with a statistical hypothesis threshold for the inspection phase based on probabilistic distributions was used to identify damage in *wind turbine blades*[5] as shown in Chapter 4. The methodology performs with the vibration responses measured by one sensor each time, and the percentage of correct classification for healthy and damaged observations was evaluated. The first analysis was to detect different damage locations and sizes in a lab-scale wind turbine blade. For small damage sizes, only sensors relatively close to the damage were able to detect successfully the damage. However large damages affect more globally to the vibration response of the methodology and therefore they were better detected for the majority of the sensors. However, when damage was located close to the root-end, damage was only detected by sensors very close to that region (e.g. damage location D3). This can be explained

---

[5] An introduction of the capability of the data-based methodology for detecting the debonding in the edges of a lab-scale WTB was presented in Garcia et al. [147].

because this region has a local effect in the vibration response of the entire blade. The tracking of the progression of the damage severity was achieved for most of the sensor locations when damage was located in D1 and D2 but the best performance was achieved for sensor located close to the corresponding damage. For the case of damage location D3, only the sensors close to the damage were able to track its progression. A relation of the magnitude of the damage indices and sensor locations was observed. Sensors which were close to the region of damage present higher magnitude of the damage index. Although, this effect could be used as a damage location indicator, there is not enough evidence that this will occur for all the cases. In the same way that this damage index is not always a good indicator of the damage progression as explained in Chapter 2.

A study of the location of the actuation (excitation point) and its influence in the damage detection was implemented in a SSP34m wind turbine blade. The results showed that the actuation location affects on the damage detection performance obtained by the distributed sensors. When the actuator was located closer to the blade tip, the damage detection was generally achieved for all sensors. However, when the actuator was located closer to the root end, only sensors located along the trailing edge (where the damage was introduced) were sensitive to damage. For these actuation location, the damage was not perfectly detected by sensors located on the leading edge (opposite to damage location). An excessive closeness of the actuator to the sensors located on the damage region, it may affect on the damage detection. Also, sensors along the trailing edge (where the damage was introduced) detect better the damage for all actuation locations than sensors located along the leading edge.

In both studies can be observed that the location of the sensor plays an important role in the damage detection. Generally, sensors located at the proximities of the damage region are more sensitive to damage. However further work should be done in this direction in order to relate the location of the sensors to the damage index towards not only detection of the damage but also its spatial localisation.

A study which explores the *self-sensing and self-diagnosis capabilities*[6] of a beam

---

[6] The exploratory study of the self-sensing and self-diagnosis capabilities of a carbon nano-enriched composite laminated beam was presented in Garcia et al. [148].

manufactured with CB nano-particles embedded between the glass/fibre laminates was developed in Chapter 5. The analysis proposes an unified approach which compromises the self-diagnosis paradigm for obtaining vibration responses of the beam coupled with the VSHM methodology for damage assessment. The main conclusions of this analysis are summarised with the following points:

- Vibratory signals can be estimated by measuring changes in voltage due to the electromechanical properties of the CB nano-particles embedded in a glass/fibre laminated beam. The forced vibration excitation is successfully measured by changes in voltage measured through the beam due to variations in its dynamical strain. The results show a sharp peak at the frequency of excitation within the frequency spectrum, which does not appear in the case of non-excitation.
- The voltage signal measurements can provide indication for the presence of damage and they can be used to distinguish between the two damage scenarios. The SSA-based methodology clearly decomposed the vibration response in RCs that contained the different oscillatory patterns within the vibration response. The frequency of excitation was contained in the first RC which has the information of the general trend of the vibration behaviour. For this analysis, the methodology was applied in the time domain to extract a particular mode of vibration.
- The voltage signal responses were processed by the damage assessment methodology to extract features qualifying the state/health of the beam, which eventually results in the self-damage assessment. The different damage scenarios were detected for both cases adding mass and drilling a hole. However, an increment of the damage severity was not successfully tracked. For the case of a damage simulated by drilling a hole in the beam was observed that the sensitivity, in terms of the magnitude of the damage index, was lower than for the case of adding mass. This can be explained because when a hole is drilled in the beam not only a damage was included but also the sensor (in this case the embedded nanocomposites) was damaged.

6.2 Recommendations and Future Work

This is one of the few works which considers singular spectrum analysis technique to address a data-based damage assessment methodology. For this reason, some important aspects should be considered for future research.

- The use of SSA as a technique for vibration modes identification can lead to an alternative technique for this kind of analysis. When the decomposition was implemented in the time domain it was observed that the reconstructed components contain separate and interpretable oscillatory components. The combination of some reconstructed components can describe the global characteristics of the vibration responses and therefore they can be associated with the natural modes of vibration [86]. Further research should be conducted in this direction for the development of SSA as a damage identification technique but also as a vibration modes identification technique.

- As discussed in Chapter 2, there are some parameters that affect on the methodology performance depending on their value. One of the most important parameters is the window sliding size which determines the number of PCs and hence the maximum dimension of the reference state within the methodology. The selection of this value depends on the problem at hand. This involves what to analyse (nature of the problem), how is the complexity of the vibration response and the need of separability in the PCs. An analysis in this direction is required to find common directions in the performance of the methodology with the aim of understanding better the behaviour of SSA as a damage identification technique.

- In the present work a statistical hypothesis was used to set a threshold for the inspection phase in order to make the decision whether the structure is healthy or damaged. Several options of these statistical classifiers exist and the comparison of the different approaches should be considered as further work. The growth of the outlier classifier techniques will need robust approaches for decision making and these statistical approaches can contribute to this direction.

- Other aspect that concerns to the data-based methods is their limitation to localise damage within the spatial boundaries of the structure/specimen to analysis. In this work, the detection of damage/delamination at different locations was achieved. This demonstrates the sensitivity of the methodology not only to detect damage but also to distinguish between damage at different locations. However, the location of the damage was known and the relation with the damage/delamination location was associated with this known location. One possible direction to address this issue is to find features that can relate sensor location and the damage index values. Also the use of simple numerical models could help in this direction but with the consideration of a proper treatment of the uncertainties between model and experiment towards damage identification.

- Delamination was the main damage studied in this thesis because it is one of the most common damage in composite structures and it introduces nonlinear effects in the vibration response of the structure. Other damage, but similar in nature, that was studied in this work was the debonding between suction and pressure shells in wind turbine blades. This damage is also one of the most common forms of damage in wind turbine blades but they are not the only ones. The consideration of other potential damages such as the effect of ice on wind turbine blades, surface erosion, fibre breakage, material discontinuity that may act in different manner and therefore additional considerations may be required.

- The experiments developed in this work were conducted in a laboratory where the variability of the environmental conditions does not significantly affect the experiment performance. Composite materials are generally used in structures that are exposed to considerable variability of the operational and environmental conditions. Although, SSA is a well-known technique to deal with the nonlinearities due to environmental changes, work should be done in this direction to identify the uncertainty of these effects in the methodology performance. The study of the performance of the methodology under the operational and environmental conditions will be implemented in the study of an operating Vestas V27 wind turbine with the collaboration of Brüel & Kjær Sound & Vibration Measurements [149].

- An exploratory study was presented in this work based on the concept of self-sensing and self-diagnosis of nano-enriched composite materials. This study open a new line of research for the combination of the measurable signals through the nano-enriched material and the damage identification by a VSHM methodology. These studies are still in an embryo stage but they have an enormous projection in a wide range of industries such as aircraft, automotive, train and different industries within the energy sector. This is one of the reasons why further work must be done in different directions such as the configuration and distribution of the nanocomposites for reducing the high resistivity of the material and hence improve the sensitivity. Other important aspect is the development and combination of novel methodologies to obtain the most from the measurements towards an integrated system for self-monitoring the structural health.

Bibliography

[1] S. Mazumdar. Market trends - growth opportunities: Materials innovation will drive composites usage to new heights. *High-performance composites*, 2012.

[2] Global wind statisitics 2015. *Global wind energy council*, 2016.

[3] G. D. et al. Materials foresight: Smart materials for the 21st century. *The Institute of Materials, Minerals and Mining*, Report no. FMP/03/04/IOM3.

[4] H. Sohn, C. R. Farrar, F. M. Hemez, D. D. Shunk, D. W. Stinemates, B. R. Nadler and J. J. Czarnecki. *A review of structural health monitoring literature: 1996-2001.* Los Alamos National Laboratory Los Alamos, NM, 2004.

[5] A. Rytter. Vibration based inspection of civil engineering structures phd thesis aalborg university denmark. 1993.

[6] G. Park and D. Inman. Smart bolts: an example of self-healing structures. *Smart Materials Bulletin*, 2001(7): 5–8, 2001.

[7] J. E. Doherty. Nondestructive evaluation. *Handbook on experimental mechanics*, 1, 1987.

[8] S. W. Doebling, C. R. Farrar, M. B. Prime *et al.* A summary review of vibration-based damage identification methods. *Shock and vibration digest*, 30(2): 91–105, 1998.

[9] K. Worden, W. J. Staszewski and J. J. Hensman. Natural computing for mechanical systems research: A tutorial overview. *Mechanical Systems and Signal Processing*, 25(1): 4–111, 2011.

[10] C. R. Farrar, H. Sohn and K. Worden. Data normalization: A key for structural health. *http://lib-www. lanl. gov/la-pubs/00818571. pdf*, page 3, 2001.

[11] H. Sohn, K. Worden and C. R. Farrar. Novelty detection under changing environmental conditions. *SPIE's 8th Annual International Symposium on Smart Structures and Materials*, pages 108–118. International Society for Optics and Photonics, 2001.

[12] B. Peeters and G. De Roeck. One-year monitoring of the z 24-bridge: environmental effects versus damage events. *Earthquake engineering & structural dynamics*, 30(2): 149–171, 2001.

[13] C. R. Farrar and K. Worden. An introduction to structural health monitoring. *Philosophical Transactions of the Royal Society of London A: Mathematical, Physical and Engineering Sciences*, 365(1851): 303–315, 2007.

[14] S. D. Fassois and J. S. Sakellariou. Time-series methods for fault detection and identification in vibrating structures. *Philosophical Transactions of the Royal Society of London A: Mathematical, Physical and Engineering Sciences*, 365(1851): 411–448, 2007.

[15] M. I. Friswell. Damage identification using inverse methods. *Philosophical Transactions of the Royal Society of London A: Mathematical, Physical and Engineering Sciences*, 365(1851): 393–410, 2007.

[16] K. Worden and G. Manson. The application of machine learning to structural health monitoring. *Philosophical Transactions of the Royal Society of London A: Mathematical, Physical and Engineering Sciences*, 365(1851): 515–537, 2007.

[17] S. W. Doebling, C. R. Farrar, M. B. Prime and D. W. Shevitz. Damage identification and health monitoring of structural and mechanical systems from changes in their vibration characteristics: a literature review. Technical report, Los Alamos National Lab., NM (United States), 1996.

[18] O. Salawu. Detection of structural damage through changes in frequency: a review. *Engineering structures*, 19(9): 718–723, 1997.

[19] C. R. Farrar, S. W. Doebling and D. A. Nix. Vibration–based structural damage identification. *Philosophical Transactions of the Royal Society of London A: Mathematical, Physical and Engineering Sciences*, 359(1778): 131–149, 2001.

[20] G. D. Roeck. The state-of-the-art of damage detection by vibration monitoring: the simces experience. *Journal of Structural Control*, 10(2): 127–134, 2003.

[21] E. Carden and P. Fanning. Vibration based condition monitoring: A review. *Structural Health Monitoring*, 3(4): 355–377, 2004.

[22] D. J. Inman, C. R. Farrar, V. Lopes Jr and V. Steffen Jr. *Damage prognosis.* Wiley Online Library, 2005.

[23] C. P. Fritzen. Vibration-based structural health monitoring–concepts and applications. *Key Engineering Materials*, volume 293, pages 3–20. Trans Tech Publ, 2005.

[24] C.-P. Fritzen. Vibration-based techniques for structural health monitoring. *Structural Health Monitoring*, pages 45–224, 2006.

[25] P. Kołakowski. Structural health monitoring–a review with the emphasis on low-frequency methods. *Engineering Transactions*, 55(3): 239–275, 2007.

[26] D. Adams. *Health monitoring of structural materials and components: methods with applications*. John Wiley & Sons, 2007.

[27] K. Worden, C. R. Farrar, J. Haywood and M. Todd. A review of nonlinear dynamics applications to structural health monitoring. *Structural Control and Health Monitoring*, 15(4): 540–567, 2008.

[28] R. Brincker, L. Zhang and P. Andersen. Modal identification from ambient responses using frequency domain decomposition. *Proc. of the 18*International Modal Analysis Conference (IMAC), San Antonio, Texas*. 2000.

[29] A. Messina, E. Williams and T. Contursi. Structural damage detection by a sensitivity and statistical-based method. *Journal of sound and vibration*, 216(5): 791–808, 1998.

[30] E. Parloo, P. Guillaume and M. Van Overmeire. Damage assessment using mode shape sensitivities. *Mechanical systems and signal Processing*, 17(3): 499–518, 2003.

[31] K. Alnefaie. Finite element modeling of composite plates with internal delamination. *Composite Structures*, 90(1): 21–27, 2009.

[32] N. Maia, J. Silva, E. Almas and R. Sampaio. Damage detection in structures: from mode shape to frequency response function methods. *Mechanical systems and signal processing*, 17(3): 489–498, 2003.

[33] G. Kawiecki. Modal damping measurement for damage detection. *Smart Materials and Structures*, 10(3): 466, 2001.

[34] C. R. Farrar and S. W. Doebling. An overview of modal-based damage identification methods. *Proceedings of DAMAS Conference*, pages 269–278. Citeseer, 1997.

[35] R. Pascual, J.-C. Golinval and M. Razeto. A frequency domain correlation technique for model correlation and updating. *Proceedings-SPIE The International Society for Optical Engineering*, pages 587–592. SPIE INTERNATIONAL SOCIETY FOR OPTICAL, 1997.

[36] N. Maia, J. Silva and A. Ribeiro. The transmissibility concept in multi-degree-of-freedom systems. *Mechanical Systems and Signal Processing*, 15(1): 129–137, 2001.

[37] G. Park, H. Sohn, C. R. Farrar and D. J. Inman. Overview of piezoelectric impedance-based health monitoring and path forward. 2003.

[38] W. D'AMBROGIO and A. Fregolent. The use of antiresonances for robust model updating. *Journal of Sound and Vibration*, 236(2): 227–243, 2000.

[39] M. Basseville, A. Benveniste, M. Goursat, L. Hermans, L. Mevel and H. Van der Auweraer. Output-only subspace-based structural identification: from theory to industrial testing practice. *Journal of Dynamic Systems, Measurement, and Control*, 123(4): 668–676, 2001.

[40] B. Peeters and G. De Roeck. Reference-based stochastic subspace identification for output-only modal analysis. *Mechanical systems and signal processing*, 13(6): 855–878, 1999.

[41] S. da Silva, M. D. Junior, V. L. Junior and M. J. Brennan. Structural damage detection by fuzzy clustering. *Mechanical Systems and Signal Processing*, 22(7): 1636–1649, 2008.

[42] Z. Peng, Z. Lang, C. Wolters, S. Billings and K. Worden. Feasibility study of structural damage detection using {NARMAX} modelling and nonlinear output frequency response function based analysis. *Mechanical Systems and Signal Processing*, 25(3): 1045 – 1061, 2011.

[43] M. Basseville, M. Abdelghani and A. Benveniste. Subspace-based fault detection algorithms for vibration monitoring. *Automatica*, 36(1): 101–109, 2000.

[44] H. Sohn, J. A. Czarnecki and C. R. Farrar. Structural health monitoring using statistical process control. *Journal of Structural Engineering*, 126(11): 1356–1363, 2000.

[45] E. P. Carden and J. M. Brownjohn. Arma modelled time-series classification for structural health monitoring of civil infrastructure. *Mechanical systems and signal processing*, 22(2): 295–314, 2008.

[46] S. D. Fassois and F. P. Kopsaftopoulos. *Statistical time series methods for vibration based structural health monitoring.* Springer, 2013.

[47] J. Sakellariou, K. Petsounis and S. Fassois. Vibration analysis based on–board fault detection in railway vehicle suspensions: a feasibility study. *Proceedings of First National Conference on Recent Advances in Mechanical Engineering, Patras, Greece.* 2001.

[48] Z. Mao and M. Todd. A model for quantifying uncertainty in the estimation of noise-contaminated measurements of transmissibility. *Mechanical Systems and Signal Processing*, 28: 470–481, 2012.

[49] D. Rizos, S. Fassois, Z. Marioli-Riga and A. Karanika. Vibration-based skin damage statistical detection and restoration assessment in a stiffened aircraft panel. *Mechanical Systems and Signal Processing*, 22(2): 315–337, 2008.

[50] H. Sohn and C. R. Farrar. Damage diagnosis using time series analysis of vibration signals. *Smart materials and structures*, 10(3): 446, 2001.

[51] K. K. Nair, A. S. Kiremidjian and K. H. Law. Time series-based damage detection and localization algorithm with application to the asce benchmark structure. *Journal of Sound and Vibration*, 291(1): 349–368, 2006.

[52] J. Sakellariou and S. Fassois. Stochastic output error vibration-based damage detection and assessment in structures under earthquake excitation. *Journal of Sound and Vibration*, 297(3): 1048–1067, 2006.

[53] D. Shu and C. N. Della. Vibrations of multiple delaminated beams. *Composite Structures*, 64(3): 467–477, 2004.

[54] W. Ostachowicz and A. Żak. Vibration of a laminated beam with a delamination including contact effects. *Shock and Vibration*, 11(3-4): 157–171, 2004.

[55] M. I. Friswell, J. E. Mottershead and H. Ahmadian. Finite–element model updating using experimental test data: parametrization and regularization. *Philosophical Transactions of the Royal Society of London A: Mathematical, Physical and Engineering Sciences*, 359(1778): 169–186, 2001.

[56] K. Worden, G. Manson and N. Fieller. Damage detection using outlier analysis. *Journal of Sound and Vibration*, 229(3): 647–667, 2000.

[57] M. Basseville, L. Mevel and M. Goursat. Statistical model-based damage detection and localization: subspace-based residuals and damage-to-noise sensitivity ratios. *Journal of sound and vibration*, 275(3): 769–794, 2004.

[58] F. Kopsaftopoulos and S. Fassois. Vibration based health monitoring for a lightweight truss structure: experimental assessment of several statistical time series methods. *Mechanical Systems and Signal Processing*, 24(7): 1977–1997, 2010.

[59] S. Park, C. Lee and H. Sohn. Reference-free crack detection using transfer impedances. *Journal of Sound and Vibration*, 329(12): 2337–2348, 2010.

[60] F.-L. Zhang, Y.-C. Ni, S.-K. Au and H.-F. Lam. Fast bayesian approach for modal identification using free vibration data, part i–most probable value. *Mechanical Systems and Signal Processing*, 70: 209–220, 2016.

[61] L. Balsamo and R. Betti. Data-based structural health monitoring using small training data sets. *Structural Control and Health Monitoring*, 22(10): 1240–1264, 2015.

[62] D. Tcherniak and L. L. Mølgaard. Vibration-based shm system: Application to wind turbine blades. *Journal of Physics: Conference Series*, volume 628, page 012072. IOP Publishing, 2015.

[63] M. A. de Oliveira, J. Vieira Filho, V. Lopes Jr and D. J. Inman. Damage detection based on electromechanical impedance principle and principal components. *Topics in Modal Analysis, Volume 7*, pages 307–315. Springer, 2014.

[64] I. T. Jolliffe. *Principal component analysis*, volume 487. Springer-Verlag New York, 1986.

[65] L. Mujica, J. Rodellar, A. Fernandez and A. Güemes. Q-statistic and t2-statistic pca-based measures for damage assessment in structures. *Structural Health Monitoring*, 10(5): 539–553, 2011.

[66] M. Johnson. Waveform based clustering and classification of ae transients in composite laminates using principal component analysis. *NDT & E International*, 35(6): 367–376, 2002.

[67] I. Lopez and N. Sarigul-Klijn. Effects of dimensional reduction techniques on structural damage assessment under uncertainty. *Journal of Vibration and Acoustics*, 133(6): 061008, 2011.

[68] A.-M. Yan, G. Kerschen, P. De Boe and J.-C. Golinval. Structural damage diagnosis under varying environmental conditionspart i: a linear analysis. *Mechanical Systems and Signal Processing*, 19(4): 847–864, 2005.

[69] A.-M. Yan, G. Kerschen, P. De Boe and J.-C. Golinval. Structural damage diagnosis under varying environmental conditionspart ii: local pca for non-linear cases. *Mechanical Systems and Signal Processing*, 19(4): 865–880, 2005.

[70] A. G. González and S. Fassois. A supervised vibration-based statistical methodology for damage detection under varying environmental conditions & its laboratory assessment with a scale wind turbine blade. *Journal of Sound and Vibration*, 366: 484–500, 2016.

[71] M. Ghil, M. Allen, M. Dettinger, K. Ide, D. Kondrashov, M. Mann, A. W. Robertson, A. Saunders, Y. Tian, F. Varadi *et al.* Advanced spectral methods for climatic time series. *Reviews of Geophysics*, 40(1): 1003, 2002.

[72] N. Golyandina, V. Nekrutkin and A. A. Zhigljavsky. *Analysis of time series structure: SSA and related techniques.* CRC Press, 2010.

[73] H. Hassani. Singular spectrum analysis: methodology and comparison. 2007.

[74] A. Basilevsky and D. P. Hum. Karhunen-loeve analysis of historical time series with an application to plantation births in jamaica. *Journal of the American Statistical Association*, 74(366a): 284–290, 1979.

[75] H. Hassani and D. Thomakos. A review on singular spectrum analysis for economic and financial time series. *Statistics and its Interface*, 3(3): 377–397, 2010.

[76] C.-H. Loh, M.-H. Tseng and S.-H. Chao. Structural damage assessment using output-only measurement: Localization and quantification. *ASME 2013 Conference on Smart Materials, Adaptive Structures and Intelligent Systems*, pages V002T05A001–V002T05A001. American Society of Mechanical Engineers, 2013.

[77] S.-H. Chao and C.-H. Loh. Application of singular spectrum analysis to structural monitoring and damage diagnosis of bridges. *Structure and Infrastructure Engineering*, 10(6): 708–727, 2014.

[78] H. Al-Bugharbee and I. Trendafilova. A fault diagnosis methodology for rolling element bearings based on advanced signal pretreatment and autoregressive modelling. *Journal of Sound and Vibration*, 369: 246–265, 2016.

[79] N. Golyandina, A. Korobeynikov, A. Shlemov and K. Usevich. Multivariate and 2d extensions of singular spectrum analysis with the rssa package. *Journal of Statistical Software*, 67(1), 2015.

[80] D. Garcia and I. Trendafilova. A multivariate data analysis approach towards vibration analysis and vibration-based damage assessment:: Application for delamination detection in a composite beam. *Journal of Sound and Vibration*, 333(25): 7036–7050, 2014.

[81] D. Garcia, R. Palazzetti, I. Trendafilova, C. Fiorini and A. Zucchelli. Vibration-based delamination diagnosis and modelling for composite laminate plates. *Composite Structures*, 130: 155–162, 2015.

[82] M. Prime and D. Shevitz. Linear and nonlinear methods for detecting cracks in beams. *Proceedings pages*, 1437: 1443, 1996.

[83] S. Park, J.-J. Lee, C.-B. Yun and D. J. Inman. Electro-mechanical impedance-based wireless structural health monitoring using pca-data compression and k-means clustering algorithms. *Journal of Intelligent Material Systems and Structures*, 19(4): 509–520, 2008.

[84] J. Zabalza, J. Ren, Z. Wang, S. Marshall and J. Wang. Singular spectrum analysis for effective feature extraction in hyperspectral imaging. *Geoscience and Remote Sensing Letters, IEEE*, 11(11): 1886–1890, 2014.

[85] B. Kilundu, X. Chiementin and P. Dehombreux. Singular spectrum analysis for bearing defect detection. *Journal of vibration and acoustics*, 133(5), 2011.

[86] I. Trendafilova. An inverse vibration-based approach towards modelling and damage identification in nonlinearly vibrating structures. application for delamination detection in a composite beam. *Journal of Physics: Conference Series*, volume 382, page 012030. IOP Publishing, 2012.

[87] K. Worden, C. R. Farrar, G. Manson and G. Park. The fundamental axioms of structural health monitoring. *Proceedings of the Royal Society of London A: Mathematical, Physical and Engineering Sciences*, volume 463, pages 1639–1664. The Royal Society, 2007.

[88] S. Mazumdar. *Composites manufacturing: materials, product, and process engineering.* CrC press, 2001.

[89] S. Sridharan. *Delamination behaviour of composites.* Elsevier, 2008.

[90] Y.Zou, L. Tong and G. Steven. Vibration-based model dependent damage (delamination) identifiaction and health monitoring for composite structures-a review. *Journal of Sound and Vibration*, 230(2): 357–378, 2000.

[91] D. Montalvao, N. Maia and A. Ribeiro. A review of vibration-based structural health monitoring with special emphasis on composite materials. *Shock and Vibration Digest*, 38(4): 295–326, 2006.

[92] E. T. Thostenson and T.-W. Chou. Carbon nanotube networks: sensing of distributed strain and damage for life prediction and self healing. *Advanced Materials*, 18(21): 2837–2841, 2006.

[93] F. Ubertini, S. Laflamme, H. Ceylan, A. L. Materazzi, G. Cerni, H. Saleem, A. DAlessandro and A. Corradini. Novel nanocomposite technologies for dynamic monitoring of structures: a comparison between cement-based embeddable and soft elastomeric surface sensors. *Smart Materials and Structures*, 23(4): 045023, 2014.

[94] M. Nofar, S. Hoa and M. Pugh. Failure detection and monitoring in polymer matrix composites subjected to static and dynamic loads using carbon nanotube networks. *Composites Science and Technology*, 69(10): 1599–1606, 2009.

[95] A. Naghashpour and S. Van Hoa. A technique for real-time detection, location and quantification of damage in large polymer composite structures made of electrically non-conductive fibers and carbon nanotube networks. *Nanotechnology*, 24(45): 455502, 2013.

[96] L. Böger, M. H. Wichmann, L. O. Meyer and K. Schulte. Load and health monitoring in glass fibre reinforced composites with an electrically conductive nanocomposite epoxy matrix. *Composites Science and Technology*, 68(7): 1886–1894, 2008.

[97] I. Brook, G. Mechrez, R. Y. Suckeveriene, R. Tchoudakov, S. Lupo and M. Narkis. The structure and electro-mechanical properties of novel hybrid cnt/pani nanocomposites. *Polymer Composites*, 35(4): 788–794, 2014.

[98] P. Dharap, Z. Li, S. Nagarajaiah and E. Barrera. Nanotube film based on single-wall carbon nanotubes for strain sensing. *Nanotechnology*, 15(3): 379, 2004.

[99] A. Todoroki and J. Yoshida. Electrical resistance change of unidirectional cfrp due to applied load. *JSME International Journal Series A*, 47(3): 357–364, 2004.

[100] H. Saghafi, A. Zucchelli, R. Palazzetti and G. Minak. The effect of interleaved composite nanofibrous mats on delamination behavior of polymeric composite materials. *Composite Structures*, 109: 41–47, 2014.

[101] J. L. Abot, Y. Song, M. S. Vatsavaya, S. Medikonda, Z. Kier, C. Jayasinghe, N. Rooy, V. N. Shanov and M. J. Schulz. Delamination detection with carbon nanotube thread in self-sensing composite materials. *Composites Science and Technology*, 70(7): 1113–1119, 2010.

[102] I. Kang, M. J. Schulz, J. H. Kim, V. Shanov and D. Shi. A carbon nanotube strain sensor for structural health monitoring. *Smart materials and structures*, 15(3): 737, 2006.

[103] T. N. Tallman, S. Gungor, K. Wang and C. E. Bakis. Damage detection via electrical impedance tomography in glass fiber/epoxy laminates with carbon black filler. *Structural Health Monitoring*, 14(1): 100–109, 2015.

[104] T.-C. Hou, K. J. Loh and J. P. Lynch. Spatial conductivity mapping of carbon nanotube composite thin films by electrical impedance tomography for sensing applications. *Nanotechnology*, 18(31): 315501, 2007.

[105] B. R. Loyola, T. M. Briggs, L. Arronche, K. J. Loh, V. La Saponara, G. OBryan and J. L. Skinner. Detection of spatially distributed damage in fiber-reinforced polymer composites. *Structural Health Monitoring*, 12(3): 225–239, 2013.

[106] K. J. Loh, J. P. Lynch, B. Shim and N. Kotov. Tailoring piezoresistive sensitivity of multilayer carbon nanotube composite strain sensors. *Journal of Intelligent Material Systems and Structures*, 19(7): 747–764, 2008.

[107] N. Hu, Y. Karube, C. Yan, Z. Masuda and H. Fukunaga. Tunneling effect in a polymer/carbon nanotube nanocomposite strain sensor. *Acta Materialia*, 56(13): 2929–2936, 2008.

[108] G. T. Pham, Y.-B. Park, Z. Liang, C. Zhang and B. Wang. Processing and modeling of conductive thermoplastic/carbon nanotube films for strain sensing. *Composites Part B: Engineering*, 39(1): 209–216, 2008.

[109] J. A. Westerhuis, T. Kourti and J. F. MacGregor. Comparing alternative approaches for multivariate statistical analysis of batch process data. *Journal of Chemometrics*, 13(3-4): 397–413, 1999.

[110] D. Garcia, M. Stickland and G. Liśkiewicz. Dynamical system analysis of unstable flow phenomena in centrifugal blower. *Open Engineering*, 5(1), 2015.

[111] Y. Komatsubara and S. Mizuki. Dynamical system analysis of unsteady phenomena in centrifugal compressor. *Journal of Thermal Science*, 6(1): 14–20, 1997.

[112] G. C. Pardoen. Effect of delamination on the natural frequencies of composite laminates. *Journal of composite materials*, 23(12): 1200–1215, 1989.

[113] P. M. Bentler and K.-H. Yuan. Tests for linear trend in the smallest eigenvalues of the correlation matrix. *Psychometrika*, 63(2): 131–144, 1998.

[114] S. S. Kessler, S. M. Spearing, M. J. Atalla, C. E. Cesnik and C. Soutis. Damage detection in composite materials using frequency response methods. *Composites Part B: Engineering*, 33(1): 87–95, 2002.

[115] D. Broomhead and G. P. King. Extracting qualitative dynamics from experimental data. *Physica D: Nonlinear Phenomena*, 20(2): 217–236, 1986.

[116] L. Parsons, E. Haque and H. Liu. Subspace clustering for high dimensional data: a review. *ACM SIGKDD Explorations Newsletter*, 6(1): 90–105, 2004.

[117] C. Fiorini. Structural vibration modeling and health monitoring method of composite structures: an investigation on two strategies. *Master thesis*, 2011.

[118] B. Nour-Omid and R. W. Clough. Short communication block lanczos method for dynamic analysis of structures. *Earthquake engineering & structural dynamics*, 13(2): 271–275, 1985.

[119] P. Mujumdar and S. Suryanarayan. Flexural vibrations of beams with delaminations. *Journal of sound and vibration*, 125(3): 441–461, 1988.

[120] E. Manoach, J. Warminski, A. Mitura and S. Samborski. Dynamics of a laminated composite beam with delamination and inclusions. *The European Physical Journal Special Topics*, 222(7): 1649–1664, 2013.

[121] Z.-F. Fu and J. He. *Modal analysis.* Butterworth-Heinemann, 2001.

[122] N.-J. Jacobsen, P. Andersen and R. Brincker. Using enhanced frequency domain decomposition as a robust technique to harmonic excitation in operational modal analysis. *International Conference on Noise and Vibration Engineering (ISMA), Leuven, Belgium.* 2006.

[123] Z. Wei, L. Yam and L. Cheng. Detection of internal delamination in multi-layer composites using wavelet packets combined with modal parameter analysis. *Composite Structures*, 64(3): 377–387, 2004.

[124] D. Lin, R. Ni and R. Adams. Prediction and measurement of the vibrational damping parameters of carbon and glass fibre-reinforced plastics plates. *Journal of composite materials*, 18(2): 132–152, 1984.

[125] N. Møller, R. Brincker and P. Andersen. Modal extraction on a diesel engine in operation. *The International Modal Analysis Conference*, pages 1845–1851. 2000.

[126] H. Chen, M. Wang and R. Bai. The effect of nonlinear contact upon natural frequency of delaminated stiffened composite plate. *Composite structures*, 76(1): 28–33, 2006.

[127] I. Ullah, J. K. Sinha and A. Pinkerton. Vibration-based delamination detection in a composite plate. *Mechanics of Advanced Materials and Structures*, 20(7): 536–551, 2013.

[128] Y. Yan and L. Yam. Detection of delamination damage in composite plates using energy spectrum of structural dynamic responses decomposed by wavelet analysis. *Computers & structures*, 82(4): 347–358, 2004.

[129] M. Friswell and J. Penny. Is damage location using vibration measurements practical? *Proceedings of EUROMECH 365 international workshop: DAMAS*, volume 97. 1997.

[130] G. C. Larsen, P. Berring, D. Tcherniak, P. H. Nielsen and K. Branner. Effect of a damage to modal parameters of a wind turbine blade. *EWSHM-7th European Workshop on Structural Health Monitoring*. 2014.

[131] H. Sohn, D. W. Allen, K. Worden and C. R. Farrar. Statistical damage classification using sequential probability ratio tests. *Structural Health Monitoring*, 2(1): 57–74, 2003.

[132] L. Andrews. Special functions of mathematics for engineers (1998).

[133] F. Bottoli and L. Pignatti. Design and processing of structural components in biocomposite materials-case study: Rotor blades for wind turbine cars. *Risø, DK: Master Thesis*, 2011.

[134] M. Nigro, S. Pakzad and S. Dorvash. Localized structural damage detection: a change point analysis. *Computer-Aided Civil and Infrastructure Engineering*, 29(6): 416–432, 2014.

[135] Y. Liu, A. Rajadas and A. Chattopadhyay. Self-sensing and self-healing of structural damage in fiber reinforced composites. *ASME 2013 Conference on Smart Materials, Adaptive Structures and Intelligent Systems*, pages V001T01A023–V001T01A023. American Society of Mechanical Engineers, 2013.

[136] Z. Rubin, S. Sunshine, M. Heaney, I. Bloom and I. Balberg. Critical behavior of the electrical transport properties in a tunneling-percolation system. *Physical Review B*, 59(19): 12196, 1999.

[137] S. Gungor and C. E. Bakis. Anisotropic networking of carbon black in glass/epoxy composites using electric field. *Journal of Composite Materials*, page 0021998314521256, 2014.

[138] Z. Li, J. Zhang and S. Chen. Effects of carbon blacks with various structures on vulcanization and reinforcement of filled ethylene-propylene-diene rubber. *Express Polym. Lett*, 2(10): 695–704, 2008.

[139] A. B. Oskouyi, U. Sundararaj and P. Mertiny. Tunneling conductivity and piezoresistivity of composites containing randomly dispersed conductive nano-platelets. *Materials*, 7(4): 2501–2521, 2014.

[140] X. Jing, W. Zhao and L. Lan. The effect of particle size on electric conducting percolation threshold in polymer/conducting particle composites. *Journal of Materials Science Letters*, 19(5): 377–379, 2000.

[141] G. Kwon, Y. Heo, K. Shin and B. J. Sung. Electrical percolation networks of carbon nanotubes in a shear flow. *Physical Review E*, 85(1): 011143, 2012.

[142] T. Theodosiou and D. Saravanos. Numerical investigation of mechanisms affecting the piezoresistive properties of cnt-doped polymers using multi-scale models. *Composites Science and Technology*, 70(9): 1312–1320, 2010.

[143] N. Hu, H. Fukunaga, S. Atobe, Y. Liu, J. Li *et al.* Piezoresistive strain sensors made from carbon nanotubes based polymer nanocomposites. *Sensors*, 11(11): 10691–10723, 2011.

[144] K. J. Loh K J and L. J. P. Self-sensing and power harvesting carbon nanotube composites based on piezoelectric polymers. *International Conference on Bridge Maintenance, Safety and Management*, pages 3329–3336. 2008.

[145] D. Garcia and I. Trendafilova. Singular spectrum analysis for identifying structural nonlinearity using free-decay responses: Application detection and diagnosis in composite laminates. *26th International Conference on Noise and Vibration Engineering*. 2014.

[146] I. T. David Garcia. vibration-based health monitoring approach for composite structures using multivariate analysis. *7th European Workshop of Structural Health Monitoring (EWSH). Nantes (France)*, 2014.

[147] D. García, D. Tcherniak and I. Trendafilova. Damage assessment for wind turbine blades based on a multivariate statistical approach. *Journal of Physics: Conference Series*, volume 628, page 012086. IOP Publishing, 2015.

[148] D. García, I. Trendafilova and D. J. Inman. A study on the vibration-based self-monitoring capabilities of nano-enriched composite laminated beams. *Smart Materials and Structures*, 25(4): 045011, 2016.

[149] M. D. Ulriksen, D. Tcherniak and L. Damkilde. Damage detection in an operating vestas v27 wind turbine blade by use of outlier analysis. *Environmental, Energy and Structural Monitoring Systems (EESMS), 2015 IEEE Workshop on*, pages 50–55. IEEE, 2015.

Appendix A

Histograms and Lognormal distribution for the training healthy data of the lab-scale WTB

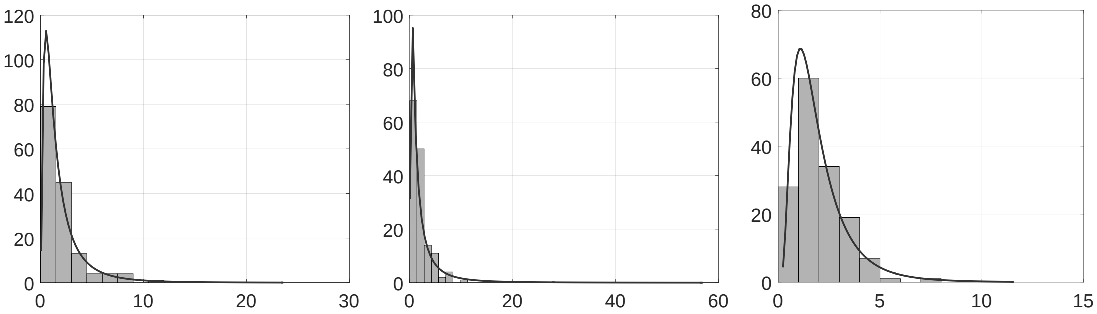

(a) Sensor 1 (b) Sensor 2 (c) Sensor 3

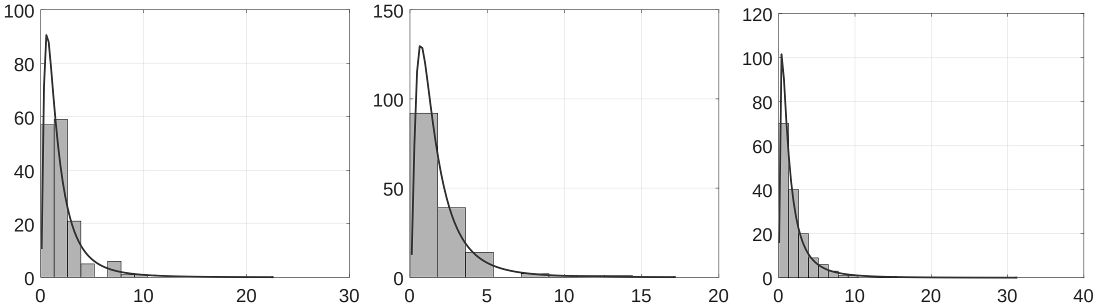

(d) Sensor 4 (e) Sensor 5 (f) Sensor 6

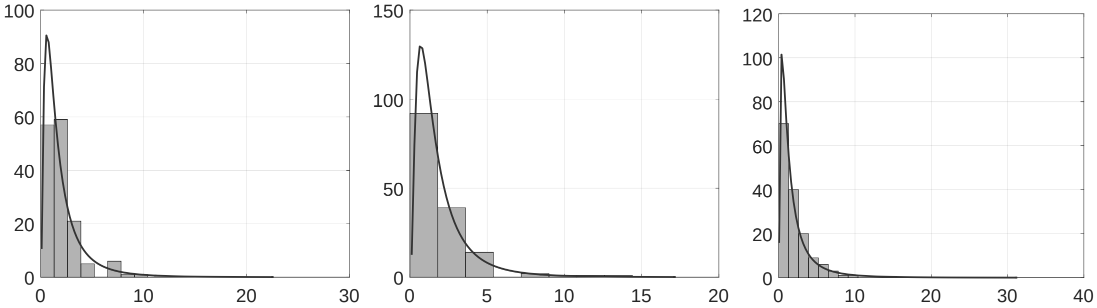

(g) Sensor 7 (h) Sensor 8 (i) Sensor 9

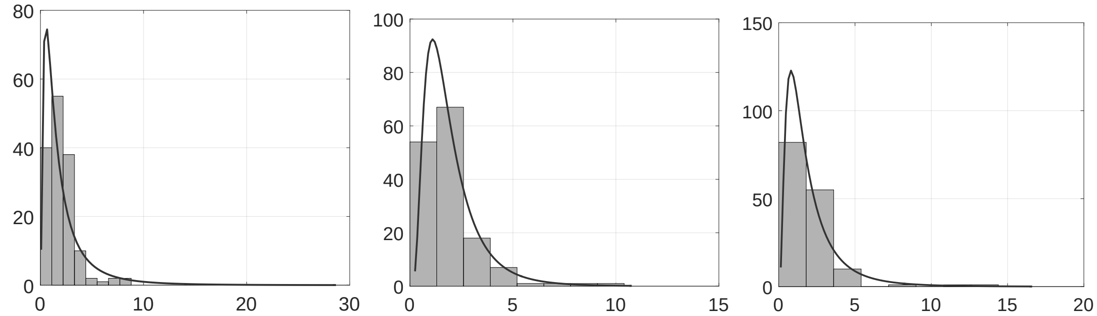

(j) Sensor 10 (k) Sensor 11 (l) Sensor 12

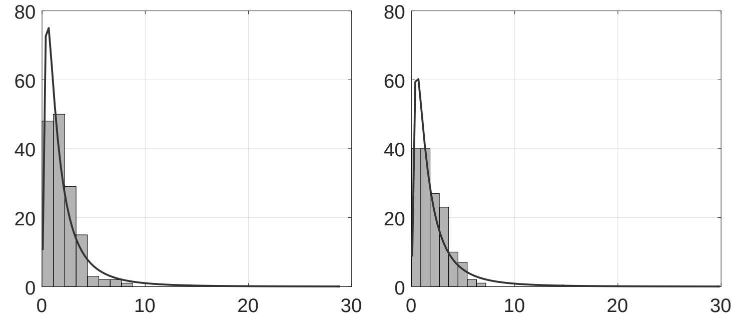

(m) Sensor 13 (n) Sensor 14

Figure A.1: Histograms and Lognormal distribution for the training healthy data of the Lab-scale WTB

Appendix B

Tables of percentage of correct classified observations (healthy vs damage) in the lab-scale wind turbine blade

	Damage location D1														
	Dimension 2					Dimension 3					Dimension 4				
Sensor	Var (%)	H	D1S	D1M	D1L	Var (%)	H	D1S	D1M	D1L	Var (%)	H	D1S	D1M	D1L
1	86	**95**	**100**	**100**	**100**	89	**93**	**100**	**100**	**100**	91	**94**	**100**	**100**	**100**
2	78	**100**	45	**98**	**98**	83	**100**	53	**100**	**100**	86	**99**	78	**100**	**100**
3	84	**99**	**100**	**100**	**100**	88	**96**	**100**	**100**	**100**	90	**94**	**100**	**100**	**100**
4	83	**94**	25	89	**93**	88	**92**	23	89	**100**	91	**93**	38	**100**	**100**
5	82	**96**	**95**	**100**	**100**	88	**94**	**98**	**100**	**100**	90	**94**	**100**	**100**	**100**
6	87	**97**	15	2	88	90	**94**	28	7	**95**	92	**94**	35	9	**93**
7	82	**96**	**100**	**100**	**100**	86	**94**	**100**	**100**	**100**	88	**93**	**100**	**100**	**100**
8	85	**97**	50	77	**98**	88	**97**	78	**98**	**100**	90	**94**	75	**95**	**100**
9	84	**95**	0	5	46	88	**93**	8	30	**95**	90	**95**	23	23	**98**
10	86	**99**	3	**91**	**100**	91	**92**	38	**100**	**100**	93	**91**	40	**100**	**100**
11	85	**95**	43	9	17	89	**96**	78	**98**	**95**	91	**94**	78	**100**	**95**
12	79	**99**	25	**91**	76	84	**92**	**93**	**100**	**100**	87	**92**	**93**	**100**	**100**
13	86	**100**	5	0	2	90	**97**	5	0	5	91	**95**	15	2	17
14	86	**100**	73	84	**95**	88	**96**	80	**91**	**100**	90	**96**	78	**91**	**100**

Table B.1: Percentage of correctly classified observations when the damage is in the location D1. In bold the percentages greater than 90%. Threshold was set up at risk of false alarm probability equal to $\alpha = 0.05$. The number of observations tested is detailed in Table 4.1

Var: Total percentage of variance contained in the dimension selected of T.

H: Healthy wind turbine blade (without loose screws).

D1S: Damage location D1 - small

D1M: Damage location D1 - medium

D1L: Damage location D1 - large

	Damage location D2														
	Dimension 2					Dimension 3					Dimension 4				
Sensor	Var (%)	H	D2S	D2M	D2L	Var (%)	H	D2S	D2M	D2L	Var (%)	H	D2S	D2M	D2L
1	86	**100**	11	10	13	89	**98**	48	**90**	**100**	91	**97**	50	**98**	**100**
2	78	**97**	23	**100**	**100**	84	**96**	32	**100**	**100**	88	**95**	39	**100**	**100**
3	85	**100**	23	69	**100**	90	**99**	23	71	**100**	92	**100**	30	**90**	**100**
4	83	**100**	0	**98**	**100**	87	**100**	75	**100**	**100**	91	**94**	89	**100**	**100**
5	82	**98**	0	26	**100**	88	**96**	25	**98**	**100**	90	**94**	41	**93**	**100**
6	88	**99**	9	36	**95**	91	**96**	18	62	**100**	93	**94**	25	60	**98**
7	82	**99**	**98**	**100**	**100**	86	**96**	**100**	**100**	**100**	89	**96**	**100**	**100**	**100**
8	85	**100**	2	7	0	88	**100**	9	19	45	90	**99**	43	83	**90**
9	85	**98**	11	33	70	89	**99**	30	62	68	91	**98**	27	76	**100**
10	87	**100**	0	2	10	92	**96**	11	43	80	94	**99**	18	86	**100**
11	87	**99**	5	14	13	91	**99**	5	10	53	93	**100**	2	5	**95**
12	80	**97**	**100**	**100**	**100**	85	**95**	**100**	**100**	**100**	88	**94**	**100**	**100**	**100**
13	86	**100**	11	36	58	89	**98**	20	38	60	90	**98**	20	45	65
14	87	**99**	11	60	85	90	**99**	27	69	**90**	93	**98**	25	76	88

Table B.2: Percentage of correctly classified observations when the damage is in the location D2. In bold the percentages greater than 90%. Threshold was set up at risk of false alarm probability equal to $\alpha = 0.05$. The number of observations tested is detailed in Table 4.1

Var: Total percentage of variance contained in the dimension selected of T.

H: Healthy wind turbine blade (without loose screws).

D2S: Damage location D2 - small

D2M: Damage location D2 - medium

D2L: Damage location D2 - large

	Damage location D3														
	Dimension 2					Dimension 3					Dimension 4				
Sensor	Var (%)	H	D3S	D3M	D3L	Var (%)	H	D3S	D3M	D3L	Var (%)	H	D3S	D3M	D3L
1	85	**91**	25	78	**93**	88	**92**	54	**95**	**100**	90	**94**	63	**95**	**100**
2	79	**99**	7	16	5	84	**98**	53	71	69	88	**94**	75	76	85
3	84	**98**	5	35	29	89	**95**	20	31	29	91	**92**	41	55	58
4	83	**95**	54	89	**91**	87	**94**	51	85	**93**	90	**92**	59	**95**	**95**
5	82	**98**	15	58	69	88	**95**	17	55	62	90	**92**	20	62	69
6	87	**97**	15	20	20	90	**93**	15	33	40	92	**93**	25	42	36
7	81	**99**	10	33	47	85	**94**	37	60	73	88	**94**	69	76	**100**
8	84	**98**	53	**91**	**98**	87	**98**	69	**98**	**100**	89	**96**	76	**96**	**100**
9	83	**97**	2	7	24	87	**97**	8	36	45	89	**93**	14	44	55
10	86	**98**	3	45	56	91	**97**	7	62	67	92	**96**	64	84	80
11	86	**97**	0	4	2	90	**95**	24	38	33	92	**92**	34	51	42
12	80	**94**	**100**	**100**	**100**	84	**91**	**100**	**100**	**100**	87	**89**	**100**	**100**	**100**
13	85	**99**	5	9	5	88	**96**	7	15	15	89	**95**	7	33	56
14	86	**98**	34	84	**95**	89	**97**	41	87	**96**	91	**95**	54	**93**	**96**

Table B.3: Percentage of correctly classified observations when the damage is in the location D3. In bold the percentages greater than 90%. Threshold was set up at risk of false alarm probability equal to $\alpha = 0.05$. The number of observations tested is detailed in Table 4.1

Var: Total percentage of variance contained in the dimension selected of T.

H: Healthy wind turbine blade (without loose screws).

D3S: Damage location D3 - small

D3M: Damage location D3 - medium

D3L: Damage location D3 - large

Appendix C

Tables of percentage of correct classified observations (healthy vs damage) in the SSP34m wind turbine blade

	Actuator 1									
Sensors TE #	1	2	3	4	5	6	7	8	9	10
					Dimension 2					
Var (%)	96	94	91	92	95	89	88	87	93	85
n. MH	0	1	0	0	0	0	0	2	0	2
n. MD	2	0	33	30	23	24	0	0	1	0
Correct H (%)	**100**	**98**	**100**	**100**	**100**	**100**	**100**	**95**	**100**	**95**
Correct D (%)	95	100	15	23	41	38	100	100	97	100
					Dimension 3					
Var (%)	98	96	93	94	96	91	90	90	95	88
n. MH	2	2	2	1	0	0	0	1	0	0
n. MD	0	0	1	4	21	21	0	0	0	0
Correct H (%)	**95**	**95**	**95**	**98**	**100**	**100**	**100**	**98**	**100**	**100**
Correct D (%)	100	100	97	90	46	46	100	100	100	100
					Dimension 4					
Var (%)	99	98	94	95	97	92	92	92	96	91
n. MH	0	1	2	2	0	0	0	0	2	2
n. MD	0	0	3	0	15	17	0	0	0	0
Correct H (%)	**100**	**98**	**95**	**95**	**100**	**100**	**100**	**100**	**95**	**95**
Correct D (%)	100	100	92	100	62	56	100	100	100	100

Table C.1: Percent of correct classification of Healthy and Damaged observations for the SSP34m-WTB by the actuation in the location A1. In bold and highlighted in grey the percentages greater than 90% for **Healthy** and Damaged observations respectively. Threshold at risk of false alarm probability equal to $\alpha = 0.01$

Var: Total percentage of variance contained in the dimension selected of T

H: Healthy WTB. Total number of healthy observations: 42

D: Damaged WTB. Total number of damaged observations: 39

n. MH: Number of observations from Healthy WTB considered as Damaged WTB

n. MD: Number of observations from Damaged WTB considered as Healthy WTB

Sensors TE: Sensors located in the Trailing Edge

	Actuator 2									
Sensor TE #	1	2	3	4	5	6	7	8	9	10
	Dimension 2									
Var (%)	87	84	88	85	87	90	89	87	85	84
n. MH	2	0	11	1	0	0	0	0	0	0
n. MD	0	0	0	0	11	0	25	0	0	0
Correct H (%)	**95**	**100**	74	**98**	**100**	**100**	**100**	**100**	**100**	**100**
Correct D (%)	100	100	100	100	72	100	36	100	100	100
	Dimension 3									
Var (%)	89	86	92	88	91	92	93	90	88	87
n. MH	2	7	11	0	2	1	0	4	0	0
n. MD	0	0	0	0	8	0	2	0	0	0
Correct H (%)	**95**	83	74	**100**	**95**	**98**	**100**	**90**	**100**	**100**
Correct D (%)	100	100	100	100	79	100	95	100	100	100
	Dimension 4									
Var (%)	91	88	94	90	93	93	95	92	90	89
n. MH	2	6	10	2	1	1	1	6	2	1
n. MD	0	0	0	0	0	0	0	0	0	0
Correct H (%)	**95**	**86**	76	**95**	**98**	**98**	**98**	86	**95**	**98**
Correct D (%)	100	100	100	100	100	100	100	100	100	100

Table C.2: Percent of correct classification of Healthy and Damaged observations for the SSP34m-WTB by the actuation in the location A2. In bold and highlighted in grey the percentages greater than 90% for **Healthy** and Damaged observations respectively. Threshold at risk of false alarm probability equal to $\alpha = 0.01$
Var: Total percentage of variance contained in the dimension selected of T
H: Healthy WTB. Total number of healthy observations: 42
D: Damaged WTB. Total number of damaged observations: 39
n. MH: Number of observations from Healthy WTB considered as Damaged WTB
n. MD: Number of observations from Damaged WTB considered as Healthy WTB
Sensors TE: Sensors located in the Trailing Edge

	Actuator 3									
Sensor TE #	1	2	3	4	5	6	7	8	9	10
	Dimension 2									
Var (%)	85	92	85	85	83	86	90	92	92	87
n. MH	12	9	0	6	3	7	7	4	11	9
n. MD	0	0	0	0	0	12	11	33	10	13
Correct H (%)	71	79	**100**	86	**93**	83	83	**90**	74	79
Correct D (%)	100	100	100	100	100	69	72	15	74	67
	Dimension 3									
Var (%)	87	94	88	88	86	88	92	95	94	90
n. MH	12	10	0	7	6	10	7	7	14	11
n. MD	0	0	0	0	0	0	6	29	8	12
Correct H (%)	71	76	**100**	83	86	76	83	83	67	74
Correct D (%)	100	100	100	100	100	100	85	26	79	69
	Dimension 4									
Var (%)	89	95	91	91	89	90	93	96	96	92
n. MH	13	11	1	7	7	10	8	7	12	15
n. MD	0	0	0	0	0	0	0	8	8	11
Correct H (%)	69	74	**98**	83	83	76	81	83	71	64
Correct D (%)	100	100	100	100	100	100	100	79	79	72

Table C.3: Percent of correct classification of Healthy and Damaged observations for the SSP34m-WTB by the actuation in the location A3. In bold and highlighted in grey the percentages greater than 90% for **Healthy** and Damaged observations respectively. Threshold at risk of false alarm probability equal to $\alpha = 0.01$
Var: Total percentage of variance contained in the dimension selected of T
H: Healthy WTB. Total number of healthy observations: 42
D: Damaged WTB. Total number of damaged observations: 39
n. MH: Number of observations from Healthy WTB considered as Damaged WTB
n. MD: Number of observations from Damaged WTB considered as Healthy WTB
Sensors TE: Sensors located in the Trailing Edge

Actuator 4										
Sensor TE #	1	2	3	4	5	6	7	8	9	10
	Dimension 2									
Var (%)	80	85	84	81	81	81	82	85	87	87
n. MH	0	0	0	1	9	1	2	5	0	2
n. MD	0	13	0	0	0	34	0	0	33	38
Correct H (%)	**100**	**100**	**100**	**98**	79	**98**	**95**	88	**100**	**95**
Correct D (%)	100	67	100	100	100	13	100	100	15	3
	Dimension 3									
Var (%)	84	88	88	86	85	85	86	89	90	90
n. MH	3	0	2	2	9	2	0	5	2	2
n. MD	0	10	0	0	0	0	0	0	25	15
Correct H (%)	**93**	**100**	**95**	**95**	79	**95**	**100**	88	**95**	**95**
Correct D (%)	100	74	100	100	100	100	100	100	36	62
	Dimension 4									
Var (%)	88	91	91	90	88	87	89	91	92	92
n. MH	7	0	6	1	9	4	3	5	2	7
n. MD	0	3	0	0	0	0	0	0	0	12
Correct H (%)	83	**100**	86	**98**	79	**90**	**93**	88	**95**	83
Correct D (%)	100	92	100	100	100	100	100	100	100	69

Table C.4: Percent of correct classification of Healthy and Damaged observations for the SSP34m-WTB by the actuation in the location A4. In bold and highlighted in grey the percentages greater than 90% for **Healthy** and Damaged observations respectively. Threshold at risk of false alarm probability equal to $\alpha = 0.01$
Var: Total percentage of variance contained in the dimension selected of T
H: Healthy WTB. Total number of healthy observations: 42
D: Damaged WTB. Total number of damaged observations: 39
n. MH: Number of observations from Healthy WTB considered as Damaged WTB
n. MD: Number of observations from Damaged WTB considered as Healthy WTB
Sensors TE: Sensors located in the Trailing Edge

	Actuator 1									
Sensor LE #	1	2	3	4	5	6	7	8	9	10
					Dimension 2					
Var (%)	93	95	92	97	97	92	89	92	89	86
n. MH	0	0	0	0	0	0	0	0	2	0
n. MD	22	26	38	25	21	5	32	26	0	37
Correct H (%)	**100**	**100**	**100**	**100**	**100**	**100**	**100**	**100**	**95**	**100**
Correct D (%)	44	33	3	36	46	87	18	33	100	5
					Dimension 3					
Var (%)	95	97	95	98	98	94	91	95	93	89
n. MH	1	0	0	0	0	0	1	2	2	1
n. MD	1	26	37	9	0	8	1	0	0	0
Correct H (%)	**98**	**100**	**100**	**100**	**100**	**100**	**98**	**95**	**95**	**98**
Correct D (%)	97	33	5	77	100	79	97	100	100	100
					Dimension 4					
Var (%)	96	98	97	99	98	95	93	96	95	91
n. MH	2	0	0	0	0	0	5	4	2	2
n. MD	0	10	31	5	0	5	0	0	0	0
Correct H (%)	**95**	**100**	**100**	**100**	**100**	**100**	88	**90**	**95**	**95**
Correct D (%)	100	74	21	87	100	87	100	100	100	100

Table C.5: Percent of correct classification of Healthy and Damaged observations for the SSP34m-WTB by the actuation in the location A1. In bold and highlighted in grey the percentages greater than 90% for **Healthy** and Damaged observations respectively. Threshold at risk of false alarm probability equal to $\alpha = 0.01$
Var: Total percentage of variance contained in the dimension selected of T
H: Healthy WTB. Total number of healthy observations: 42
D: Damaged WTB. Total number of damaged observations: 39
n. MH: Number of observations from Healthy WTB considered as Damaged WTB
n. MD: Number of observations from Damaged WTB considered as Healthy WTB
Sensors LE: Sensors located in the Leading Edge

Actuator 2										
Sensor LE #	1	2	3	4	5	6	7	8	9	10
	Dimension 2									
Var (%)	97	96	94	92	90	94	94	90	90	87
n. MH	0	6	0	0	3	0	0	3	4	0
n. MD	0	11	2	39	0	11	8	3	1	3
Correct H (%)	**100**	86	**100**	**100**	**93**	**100**	**100**	**93**	**90**	**100**
Correct D (%)	100	72	95	0	100	72	79	92	97	92
	Dimension 3									
Var (%)	98	97	96	95	93	96	97	92	92	90
n. MH	0	4	1	2	2	2	1	3	8	0
n. MD	0	1	4	35	0	0	6	4	0	6
Correct H (%)	**100**	**90**	**98**	**95**	**95**	**95**	**98**	**93**	81	**100**
Correct D (%)	100	97	90	10	100	100	85	90	100	85
	Dimension 4									
Var (%)	98	98	97	96	94	97	98	94	94	92
n. MH	0	6	2	2	3	3	2	3	8	0
n. MD	0	0	1	35	0	0	6	0	0	2
Correct H (%)	**100**	86	**95**	**95**	**93**	**93**	**95**	**93**	81	**100**
Correct D (%)	100	100	97	10	100	100	85	100	100	95

Table C.6: Percent of correct classification of Healthy and Damaged observations for the SSP34m-WTB by the actuation in the location A2. In bold and highlighted in grey the percentages greater than 90% for **Healthy** and Damaged observations respectively. Threshold at risk of false alarm probability equal to $\alpha = 0.01$

Var: Total percentage of variance contained in the dimension selected of T

H: Healthy WTB. Total number of healthy observations: 42

D: Damaged WTB. Total number of damaged observations: 39

n. MH: Number of observations from Healthy WTB considered as Damaged WTB

n. MD: Number of observations from Damaged WTB considered as Healthy WTB

Sensors LE: Sensors located in the Leading Edge

	Actuator 3									
Sensor LE #	1	2	3	4	5	6	7	8	9	10
	Dimension 2									
Var (%)	88	88	88	87	88	91	89	95	92	88
n. MH	8	7	9	9	0	13	10	12	11	7
n. MD	20	9	14	13	36	13	14	20	9	13
Correct H (%)	81	83	79	79	**100**	69	76	71	74	83
Correct D (%)	49	77	64	67	8	67	64	49	77	67
	Dimension 3									
Var (%)	91	91	91	90	90	93	91	97	94	90
n. MH	6	6	9	9	1	13	8	13	11	9
n. MD	11	9	15	14	28	10	15	10	8	12
Correct H (%)	86	86	79	79	**98**	69	81	69	74	79
Correct D (%)	72	77	62	64	28	74	62	74	79	69
	Dimension 4									
Var (%)	93	92	93	92	92	94	92	98	95	92
n. MH	8	5	10	10	0	12	12	13	11	9
n. MD	1	8	13	4	29	11	4	7	4	12
Correct H (%)	81	88	76	76	**100**	71	71	69	74	79
Correct D (%)	97	79	67	90	26	72	90	82	90	69

Table C.7: Percent of correct classification of Healthy and Damaged observations for the SSP34m-WTB by the actuation in the location A3. In bold and highlighted in grey the percentages greater than 90% for **Healthy** and Damaged observations respectively. Threshold at risk of false alarm probability equal to $\alpha = 0.01$

Var: Total percentage of variance contained in the dimension selected of T

H: Healthy WTB. Total number of healthy observations: 42

D: Damaged WTB. Total number of damaged observations: 39

n. MH: Number of observations from Healthy WTB considered as Damaged WTB

n. MD: Number of observations from Damaged WTB considered as Healthy WTB

Sensors LE: Sensors located in the Leading Edge

	Actuator 4									
Sensor LE #	1	2	3	4	5	6	7	8	9	10
	Dimension 2									
Var (%)	89	90	84	86	86	90	88	90	92	84
n. MH	0	0	0	0	0	0	0	0	0	0
n. MD	34	0	39	37	38	39	39	35	38	39
Correct H (%)	**100**	**100**	**100**	**100**	**100**	**100**	**100**	**100**	**100**	**100**
Correct D (%)	13	100	0	5	3	0	0	10	3	0
	Dimension 3									
Var (%)	91	93	88	89	90	92	90	93	95	86
n. MH	1	0	0	0	0	1	0	0	0	0
n. MD	13	0	0	0	11	39	39	25	37	39
Correct H (%)	**98**	**100**	**100**	**100**	**100**	**98**	**100**	**100**	**100**	**100**
Correct D (%)	67	100	100	100	72	0	0	36	5	0
	Dimension 4									
Var (%)	93	94	91	91	93	93	91	94	96	88
n. MH	2	1	0	3	0	1	0	0	0	0
n. MD	15	0	0	0	0	39	39	26	36	39
Correct H (%)	**95**	**98**	**100**	**93**	**100**	**98**	**100**	**100**	**100**	**100**
Correct D (%)	62	100	100	100	100	0	0	33	8	0

Table C.8: Percent of correct classification of Healthy and Damaged observations for the SSP34m-WTB by the actuation in the location A4. In bold and highlighted in grey the percentages greater than 90% for **Healthy** and Damaged observations respectively. Threshold at risk of false alarm probability equal to $\alpha = 0.01$

Var: Total percentage of variance contained in the dimension selected of T

H: Healthy WTB. Total number of healthy observations: 42

D: Damaged WTB. Total number of damaged observations: 39

n. MH: Number of observations from Healthy WTB considered as Damaged WTB

n. MD: Number of observations from Damaged WTB considered as Healthy WTB

Sensors LE: Sensors located in the Leading Edge